Methods for analysis and classification of non-stationary signals based on eigenvalue decomposition of Hankel matrix

Ph.D. Thesis

by

Vivek Kumar Singh
Roll No. 1901102012

DEPARTMENT OF ELECTRICAL ENGINEERING
INDIAN INSTITUTE OF TECHNOLOGY INDORE

JANUARY 2025

Methods for analysis and classification of non-stationary signals based on eigenvalue decomposition of Hankel matrix

A Thesis

Submitted in partial fulfillment of the
requirements for the award of the degrees
of
Doctor of Philosophy

by
Vivek Kumar Singh
Roll No. 1901102012

DEPARTMENT OF ELECTRICAL ENGINEERING
INDIAN INSTITUTE OF TECHNOLOGY INDORE

JANUARY 2025

INDIAN INSTITUTE OF TECHNOLOGY INDORE

I hereby certify that the work which is being presented in the thesis entitled **Methods for analysis and classification of non-stationary signals based on eigenvalue decomposition of Hankel matrix** in the partial fulfillment of the requirements for the award of the degree of **Doctor of Philosophy** and submitted in the **Department of Electrical Engineering, Indian Institute of Technology Indore**, is an authentic record of my own work carried out during the time period from **June 2019** to **January 2025** under the supervision of **Prof. Ram Bilas Pachori, Professor (HAG), Department of Electrical Engineering, Indian Institute of Technology Indore**.

The matter presented in this thesis has not been submitted by me for the award of any other degree of this or any other institute.

13/10/2025

Signature of the student with date

(Vivek Kumar Singh)

This is to certify that the above statement made by the candidate is correct to the best of my knowledge.

13.10.2025

Signature of Thesis Supervisor with date

(Prof. Ram Bilas Pachori)

Vivek Kumar Singh has successfully given his Ph.D. Oral Examination held on 06 October 2025.

13.10.2025

Signature of Thesis Supervisor with date

(Prof. Ram Bilas Pachori)

ACKNOWLEDGEMENTS

I would like to take the opportunity to thank the people who supported and guided me throughout my PhD journey. This research work would not have been possible without their invaluable contributions.

First of all, I would like to express my sincere gratitude to my PhD supervisor, Prof. Ram Bilas Pachori, for his unwavering support, guidance, and continuous encouragement throughout the duration of my PhD course. His expertise has been invaluable and I am grateful for the same. His passion and dedication have kept me motivated. This thesis would not have been completed without his supervision and support. It was a nice experience to work under him.

I am thankful to the Department of Electrical Engineering, Indian Institute of Technology Indore, for providing resources and a conducive research environment. My grateful thanks to the members of the Postgraduate Student's Progress Committee (PSPC), Prof. Santosh Kumar Vishwakarma and Prof. Sandeep Chaudhary, for their constructive suggestions during my research progress seminars. I would like to acknowledge the Ministry of Human Resource (MHRD) and the Council of Scientific and Industrial Research (CSIR) for providing financial support during this course.

I would like to thank the members of Signal Analysis Research Lab especially, Dr. Pradeep Kumar Chaudhary, Dr. Kritiprasanna Das, Dr. Shailesh Vithhalrao Bhalerao, Mr. Vaibhav Mishra, Col. Makam Kiran Kumar, Mr. Ashok Mahato, Mr. Aditya Nalwaya, Dr. Shailesh Mohine, Mrs. Nabasmita Phukan, Mr. Achinta Mondal, Ms. Amishi Vijay, and Mr. Krishnakant Sharma. It was a nice experience to work with them and have a healthy and fruitful discussion.

I would also like to thank my friends from IIT Indore especially, Dr. Maharana Pratap Singh, Dr. Deepak Kumar, Dr. Justin Jose, Dr. Mayank Singh, Dr. Abhishek Ojha, Dr. Kulbhushan Mishra, Dr. Bikas Kumar Sahu, and Mr. Swapnesh Khade for always being there to celebrate my good times and to support me in hard times. I would also like to thank Dr. Pratik Singh for always motivating me. Further, I would like to thank Mr. Manish Sharma and Mr. Prabhat Singh for all the encouragement they provided.

I must express my profound gratitude to my grandparents, my parents, and my brother for providing me with unfailing and continuous support throughout my years of dissertation. This accomplishment would not have been possible without them. Finally, I would like to offer my prayers to Lord Shiva for blessing me with good health.

Vivek Kumar Singh

Dedicated

to

My Parents, Teachers, and Lord Shiva

ABSTRACT

The natural signals observed in real life are non-stationary and have a time-varying frequency spectrum. Time-frequency analysis (TFA) methods are used to analyze such signals as they provide joint time and frequency information. The signal decomposition methods have gained popularity in TFA after the development of the Hilbert-Huang transform method. Eigenvalue decomposition of the Hankel matrix (EVDHM) is one of these methods from the literature, which has been successfully applied to various applications related to the analysis and classification of non-stationary signals. However, these methods have certain limitations. For instance, they can not separate the signal components overlapping in the frequency domain. Additionally, the decomposed components are obtained from the components corresponding to eigenvalue pairs using frequency-domain information. Furthermore, they do not preserve the mutual information among decomposed components of the multichannel signals. Lastly, these methods are iterative in nature and become computationally expensive. This thesis addresses the limitations of EVDHM-based methods for signal analysis and classification tasks.

The sliding eigenvalue decomposition (EVD) is proposed to separate the signal components, including those overlapped in the frequency domain. In this method, the signal is first divided into small duration overlapping segments, assuming that components within a particular segment are not overlapped in the frequency domain. Then, EVDHM combined with time-domain parameter-based grouping is used to obtain the components of each segment. The decomposed components are obtained by applying the component tracking method to align the decomposed components throughout the segment. The sliding EVD method successfully separated the signal components which are overlapped in the frequency domain. Furthermore, the time-frequency distribution (TFD) of the signal is obtained by applying Hilbert spectrum analysis (HSA) and Wigner-Ville distribution methods to the decomposed components of the signal.

An iterative framework based on EVDHM method and frequency spread and instantaneous frequency-based grouping method is developed, termed empirical mode decomposition (EMD)-like EVDHM, to separate the most dominant signal component in each iter-

ation. The decomposition results of developed framework is compared with the improved EVDHM, EMD, ensemble EMD, empirical wavelet transform (EWT), Fourier-Bessel series expansion-based EWT, variational mode decomposition (VMD), singular spectrum analysis, iterative filtering, Fourier decomposition method (FDM), and empirical FDM methods for clean and noisy signals using quality reconstruction factor and average correlation measures. The EMD-like EVDHM provided superior performance with respect to compared methods in terms of aforementioned performance measures. The TFD of the signal is obtained by applying HSA to the decomposed components. Additionally, proposed method is studied for trend line extraction and weak component extraction.

The multichannel EVDHM (MCh-EVDHM) and improved MCh-EVDHM methods are developed to decompose the multichannel signals while preserving mutual information among the decomposed components across the channel. These methods extract a particular component of all channels using a common eigenvector. The developed methods have been successfully applied for eye movement and Alzheimer's disease detection from electrooculogram and electroencephalogram signals, respectively.

The relationship between eigenvalue of a Hankel matrix of a sinusoidal signal and amplitude of the sinusoidal signal is derived. The mean of magnitude of eigenvalue pairs (MMSEPs) of the sinusoidal signals are found to be linearly related to their amplitude. By utilizing this information, a novel TFD is proposed based on short-duration EVDHM. The short-duration EVDHM provides the time-varying MMSEPs of the signal. Further, TFD is obtained by representing these MMSEPs in the time-frequency plane. The proposed method provides high-resolution TFD as compared to spectrogram, scalogram, short-time Fourier transform-based synchrosqueezing transform, and VMD-based HSA, even for the signal whose components cross each other in time-frequency plane. At last, computationally efficient EVDHM (CEEVDHM) is developed to reduce computational time required to decompose signals using EVDHM method. The CEEVDHM method provides identical decomposed signal components to the EVDHM with significantly reduced computation time.

Keywords: Eigenvalue decomposition of Hankel matrix, time-frequency representation, signal representation, signal analysis, electroencephalogram, electrooculogram, machine learning.

Contents

List of Figures

List of Tables

List of Abbreviations

AFM	Amplitude and frequency modulation
AE	Amplitude envelope
IF	Instantaneous frequency
DFT	Discrete Fourier transform
FM	Frequency modulation
TFA	Time-frequency analysis
TFD	Time-frequency distribution
STFT	Short-time Fourier transform
WVD	Wigner-Ville distribution
HSA	Hilbert spectrum analysis
CWT	Continuous Wavelet transform
HTSA	Hilbert transform separation alogrithm
EMD	Empirical mode decomposition
IMF	Intrinsic mode function
EEMD	Ensemble EMD
VMD	Variational mode decomposition
EWT	Empirical wavelet transform
FBSE	Fourier-Bessel series expansion
FBSE-EWT	FBSE-based EWT
SSA	Singular spectrum analysis
EVDHM	Eigenvalue decomposition of Hankel matrix
FDM	Fourier decomposition method
EFDM	Empirical Fourier decomposition method
EEG	Electroencephalogram
AM	Amplitude modulation
ECG	Electrocardiogram
LDA	Linear discriminant analysis
EMG	Electromyogram

SVM	Support vector machine
EVD	Eigenvalue decomposition
CEEVDHM	Computationally efficient EVDHM
QRF	Quality reconstruction factor
MMSEP	Mean of magnitude of significant eigenvalue pair
MDMS	Most dominant monocomponent signal
MCh-EVDHM	Multichannel EVDHM
EOG	Electrooculogram
MSC	Monocomponent signal criteria
STP	Significant threshold percentage
MSTP	Modified STP
MMSC	Modified MSC
HHT	Hilbert-Huang transform
CW	Choi-Williams
SPWVD	Smoothed pseudo WVD
EMD-WVD	EMD and WVD
HAC	Hierarchical agglomerative clustering
AWGN	Additive white Gaussian noise
SNR	Signal to noise ratio
DWT	Discrete wavelet transform
DMS	Dominant monocomponent signal
ESR	Error to signal ratio
AD	Alzheimer's disease
LSTM	Long short-term memory
TAFD	Time and frequency domain
FSST	STFT-based synchrosqueezing transform

Mathematical Notations

Notation	Signification
$\sin(\cdot)$	Sinusoidal function
$\cos(\cdot)$	Cosine function
$\cosh(\cdot)$	Cosine hyperbolic function
$\arctan(\cdot)$	Inverse tangent function
$X(\tau, \omega)$	Short-time Fourier transform of $x(t)$
$\mathbf{WT}_x(a, b)$	Continuous wavelet transform of $x(t)$
$\psi(t)$	Mother wavelet
$x^*(t)$	Complex conjugate of $x(t)$
$\mathbf{WVD}_x(t, \omega)$	Wigner-Ville distribution of $x(t)$
$\mathcal{H}\{\cdot\}$	Hilbert transform operator
$z_x(t)$	Analytic representation of $x(t)$
$*$	Convolution operator
$\Im\{z\}$	Imaginary part of z
$\Re\{z\}$	Real part of z
$\mathbb{R}$	Set of real numbers
$\mathrm{Tr}(X)$	Trace of the matrix X
$(X)^T$	Transpose of the matrix X
$\log_{10}(x)$	Base-10 logarithm of x
$\ln(x)$	Natural logarithm of x
$\mathcal{F}(x[n])$	Discrete-time Fourier transform of $x[n]$
$\mathcal{F}^{-1}(X(e^{j\omega}))$	Inverse discrete-time Fourier transform of $X(e^{j\omega})$
$\langle a[n], b[n] \rangle$	$(a[n])^T b[n]$ provided $a[n], b[n] \in \mathbb{R}^{1\times N}$
$\mathrm{argmin}(x[n])$	The value of n which minimizes $x[n]$
$x[(n)_M]$	$x[n$ modulo $M]$

Chapter 1

Introduction

Signal is a function of independent variables that conveys some information [2]. It is considered as the output of a system in order to have a meaningful interpretation, whereas a system is associated with input and output signals. For example, the speech signal is the output of the vocal tract filter for which input is source excitation [3, 4]. A signal with N independent variables is known as N-dimensional signal. The speech signal is a one-dimensional signal, i.e., the function of time [3] and the image is a two-dimensional signal, i.e., the function of spatial coordinates [5]. An example of both the signals is shown in Fig. 1.1. Signals can be classified into several classes based on various aspects like the nature of dependent and independent variables, periodicity, causality, variability of characteristic parameters, etc. The signals are represented using mathematical models. It can be classified into two classes, stationary and non-stationary signals, based on the variability of characteristic parameters used to mathematically model the signal. The signal whose parameters, like amplitude and frequency, do not vary with time is stationary; otherwise, it is a non-stationary signal. The sum of sinusoidal signals is considered as a stationary signal and it can be mathematically expressed as,

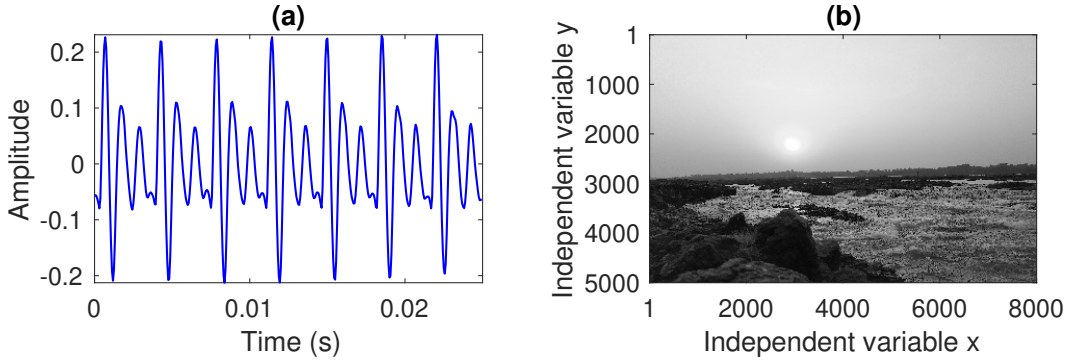

Figure 1.1: Representation of an one-dimensional speech signal taken from CMU ARCTIC speech dataset [1] is shown in (a) and a two-dimensional image is shown in (b).

$$x(t) = \sum_{i=1}^{I} A_i \sin\left(2\pi f_i t + \phi_i\right) \tag{1.1}$$

where A_i, f_i, and ϕ_i are the amplitude, frequency, and phase shift of i^{th} sinusoidal component of the signal, respectively. Whereas, the sum of amplitude-frequency modulated (AFM) signals is a non-stationary signal which is mathematically expressed as,

$$x(t) = \sum_{i=1}^{I} A_i(t) \sin\left(2\pi \int_{-\infty}^{t} f_i(\tau) d\tau + \phi_i\right) \tag{1.2}$$

where $A_i(t)$, $f_i(t)$, and ϕ_i are the amplitude envelope (AE), instantaneous frequency (IF), and phase shift of i^{th} mono-component of the signal, respectively. The time-varying nature of the AE and IF leads to the time-varying spectrum of the signal. For an example, a stationary signal $x_1(t)$ and a non-stationary signal $x_2(t)$ are considered, which are mathematically defined as,

$$x_1(t) = 0.8 \sin\left(20\pi t\right) + 0.6 \sin\left(240\pi t\right) \tag{1.3}$$

$$x_2(t) = 0.85 \sin\left(2\pi \left(10 + 20t\right) t\right) + 0.5 \sin\left(2\pi \left(150 + 10t\right) t\right) \tag{1.4}$$

For the simulation study, $x_1(t)$ and $x_2(t)$ are sampled at sampling rate $f_s = 1000$ Hz and denoted as $x_1[n]$ and $x_2[n]$, respectively. The mathematical representation of discrete-time

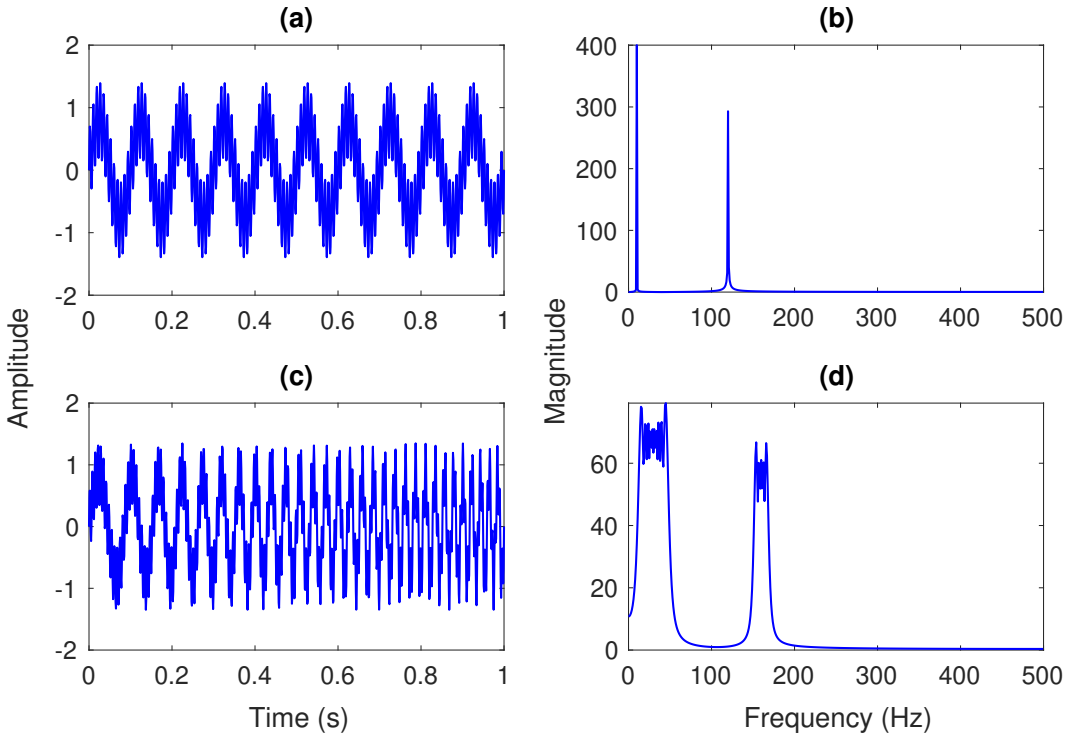

Figure 1.2: Representation of signals $x_1[n]$ and $x_2[n]$ are shown in (a) and (b), respectively. The magnitude of DFT coefficients of $x_1[n]$ and $_2[n]$ are shown in (b) and (d), respectively.

signals $x_1[n]$ and $x_2[n]$ are given by equations (1.5) and (1.6), respectively.

$$x_1[n] = 0.8\sin\left(20\pi\frac{n}{f_s}\right) + 0.6\sin\left(240\pi\frac{n}{f_s}\right) \tag{1.5}$$

$$x_2[n] = 0.85\sin\left(2\pi\left(10 + 20\frac{n}{f_s}\right)\frac{n}{f_s}\right) + 0.5\sin\left(2\pi\left(150 + 10\frac{n}{f_s}\right)\frac{n}{f_s}\right) \tag{1.6}$$

where $n = 0, 1, \ldots, N-1$ and N is the number of samples in the signal. In this chapter, the value of N is considered as 1001 for further studies.

1.1 Signal analysis

The analysis of signal provides the insight about the information they are carrying. The information conveyed by the signal can be analyzed in the time-domain, frequency-domain,

and joint time-frequency domain.

In time-domain analysis, the amplitude of the signal is plotted for each time-instants. For example, the time-domain representations of the signals $x_1[n]$ and $x_2[n]$ are shown in Fig. 1.2 (a) and (c), respectively. For time-localization of the signal $x(t)$, the mean time μ_t and standard deviation σ_t are studied. These parameters are mathematically defined as [6],

$$\mu_t = \frac{\int_{-\infty}^{\infty} t \left|x(t)\right|^2 dt}{\int_{-\infty}^{\infty} \left|x(t)\right|^2 dt} \tag{1.7}$$

$$\sigma_t = \sqrt{\frac{\int_{-\infty}^{\infty} (t-\mu_t)^2 \left|x(t)\right|^2 dt}{\int_{-\infty}^{\infty} \left|x(t)\right|^2 dt}} \tag{1.8}$$

where $\frac{|x(t)|^2}{E}$ is the energy per unit time or energy density and $E = \int_{-\infty}^{\infty} \left|x(t)\right|^2 dt$ is the total energy of the signal $x(t)$. The parameter σ_t is related with the duration of the signal, i.e., duration $= 2\sigma_t$ [2, 6].

The Fourier transform is an approach to obtain the frequency-domain information from the time-domain signal. The Fourier transform $X(\omega)$ of a signal $x(t)$ can be represented as [2, 7],

$$X(\omega) = \int_{-\infty}^{\infty} x(t) e^{-j\omega t} dt \tag{1.9}$$

where $j = \sqrt{-1}$. The Fourier transform is suitable for analysis of stationary signal as the nature of basis function is also stationary. The frequency localization of the signal $x(t)$ is studied with the help of mean frequency μ_ω and σ_ω parameter which are mathematically represented as [6],

$$\mu_\omega = \frac{\int_{-\infty}^{\infty} \omega \left|X(\omega)\right|^2 d\omega}{\int_{-\infty}^{\infty} \left|X(\omega)\right|^2 d\omega} \tag{1.10}$$

$$\sigma_\omega = \sqrt{\frac{\int_{-\infty}^{\infty} (\omega - \mu_\omega)^2 \left|X(\omega)\right|^2 d\omega}{\int_{-\infty}^{\infty} \left|X(\omega)\right|^2 d\omega}} \tag{1.11}$$

where $\frac{|X(\omega)|^2}{E}$ is the energy per unit frequency or energy density spectrum and $E = \int_{-\infty}^{\infty} \left|X(\omega)\right|^2 d\omega$ is the total energy of the signal $x(t)$. The quantity $2\sigma_\omega$ is the bandwidth of the signal $x(t)$ [2, 6].

The Fourier transform is defined for continuous-time signals and for simulation studies, the discrete Fourier transform (DFT) is considered. The DFT of a discrete-time signal $x[n]$ (sampled version of continuous-time signal $x(t)$) for $n = 0, 1, \ldots, N-1$ is defined as [8–10],

$$X[k] = \sum_{n=0}^{N-1} x[n] e^{-j2\pi \frac{nk}{N}} \quad \text{for } k = 0, 1, \ldots, N-1 \tag{1.12}$$

The fast Fourier transform is an efficient algorithm with respect to computation time for computation of the DFT of a discrete-time signal [8, 9, 11]. The magnitude of DFT coefficients of signals $x_1[n]$ and $x_2[n]$ are shown in Fig. 1.2 (b) and (d), respectively. From the aforementioned figure, it can be observed that it provides the frequency information for both stationary and non-stationary signals and does not provide information about their time-localization. Consider a mono-component frequency modulated (FM) signal $x_3[n]$ for $n = 0, 1, \ldots, N-1$ defined as,

$$x_3[n] = 0.85 \sin\left(2\pi \left(10 + 20\frac{n}{f_s}\right) \frac{n}{f_s}\right) \tag{1.13}$$

where $N = 1001$ and $f_s = 1000$ Hz. The time-domain signal $x_3[n]$ and its magnitude of DFT coefficients $X_3[k]$ are shown in Figs. 1.3 (a) and (b), respectively. The signal $x_4[n]$ (obtained as real part of inverse DFT of $X_3[k]$) and its magnitude of DFT coefficients are shown in Figs. 1.3 (c) and (d), respectively. Comparison of Figs. 1.3 (b) and (d) shows

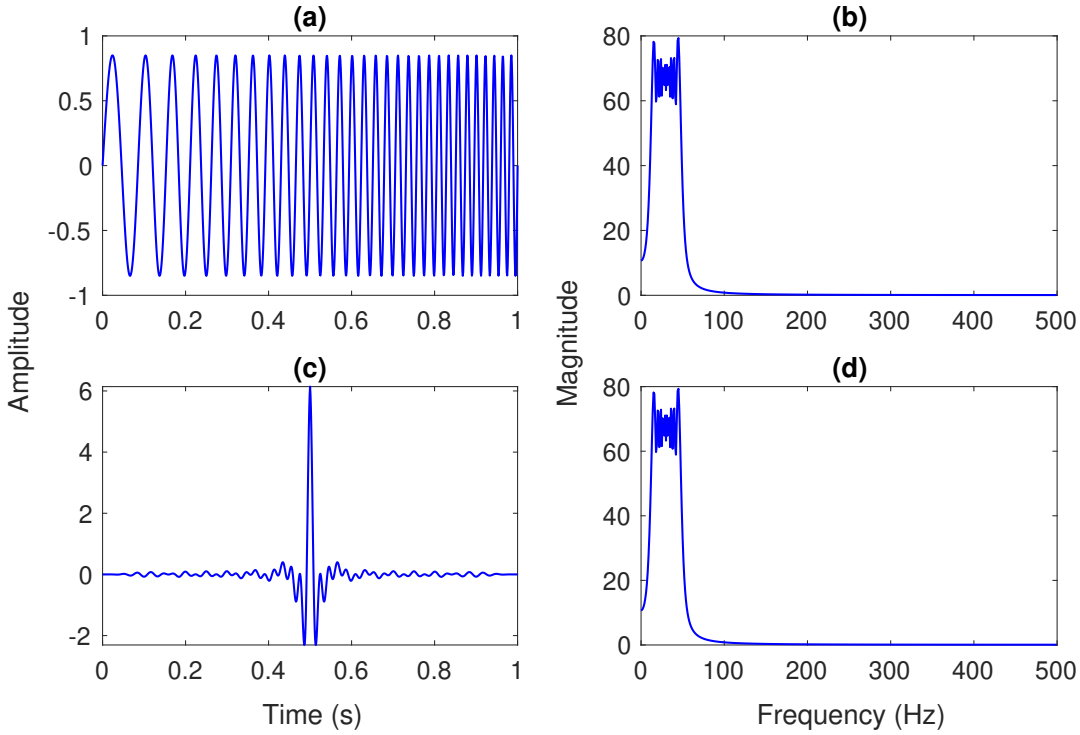

Figure 1.3: The signal $x_3[n]$ and the magnitude of its DFT are shown in (a) and (b), respectively. The signal $x_4[n]$ and its magnitude of DFT are shown in (c) and (d), respectively.

that, the two different signals can have similar magnitude spectrum. The studies based on Figs. 1.2 and 1.3 indicate that Fourier transform-based methods do not provide meaningful analysis of non-stationary signals also the magnitude spectrum is not unique.

1.2 Time-frequency analysis

The non-stationary signals can be better analyzed with the help of time-frequency analysis (TFA) methods which result the time-frequency distribution (TFD). The TFD provides the time-varying frequency characteristics of the signals. There are various time-frequency analysis methods in literature namely, short-time Fourier transform (STFT) [12], wavelet transform [13], Wigner-Ville distribution (WVD) [14, 15], Hilbert spectrum analysis (HSA) [16], etc.

The TFA methods performs the meaningful analysis of the non-stationary signals by providing its TFD. There are several TFA methods, each with their respective advantages and disadvantages. They are briefly presented in this section.

1.2.1 Short-time Fourier transform

The STFT assumes that the signal under analysis is stationary for small duration of time. In this method, the signal is segmented into frames with the help of a suitable window function. The Fourier transform of each frame is computed to obtain the frequency-domain information of the particular frame [11, 17]. The STFT of a signal $x(t)$ is mathematically represented as [2, 18, 19],

$$X(\tau, \omega) = \int_{-\infty}^{\infty} x(t)p(t-\tau)e^{-j\omega t}dt \tag{1.14}$$

where $p(t)$ is the analysis window function. It is a complex-valued quantity. For representation purposes, the squared magnitude of STFT, which is known as spectrogram, is used [19, 20]. The spectrogram of the signal is represented as,

$$\text{Spectrogram} = |X(\tau, \omega)|^2 = \left| \int_{-\infty}^{\infty} x(t)p(t-\tau)e^{-j\omega t}dt \right|^2 \tag{1.15}$$

It is a non-linear operation. For visual representation, the spectrogram of a signal is contour plotted. The simple steps for calculation and ease of interpretation made it popular in several domains including speech signal processing. The spectrogram is a very basic TFA method and its resolution is dependent on the length and type of the used window. For smaller duration window, the time resolution is good and frequency resolution is poor and vice-versa due to the principle of uncertainty [19, 21]. These conflicting statements render STFT of limited use. For an example, the contour plots of the spectrogram of the signal $x_2[n]$

defined in equation (1.6) using a Hamming window of various lengths and step size of 10 samples are provided in Fig. 1.4. From the aforementioned figure, it can be seen that the frequency resolution of the spectrogram is becoming better by increasing the window size, whereas time resolution is getting poor. The preliminary assumption made while computing STFT is that the signal should be stationary within the window considered for analysis, which is not always the case with real-time signals. Also, choosing a proper window length for STFT-based analysis is a challenging task. In adaptive STFT, the window length of the signal is computed adaptively from the signal using the cone length of optimal cone kernel distribution [22]. The optimal cone kernel distribution cone length is the duration over which the signal is either stationary or has a slowly varying frequency structure [23].

The spectrogram can be narrowband or wideband based on the large or short-duration analysis windows, respectively. These two types of spectrograms are commonly used in speech analysis [17, 21]. In a narrowband spectrogram, a longer analysis window is considered for better frequency resolution. The fundamental frequency of the speech signal and its harmonics are visible as horizontal striations in narrowband spectrogram [3, 21]. In a wideband spectrogram, a shorter analysis window is considered in order to achieve high time resolution. The instants of significant excitation in the speech signal are visible as vertical striations in wideband spectrogram [3, 21].

1.2.2 Continuous wavelet transform

The signal components in the lower frequency region i.e., sinusoids require good frequency resolution which can be achieved using longer duration window size; whereas the components in higher frequency region i.e., transients require good time-resolution which can be achieved using shorter duration window. This type of analysis is not possible using spectrogram-based approach. This has been achieved using wavelet transform method.

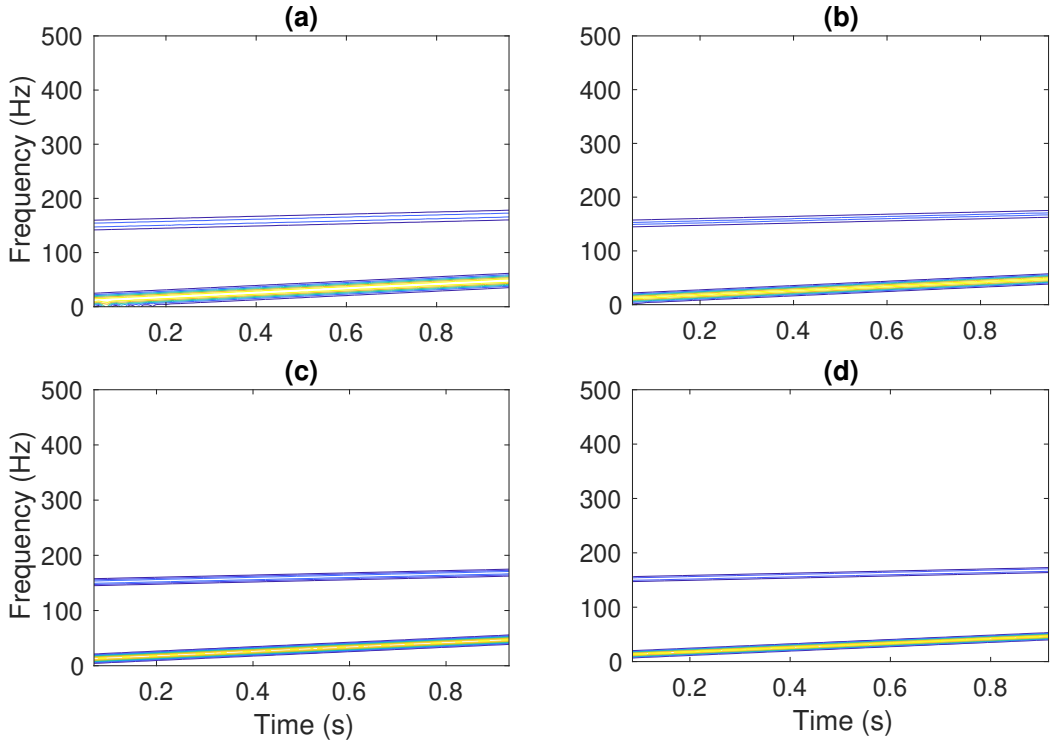

Figure 1.4: Contour plots of spectrogram of the signal $x_2[n]$ obtained using Hamming window of lengths 80, 110, 140, and 170 samples are shown in (a), (b), (c), and (d), respectively.

In continuous wavelet transform (CWT), a mother wavelet is selected and it has been dilated and translated to obtain daughter wavelets that are set of basis functions [13]. The mathematical representation of the CWT is represented as [13, 24, 25],

$$\mathrm{WT}_x(a,b) = \int_{-\infty}^{\infty} x(t)\frac{1}{\sqrt{a}}\psi^*\left(\frac{t-b}{a}\right)dt = \int_{-\infty}^{\infty} x(t)\psi^*_{a,b}(t)dt \tag{1.16}$$

where $\psi_{a,b}(t)$ are the basis functions, b is the translation parameter, a is the scaling parameter, and $a > 0$ [26]. The mother wavelet $\psi(t)$ has to satisfy three properties in order to have meaningful analysis and proper reconstruction of the signal. These properties are defined below [13, 24].

1. The function $\psi(t)$ has zero mean, i.e., it is of oscillatory nature. This is mathemati-

cally defined as,

$$\int_{-\infty}^{\infty} \psi(t)dt = 0 \tag{1.17}$$

or $\Psi(0) = 0$, where $\Psi(\omega)$ is the Fourier transform of $\psi(t)$.

2. The function $\psi(t)$ is square integrable, i.e., it has finite energy.

$$\int_{-\infty}^{\infty} |\psi(t)|^2 \, dt < \infty \tag{1.18}$$

3. It should satisfy admissibility condition in order to have proper reconstruction, i.e. [27],

$$\int_{0}^{\infty} \frac{|\Psi(\omega)|^2}{|\omega|} d\omega < \infty \tag{1.19}$$

The scalogram is defined as the squre of magnitude of the CWT coefficients of the signals. This is mathematically defined as,

$$|\mathrm{WT}_x(a,b)|^2 = \left| \int_{-\infty}^{\infty} x(t)\psi^*_{a,b}(t)dt \right|^2 \tag{1.20}$$

The resolution of scalogram of a signal is dependent on the type of mother wavelet selected for analysis. For example, the scalogram of the signal $x_2[n]$ (defined using equation (1.6)) computed using the Morse, analytic Morlet, and bump mother wavelets are shown in Fig. 1.5. It can been seen that, the bump wavelet have higher frequency resolution among the three considered mother wavelets. However, it will not be case always. The selection of mother wavelet is done based on the characteristics of signal under analysis for better analysis. The CWT has been proven to be an useful tool in singularity detection in the signal under analysis [28].

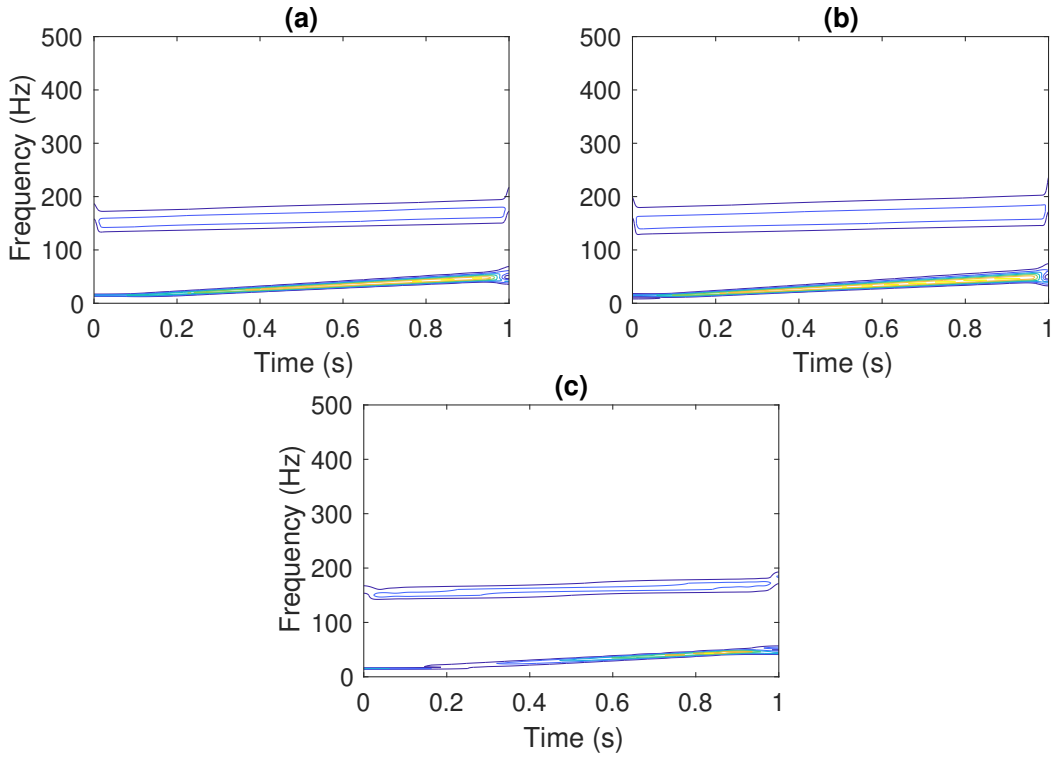

Figure 1.5: Contour plot of scalogram of the signal $x_2[n]$ obtained using CWT with Morse, analytic Morlet, and bump mother wavelets are shown in (a), (b), and (c), respectively.

1.2.3 Wigner-Ville distribution

The WVD of a non-stationary signal can be considered as a classical method for obtaining TFD. It is the Fourier transform of the central autocovariance function of the signal. The mathematical expression for computation of WVD of a signal $x(t)$ in the time-domain can be given by the following equation [14, 29, 30]:

$$\text{WVD}_x\left(t,\omega\right) = \int_{-\infty}^{\infty} \left[x\left(t+\frac{\eta}{2}\right) x^*\left(t-\frac{\eta}{2}\right)\right] e^{-j\omega\eta} d\eta \tag{1.21}$$

where $x^*(t)$ represents the complex conjugate of $x(t)$. Some of the properties of WVD, like time and frequency support preservation, very high time and frequency resolutions, etc, make it a very useful tool for signal analysis [14]. However, due to its bilinear nature, some spurious components or cross-term get introduced in between the true signal components

which lead to deterioration of TFD [31]. To understand the nature of cross-term, we have considered a signal which is defined by Eq. 1.22 [31, 32].

$$x(t) = x_1(t) + x_2(t) = \sum_{i=1}^{2} a_i(t)\, \mathrm{e}^{j(\omega_0 + \frac{1}{2}\beta t)t} \tag{1.22}$$

Where, $a_1(t) = A_1\, \mathrm{e}^{j\omega_1 t}$, $a_2(t) = A_2\, \mathrm{e}^{j\omega_2 t}$. The WVD of the multicomponent signal $x(t)$ has the following form:

$$\mathrm{WVD}_x(t,\omega) = \mathrm{WVD}_a(t,\omega) + \mathrm{WVD}_c(t,\omega) \tag{1.23}$$

Where, $\mathrm{WVD}_a(t,\omega)$ represents the auto-term of WVD which can be expressed as [31],

$$\begin{aligned}\mathrm{WVD}_a(t,\omega) = \int_{-\infty}^{\infty} \left[x_1\left(t+\frac{\eta}{2}\right) x_1^*\left(t-\frac{\eta}{2}\right)\right] e^{-j\omega\eta} d\eta \\ + \int_{-\infty}^{\infty} \left[x_2\left(t+\frac{\eta}{2}\right) x_2^*\left(t-\frac{\eta}{2}\right)\right] e^{-j\omega\eta} d\eta\end{aligned} \tag{1.24}$$

For the signal $x(t)$ represented in equation (1.22), the auto-term is obtained as follows:

$$\mathrm{WVD}_a(t,\omega) = 2\pi \left(A_1^2\, \delta\left(\omega - (\omega_1 + \omega_0) - \beta t\right) + A_2^2\, \delta\left(\omega - (\omega_2 + \omega_0) - \beta t\right)\right) \tag{1.25}$$

where $\delta(t)$ is the Dirac delta function. The term $\mathrm{WVD}_c(t,\omega)$ represents the cross-term of WVD which can be expressed as [31],

$$\mathrm{WVD}_c(t,\omega) = 2\Re\left[\int_{-\infty}^{\infty} \left[x_1\left(t+\frac{\eta}{2}\right) x_2^*\left(t-\frac{\eta}{2}\right)\right] e^{-j\omega\eta} d\eta\right] \tag{1.26}$$

where $\Re$ is the real part of a complex value. Similarly, for the signal $x(t)$ represented in equation (1.22), the cross-term is obtained as follows:

$$\mathrm{WVD}_c(t,\omega) = 2\Re\left[2\pi A_1 A_2\, \delta\left(\omega - \left(\frac{\omega_1+\omega_2}{2} + \omega_0\right) - \beta t\right)\, e^{j(\omega_2 - \omega_1)t}\right] \tag{1.27}$$

From the equations (1.25) and (1.27), it is observed that the cross-term occurs at the mid-frequency of auto-term and oscillates at differences in the auto-term frequencies. Furthermore, it is observed that the cross-term can have an even larger amplitude than the auto-term.

If the signal under analysis ($x(t)$) is not a non-analytic real-valued mono-component signal, the WVD will have a cross-term at 0 Hz frequency occurring because of the positive and negative frequency components [33]. It is necessary to first compute the analytic representation of $x(t)$, i.e., $z_x(t)$, and then compute the WVD of it to get the cross-term free WVD of a real-valued mono-component signal [33, 34]. The analytic representation of $x(t)$ is obtained as[35–37],

$$z_x(t) = x(t) + j\mathcal{H}\left\{x(t)\right\} \tag{1.28}$$

where

$$\mathcal{H}\left\{x(t)\right\} = x(t) * \frac{1}{\pi t} = \frac{1}{\pi}\text{p.v.} \int_{-\infty}^{\infty} \frac{x(\tau)}{t-\tau} d\tau \tag{1.29}$$

The $*$ is the convolution operator and p.v. denotes the Cauchy's principal value of the improper integral.

The WVD of two signals $x_3[n]$ and $x_2[n]$ defined by equations (1.13) and (1.6), respectively, is depicted in Figs. 1.6 (a) and (b). The signal $x_3[n]$ is a mono-component signal, hence, its WVD has only an auto-term. However, the signal $x_2[n]$ is a multicomponent signal and its WVD has two auto-terms and a cross-term in between the auto-terms. Presence of cross-term in the WVD-based TFD makes it hard to interpret which one is auto-term and which one is cross-term unless we know the instantaneous frequency law of the signal components. So, cross-term free WVD is required to give interpretable TFD.

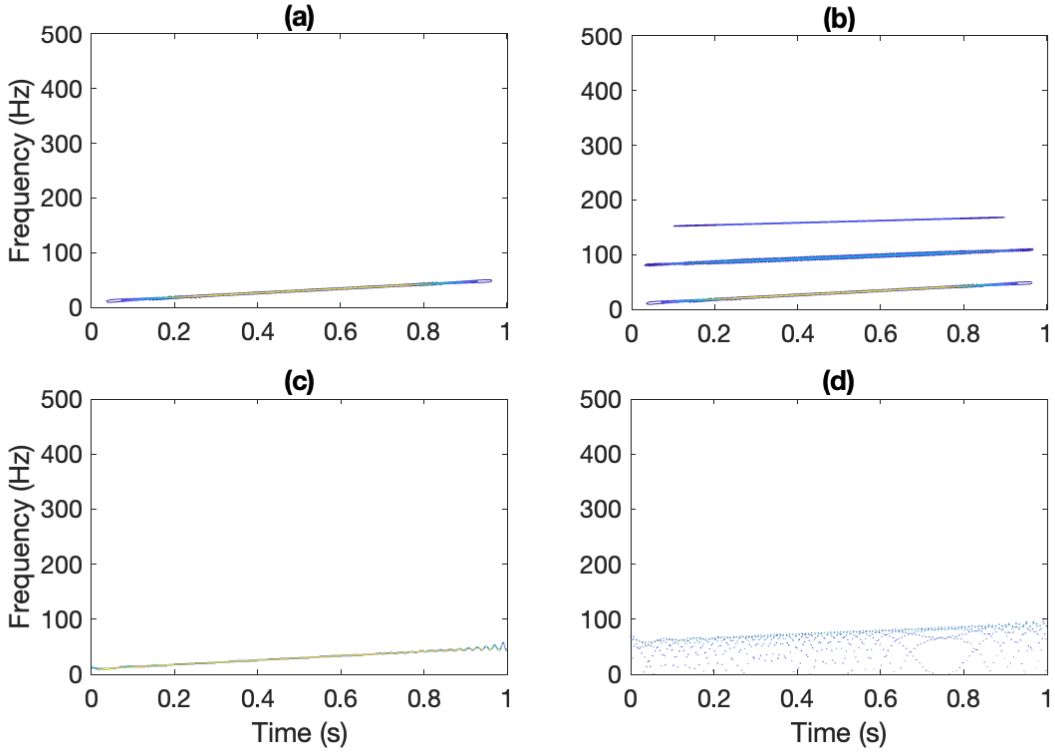

Figure 1.6: Contour plots of magnitude of WVD of the signals $x_2[n]$ and $x_3[n]$ are shown in (a) and (b), respectively. TFDs of the signals $x_2[n]$ and $x_3[n]$ obtained using HSA are shown in (c) and (d), respectively.

1.2.4 Hilbert spectrum analysis

This method provides the TFD of a signal by representing its AE and IF in time-frequency plane. The AE and IF of the signal is obtained using Hilbert transform separation algorithm (HTSA) [35]. Consider a signal $x(t)$, AE and IF parameters are computed with the help of its analytic representation as given in equation (1.28. The aforementioned equation can be represented in polar form as,

$$z_x(t) = a(t)e^{j\phi(t)} \tag{1.30}$$

where $a(t) = \sqrt{(x(t))^2 + (\mathcal{H}\{x(t)\})^2}$ is AE and $\phi(t) = \arctan\left(\frac{\mathcal{H}\{x(t)\}}{x(t)}\right)$ is the instantaneous phase. Furthermore, the IF of the signal is obtained using, $\omega(t) = \frac{d}{dt}\phi(t)$ [2, 38].

The HSA of a discrete-time signal $x[n]$ of length N samples is performed by computing its corresponding analytic signal $z_x[n]$ using a fast Fourier transform-based approach, which is described below from steps S1 to S3 [39].

S1: Compute the DFT coefficients $X[k]$ of signal $x[n]$ using fast Fourier transform method.

S2: Obtain the DFT coefficients corresponding to analytic representation of $x[n]$ using,

$$Z_x[k] = \begin{cases} X[k], & i = 0, \frac{N}{2} \\ 2X[k], & i = 1, 2, \ldots, \frac{N}{2} - 1 \\ 0, & i = \frac{N}{2} + 1, \frac{N}{2} + 2, \ldots, N - 1 \end{cases} \tag{1.31}$$

S3: Computed inverse DFT of $Z_x[k]$ to obtain the analytic representation of the signal $x[n]$, i.e., $z_x[n]$.

There are several finite impulse response filter-based approaches in literature to obtain the analytic representation of $x[n]$ [40, 41]. The AE ($a[n]$) and IF ($\omega[n]$) of the signal $x[n]$ obtained from its analytic representation are defined as,

$$a[n] = |z_x[n]| \tag{1.32}$$

and

$$\omega[n] = \arctan\left(\frac{\Im\{z_x[n+1]\}}{\Re\{z_x[n+1]\}}\right) - \arctan\left(\frac{\Im\{z_x[n]\}}{\Re\{z_x[n]\}}\right) \tag{1.33}$$

where $\Im$ is imaginary part of a complex value. The TFD is obtained by representing the instantaneous energy (square of AE) and IF in time-frequency plane [16].

1.2.4.1 mono-component signal

Consider an analytic AFM mono-component signal defined as, $x(t) = a(t)e^{j\phi(t)}$. The AE and IF of the signal are $a(t)$ and $\frac{d}{dt}\phi(t)$. Similarly, the AE and IF of a complex exponential signal $x(t) = Ae^{j\omega_0 t}$ are A and ω_0, respectively.

1.2.4.2 Multicomponent signal

Consider an analytic multicomponent signal defined as, $x(t) = \sum_{i=1}^{I} a_i(t)e^{j\phi_i(t)}$. The AE and IF of the signal are $a(t)$ and $\phi(t)$, respectively such that, $x(t) = a(t)e^{j\phi(t)}$. These extracted IA and IF parameters of multicomponent signal $x(t)$ are not meaningful. To understand it better, consider a multicomponent signal as sum of two complex exponential signals, i.e., $x(t) = a_1 e^{j\omega_1 t} + a_2 e^{j\omega_2 t}$. This can be further expanded as [38],

$$x(t) = (a_1 \cos(\omega_1 t) + a_2 \cos(\omega_2 t)) + j\,(a_1 \sin(\omega_1 t) + a_2 \sin(\omega_2 t)) = a(t)e^{j\phi(t)} \tag{1.34}$$

where

$$a(t) = \sqrt{a_1^2 + a_2^2 + 2a_1 a_2 \cos\left(\omega_1 - \omega_2\right) t} \tag{1.35}$$

and

$$\phi(t) = \arctan\left(\frac{a_1 \sin(\omega_1 t) + a_2 \sin(\omega_2 t)}{a_1 \cos(\omega_1 t) + a_2 \cos(\omega_2 t)}\right) \tag{1.36}$$

Furthermore, the IF of the signal is computed as,

$$\omega(t) = \frac{d}{dt}\phi(t) = \frac{\omega_1 + \omega_2}{2} + \frac{\left(\omega_1 - \omega_2\right)\left(a_1^2 - a_2^2\right)}{2\left(a_1^2 + a_2^2 + 2a_1 a_2 \cos\left(\omega_1 - \omega_2\right) t\right)} \tag{1.37}$$

The TFD of signals $x_3[n]$ and $x_2[n]$, defined by equations (1.13) and (1.6), respectively, obtained using HSA method are shown in Figs. 1.6 (c) and (d). The TFD of the mono-component signal $x_3[n]$ is is well defined. However, TFD of the multicomponent signal

$x_2[n]$ is not meaningful because the AE and IF parameters of multicomponent signal obtained using HTSA method are not meaningful.

1.3 Data-adaptive signal decomposition

A multicomponent or composite signal consist of a set of mono-component or its constituent signals. The constituent components of a multicomponent signal can be obtained using decomposition techniques [42].

1.3.1 Univariate signal decomposition

The concept of signal decomposition was popularized after the development of the empirical mode decomposition (EMD) method to decompose the signal into a set of intrinsic mode function (IMFs) [16, 43]. The IMFs possess two properties: (1) the number of extrema and zero crossings differ at most by one, and (2) the mean of the upper and lower envelopes is zero. After the development of EMD, various new and improved signal decomposition methods were presented in the literature to decompose the signal into its constituent components. A few of them are namely, ensemble EMD (EEMD) [44], variational mode decomposition (VMD) [45], empirical wavelet transform (EWT) [46], variable spectral segmentation EWT [47], Fourier-Bessel series expansion (FBSE)-based EWT (FBSE-EWT) [48], singular spectrum analysis (SSA) [49], sliding SSA [50], eigenvalue decomposition of Hankel matrix (EVDHM) [51], iterative EVDHM [52], improved EVDHM [53], Fourier decomposition method (FDM) [54], empirical FDM (EFDM) [55] etc. In these methods, the signal is first decomposed then TFD is obtained by applying HSA on the decomposed components.

The EMD method decomposes the signal into a set of IMFs using the sifting process [16]. The HSA of the IMFs provides the TFD of the signal. The EMD suffers from mode-mixing problem, i.e., a single IMF component contains the parts of two different scale

components of the signal. Furthermore, the IMFs of a noisy signal contain part of the noise due to the completeness of the EMD technique. To overcome these problems of EMD, the EEMD was proposed in literature [44]. The EEMD decomposes an ensemble of noisy signals and obtains the IMFs as the average of IMFs of each noisy signal. However, EEMD has two limitations: firstly, the reconstructed signal contains the noise, and secondly, the number of IMFs in each noisy signal might differ. To overcome these limitations of EEMD, the complementary EMD, complete EEMD, and improved complete EEMD methods were proposed in literature [56–58]. The steps involved in the EMD-based methods are intuitive and do not have a mathematical foundation.

The EWT was proposed in the literature to decompose the signal in terms of empirical modes. In EWT method [46], a method to develop data-adaptive wavelets is presented, which is useful in extracting the AFM components of the signal having compact frequency boundaries. The boundaries of the components on the frequency spectrum are identified, and the components are extracted between two consecutive boundaries using the adaptive wavelet-based approach [46]. The boundary detection proposed in EWT fails to identify the proper boundaries for noisy signals [59]. To overcome this issue, the enhanced EWT method [59] was developed in which the boundaries are detected based on the spectrum of the envelope of the signal obtained using an order statistic filter [60]. The FBSE spectrum has several advantages over the Fourier transform-based spectrum, like double frequency resolution and the use of non-stationary basis functions [61–64]. In [48], the higher resolution of the FBSE spectrum is utilized to efficiently obtain the spectral boundaries based on scale space [65] and Otsu's [66] methods in order to design the adaptive wavelets for mode extraction. The VMD is a spectral segmentation-based signal decomposition method. In VMD [45], firstly, the number of modes, modes, and their center frequency are initialized, then minimize the bandwidth by solving the variational problem defined using augmented

Lagrangian [67, 68] based on alternate direction method of multipliers [69, 70] until the modes converge. Later, the extensions of the VMD method have been proposed in the literature, namely adaptive VMD [71] and successive VMD [72].

The FDM decomposes the signal into a set of Fourier intrinsic band functions [54]. The Fourier intrinsic band functions are zero mean and have positive AE and IF parameters. These are extracted based on frequency scanning techniques, namely, low-to-high and high-to-low scanning of the Fourier spectrum of the signal. It is a recursive process. The results obtained from both scanning techniques are different. Hence, it is unclear when to use one of these scanning techniques for signal decomposition based on FDM. The EFDM decomposes the signal into components based on an improved segmentation technique and zero-phase filter [55]. The improved segmentation technique divides the magnitude of the Fourier-based spectrum into N contiguous segments based on the lowest minima technique [55, 73]. Further, a zero-phase band-pass filter bank is constructed based on the obtained segments to extract the signal components. In the EFDM, the number of segments needs to be given input for the decomposition of the signal, which is not known for real-life signals.

The SSA and EVDHM are the data-adaptive signal decomposition techniques, which first compute the Hankel matrix corresponding to the input signal and then perform singular value decomposition and eigenvalue decomposition, respectively [49, 51, 74]. In the SSA method, the elementary components of the signals are computed by performing diagonal averaging of the symmetric matrices corresponding to each singular value [49]. However, in EVDHM, decomposed signal components are obtained by averaging skew-diagonal elements of the symmetric matrices obtained from a significant eigenvalue pair and their respective eigenvectors [51, 74]. The extension of SSA, namely automated SSA [75] and sliding SSA [50], are developed in the literature. The iterative EVDHM [52] and improved EVDHM [53] methods are extensions of the EVDHM method. Both iterative and improved

EVDHM methods are iterative in nature and utilize the spectral overlap-based grouping method to obtain the mono-component signals from the decomposed components.

1.3.2 Multivariate signal decomposition

Due to developments in sensor technologies, the multichannel signals, e.g., doppler radar signals, float drift data, electroencephalogram (EEG) signals, etc., are arising routinely [76–78]. The processing of these signals using univariate signal analysis methods does not preserve the mutual information among the channels. The multivariate signal processing methods are developed to preserve the mutual information between the channels for time-frequency analysis [76, 79, 80]. These concepts for the analysis of multichannel signals are based on the multivariate oscillation model, i.e., common oscillations or signal components that fit for all channels [76]. The concept of multivariate TFD is developed from synchrosqueezing transform-based decomposition of signals into subband signals and obtaining joint AE and IF [77]. Furthermore, the extension of univariate signal decomposition methods for the analysis of multichannel signals while preserving mode alignment is studied.

In the multivariate extension of the EMD method, the computation of the local mean of the multichannel signal is challenging. For the same, the directional vectors are obtained from hyperspheres using uniform angular sampling and quasi-Monte Carlo-based low discrepancy sequences [81, 82]. The real-valued projection of these directional vectors provides the mean of the multivariate signals which is used for decomposition of these signals into a set of mode-aligned IMFs [83, 84].

The multivariate extension of EWT method based on a new boundary detection approach for decomposition of multichannel signals is developed [85]. The mean of the magnitude of Fourier spectrum of the multichannel signals is utilized to obtain the spectral boundaries.

The Littlewood-Paley and Meyer's wavelet filter bank are developed based on the obtained spectral boundaries [46, 85]. This filter bank is utilized to obtain the subband signals corresponding to each channels of the multivariate signal. The subband signals of each channel have aligned oscillatory nature as they are extracted using the same filter bank [85]. In another study [86], the boundary detection is performed on the magnitude of zero-order FBSE coefficients instead of the Fourier spectrum. The obtained spectral boundaries are utilized to develop a Littlewood-Paley and Meyer's wavelet filter bank in Fourier domain. The subband signals are obtained by processing the multivariate signal using the developed filter bank [86].

Several other multivariate extension of the univariate signal decomposition methods are presented in the literature. Few of them are partial noise assisted multivariate EMD [87], multivariate VMD [88], multivariate nonlinear chirp mode decomposition [89], multivariate intrinsic chirp mode decomposition [90], adaptive multivariate chirp mode decomposition [91], multivariate SSA [92], multivariate iterative filtering [78, 93], multivariate dynamic mode decomposition [94, 95], etc.

1.3.3 Complex-valued signal decomposition

Various real-life signals like, center of pressure signal [96], wind signal [97–100], mechanical rubbing signal [101], float drift data [101], radio frequency signal [102] etc. are represented in terms of complex-valued signal for analysis and processing. The real and imaginary parts of these complex-valued signals are mutually dependent [100]. Processing of real and imaginary parts separately using univariate signal analysis methods will lead to loss of the mutual information.

To preserve mutual information and decompose them into their constituent components, the complex EMD was first introduced in the literature [100]. In complex EMD method, the

real-valued positive and negative frequency components of the signal are obtained using an ideal band-pass filter defined as [100],

$$H(\omega) = \begin{cases} 1, & 0 \leq \omega < \pi \\ 0, & -\pi \leq \omega < 0 \end{cases} \tag{1.38}$$

The positive and negative frequency components are separately decomposed into a set of IMFs with the help of EMD method. The complex-valued IMFs are then obtained with the help of Hilbert transform. The TFD of the complex-valued signal is obtained by applying HSA on the IMFs.

In literature, there are various extensions of univariate signal decomposition method for analysis of complex-valued signals. These are complex VMD [101], continuous empirical wavelet systems [103], complex improved EVDHM [104], complex flexible analytic wavelet transform [102], complex FBSE-EWT [105], etc.

1.4 Applications of signal decomposition-based analysis

The TFD of the signal and its constituent components obtained using the decomposition methods discussed in section 1.3 provide a meaningful insight about the signal. These methods have been utilized to extract meaningful features to study the real-life signals for various application like, emotion recognition [106–110], speech recognition [111–113], speech enhancement [114–116], disease diagnosis and detection [117–122], etc.

In [118], the EEG signals are decomposed into set of IMFs using EMD method [16], the amplitude modulation (AM) and FM bandwidth [123] are computed from the IMFs and classified into seizure and non-seizure classes using least square support vector machine (SVM) classifier [124]. In [125], electrocardiogram (ECG) signals are decomposed using the EMD method into a set of IMFs. From these IMFs, the baseline wander noise is reduced

by removing higher indexed IMFs based on the global slope minimization method, and then high-frequency noise is suppressed by discarding higher indexed IMFs. From the remaining IMFs, a partial reconstruction is performed for QRS detection. In [126], the multichannel EEG signals are decomposed using multivariate EMD [83] into a set of IMFs, the common spatial pattern [127]-based features are extracted from the IMFs and classified into different imagery tasks. In [96], the center of pressure signals is decomposed into a set of complex IMFs using complex EMD [100] method. Then, the postural stability is identified based on the area of the analytic IMFs in the complex plane and its average rotation frequency features.

In [110], the 31-second duration EEG signals are decomposed into subband signals using the VMD method. The differential entropy [128] and signal-time energy [129] features are extracted from the 4-second segments of the subband signals using a sliding window approach. The optimal features are selected using linear discriminant analysis (LDA) [130] and classified into different emotional states using XGBoost classifier with Bayesian optimizer [131, 132]. In [133], the ECG signal is decomposed into a set of subband signals, and then low and high-frequency noises are suppressed by performing selective reconstruction. R-peak detection is performed from the reconstructed signal. In [134], the three time-series namely, newbuilding ship price, secondhand ship price, and ship scrap value, are decomposed into common oscillatory modes using multivariate VMD method. The machine learning-based forecast model is trained for each common mode to forecast their future values. The final forecast of each of the three time series is performed by adding their respective forecast for all modes. In [101], the analysis of wind signal, mechanical rubbing signal, and float drift data is performed with the help of the complex VMD method and HSA.

In [135], each column of the seismic signal is decomposed using the EWT method,

and the corresponding TFD is obtained by applying HSA on the decomposed modes. In this way, the two-dimensional seismic signal is transformed into a three-dimensional representation. For frequency specific analysis of the seismic signals, a particular slice of the three-dimensional representation is considered corresponding to the specific frequency. In [136], the EEG signals are decomposed using the EWT method into modes. The statistical features are extracted from the modes. The optimal set of features is selected based on the t-test method and classified using machine learning algorithms into alcoholic and non-alcoholic subjects. In [85], the EEG signals are decomposed using multivariate EWT method into set of modes. Further, time-frequency domain-based features are extracted from the obtained modes and classified into seizure and seizure-free classes. In [86], the multichannel EEG signals are decomposed using a multivariate FBSE-EWT method. The marginal multiscale joint TFDs are obtained from the decomposed modes from which entropy features are computed. These features are classified into different emotional states using an autoencoder-based random forest classifier.

In [137], the surface electromyogram (EMG) signals are decomposed using FDM into set of Fourier intrinsic band functions. The entropy, kurtosis, and L1-norm features are extracted from the decomposed components and classified into six hand movement classes using a machine learning classifier. In [138], the alcoholism detection framework is developed based on FDM from the EEG signals. The EEG signals are decomposed using FDM and statistical features are extracted from the decomposed components. The significant features are selected and classified using a machine learning classifier into alcoholic and non-alcoholic classes. In [78], multivariate iterative filtering is utilized to decompose the EEG signals into multivariate IMFs. The rhythms are separated from the multivariate IMFs based on their mean frequencies. The time-domain features are extracted from the separated rhythms to detect schizophrenia. In [139], the cognitive visual object identifica-

tion task is performed based on multivariate sparse swarm decomposition from EEG and magnetoencephalogram signals.

In [74], the instantaneous fundamental frequency of the voiced speech signal is estimated using the EVDMH method. In [53], the seizure and seizure-free EEG signal classification is performed based on improved EVDHM and Hilbert transform and machine learning methods. The EEG signals are decomposed using the improved EVDHM method, and TFD is obtained by applying HSA on the decomposed components. The features namely, energy concentration measure [140], Rényi entropy measure [141], fractal dimension [142], and focus measure operators [143] are extracted from the TFD and classified into seizure and seizure-free classes using least square support vector machine (SVM) classifier. In [144], the heart rate variability signal is decomposed using the EVDHM method. The lowest frequency and highest frequency components are selected and features are extracted from them. The extracted features are provided input to a machine learning classifier for congestive heart failure detection.

These diverse applications of the data-adaptive signal decomposition methods showcase its demand. There have been a lot of advancements in the area of signal decomposition since the development of the EMD method. However, each of the developed methods has its advantages and limitations. There is still a significant research gap in the literature that needs to be addressed and solved. This thesis makes an attempt towards the same.

1.5 Motivation

The EVDHM-based methods are well-explored for univariate signal decomposition. However, there are a few limitations to the EVDHM-based signal analysis. For example, the two mono-components of a real-life signal might overlap in the frequency-domain. However, all the EVDHM-based methods in the literature use the spectral overlapped-based

grouping. Hence, they cannot separate these components from a signal. In such cases, the short-duration analysis can help to improve the analysis, as in short-duration (with constraint to segment length considered carefully) the signal components will have well-separated frequency content. The sliding SSA [50] uses the short-duration automated SSA to separate the signal components overlapped in the frequency-domain. Motivated by this, the sliding eigenvalue decomposition (EVD) method is proposed to separate signal components overlapped in the frequency-domain. Further, motivated by cross-term suppression in WVD based on signal decomposition [32], we developed a new method based on sliding EVD and WVD, termed sliding EVD-WVD, to obtain cross-term free WVD.

In iterative EVDHM and improved EVDHM methods, the components extracted corresponding to each significant eigenvalue pair are then grouped based on the spectral overlapping concept, i.e., components sharing a common spectral band are suggested to be added together. The aforementioned component grouping is based on the frequency-domain information only. However, in [145], a time-frequency domain-based approach is suggested to verify whether the sum of two components is a mono-component or multicomponent signal and the same is utilized to group components extracted from the EVDHM method efficiently.

The decomposition of multichannel signals using univariate EVDHM-based methods has shown its utilization in the analysis and classification of single-channel and multichannel signals. However, decomposing multichannel signals using univariate EVDHM-based methods does not preserve the mutual information shared among the channels. This research gap in the literature on EVDHM-based signal processing motivated us to develop the multichannel extension of EVDHM to preserve the mutual information shared among the channels of a multichannel signal.

The magnitude of the eigenvalue pair of a sinusoidal signal is linearly related to its

amplitude [52]. Furthermore, the component extracted using the eigenvalue pairs and corresponding eigenvectors possess the frequency information of it. However, there is no mathematical derivation for relationship between eigenvalue of Hankel matrix of a sinusoidal signal and amplitude of the sinusoidal signal, which motivated us to derive this relationship. In multicomponent stationary signal decomposition based on EVDHM, each significant eigenvalue pair and corresponding decomposed component carry the amplitude and frequency information, respectively, of the constituent sinusoids of the signal. This motivated us to develop a new TFD where the time-varying eigenvalues of the signal are represented in the time-frequency plane.

The EVDHM-based methods like, iterative EVDHM, improved EVDHM perform decomposition of the signal in multiple iterations or they are based on short-duration analysis. These approaches increase the computation time required to decompose a signal by a huge amount. This becomes a limitation for EVDHM-based methods for choosing it to deploy in real-time systems as they care about computation time very seriously. Furthermore, in [146], a convolution-based component extraction approach is developed to improve the computational efficiency of the SSA technique. Motivated by this, computationally efficient EVDHM (CEEVDHM) is developed as a fast alternative algorithm for EVDHM.

1.6 Objectives

The signal decomposition methods are useful in obtaining high-resolution TFDs. The EVDHM-based methods decompose the signal into a set of data-adaptive components of the signals. However, these methods have certain limitations. This thesis aims to develop new EVDHM-based methods for analyzing and classifying signals. The specific objectives of the thesis are listed below.

Objective 1: To develop a short-duration EVDHM-based technique to separate the components overlapped in the frequency-domain and its utilization in cross-term suppression in WVD.

Objective 2: To iteratively extract the signal components using EVDHM and frequency spread and IF-based grouping methods.

Objective 3: To develop multichannel extensions of EVDHM and their applications to eye movement and Alzheimer's disease detection.

Objective 4: To develop a method to represent the time-varying eigenvalues in a time-frequency plane based on short-duration EVDHM.

Objective 5: To develop a computationally efficient signal decomposition method based on EVDHM.

1.7 Contributions

The contributions of the thesis are as follows:

Contribution 1: A new method based on short-duration automated eigenvalue decomposition, termed sliding EVD, has been developed to separate the signal components. The quality reconstruction factor (QRF) measure measures decomposition quality. Furthermore, two different approaches are proposed for obtaining sliding EVD-based TFD of a signal. The first approach is based on the sliding EVD and HSA methods, termed sliding EVD-HSA in which HSA is applied on the decomposed components to obtain the TFD of the signal. The TFDs of signals obtained using the sliding EVD-HSA method are compared with TFDs obtained from HHT and improved EVDHM-based HSA (improved EVDHM-HSA) methods. In the second approach,

the sliding EVD and WVD methods are combined, termed sliding EVD-WVD, to obtain cross-term free TFD of a signal. This method adds the WVDs of each of the analytic representations of the sliding EVD-based decomposed components to obtain the cross-term free TFD. The performance of sliding EVD-WVD is compared with methods from literature for synthetic signals in clean and noisy conditions and a clean real-life voiced speech signal taken from CMU ARCTIC speech database [1]. The computational time required to obtain cross-term free WVD of the signals using the sliding EVD-WVD and compared methods is also studied.

Contrubution 2: In this work, an EVDHM-based iterative method is developed to decompose a signal in which the most dominant mono-component signal (DMS) (MDMS) is extracted in each iteration, termed EMD-like EVDHM. In the developed method, the EVDHM decomposes the signal into a set of components from which the most dominant mode of the signal is extracted based on the frequency spread and IF-based grouping method, and the residue is considered the signal for the next iteration. The frequency and amplitude separability analysis is performed for the sum of two sinusoidal signals using the developed method. Then, the HSA is applied to the MDMS to obtain the TFD of the signal. The TFD of three synthetic signals and one real-life voiced speech signal obtained from the developed method is compared with methods from the literature. Furthermore, the QRF and average correlation measures obtained from the proposed method and compared methods are also studied for clean and noisy synthetic signals. The developed method is also studied for trend line extraction and weak component extraction.

Contrubution 3: We have proposed a multichannel extension of the EVDHM method termed multichannel EVDHM (MCh-EVDHM) to decompose the multichannel sig-

nal into a set of mode-aligned components. The MCh-EVDHM-based framework for eye movement detection using electrooculogram (EOG) signals is developed and its performance is studied. Furthermore, the improved MCh-EVDHM is proposed, and based on this, a rhythms separation method is also developed. The rhythm separation method is utilized to develop the Alzheimer's disease detection framework from EEG signals.

Contrubution 4: We have derived the relationship between eigenvalue of the Hankel matrix of a sinusoidal signal and its amplitude. The mean of magnitude of significant eigenvalue pair (MMSEP) is found to be proportional to amplitude of the sinusoidal signal. Hence, we developed a new method for obtaining the TFD of the signal by representing the time-varying MMSEPs in the time-frequency plane based on short-duration EVDHM. The effect of window size on the resolution of obtained TFD is studied. Furthermore, the comparison of the proposed TFD with methods from the literature is studied with the help of one synthetic and one real-life audio signal.

Contrubution 5: This work aims to improve the computational efficiency of the EVDHM method. The same has been achieved by developing the CEEVDHM method to decompose a signal into its constituent components. The comparison of the computational time required to decompose synthetic and real-life signals using EVDHM and CEEVDHM methods is studied. Furthermore, the decomposed components obtained from EVDHM and CEEVDHM are also compared in this study.

1.8 Outline

The thesis contains eight chapters. Initially, the different signal analysis approaches are introduced. Further signal decomposition and their application to signal analysis and

classification are briefed, followed by motivation, objective, and contributions of the thesis.

Chapter 2 provides a detailed literature review on EVDHM-based signal decomposition methods, signal analysis, and classification frameworks. Chapter 3 presents the SEVD method followed by HSA and WVD-based frameworks for signal analysis. The EMD-like EVDHM is proposed for signal decomposition in Chapter 4. The multichannel extensions of EVDHM are presented along with their applications to eye movement and Parkinson's disease detection in Chapter 5. The new TFD obtained by representing the time-varying eigenvalues in the time-frequency plane is presented in Chapter 6. Chapter 7 presents the CEEVDHM methods, which is a faster alternative to EVDHM. Finally, Chapter 8 concludes the thesis and presents the future research directions.

Chapter 2

Literature review

The EVDHM method decomposes the signals into set of components by obtaining a Hankel matrix from the signal followed by EVD. This chapter presents a comprehensive review of EVDHM-based signal decomposition and analysis methods. The application of EVDHM-based methods are also discussed in this chapter.

2.1 Eigenvalue decomposition of Hankel matrix

The EVDHM is a data-adaptive signal decomposition method to obtain the mono-component signals of a multicomponent signal. The decomposition of a signal $x[n]$ for $n = 0, 1, \ldots, N-1$ using EVDHM method is performed using the following steps:

Step 1: Generate the Hankel matrix X of the signal $x[n]$ using the below expression [51, 147],

$$X = \begin{bmatrix} x[0] & x[1] & \ldots & x[K-1] \\ x[1] & x[2] & \ldots & x[K] \\ \vdots & \vdots & \ddots & \vdots \\ x[K-1] & x[K] & \ldots & x[N-1] \end{bmatrix} \tag{2.1}$$

where $K = \frac{N+1}{2}$. The matrix X is a symmetric matrix such that $X = (X)^T$, where

$(\cdot)^T$ is the transpose operator.

Step 2: The EVD of the obtained Hankel matrix X is performed using following expression [51]:

$$X = U\Lambda(U)^T \tag{2.2}$$

where Λ is a diagonal matrix of dimension $K \times K$ with eigenvalues λ_i, $i = 1, 2, \ldots, N$ on its diagonal and U is an orthogonal matrix with eigenvectors u_i, $i = 1, 2, \ldots, N$ as its columns. The two eigenvectors (u_i and u_j) corresponding to two different eigenvalues (λ_i and λ_j) are orthogonal iff $i \neq j$ [147].

Step 3: The Hankel matrix X can be expressed as sum of Hankel matrices corresponding to mono-component signals as,

$$X = \sum_{i=1}^{R} X_i, \text{ where } X_i = (X_i)^T \tag{2.3}$$

The number of non-zero eigenvalues and rank of X is not greater than $2R$ where R is the number of harmonically related sinusoids in $x[n]$ [51].

Step 4: The matrix X_i can be obtained preserving only i^{th} eigenvalue pairs of Λ as [51],

$$\tilde{\Lambda} = \text{diag}\,(0, \ldots, 0, \lambda_i, 0, \ldots, 0, \lambda_{K-i+1}, 0, \ldots, 0) \tag{2.4}$$

The i^{th} sub-matrix X_i is obtained as, $X_i = U\tilde{\Lambda}(U)^T$. It can be simplified as, $X_i = \lambda_i u_i (u_i)^T + \lambda_{K-i+1} u_{K-i+1} (u_{K-i+1})^T$ [52].

Step 5: The i^{th} mono-component signal of $x[n]$ is computed by performing the average of skew diagonal elements of X_i as [51],

$$x_i[n] = \text{mean}\left(\sum_m \sum_l X_i(l, m)\right), \text{ with constraint that } l + m = n + 2 \tag{2.5}$$

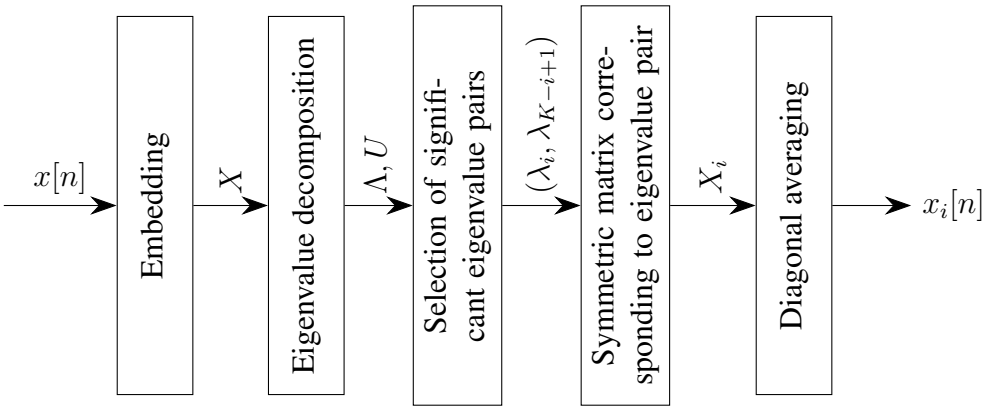

Figure 2.1: Block diagram representation of the EVDHM method illustrating the steps involved in decomposition of a signal $x[n]$ into a set of mono-component signals.

where $n = 0, 1, \ldots, N-1$, $l = 1, 2, \ldots, K$, $m = 1, 2, \ldots, K$, mean$(\cdot)$ denotes the mean value, and $X_i(l, m)$ is the l^{th} row and m^{th} column element of X_i.

Consider a multicomponent signal $x[n]$ as a sum of I harmonically related sinusoidal signals which is mathematically represented as [51],

$$x[n] = \sum_{i=1}^{I} x_i[n] = \sum_{i=1}^{I} a_i \cos\left(2\pi i \frac{f_0}{F_s} n + \phi_i\right) \tag{2.6}$$

where a_i and ϕ_i are the amplitude and phase shift of i^{th} component, f_0 is fundamental frequency, and F_s is sampling frequency. It is assumed that $a_i \neq a_k$ for $i \neq k$ for $i, k = 1, 2, \ldots, I$. From the EVDHM steps S1 to S3, The Hankel matrix X can be represented as sum of I matrices, i.e., $X = \sum_{i=1}^{I} X_i$. The matrices X and X_i contains a total I and 1 sinusoids, respectively. Also, the rank and non-zero eigenvalues of matrices X and X_i are $2I$ and 2, respectively [51]. The trace of a matrix is equal to sum of its eigenvalues. Hence,

$$\text{Tr}\,(X) = \sum_{i=1}^{K} \lambda_k \tag{2.7}$$

where $\text{Tr}\,(\cdot)$ is the trace of the matrix. Now, two different cases for value of K had been studied in literature:

Case 1: When $K = \alpha N_0$, where σ is a positive integer and $N_0 = \frac{F_s}{f_0}$.

$$\text{Tr}\left(X_i\right) = a_i \sum_{n=0}^{\alpha N_0 - 1} \cos\left(2\pi i \frac{f_0}{F_s} 2n + \phi_i\right) = a_i \Re\left(e^{j\phi_i} \sum_{n=0}^{\alpha N_0 - 1} e^{j2\pi i \frac{f_0}{F_s} 2n}\right) = 0 \; \forall \; i \tag{2.8}$$

where $\Re\left(\cdot\right)$ is the real part. Also,

$$\text{Tr}\left(X\right) = \sum_{i=1}^{I} \text{Tr}\left(X_i\right) = 0 \tag{2.9}$$

Also, the p^{th} row/column of matrix X_k is orthogonal to q^{th} row/column of matrix X_l for $k \neq l$. This indicated that the $2I$ non-zero eigenvalues and corresponding eigenvectors of X are equal to the set of eigenvalues and eigenvectors of X_i for $i = 1, 2, \ldots, I$. Also, the non-zero eigenvalue λ_1 is proportional to the amplitude of the harmonic mono-component signal, i.e., $\lambda_i = \frac{Ka_i}{2}$.

Case 2: When $K \neq \alpha N_0$, the aforementioned condition does not hold. The signal component is extracted by preserving a particular eigenvalue pair and performing steps S4 and S5.

For example, two different discrete-time signals $x_1[n]$ and $x_2[n]$ are considered which are mathematically defined using equations (2.10) and (2.11), respectively.

$$x_1[n] = \sin\left(60\pi \frac{n}{f_s}\right) + 0.8\sin\left(100\pi \frac{n}{f_s}\right) + 0.7\sin\left(110\pi \frac{n}{f_s}\right) \tag{2.10}$$

$$x_2[n] = \sin\left(60\pi \frac{n}{f_s}\right) + 0.8\sin\left(2\pi\left(50 + 10\frac{n}{f_s}\right)\frac{n}{f_s}\right) \tag{2.11}$$

where $n = 0, 1, \ldots, N-1$, $N = 1001$, and $f_s = 1000$ Hz. The time-domain representation of the aforementioned signals are depicted in Fig. 2.2. The signal $x_1[n]$ is sum of three sinusoids, while $x_2[n]$ comprises a sinusoid and a linear chirp. The significant threshold percentage (STP)-based eigenvalue threshold computation for selection of signif-

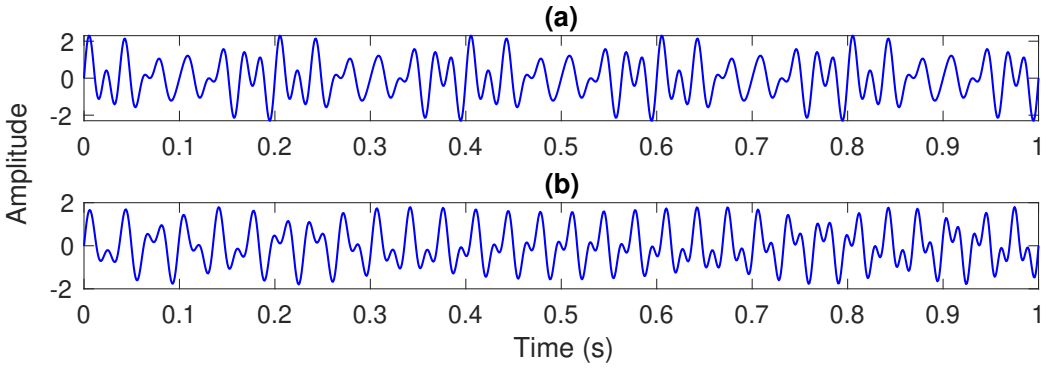

Figure 2.2: Time-domain representations of signals $x_1[n]$ and $x_2[n]$ are shown in (a) and (b), respectively.

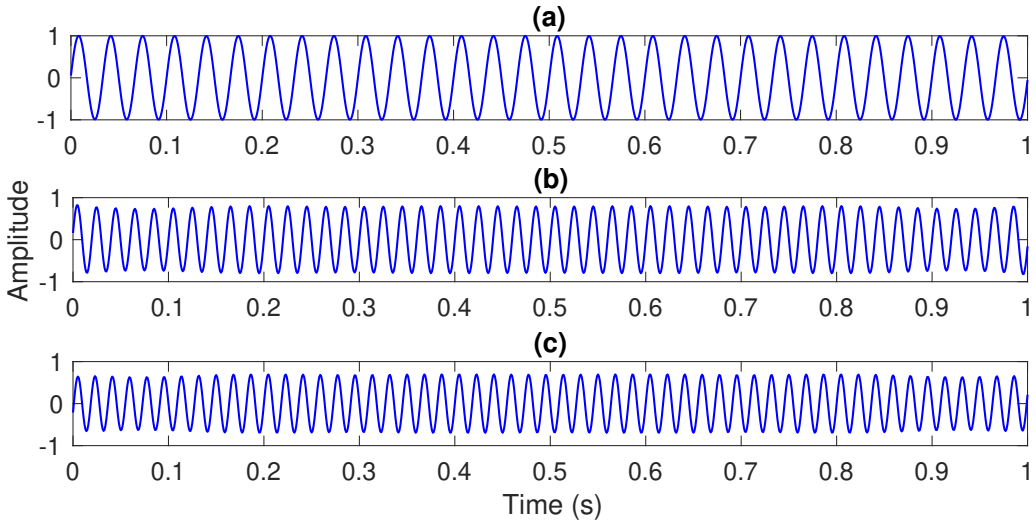

Figure 2.3: The mono-component signals, obtained from the decomposition of $x_1[n]$ using EVDHM method, are shown in (a)–(c).

icant eigenvalue pairs is studied in iterative EVDHM method for decomposition of a non-stationary signal [52]. The STP-based selection of significant eigenvalue pair, with STP = 10%, is considered for decomposition of non-stationary signal using EVDHM method. The decomposed mono-component signals of the signals $x_1[n]$ and $x_2[n]$, obtained using EVDHM method, are presented in Figs. 2.3 and 2.4, respectively. The aforementioned decomposition results indicate that, the EVDHM method is effective for separating sinusoidal signals. However, EVDHM of $x_2[n]$ provides seven components with significant energy, resulting in over decomposition.

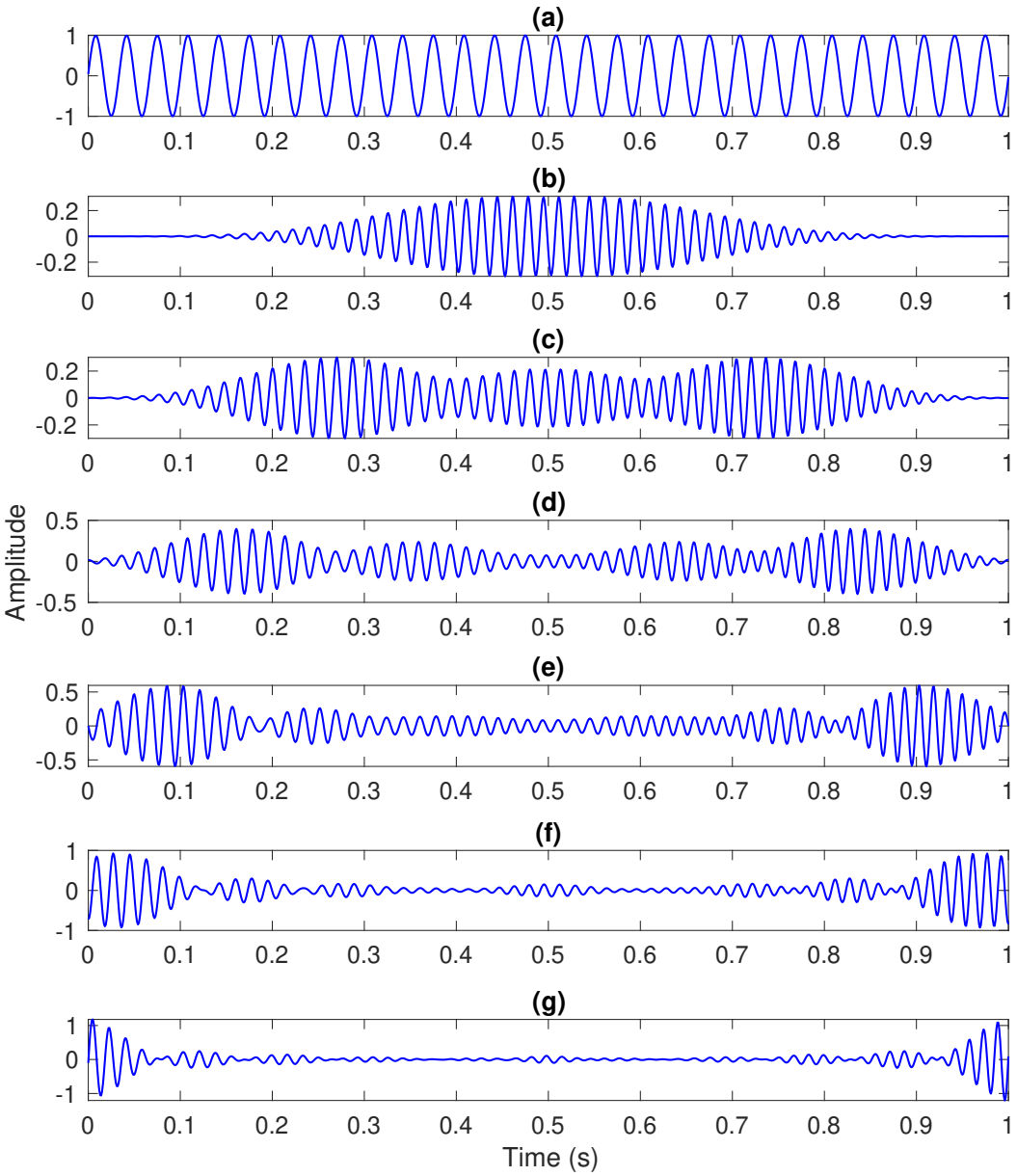

Figure 2.4: Time-domain representations of mono-component signals obtained from EVDHM-based decomposition of $x_2[n]$ are shown in (a)–(g).

An iterative framework based on EVDHM was developed to extract the time-varying fundamental frequency component of low-frequency region voiced speech signal. Further, the glottal closure instants were identified using the extracted fundamental frequency component [51]. In [51], the low-frequency region voiced speech signal with a frequency range of 50-500 Hz was obtained using the FBSE-based method. The filtered speech signal was

represented as the sum of AFM signals. Further, an iterative framework based on EVDHM was developed to extract the time-varying F_0 component of the filtered speech signal. Further, the glottal closure instants were identified from the extracted F_0 component.

2.2 Iterative eigenvalue decomposition of Hankel matrix

The decomposition of a signal $x[n]$ using EVDHM provides significant side lobes, which means the component consists of two or more mono-component of the signal [52, 74]. The components are checked to determine whether they satisfy mono-component signal criteria (MSC). It it does not satisfy, the decomposed component is suggested to decompose further. The developed decomposition method was termed as iterative EVDHM [52]. The steps are as follows [52]:

Step 1: The Hankel matrix X of the signal $x[n]$ is obtained using Step 1 defined in Section 2.1.

Step 2: The EVD is performed on the matrix X to obtain the set of eigenvalues $(\lambda_1, \lambda_2, \ldots, \lambda_K)$ and corresponding eigenvector $(u_1, u_2, \ldots, u_K)$ using Step 2 defined in Section 2.1.

Step 3: The significant eigenvalue pairs are selected using STP-based threshold, which states that the eigenvalue pairs are significant if magnitude of one of its eigenvalues is greater than or equal to STP of maximum eigenvalue of X [52]. It was suggested to use STP as 10% [52]. However, it is a design issue and depends on the application [52].

Step 4: The i^{th} mono-component signal can be extracted by first preserving the i^{th} eigenvalue pair to obtain the symmetric matrix X_i followed by performing mean of skew-

diagonal elements of matrix X_i using Steps 4 and 5 defined in Section 2.1.

Step 5: The extracted mono-component signal is verified to satisfy the MSC [52] which states that,

1. The absolute value of difference between the number of extrema and the number of zero crossings of the component is less than or equal to one.
2. The EVDHM of the extracted component should have only one significant eigenvalue pair.

Step 6: The extracted component not satisfying MSC is considered a multicomponent signal for the next iteration and it undergoes for decomposition following from Step 1 [52]. The extracted components satisfying MSC are considered for the next step. The decomposition is terminated after 4^{th} iteration [52]. At the end of this step, assume P number of components satisfied MSC criteria, i.e., $x_i[n]$ for $i = 1, 2, \ldots, P$.

Step 7: The MSC satisfying components having a spectral overlap of 1 dB bandwidth are added together [52]. The 1 dB bandwidth of a signal mono-component $x_i[n]$ is computed as the range of frequencies over which the the value of $E_i(f_k)$ is greater than or equal to $(\max(E_i(f_k)) - 1)$ dB threshold. The parameter, $\max(E_i(f_k))$, is the maximum value of $E_i(f_k)$ which can be expressed as [52],

$$E_i(f_k) = 10 \log_{10} \left(|X_i(f_k)|^2 \right) \tag{2.12}$$

where $f_k = \frac{k}{N_{\text{DFT}}}$ and $X_i(f_k)$ is the N_{DFT}-point DFT of $x_i[n]$.

At the end of Step 7, the reconstructed signal $\hat{x}[n]$ is represented as,

$$\hat{x}[n] = \sum_{i=1}^{R} \tilde{x}_i[n] \tag{2.13}$$

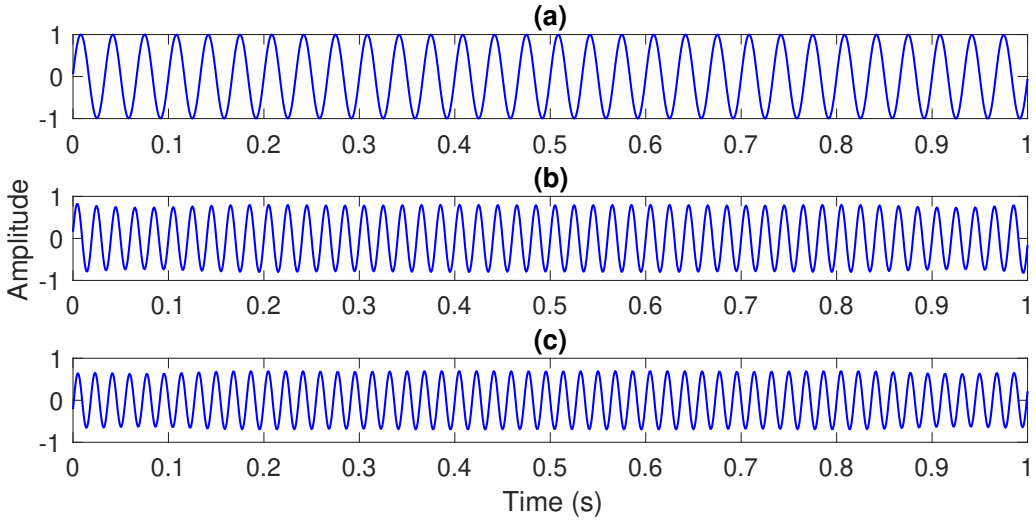

Figure 2.5: The mono-component signals obtained from the decomposition of $x_1[n]$ using iterative EVDHM method are shown in (a)–(c).

The signals $x_1[n]$ and $x_2[n]$ defined by equations (2.10) and (2.11), respectively are decomposed using iterative EVDHM method. The decomposed components are shown in Figs. 2.5 and 2.6, respectively. The iterative EVDHM successfully separated the three sinusoids of $x_1[n]$, as shown in Fig. 2.5. Whereas, it over decomposes the signal frequency-modulated component of the signal $x_2[n]$, as illustrated in Fig. 2.6.

2.3 Improved eigenvalue decomposition of Hankel matrix

In [53], it had been experimentally shown that the EVDHM method is not able to extract the signal component whose energy is relatively less than the component having highest energy. Also, the 1 dB bandwidth overlapping-based grouping criteria [52] fails to add the components corresponding to a FM signal whose frequency is modulated over wide range of frequencies. To overcome all these issues, the improved EVDHM was developed [53].

The decomposition of a signal $x[n]$ for $n = 1, 2, \ldots, N$ based on improved EVDHM is performed with the following steps:

Step 1: The Hankel matrix X of the considered signal $x[n]$ is computed using the proce-

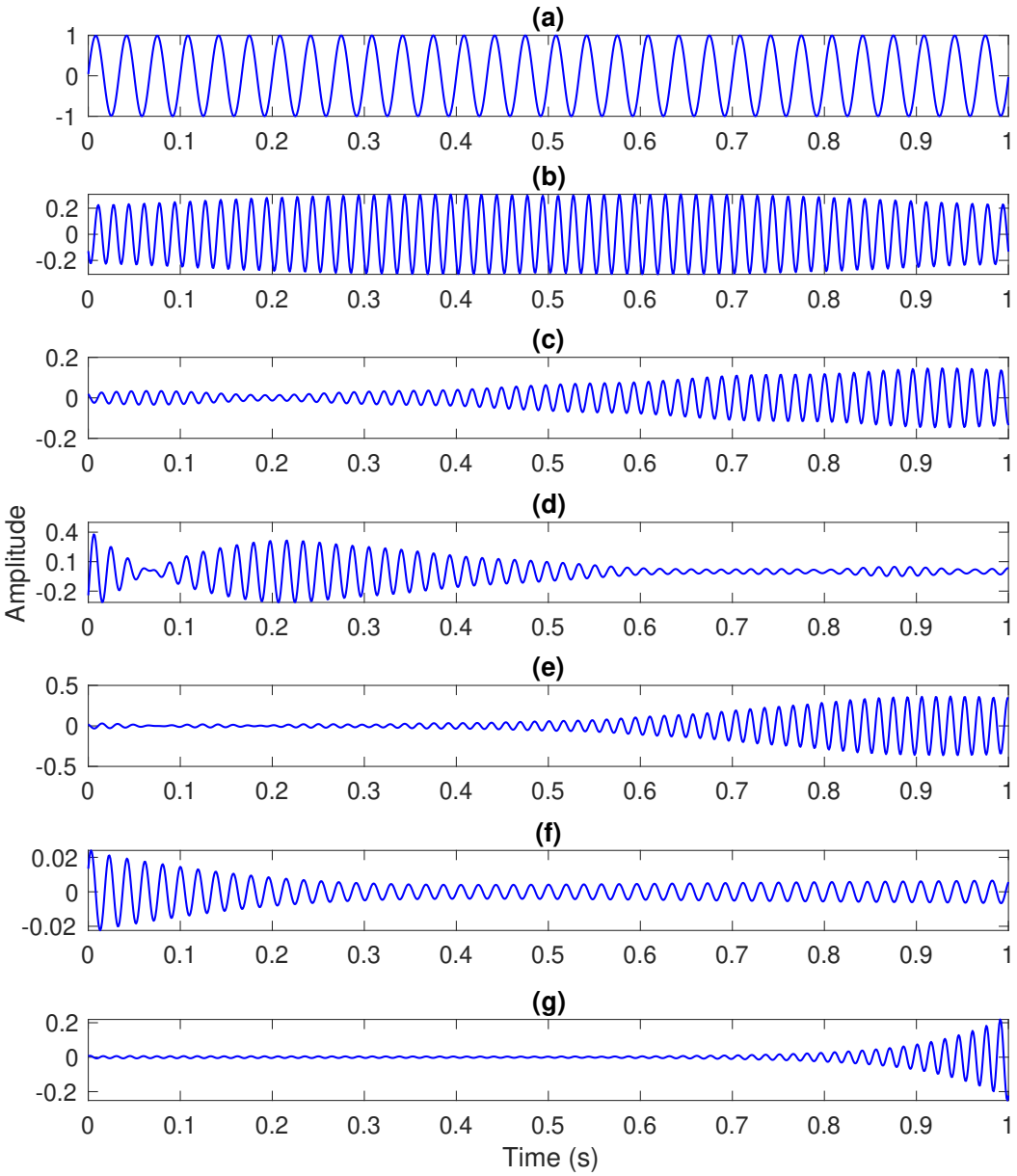

Figure 2.6: Time-domain representations of the decomposed components obtained from the iterative EVDHM-based decomposition of signal $x_2[n]$.

dure defined in Step 1 of the Section 2.1. The obtained matrix X is mathematically represented using equation (2.1).

Step 2: The eigenvalue decomposition of the Hankel matrix X is performed to obtain the eigenvector matrix U and eigenvalue matrix Λ. The procedure for the same is defined in Step 2 of the Section 2.1. The set of significant eigenvalue pairs is obtained using

modified significant threshold point (MSTP) [53]. The MSTP is defined based on the sum of magnitude of the eigenvalues of the matrix X as it is associated with the signal energy [53]. The eigenvalue pairs having the sum of their magnitude greater than or equal to 95% of sum of magnitude of all eigenvalues are significant.

Step 3: The signal components corresponding to each significant eigenvalue pairs are computed. The component corresponding to i^{th} eigenvalue pair is obtained as $x_i[n] = \lambda_i f(u_i[n]) + \lambda_{K-i+1} f(u_{K-i+1}[n])$, where $f(u_i[n]) = \sum_{m=1}^{K} u_i[n-m]u_i[m]/m + \sum_{m=K+1}^{N} u_i[n-m]u_i[m]/(N-m+1)$ [53].

Step 4: The decomposed components are verified to satisfy modified MSC (MMSC). The MMSC is defined as [53],

Condition 1: The number of extrema and the number of zero crossings are differ atmost by one.

Condition 2: The mean value of upper and lower envelope is zero.

The signal $x[n]$ can be represented as,

$$x[n] = \sum_{i_1=1}^{I_1} x_{\text{MMSC-S}_{i_1}}[n] + \sum_{i_2=1}^{I_2} x_{\text{MMSC-US}_{i_2}}[n] \tag{2.14}$$

where $x_{\text{MMSC-S}_{i_1}}[n]$ and $x_{\text{MMSC-US}_{i_2}}[n]$ are the i_1^{th} MMSC satisfying and i_2^{th} MMSC not satisfying components, respectively. The components not satisfying MMSC undergoes for further decomposition following step S1 whereas components satisfying MMSC are considered for next iteration (the MSTP is considered as 90% and 85% for second and third iterations, respectively) [53]. The reconstructed signal after further

iteration is represented as,

$$x[n] = \sum_{i_1=1}^{I_1+P} x_{\text{MMSC-S}_{i_1}}[n] + \sum_{i_2=1}^{I_3} x_{\text{MMSC-US}_{i_2}}[n] \tag{2.15}$$

where P is the number of MMSC satisfying components obtained in further iterations.

Step 5: If energy of signal $\sum_{i_2=1}^{I_3} x_{\text{MMSC-US}_{i_2}}[n]$ is less than or equal to 5% of energy of $x[n]$, the further iterations are not required. Whereas, for real-time signals, the process is suggested to terminate after third iteration only. After termination of decomposition iteration, the components from $x_{\text{MMSC-US}_{i_2}}[n]$ group with frequency deviation less than 20% of sampling rate of $x[n]$ along with MMSC satisfying components are considered for next step [53].

Step 6: The MMSC satisfying components having 3 dB bandwidth overlap are added together [53].

The improved EVDHM method is applied to decompose the signals $x_1[n]$ and $x_2[n]$, defined in equations (2.10) and (2.11), respectively. The decomposed components of $x_1[n]$ are shown in Fig. 2.7, demonstrating it successfully separated the constituent components. The decomposition results for $x_2[n]$, shown in Fig. 2.8, indicates that it successfully extract sinusoidal and frequency modulated components along with some low energy components.

2.4 Eigenvalue decomposition of Hankel matrix and Hilbert spectrum analysis-based signal analysis

This section discusses two different EVDHM-based approaches for obtaining the TFD of a signal. The block diagram representation of the same depicted in Fig. 2.9. One of the approach utilizes the iterative EVDHM for signal decomposition whereas the other one uses

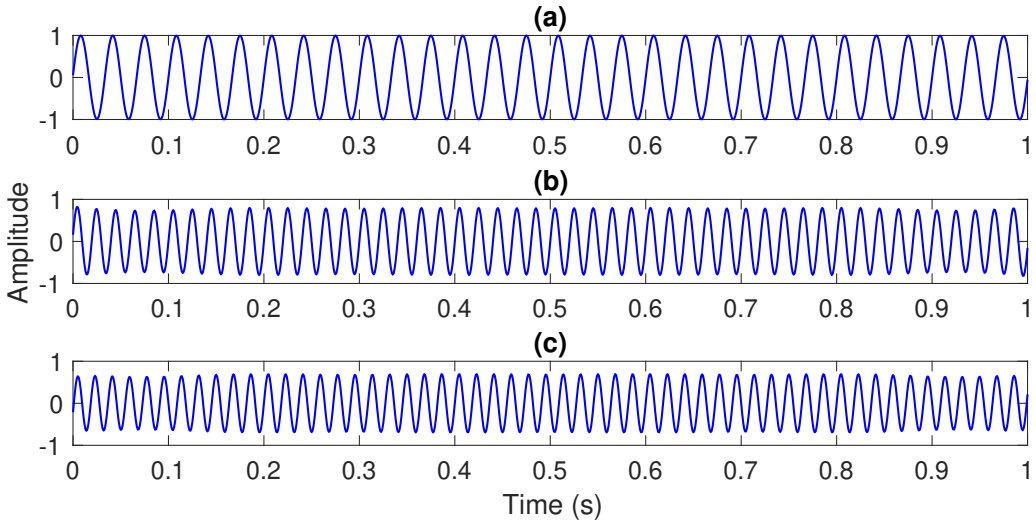

Figure 2.7: The decomposed components obtained from the improved EVDHM-based decomposition of $x_1[n]$ are depicted in (a)–(c).

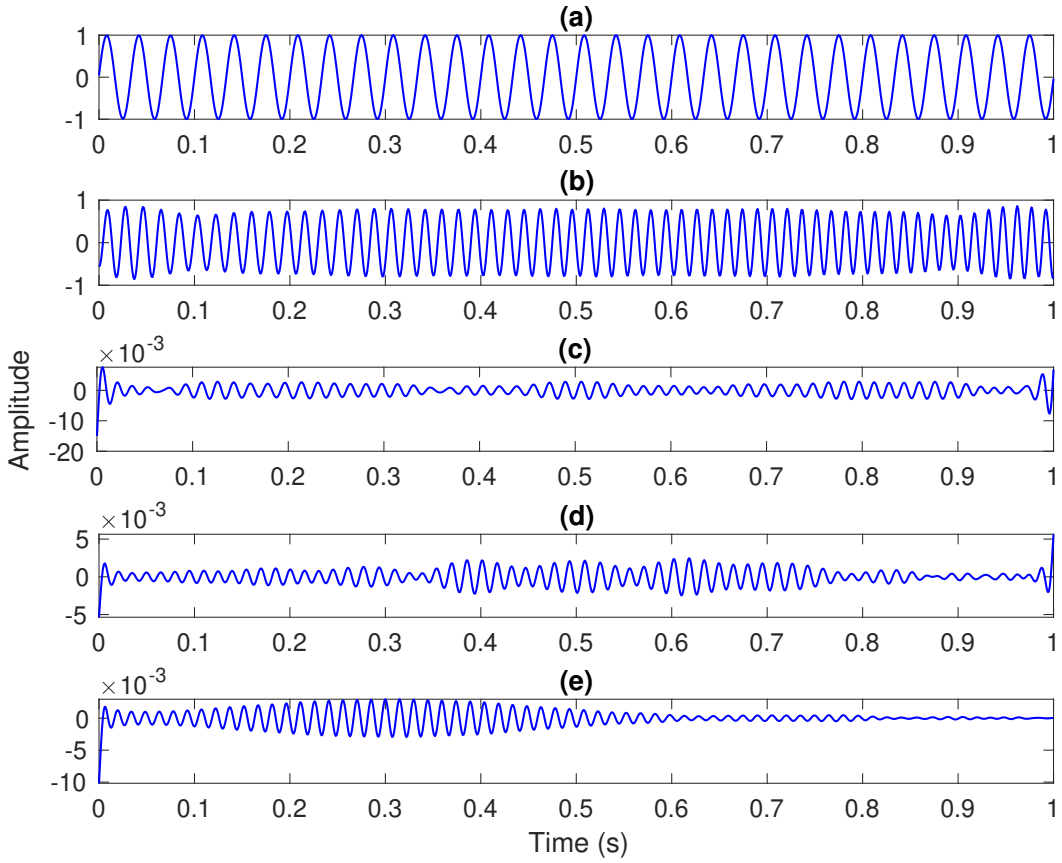

Figure 2.8: The mono-component signals of $x_2[n]$ obtained from improved EVDHM-based decomposition are shown in (a)–(e).

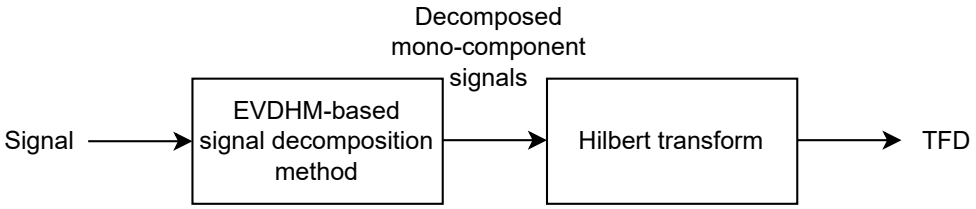

Figure 2.9: The EVDHM-based general framework for obtaining TFD of a signal.

the improved EVDHM method.

In [148], Sharma and Pachori suggested a method to obtain the TFD of a multicomponent signal based on iterative EVDHM and Hilbert transform methods. In this method, the constituent mono-components of a multicomponent signal is obtained using iterative EVDHM method (described in section 2.2) [52, 148]. Furthermore, Hilbert transform-based method is applied on the decomposed mono-components to obtain their respective AE and IF. Here, the analytic mono-component signal is obtained with the help of Hilbert transform. Further, the polar form representation of analytic mono-component provided the AE and instantaneous phase. The IF is computed with the help of derivative of the instantaneous phase with respect to time. At the end, the TFD of the signal is obtained by representing the IF and squared AE in time-frequency plane.

In [53], Sharma and Pachori developed an extension of iterative EVDHM namely improved EVDHM (described in section 2.3) to decompose the signal and obtained TFD based on Hilbert transform method applied to the decomposed mono-component signals.

2.5 Improved eigenvalue decomposition of Hankel matrix for complex-valued signal analysis

The spectrum of the complex-valued signal do not symmetry along $\omega = 0$ axis. Hence, both positive and negative frequency part of the spectrum needs to be decomposed sepa-

rately. The same is performed by first separating the positive and negative frequency range components, $x_+[n]$ and $x_-[n]$, respectively, of a complex-valued signal $x[n]$ computed as suggested below [100, 104].

$$x_+[n] = \Re\left[\mathcal{F}^{-1}\left(H(e^{j\omega})X(e^{j\omega})\right)\right] \tag{2.16}$$

$$x_-[n] = \Re\left[\mathcal{F}^{-1}\left(H(e^{j\omega})X^*(e^{j\omega})\right)\right] \tag{2.17}$$

where $\mathcal{F}^{-1}(X(e^{j\omega}))$ is the inverse discrete-time Fourier transform operation of $X(e^{j\omega})$, $X(e^{j\omega}) = \mathcal{F}(x[n])$ is the discrete-time Fourier transform of $x[n]$, and $H(e^{j\omega})$ is an ideal band-pass filter defined in equation (1.38). The complex-valued signal $x[n]$ can be obtained from $x_+[n]$ and $x_-[n]$ signals using following expression:

$$x[n] = (x_+[n] + j\mathcal{H}\{x_+[n]\}) + (x_-[n] + j\mathcal{H}\{x_-[n]\})^* \tag{2.18}$$

Furthermore, the positive and negative frequency range components are separately decomposed using improved EVDHM method (described in section 2.3) into mono-component signals. The same is represented as,

$$x_+[n] = \sum_{i=1}^{I_1} x_i[n] \tag{2.19}$$

$$x_-[n] = \sum_{i=-I_2}^{-1} x_i[n] \tag{2.20}$$

where I_1 and I_2 are the number of mono-components obtained after decomposition of $x_+[n]$ and $x_-[n]$, respectively. Further, the complex-valued signal $x[n]$ can be represented as,

$$x[n] = \sum_{i=-I_2, i\neq 0}^{I_1} z_i[n] \tag{2.21}$$

where

$$z_i[n] = \begin{cases} x_i[n] + j\mathcal{H}\left\{x_i[n]\right\}, & \text{for } i = 1, 2, \ldots, I_1 \\ \left(x_i[n] + j\mathcal{H}\left\{x_i[n]\right\}\right)^*, & \text{for } i = -I_2, -I_2 + 1, \ldots, -1 \end{cases} \tag{2.22}$$

The equation (2.21) is represented in polar form to obtain the AE and IF of the components. The same is represented below,

$$x[n] = \sum_{i=-I_2, i\neq 0}^{I_1} z_i[n] = \sum_{i=-I_2, i\neq 0}^{I_1} a_i[n] e^{j\phi_i[n]} \tag{2.23}$$

The TFD of the signal $x[n]$ is obtained by representing the IF and squared of AE in time-frequency plane.

2.6 Application of eigenvalue decomposition of Hankel matrix-based methods

The EVDHM-based methods discussed in the early sections of this chapter have been studied for various real-time applications like preprocessing of ECG signals, coronary artery disease diagnosis from ECG signals, amyotrophic lateral sclerosis and myopathy detection from electromyogram (EMG) signals, epilepsy detection from EEG signals, etc.

In [149], the Hankel matrix is obtained corresponding to a noisy ECG signal. The EVD is performed on the Hankel matrix to get the eigenvalues and corresponding eigenvectors. Then, an iterative differentiation-based search algorithm is utilized to get the eigenvalues corresponding to baseline wander noise and power line interference. These eigenvalues are set to zero and the signal is reconstructed from the remaining eigenvalues to get the preprocessed clean ECG signal.

In [150], an improved EVDHM-based framework for coronary artery disease detection framework is developed from ECG signals. The baseline wander and power line noises from

the ECG signals are eliminated using Daubechies 6 (db6)-based discrete wavelet transform (DWT) method [151]. The TFD of the preprocessed ECG signal is then computed using the improved EVDHM and Hilbert transform method from which the time-frequency flux [152], coefficient of variation [152], and energy concentration measure [140] features are extracted. These features are classified into healthy and unhealthy classes with an accuracy of 93.77% using a random forest classifier.

There are several other applications of EVDHM-based methods, like time-series forecast using EVDHM and auto-regressive integrated moving average methods with application to COVID-19 [153], signal analysis based on improved EVDHM and WVD [154], analysis of EMG signals using improved EVDHM [155], classification of EMG signals using EVDHM-based method [156], epilepsy detection from EEG signal using improved EVDHM method [157], etc.

2.7 Summary

In this chapter, a detailed review of three different EVDHM-based signal decomposition methods is presented, along with a discussion of their limitations. Furthermore, signal analysis methods based on EVDHM and HSA are reviewed for both real-valued and complex-valued signals. Finally, the real-time applications of these methods in signal analysis and classification frameworks are examined.

Chapter 3

Sliding eigenvalue decomposition for signal analysis

3.1 Introduction

The TFA aims the analysis of non-stationary signals (having time-varying parameters) like speech signals, biomedical signals, seismic signals, etc. Such signals are best described by TFD [30]. Later, TFD-based features can be exploited for further processing. Some of the applications of TFD are time-frequency interference mitigation in spread spectrum [158], time-frequency motion compensation for inverse synthetic aperture radar imaging [159], classification of focal and non-focal EEG signal based on TFD matrix [160] etc.

To get TFD of non-stationary signals, several methods have been proposed in literature like spectrogram obtained from STFT [12], scalogram obtained from CWT [13], WVD [14], Hilbert-Huang transform (HHT) [16], iterative EVDHM and Hilbert transform [53], and FBSE-based discrete energy separation algorithm [161].

In STFT, the signal is sliced into small duration frames with the help of a moving window and then Fourier analysis is performed to obtain time-localized spectral information [12, 36]. The resolution of spectrogram-based TFD is dependent on the size of the

analysis window. The CWT is essentially an adjustable window-based analysis, i.e., different scale or frequency components are analyzed using different durations window [13]. It also offers flexibility on basis selection, unlike STFT. However, the scalogram exhibits poor time resolution at low frequencies and poor frequency resolution at high frequencies.

The HHT is a data-adaptive technique that yields TFD of non-stationary signals [16]. It consists of two steps: the first one is EMD, which decomposes signals into a set of IMFs, and the second one is HSA, which represents IMFs in the time-frequency plane. It suffers from a mode-mixing problem. The iterative and improved EVDHM methods, firstly, obtain the significant components of the signal using an iterative decomposition approach [52, 53]. Then, the signal components are extracted by using a spectral overlap-based grouping of these significant components. The iterative EVDHM and improved EVDHM fail to decompose the signal when components are overlapped in the frequency domain. To overcome this issue, we have proposed the sliding EVD method in this chapter. Furthermore, the sliding EVD-HSA method has been developed, in which the HSA is applied to the decomposed components obtained from the sliding EVD method to generate the TFD of the signal.

The WVD is the Fourier analysis of central autocovariance of the signal [29, 162]. It provides a high (theoretically infinite) resolution TFD of a non-stationary mono-component signal. In the case of multicomponent signal, some spurious components or cross-term appear in between the true signal components in TFD; this is because of its bilinearity in signal [32]. The presence of cross-term makes the obtained TFD difficult to interpret. Due to this reason, WVD has limited applicability to real-world signals.

In the last few decades, many methods have been proposed in the literature with the aim of cross-term suppression. The masked WVD has been one of them to reduce cross-terms by multiplying WVD with the spectrogram of the signal [30]. The exponential kernel-based approach to reduce cross-term has been studied, and the obtained TFD is known

as Choi-William (CW) distribution [163]. Several window-based methods (pseudo-WVD) have been studied to reduce the cross-term of WVD [164, 165]. The pseudo-WVD is a window-based method for cross-term suppression in signal. It does not separate the cross-term between the concurrence auto-term. For general multicomponent signals, the smoothed pseudo WVD (SPWVD) was developed, compromising the resolution [166]. Signal decomposition-based techniques have also been investigated to suppress cross-term in WVD like, FBSE-based technique [32], tunable-Q wavelet transform-based technique [63], EWT-based technique [167], and iterative EVDHM-based technique [104] etc. The EMD-WVD-based TFD is also presented to reduce the cross-term, but this is limited to some specific types of signals because of the mode mixing problem of EMD [168]. However, EMD-WVD has been successfully applied to obtain gear fault features [169] and high-frequency current analysis of low voltage arc [170]. The sliding SSA-based cross-term elimination of WVD is also presented [171]. In several other methodologies, the WVD of a multicomponent signal has been considered as an image, and then image processing techniques are used to reduce the cross-term effect from TFD [172, 173]. The decomposition of the signal into its constituent components, followed by the summation of the WVD of analytic representation of these obtained components, provided cross-term free WVD [167, 168]. Most of these methods are focused on multicomponent signals whose components are well separated in the spectral domain. However, in a real-time scenario, the signal components may be overlapped in the frequency domain, and these methods fail to provide cross-term free WVD. This motivated us to develop sliding EVD-WVD method to obtain cross-term free TFD.

In this chapter, a short-time EVD-based signal decomposition technique named sliding EVD is proposed. The sliding EVD is motivated by sliding SSA [50]. In sliding EVD, firstly, the signal is segmented into short-duration frames. Then, automated EVD was per-

formed on each segment, followed by Euclidean distance-based grouping to obtain the decomposed component. Later, it was found that decomposed components obtained from two consecutive segments might not be in order, so a component tracking method to track components between adjacent frames is used in order to yield meaningful mono-components. As EVD does not consider the stationarity of the signal, the selection of frame duration only depends on the components that are non-overlapped in the frequency domain during that frame. Later, HSA was performed on the obtained components to get TFD. The TFD of the signal obtained from sliding EVD and HSA is compared with TFDs obtained from HHT and improved EVDHM-HSA methods, yielding significantly higher resolution for the studied signals. Later, the sliding EVD method is utilized to develop a framework for cross-term suppression in WVD.

3.2 Sliding eigenvalue decomposition for signal decomposition

The sliding EVD method is proposed to decompose signal into a set of its constituents based on the short-duration analysis. It comprises two steps. First, the automated EVD decomposes the short-duration frames of the signal into a set of its constituent components. Second, the signal components are extracted from the decomposed components of each frame. The same is provided in the following subsections:

3.2.1 Automated eigenvalue decomposition

Automated EVD aims at decomposing multi-component signal $x[n]$ for $n = 1, 2, \ldots, N$ as a sum of R mono-components $x_r[n]$ for $r = 1, 2, \ldots, R$. The steps involved in the automated EVD method are explained below.

3.2.1.1 Embedding

The Hankel matrix X of dimension $K \times K$ is computed from the signal $x[n]$ using Step 1 described in Section 2.1). Each row of the matrix X is obtained by applying a rectangular window of length K samples and sliding it over the signal length with step size one sample. The matrix X is symmetric, and elements on the skew diagonal are the same. The process of obtaining these matrices from a signal is called embedding.

3.2.1.2 Eigenvalue decomposition

The EVD is performed on matrix X to obtain a set of eigenvectors and corresponding eigenvalues using Step 2 described in Section 2.1). The matrix X is represented as, $X = U\Lambda U^T$, where Λ is a diagonal matrix containing eigenvalues $(\lambda_1, \lambda_2, \ldots, \lambda_K)$ as its diagonal elements and U is an orthogonal matrix containing eigenvectors $(u_1, u_2, \ldots, u_K)$ as its column vectors.

3.2.1.3 Symmetric matrix computation

The selection of significant eigenvalues and obtaining the symmetric matrices corresponding to them are crucial steps for component extraction [52, 53]. In this chapter, two different approaches have been studied which are defined below.

Approach 1: For analysis of the clean signal, all the eigenvalue pairs are considered as significant $(\lambda_i, \lambda_{K-i+1})$ for $i \in I$ and $I = \{1, 2, \ldots, \lfloor \frac{K}{2} \rfloor\}$. Furthermore, the i^{th} symmetric matrix X_i corresponding to eigenvalue pair $(\lambda_i, \lambda_{K-i+1})$ is computed using Step 4 described in Section 2.1).

Approach 2: The set of significant eigenvalues is obtained as the eigenvalues which have their magnitudes greater than the $\sqrt{0.1}$ times magnitude of the first eigenvalue. The i^{th}

symmetric matrix X_i corresponding to i^{th} significant eigenvalue λ_i is obtained as,

$$X_i = \lambda_i u_i \left(u_i\right)^T \ \forall \ i \ \in \ I \tag{3.1}$$

where $I = \left\{ i \ : \ |\lambda_i| > \sqrt{0.1} \times |\lambda_1| \right\}$.

3.2.1.4 Diagonal averaging

The matrix X_i turns out to be almost Hankel i.e, matrix is symmetric and skew-diagonal elements are almost same. The averaging across skew-diagonal of X_i gives the closest Hankel matrix to it in the least square error sense [50]. This helps to recover signal component $x_i[n]$ corresponding to X_i. This can be mathematically represented by equation (3.2).

$$x_i[n] = \begin{cases} \frac{1}{n} \sum_{m=1}^{n} X_i(m, n-m+1), & \text{if } 1 \leq n \leq K-1 \\ \frac{1}{N-n+1} \sum_{m=n-K+1}^{K} X_i(m, n-m+1), & \text{if } K \leq n \leq N. \end{cases} \tag{3.2}$$

where, $X_i(p, q)$ represents p^{th} row and q^{th} column element of matrix Y_i. After this step, the signal $x[n]$ can be represented as follows:

$$x[n] \approx \sum_{i \in I} x_i[n] \tag{3.3}$$

3.2.1.5 Grouping

As more than one components obtained from the previous step belong to a single mono-component or constituent signal component [154]. Hence, the grouping of the components needs to be performed in order to have meaningful signal components. The decomposed $x_i[n] \ \forall \ i \ \in \ I$ obtained from the previous step are grouped to R number of clusters with the help of agglomerative hierarchical clustering (AHC) [50, 174]. In AHC, firstly components

are assigned into different clusters. Then iteratively two nearest classes are merged together until we get desired number of classes. The distance between the two clusters is computed using two different distance measures in this study.

Distance measure 1: The distance between two classes is computed as Euclidean distance between the components assigned to them.

Distance measure 2: The distance between two classes is computed as [50],

$$d(x_i[n], x_k[n]) = 1 - \frac{| < x_i[n], x_k[n] >_w |}{||x_i[n]||_w ||x_k[n]||_w} \tag{3.4}$$

with $< x_i[n], x_k[n] >_w = (w[n]^T x_i[n])^T x_k[n]$, where

$$w[n] = \begin{cases} n, & \forall\, 1 \leq n < p \\ N - n + 1, & \forall\, p \leq n < N \end{cases} \tag{3.5}$$

and $||x_i[n]||_w = \sqrt{< x_i[n], x_i[n] >_w}$. At the end of automated EVD, the signal $x[n]$ is represented in the following form:

$$x[n] \approx \sum_{r=1}^{R} \tilde{x}_r[n] \tag{3.6}$$

Where $\tilde{x}_r[n]$ for $r = 1, 2, \ldots, R$ are the components obtained after the grouping. The block diagram of the same is provided in the Fig. 3.1.

3.2.2 Sliding eigenvalue decomposition

Sliding EVD is an extension of automated EVD which adds flexibility for separation of a wide variety of non-stationary signals into a well behaved AFM components. The sliding EVD is motivated by the following drawbacks of automated EVD:

1. As components being merged in automated EVD are derived from orthogonal eigen-

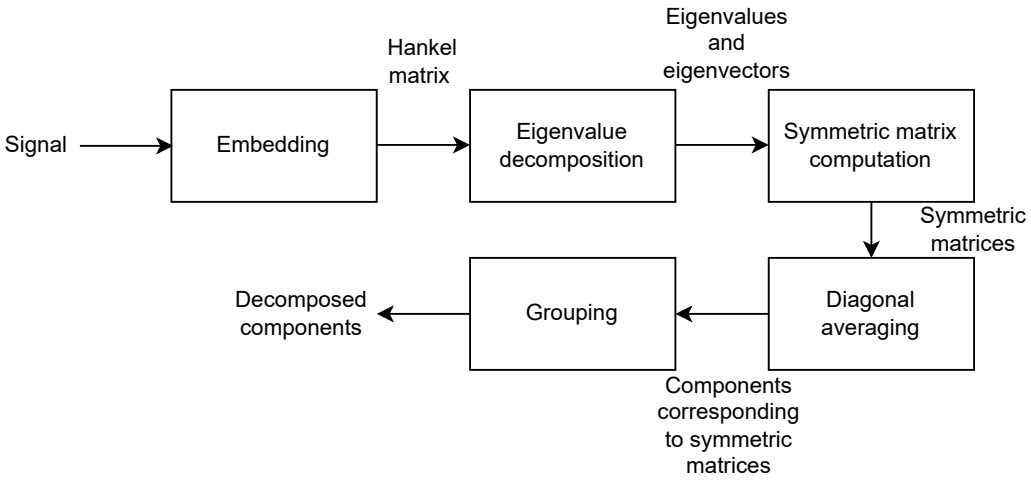

Figure 3.1: Block diagram representation of automated EVD-based decomposition of a signal into its constituent components.

vectors, they are having very low-level of long-term interdependence.

2. Due to spectral overlap between the mono-components, mode mixing problem occurs.

The sliding EVD improves the automated EVD's component separation capabilities for multicomponent non-stationary signals by applying it on short-duration segments of the signal. The steps involved in sliding EVD are explained below.

A sliding window of length L is selected and moved throughout the length of the signal with a step size δ for the decomposition process. Each of the frames obtained from the signal using the aforementioned process is decomposed into a set of R components using automated EVD method. For the first frame of sliding window ($l = 1$, l is starting index of the frame), the signal components $\hat{x}_r[n]$ are initialized with the decomposed components provided by automated EVD $\tilde{x}_r[n]$ for $n = 1, 2, \ldots, n_c$, where n_c is the center index of the window. Then, for the next frame ($l > 1$), the current decomposed components provided by automated EVD $\tilde{x}_m[n]$ for $m = 1, 2, \ldots, R$ and $n = 1, 2, \ldots, n_c$, are matched with the signal components of the previous frame $\hat{x}_r[l - \delta + n]$ for $n = 1, 2, \ldots, n_c$. For the

component matching between two consecutive frames is performed by minimizing either of the two measures mentioned below,

Measure 1: The distance function provided in equation (3.4) with $w[n] = 1 \; \forall \; 0 \leq n \leq N-1$

Measure 2: The difference between mean frequencies

For matching procedure, a variable M is used to store the previously associated components m to ensure that, each one is only associated once. When $l > 1$ and $l \neq N - L + 1$, samples ranging in $[n_c - \delta + 1, n_c]$ of $\tilde{x}_m[n] \; \forall \; m \; \in \; M$ are appended at the end of $\hat{x}_r[n]$ for $r = 1, 2, \ldots, R$. When the last frame is reached ($l = N - L + 1$), the samples ranging in $[n_c - \delta + 1, L]$ of $\tilde{x}_m[n] \; \forall \; m \; \in \; M$ are appended at the end of $\hat{x}_r[n]$ for $r = 1, 2, \ldots, R$. In this way, $\hat{x}_r[n]$ for $r = 1, 2, \ldots, R$ represents well-behaved mono-components of signal $x[n]$.

3.3 Sliding eigenvalue decomposition and Hilbert spectrum analysis for time-frequency analysis

In this work, the sliding EVD and HSA methods are utilized to obtain the TFD of a signal. The signal is decomposed into its constituent components using sliding EVD method described in section 3.2. In this study, the significant symmetric matrix computation explained in section 3.2.1.3 is computed using the approach 1, i.e., symmetric matrix corresponding to all the eigenvalue pair is significant. Further, the grouping of the components is performed using AHC based on distance measure 1, i.e., Euclidean distance measure, as explained in section 3.2.1.5. The component tracking to align the current frame components with the components of previous frame, the measure 1 is utilized as mentioned in section 3.2.2. The sliding EVD provides the decomposed components $\hat{x}_r[n]$ for $r = 1, 2, \ldots, R$

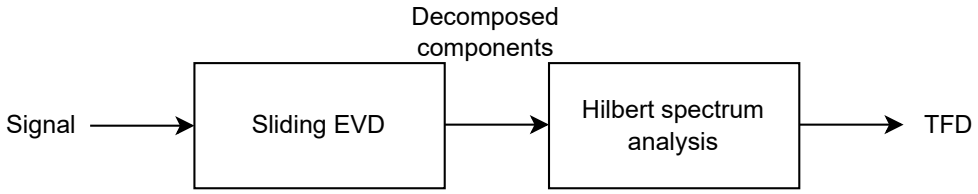

Figure 3.2: Block diagram representation to obtain TFD of a signal using sliding EVD-HSA method is shown.

of the signal $x[n]$. Furthermore, the HSA method (provided in section 1.2.4) is applied on the decomposed components to obtain the TFD of the signal. The block diagram of the same is depicted in Fig. 3.2.

3.4 Cross-term free time-frequency distribution using sliding eigenvalue decomposition and Wigner-Ville distribution

The sliding EVD-based new technique to suppress the cross-term in WVD of the multicomponent signal is developed. The sliding EVD decomposes the signal into its constituent components [175]. In sliding EVD, the significant symmetric matrix of each frame is computed from eigenvalues having magnitude greater than $\sqrt{0.1}$ times magnitude of first eigenvalue of the particular frame signal (as described in approach 2 of section 3.2.1.3). Furthermore, the grouping of obtained components of a frame is performed using the distance measure 2 defined in section 3.2.1.5. The components between two consecutive frames are tracked and aligned using measure 2, i.e., difference of mean frequency, as mentioned in section 3.2.2. The analytic representation of the decomposed components obtained from sliding EVD is computed followed by WVD [32]. Finally, WVDs of all the decomposed components are added together to get cross-term free WVD of the multicomponent signal. The block diagram of the proposed technique is depicted in Fig. 3.3. All these steps are

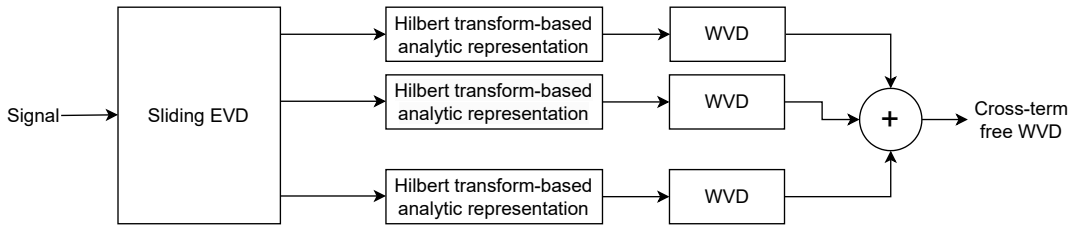

Figure 3.3: Block diagram of the sliding EVD and WVD method for obtaining cross-term free WVD of a signal is shown.

discussed in detail in the following subsections.

The analytic representation of the decomposed components $\hat{x}_r[n]$ are obtained with the help of Hilbert transform as shown in equation (3.7), to overcome the aliasing problem of WVD at zero frequency.

$$z_r[n] = \hat{x}_r[n] + j\mathcal{H}\{\hat{x}_r[n]\} \tag{3.7}$$

The WVDs $W_{\hat{x}_r}[n,k]$ of the analytic signal components $x_r[n]$ for $r = 1, 2, \ldots, R$ are computed. The cross-term free WVD of signal $x[n]$, $W_x[n,k]$, is obtained by summing the WVDs of individual extracted components obtained using sliding EVD method, which is shown in equation (3.8).

$$W_x[n,k] = \sum_{r=1}^{R} W_{\hat{x}_r}[n,k] \tag{3.8}$$

3.5 Results and discussion

Two separate studies are provided, one using sliding EVD-HSA whereas the other using sliding EVD-WVD, to obtain the TFD of a signal. The results obtained using these approaches are provided and discussed in the following subsection:

3.5.1 Hilbert spectrum analysis-based study

Real-time signals can be represented with the help of a combination of sinusoids, linear/quadratic frequency modulated (FM) signals, and sinusoidal FM signals. Hence for the

evaluation of the proposed method, combinations of these three signals are taken. All the signals considered in this subsection are sampled at a sampling rate $f_s = 2000$ Hz. To verify how well the proposed method decomposes the signals into its constituent mono-components, the quality reconstruction factor (QRF) as a performance measure has been used [50], which is computed by using equation (3.9).

$$\text{QRF}(\hat{x}_r[n], x_i[n]) = 20\log_{10}\left(\frac{||x_i[n]||_2}{||x_i[n] - \hat{x}_r[n]||_2}\right) \tag{3.9}$$

where $\hat{x}_r[n]$ is r^{th} decomposed component, $x_i[n]$ is i^{th} actual signal component, and $||x[n]||_2$ is the $\mathcal{L}_2$ norm of $x[n]$.

In this subsection, there are five different study conducted. The first study is an ablation study to assess the need of component tracking step in sliding EVD method. The second study assesses the performance of the sliding EVD method for abruptly changing signals. The third study analyzes the sensitivity of decomposition using the sliding EVD method to parameters such as window length and step size. The fourth and fifth studies are comparitive analysis of the proposed method with the improved EVDHM and HHT, respectively.

3.5.1.1 Ablation study of sliding eigenvalue decomposition

The component tracking method is used to track and align the decomposed component obtained from decomposition two consecutive frames in the proposed method to accurately obtain the constituent signal components. Consider a signal $x_1[n]$ for $n = 0, 1, \ldots, 1000$ defined by equation (3.10), which is the sum of two chirps signals. The signal $x_1[n]$ and its

two components are shown in Figs 3.4(a), (b), and (c), respectively.

$$x_1[n] = \left(1 + 0.8\sin\left(4\pi\frac{n}{f_s}\right)\right)\sin\left(2\pi\left(430 + 300\frac{n}{f_s}\right)\frac{n}{f_s}\right) + 0.55\sin\left(2\pi\left(110 + 300\frac{n}{f_s}\right)\frac{n}{f_s}\right) \quad (3.10)$$

The signal $x_1[n]$ is decomposed using the proposed sliding EVD method with a window length of 39 samples, a step size of 1 sample, and $R = 2$. The two decomposed mono-component signals of $x_1[n]$ obtained using sliding EVD are shown in Figs. 3.4(d) and (e), achieving QRF values of 23.4021 dB and 17.0036 dB, respectively. The comparison of Figs. 3.4(d) and (e) with Figs. 3.4(b) and (c) indicates that the decomposed components closely resemble the actual signal components. Thereafter, the signal $x_1[n]$ is decomposed using the sliding EVD method without component matching (with a window length of 39 samples, a step size of 1 sample, and $R = 2$), i.e., considering $J = \{1, 2, \ldots, R\}$ for all frames. The decomposed mono-component signals of $x_1[n]$ using sliding EVD without component matching are shown in Figs. 3.4(f) and (g), achieving QRF values 10.3820 dB and 3.9835 dB, respectively. Comparison of Figs. 3.4(f) and (g) with Figs. 3.4(b) and (c) indicates that the part of the decomposed mono-component signals are swapped with each other in the duration 0.3 to 0.45 s, causing reduction in QRF values. Therefore, it can be concluded that the component tracking method is an important step in the proposed sliding EVD method to accurately separate the signal components.

3.5.1.2 Analysis of abruptly changing signal using sliding eigenvalue decomposition

An abruptly changing signal $x_2[n]$ for $n = 0, 1, \ldots, 1000$, defined by equation (3.11), is considered to study the performance of sliding EVD for abruptly changing signals. The sig-

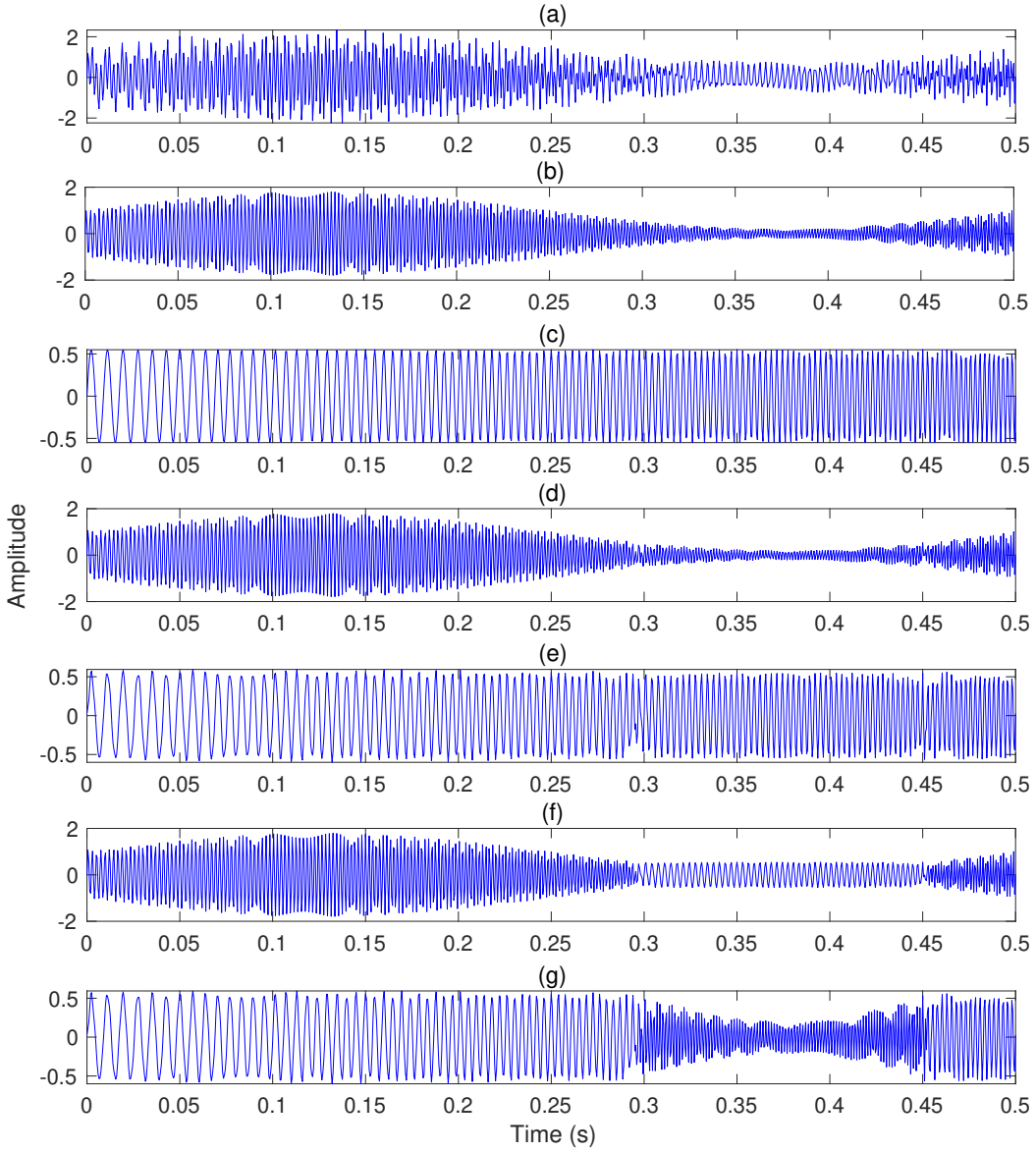

Figure 3.4: The signal $x_1[n]$ is shown in (a) and its actual components are shown in (b) and (c). The decomposed mono-component signals obtained from proposed method with component tracking are shown in (d) and (e) and without component tracking are shown in (f) and (g).

nal $x_2[n]$ and its two actual components are shown in Figs. 3.5(a), (b), and (c), respectively,

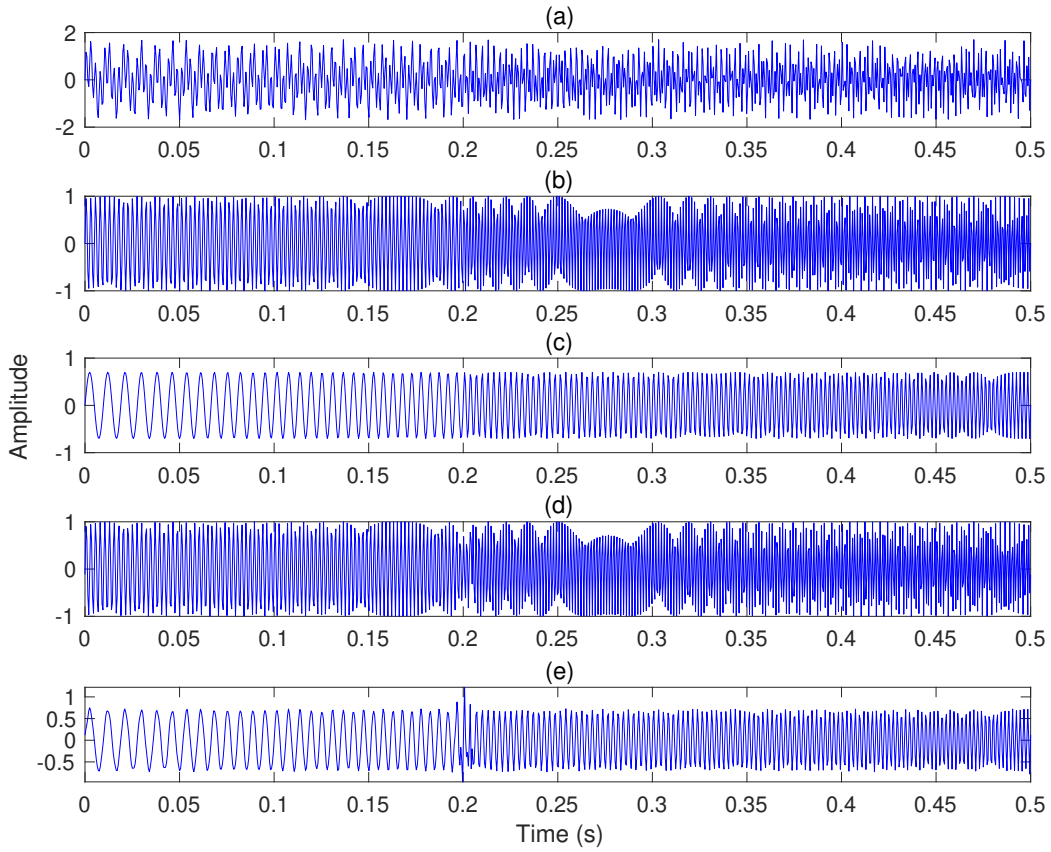

Figure 3.5: The signal $x_2[n]$ and its two actual components are shown in (a), (b) and (c), respectively. The decomposed mono-component signals obtained from sliding EVD are shown in (d) and (e).

showing an abrupt change in signal at 0.2 s.

$$x_2[n] = \begin{cases} 0.7\sin\left(2\pi\left(100+300\frac{n}{f_s}\right)\frac{n}{f_s}\right)+\sin\left(2\pi\left(400+300\frac{n}{f_s}\right)\frac{n}{f_s}\right), \\ \qquad\qquad\qquad\qquad\qquad\qquad \text{for } 0 \le n < 400 \\ 0.7\sin\left(2\pi\left(200+300\frac{n}{f_s}\right)\frac{n}{f_s}\right)+\sin\left(2\pi\left(500+300\frac{n}{f_s}\right)\frac{n}{f_s}\right), \\ \qquad\qquad\qquad\qquad\qquad\qquad \text{for } 400 \le n < 1000 \end{cases} \tag{3.11}$$

The signal $x_2[n]$ is decomposed using sliding EVD method with a window size of 39 samples, a step size of 1 sample, and $R = 2$. The obtained decomposed components are shown in Figs. 3.5(d) and (e), having QRF values 21.3692 and 18.2712 dB, respectively. The decomposed mono-component signals completely resemble the actual components of

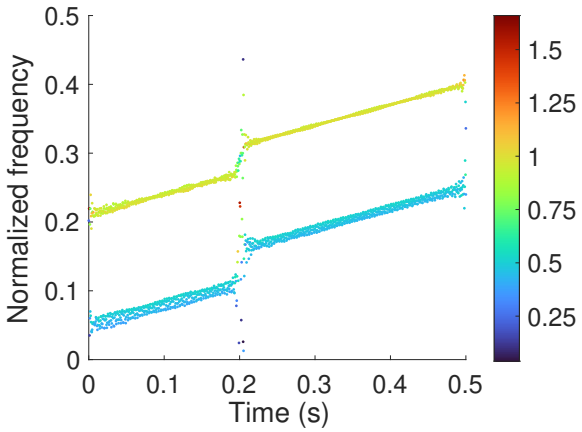

Figure 3.6: The TFD of the signal $x_2[n]$ obtained using sliding EVD-HSA.

the signal, except for a slight distortion at the time when the signal changes abruptly (0.2 s). Furthermore, the TFD of $x_2[n]$ obtained using sliding EVD-HSA is shown in Fig. 3.6, indicating the ability of the proposed method to represent abrupt changes of $x_2[n]$ in TFD.

3.5.1.3 Sensitivity analysis of sliding eigenvalue decomposition to window length and step size

The performance of the sliding EVD method depends on the selection of parameters, namely, window length and step size. Hence, it becomes of interest to study the sensitivity analysis of sliding EVD to these parameters. Consider a signal $x_3[n]$ for $n = 0, 1, \ldots, 1010$ defined as follows:

$$x_3[n] = 0.7 \sin\left(2\pi\left(100 + 500\left(\frac{n}{f_s}\right)^2\right)\frac{n}{f_s}\right) + \sin\left(2\pi\left(400 + 500\left(\frac{n}{f_s}\right)^2\right)\frac{n}{f_s}\right) \tag{3.12}$$

The signal $x_3[n]$ is decomposed using the sliding EVD method. To analyze the effect of window length, the signal $x_3[n]$ is decomposed using the sliding EVD-HSA method with step size of 1 sample and window lengths of 29, 39, 49, and 59 samples. The TFDs of $x_3[n]$ obtained using sliding EVD-HSA with different window lengths are shown in Fig. 3.7, indicating that the resolution first increases and then decreases. Furthermore, the comparison

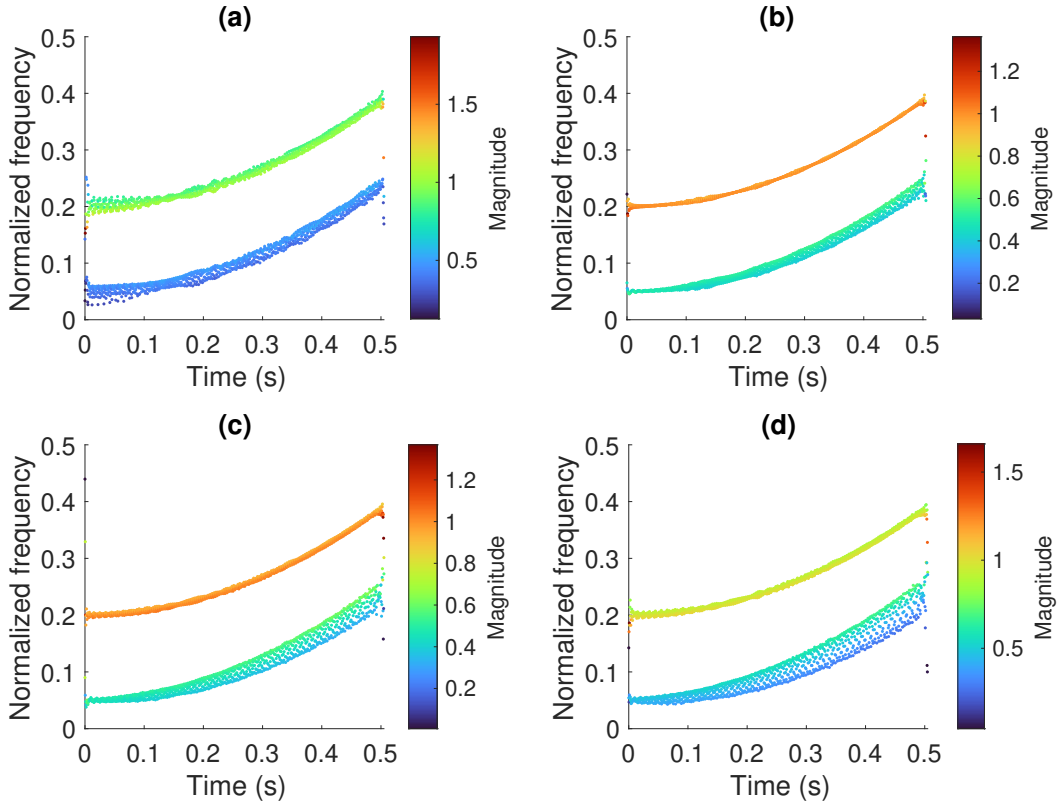

Figure 3.7: The TFDs of the signal $x_3[n]$ obtained using sliding EVD-HSA method with step size of 1 sample and window sizes 29, 39, 49, and 59 samples are shown in (a), (b), (c), and (d), respectively.

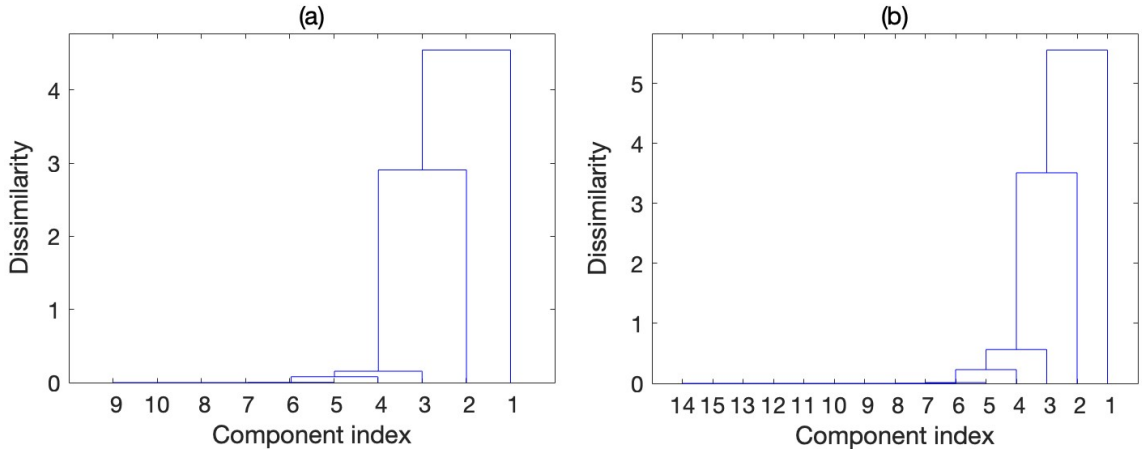

Figure 3.8: Dendrogram plots of AHC-based grouping for the 400^{th} frame in decomposition of $x_3[n]$ using sliding EVD method with (a) a window length of 39 samples and (b) a window length of 59 samples.

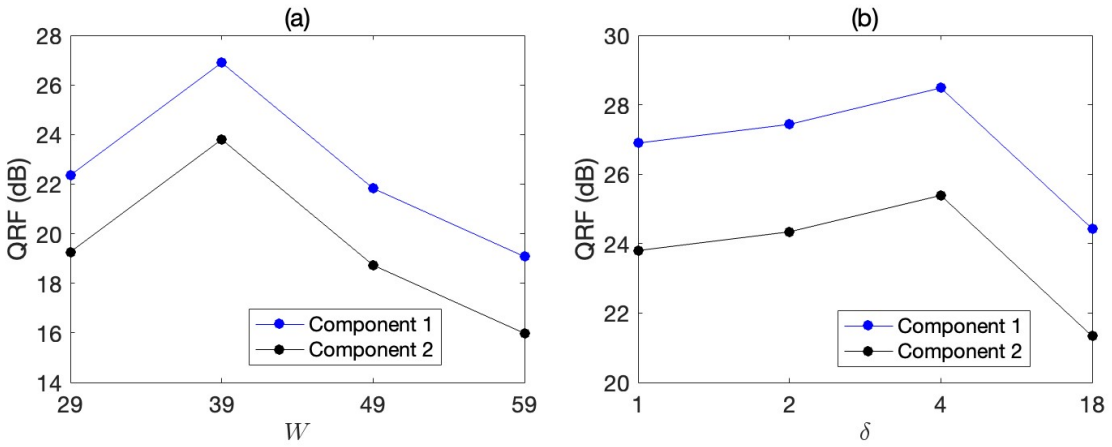

Figure 3.9: The QRF values of decomposed components of $x_3[n]$ obtained using sliding EVD is shown in (a) with window length (W) and step size of 1 sample and (b) with window length of 39 samples and step size δ.

of Figs. 3.7(b)–(d) indicates that the resolution of the low-energy component decreases relatively more as compared to high-energy component with increase in the window length, because more number of insignificant components are being added to it during AHC, as can be seen from the dendrogram shown in Fig. 3.8. Furthermore, the QRF values of the decomposed mono-component signals of $x_3[n]$, obtained using the sliding EVD method, first increases and then decreases with increasing window length for a fixed step size of 1 sample. The same is shown in Fig. 3.9(a).

To analyze the effect of step size, the signal $x_3[n]$ is decomposed using sliding EVD with fixed window size of 39 samples and four different values of step size (1, 2, 4, and 18 samples). The TFDs of $x_3[n]$ obtained using sliding EVD-HSA with different step sizes are shown in Fig. 3.10, indicating reduction in resolution after certain step size. Additionally, the QRF values of decomposed mono-component signals of $x_3[n]$ are computed for different step sizes as shown in Fig. 3.9(b), indicating QRF initially increases and then decreases for step size of 18 samples.

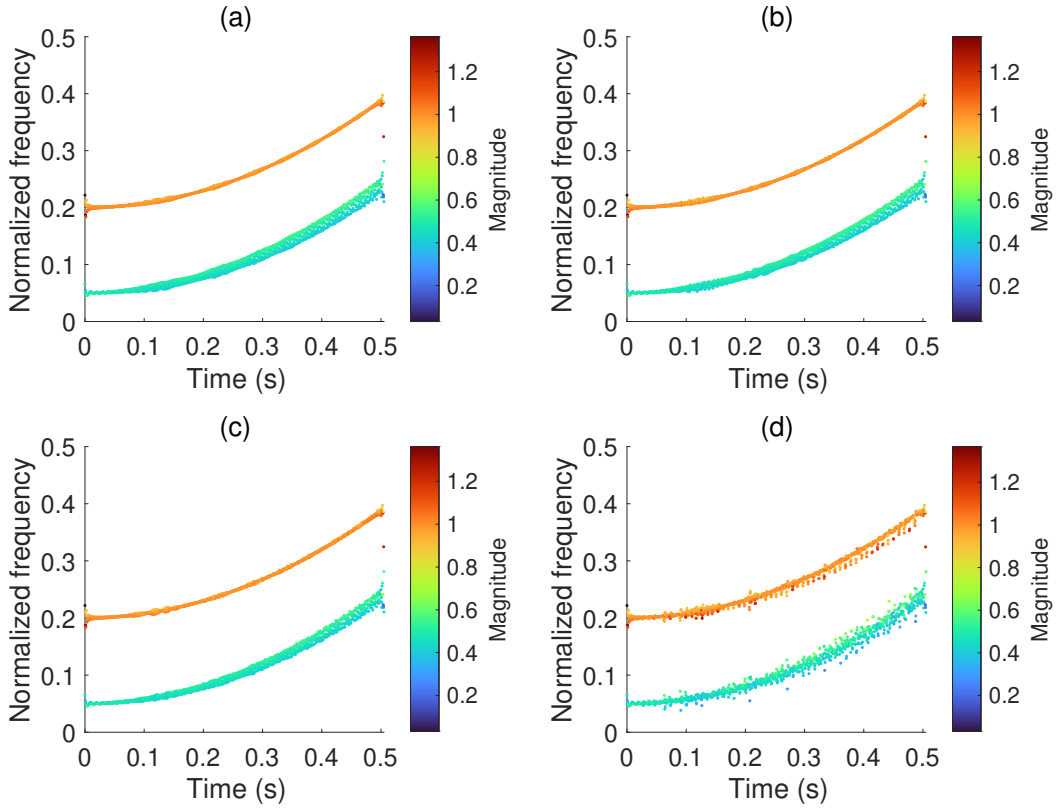

Figure 3.10: The TFDs of the signal $x_3[n]$ obtained using sliding EVD-HSA method with window size of 39 and step sizes of 1, 2, 4, and 18 samples are shown in (a), (b), (c), and (d), respectively.

3.5.1.4 Proposed sliding eigenvalue decomposition versus improved eigenvalue decomposition of Hankel matrix

The TFD obtained from proposed sliding EVD-HSA and improved EVDHM-HSA is presented and discussed for a signal $x_4[n]$ for $n = 0, 1, \ldots, 1000$, expressed using equation (3.13), having components having non-overlapped frequency spectrum and a signal $x_5[n]$ for $n = 0, 1, \ldots, 1000$, defined mathematically using equation (3.14), having two of its components with overlapped frequency spectrum. The signal $x_4[n]$ is sum of three sinusoids of frequencies 150, 200, and 400 Hz. Whereas, the signal $x_5[n]$ is sum of a sinusoid of 120 Hz and two quadratic chirps. The frequency of two chirp signals are starting from 280 and

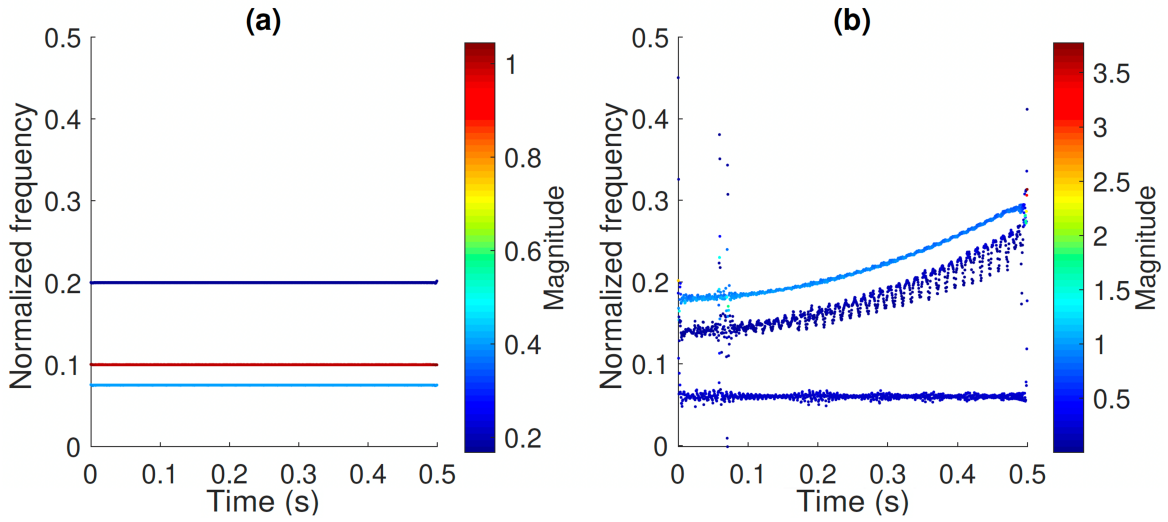

Figure 3.11: TFDs of signals $x_4[n]$ and $x_5[n]$ obtained using sliding EVD-HSA are shown in (a) and (b), respectively.

360 Hz and ending at 520 and 600 Hz, respectively.

$$x_4[n] = 0.85\cos\left(300\pi\frac{n}{f_s}\right) + \cos\left(400\pi\frac{n}{f_s}\right) + 0.65\cos\left(800\pi\frac{n}{f_s}\right) \tag{3.13}$$

$$x_5[n] = 0.7\cos\left(240\pi\frac{n}{f_s}\right) + 0.55\cos\left(2\pi\left(280 + 320\left(\frac{n}{f_s}\right)^2\right)\frac{n}{f_s}\right) + \cos\left(2\pi\left(360 + 320\left(\frac{n}{f_s}\right)^2\right)\frac{n}{f_s}\right) \tag{3.14}$$

The signal $x_4[n]$ and $x_5[n]$ are decomposed into their constituent components using the proposed sliding EVD method with window lengths of 239 and 91 samples and step sizes of 20 and 2 samples, respectively. The TFD of the signal is obtained by applying HSA on the decomposed components. The TFD of the signals $x_4[n]$ and $x_5[n]$ are provided in Fig. 3.11(a) and (b), respectively. Furthermore, the improved EVDHM-HSA-based TFD of the signals $x_4[n]$ and $x_5[n]$ are obtained and presented in Fig. 3.12.

From Figs. 3.11(a) and 3.12(a), it can be clearly seen that both the methods provide

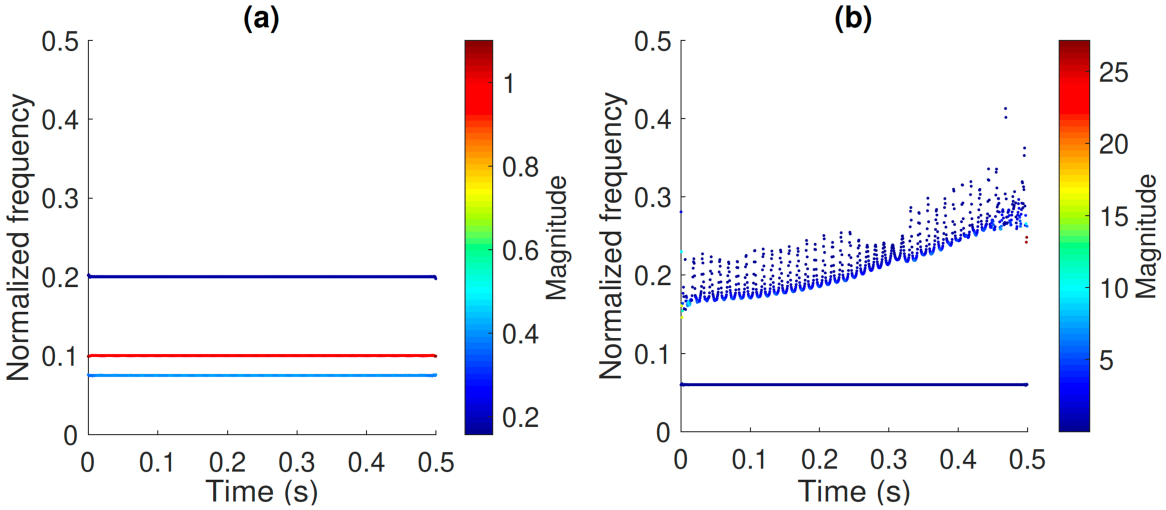

Figure 3.12: TFDs of signals $x_4[n]$ and $x_5[n]$ obtained using improved EVDHM-HSA are shown in (a) and (b), respectively.

very high resolution TFD for the stationary signal $x_4[n]$. The Fig. 3.12(b) indicates that improved EVDHM method is not able to separate the signal components of $x_5[n]$ which are overlapped in the frequency domain. However, the sliding EVD method is able to separate the signal components of $x_5[n]$ overlapped in frequency domain and is able to provide the frequency variation in time-frequency plane as shown in Fig. 3.11(b).

3.5.1.5 Proposed sliding eigenvalue decomposition-based Hilbert spectrum analysis versus Hilbert-Huang transform

The EMD method has showcased its efficacy in separating the components of a signal having overlapped frequency spectrum [176]. Hence, a comparative study of EMD and HSA, i.e., HHT-based TFD and sliding EVD-HSA-based TFD for signals with components overlapped frequency spectrum is performed. Further, the decomposed components of the studied signals obtained from sliding EVD-based decomposition and their respective QRFs are also provided.

The sixth signal selected to verify our algorithm is a combination of two quadratic FM

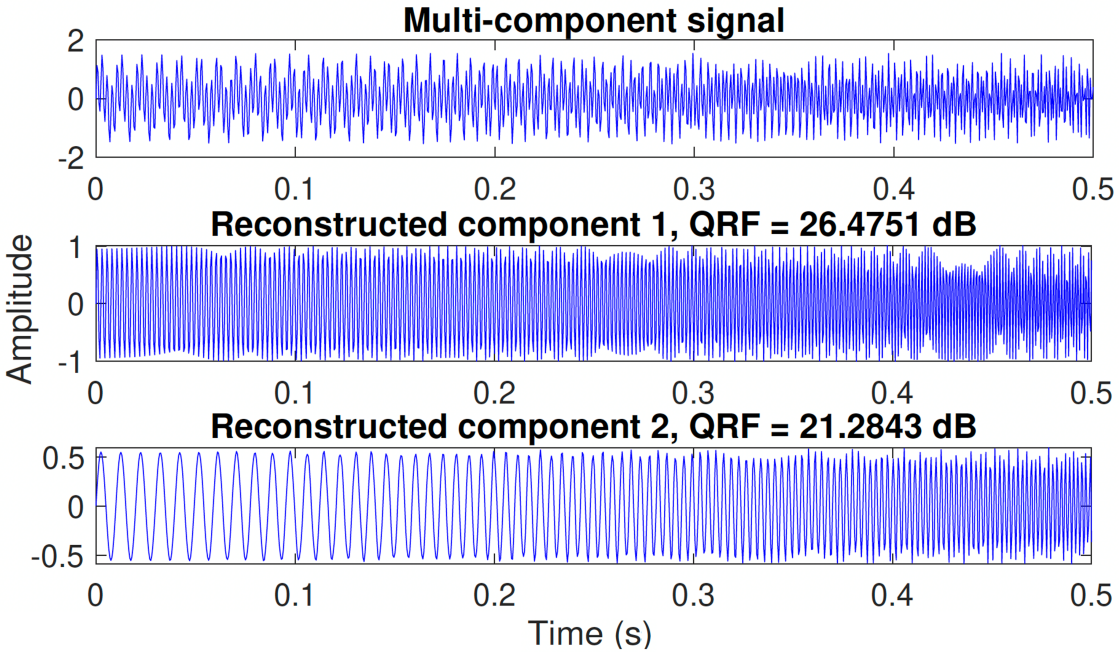

Figure 3.13: Signal $x_6[n]$ and its decomposed components using sliding EVD are shown.

signals as expressed in equation (3.15).

$$x_6[n] = 0.55\sin\left(2\pi\left(100+\frac{1600}{3}\left(\frac{n}{f_s}\right)^2\right)\frac{n}{f_s}\right)+\sin\left(2\pi\left(400+\frac{1400}{3}\left(\frac{n}{f_s}\right)^2\right)\frac{n}{f_s}\right) \tag{3.15}$$

where $n = 0, 1, \ldots, 1000$. The duration of the signal considered for analysis is 500 ms. For analysis, window length $L = 39$ samples and step size $\delta = 1$ sample are considered. The decomposed components and TFD of signal $x_6[n]$ are represented in Figs. 3.13 and 3.14, respectively.

The seventh signal that has been selected to verify our algorithm is a combination of two sinusoidal FM signals as expressed in equation (3.16).

$$x_7[n] \;=\; 0.5\sin\left(500\pi\frac{n}{f_s}+30\sin\left(\frac{20\pi n}{3f_s}\right)\right)+\sin\left(850\pi\frac{n}{f_s}+42.5\sin\left(\frac{20\pi n}{3f_s}\right)\right) \tag{3.16}$$

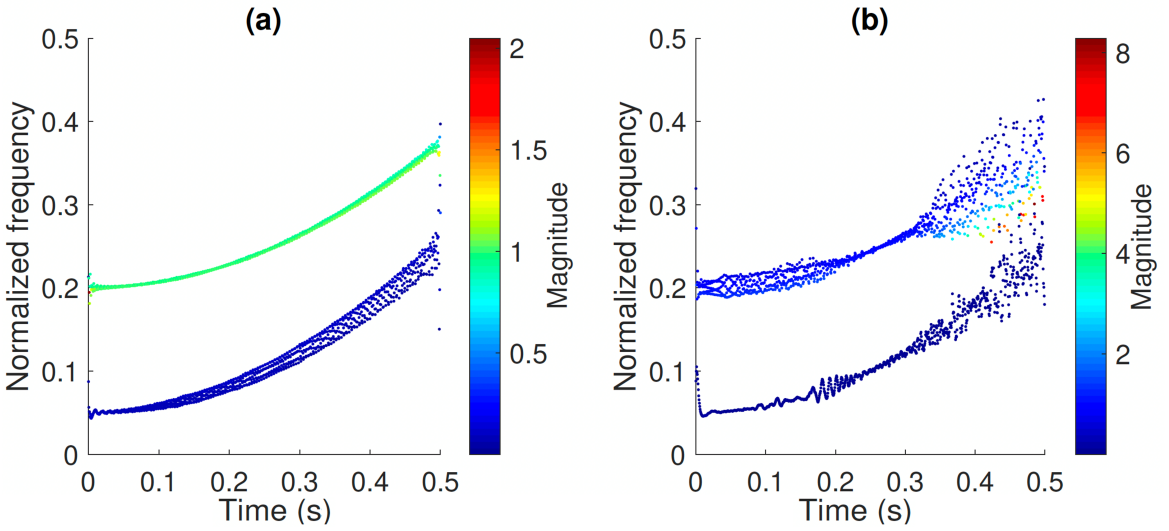

Figure 3.14: TFDs of $x_6[n]$ using sliding EVD-HSA and HHT methods are shown in (a) and (b), respectively.

where $n = 0, 1, \ldots, 4000$. The duration of the signal considered for analysis is 2 seconds. For analysis, window length $L = 39$ samples and step size $\delta = 3$ samples are considered. The decomposed components and TFD of signal $x_7[n]$ are represented in Figs. 3.15 and 3.16, respectively.

The TFD obtained using the proposed technique is found to be much better as compared to the TFD obtained from HHT. Along with that, the QRF parameter for decomposed components is also found to be good. One point to observe here is that the selection of window length L depends on the rate of change of instantaneous frequencies in the signal, i.e., the slower the rate of change, the wider the window can be selected and the better the TFD. While the step size δ value depends on the stationarity of the signal i.e, if the signal is stationary (like, $x_4[n]$) then its value is suggested to assume large (20-30 samples) and if the signal is non-stationary (like, $x_5[n]$) then its value is suggested to assume either 1 or 2 or 3.

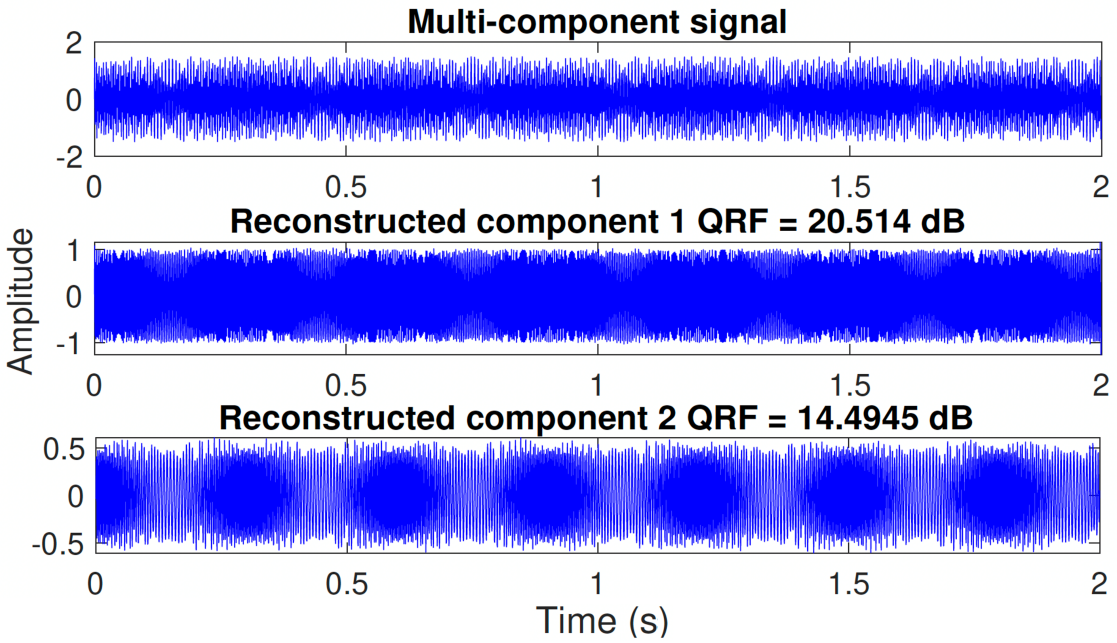

Figure 3.15: Signal $x_7[n]$ and its decomposed components using sliding EVD are shown.

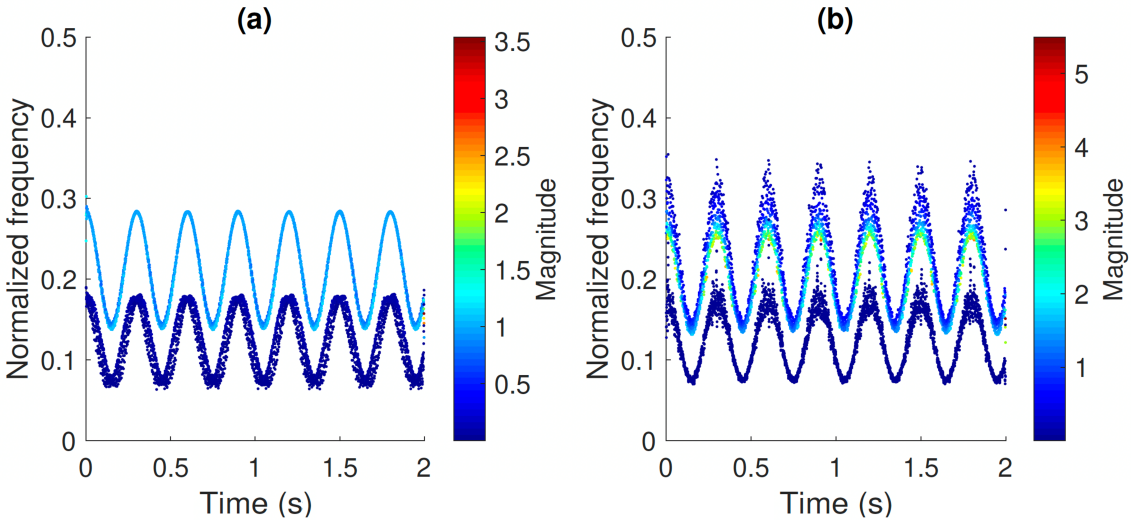

Figure 3.16: TFDs of $x_7[n]$ obtained using sliding EVD-HSA and HHT methods are shown in (a) and (b), respectively.

3.5.2 Wigner-Ville distribution-based study

The proposed sliding EVD-WVD-based cross-term suppression is illustrated for various types of synthetic signals under clean and noisy conditions and also on a speech signal. For

noisy conditions, additive white Gaussian noise (AWGN) at three signal to noise ratio (SNR) levels, i.e., 10, 15, and 20 dB are considered. To measure the performance of the proposed technique over existing techniques, normalized Rényi entropy [141, 177] is considered, which can be mathematically represented by equation (3.17).

$$R_\alpha = \frac{1}{1-\alpha}\log_2\left(\frac{\sum_{n=1}^{N}\sum_{k=1}^{K} W^\alpha[n,k]}{\sum_{n=1}^{N}\sum_{k=1}^{K} W[n,k]}\right), \quad \alpha \geq 2 \tag{3.17}$$

Here, $W[n,k]$ is the TFD and α is the order of information. The constraint on α is defined for $R_\alpha(C_x) = \frac{1}{1-\alpha}\log_2 \int_{-\infty}^{\infty}\int_{-\infty}^{\infty} C_x^\alpha(t,f)dtdf$, where $C_x^\alpha(t,f)$ is the Cohen's class TFD of a signal $x(t)$ with kernel $\phi(\theta,\tau)$, in [177]. In order to $R_\alpha(C_x)$ be a real-valued number, the expression inside $\log_2(\cdot)$ must be greater than or equal to 0. The value of $\int_{-\infty}^{\infty}\int_{-\infty}^{\infty} C_x^\alpha(t,f)dtdf$ is greater than or equal to 0, for all integers $\alpha \geq 1$ provided $\phi(\theta,\tau) \in \mathcal{L}_\infty$ and $\phi(0,0) > 0$ [177]. Hence, it becomes essential to consider the condition $\alpha \geq 1$ for the term inside $\log_2(\cdot)$ to be greater than or equal to 0. Additionally, R_α is not defined for $\alpha = 1$. Hence, there is constraint on α to be greater than or equal to 2. The same constraint was adapted for R_α defined in equation (3.17) [141]. In the current subsection, the value of the parameter α is considered as 3 for all simulations. The R_α is the measure of complexity of TFD which is similar to information measure in probability theory with two random variables. For measuring TFD complexity, the lower value of R_α represents the better resolution. The SPWVD [166], CW distribution [163], and EMD-WVD [168] are used as a baseline to compare the results obtained from the proposed technique. In SPWVD, we have considered 0.3 times signal length long Hamming window to get smoothed WVD. In order to obtain TFD from CW technique, we have used the code provided in [178]. In EMD-WVD method, the EMD part has been performed using the code provided in [179].

The TFDs obtained from the proposed technique and the baselines considered are discussed and illustrated in the following subsections. Note that for all the synthetic signals, the sampling frequency f_s is considered as 1000 Hz.

3.5.2.1 Signal 1

A multicomponent signal $y_1[n]$ is considered which comprises of three AM mono-component signals [171]. The mathematical expression of $y_1[n]$ is provided in equation (3.18).

$$y_1[n] = \sum_{i=1}^{3} \Big(A_i + \mu_i \cos\Big(2\pi k_i \frac{n}{f_s}\Big)\Big) \sin\Big(2\pi f_i \frac{n}{f_s}\Big) \tag{3.18}$$

Where $A_1 = 0.75$, $A_2 = 1.1$, $A_3 = 1.5$, $\mu_1 = 0.2$, $\mu_2 = 0.2$, $\mu_3 = 0.2$, $k_1 = 3/4$, $k_2 = 4/3$, $k_3 = 1/3$, $f_1 = 20$ Hz, $f_2 = 30$ Hz, and $f_3 = 97$ Hz are considered for $n = 0, 1, \ldots, 1000$. For the analysis using sliding EVD-WVD, the window length (L) and step size (δ) are set to 499 and 1 samples respectively. The time-domain representation of $y_1[n]$ along with the TFD obtained from baselines and proposed technique are represented in Fig. 3.17. The CW distribution and proposed sliding EVD-WVD are able to successfully remove the cross-term with good resolution for the considered signal. Whereas, SPWD and EMD-WVD are not able to remove the cross-term for the considered signal. Further, we have performed analysis of the signal $y_1[n]$ in noisy condition (AWGN) at different SNRs, the Rényi entropy measure of the obtained TFDs using baselines and sliding EVD-WVD technique are shown in Table 3.1.

3.5.2.2 Signal 2

A multicomponent signal $y_2[n]$ is considered which comprises of three nonlinear FM mono-component signals with two of them having spectral overlap. The mathematical ex-

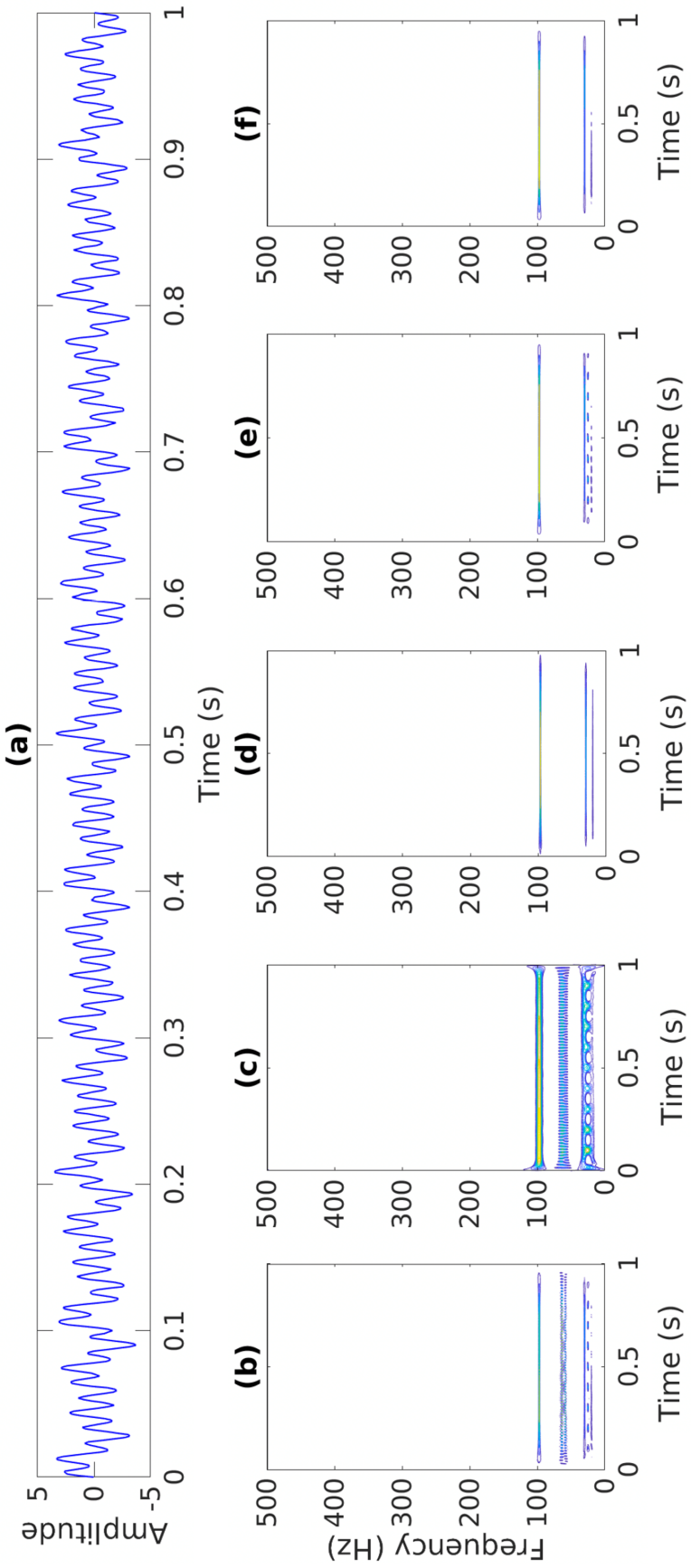

Figure 3.17: The time-domain represenation of signal $y_1[n]$ is shown in (a). The TFD of $y_1[n]$ obtained from WVD, SPWVD, CW distribution, EMD-WVD, and proposed sliding EVD-WVD techniques are shown in (b)–(f), respectively.

pression of $y_2[n]$ is shown in equation (3.19).

$$y_2[n] = \sum_{i=1}^{3} A_i \cos\Big(2\pi\Big(f_i + \frac{\beta_i}{3}\Big(\frac{n}{f_s}\Big)^2\Big)\frac{n}{f_s}\Big) \tag{3.19}$$

The considered parameters in equation (3.19) are as follows: $A_1 = 0.55$, $A_2 = 0.8$, $A_3 = 1$, $\beta_1 = 112$, $\beta_2 = 140$, $\beta_3 = 116$, $f_1 = 94$ Hz, $f_2 = 160$ Hz, $f_3 = 334$ Hz, and n = 0, 1, 2, ..., $N - 1$. In order to obtain TFD using sliding EVD-WVD technique, the L and δ are considered as 79 and 1 samples respectively. The temporal structure of the signal $y_2[n]$ and the TFDs obtained using the baseline techniques and the proposed sliding EVD-WVD technique are shown in Fig. 3.18. For considered signal $y_2[n]$, proposed sliding EVD-WVD gives high resolution TFD as compared to baselines. The SPWVD is not able to remove cross-term of the components which are overlapped in spectral domain. Whereas, EMD-WVD is not able to suppress cross-terms due to mode-mixing problem of EMD. Further, Rényi entropy measure is computed of the TFD obtained using baselines and proposed technique in clean and noisy cases, and it is shown in Table 3.1.

3.5.2.3 Signal 3

A multicomponent signal $y_3[n]$ is considered which comprises of two nonlinear FM mono-component signals with one of them having frequency increasing with time and other one is having frequency decreasing with time [30]. The mathematical expression of $y_3[n]$ is shown in equation (3.20).

$$y_3[n] = \sum_{i=1}^{2} A_i \cos\Big(2\pi\Big(f_i + \frac{\beta_i}{3}\Big(\frac{n}{f_s}\Big)^2\Big)\frac{n}{f_s}\Big) \tag{3.20}$$

The parameters $A_1 = 0.55$, $A_2 = 0.8$, $\mu_1 = 0.2$, $\beta_1 = 170$, $\beta_2 = -133$, $f_1 = 20$ Hz, $f_2 = 400$ Hz, and n = 0, 1, 2, ..., $N - 1$ have been considered for study. For simula-

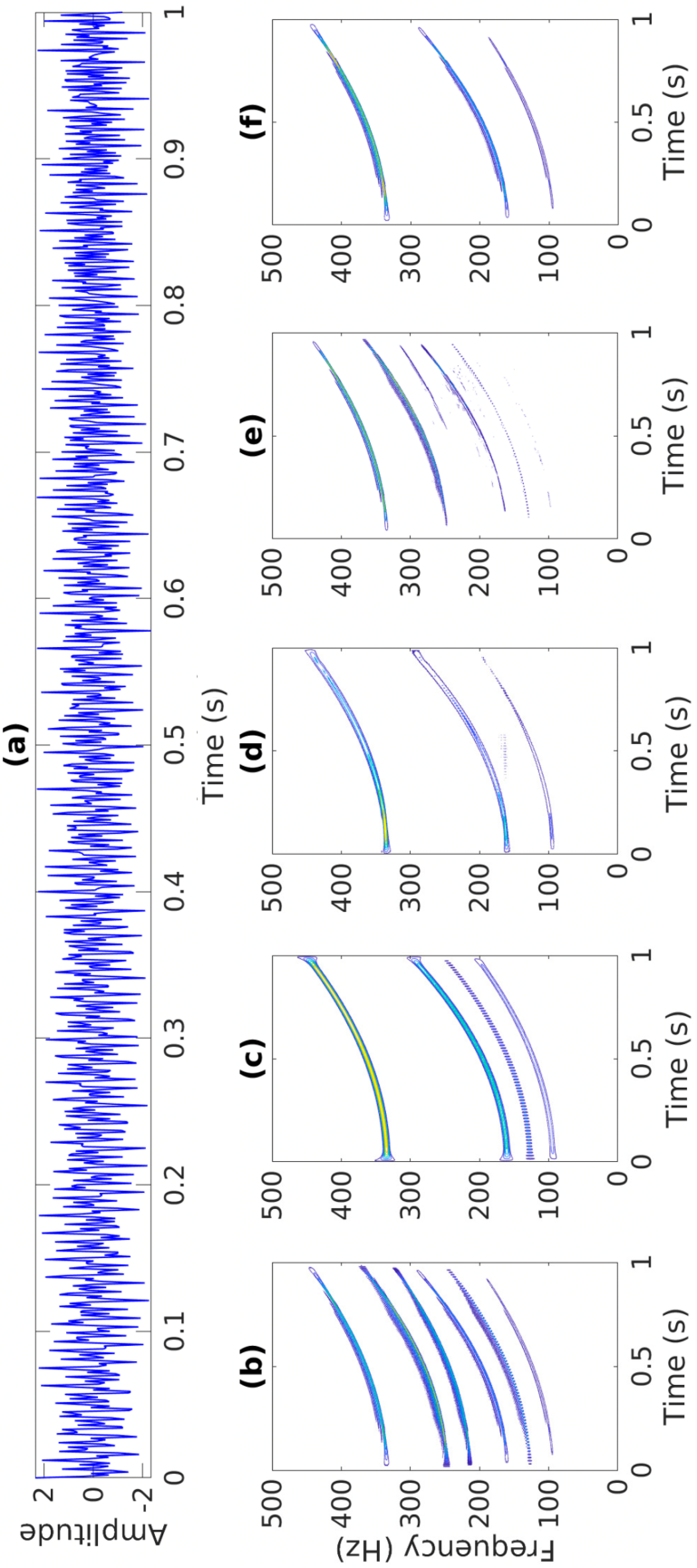

Figure 3.18: The temporal structure of the signal $y_2[n]$ is shown in (a). The TFDs of the same signal obtained using WVD, SPWVD, CW distribution, EMD-WVD, and proposed sliding EVD-WVD methods are shown in (b)–(f), respectively.

Table 3.1: The Rényi entropy measure of the signals $y_1[n]$, $y_2[n]$, and $y_3[n]$ in clean and various SNR levels in AWGN obtained from WVD, SPWVD, CW distribution, EMD-WVD, and proposed sliding EVD-WVD are provided.

Signal	SNR	WVD	SPWVD	CWD	EMD-WVD	Sliding EVD-WVD
$y_1[n]$	Clean	4.91	5.06	4.40	4.75	4.70
	20	4.97	5.07	4.42	4.85	4.69
	15	5.03	5.10	4.44	5.12	4.70
	10	5.16	5.15	4.50	5.44	4.71
$y_2[n]$	Clean	5.27	5.02	5.27	5.41	5.04
	20	5.33	5.10	5.29	5.46	5.04
	15	5.40	5.19	5.33	5.49	5.04
	10	5.54	5.33	5.41	5.62	5.12
$y_3[n]$	Clean	5.39	4.83	5.07	5.20	5.01
	20	5.46	4.93	5.12	5.28	5.01
	15	5.54	5.04	5.17	5.37	5.02
	10	5.71	5.28	5.33	5.50	5.07

tion using sliding EVD-WVD technique, the parameters i.e., L and δ were set to 119 and 1 samples, respectively. The temporal structure of the signal along with the TFD obtained from baselines and proposed technique are depicted in Fig. 3.19. The proposed technique has been found to be giving high resolution TFD as compared to baselines. Further, the Rényi entropy measure is computed as objective measure to show the effectiveness of proposed technique over the baselines in clean and noisy cases. The obtained Rényi entropy measures are shown in Table. 3.1.

From the Table 3.1, it can be concluded that the proposed method gives comparatively low Rényi entropy measure for the considered signals as compared to WVD, SPWVD, CW distribution, and EMD-WVD except for the signal $y_1[n]$. Further, it can be observed that the proposed method is more robust to AWGN as compared to other methods considered to suppress cross-term in WVD.

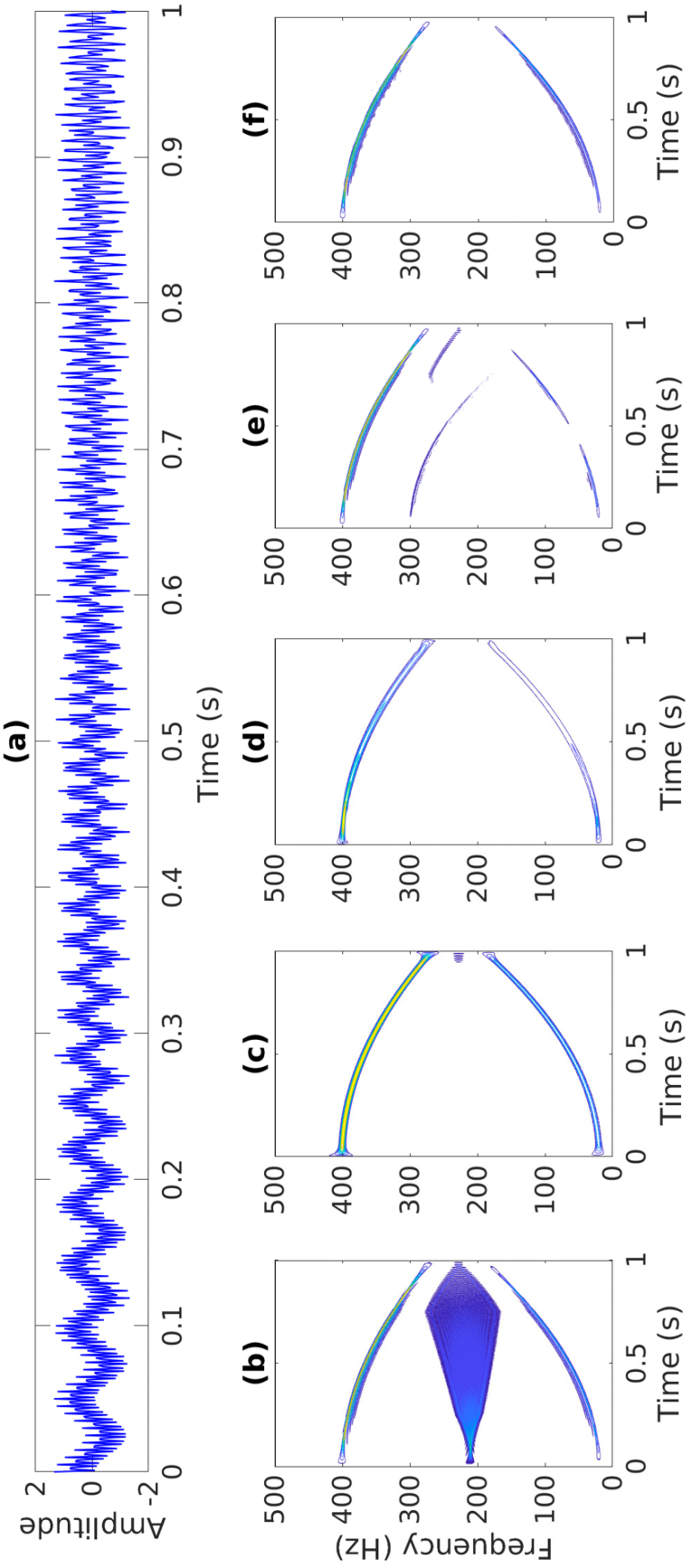

Figure 3.19: The multicomponent signal $y_3[n]$ is represented in (a). The TFDs of $y_3[n]$ obtained using WVD, SPWVD, CW distribution, EMD-WVD, and proposed sliding EVD-WVD technique are shown in (b),(c),(d),(e), and (f) respectively.

3.5.2.4 Real-world signal

A speech signal of voiced sound unit from CMU arctic database [1] is considered to show the performance of the proposed technique for real-world signals. The considered signal is sampled as sampling frequency 32 kHz. For the analysis of the cosidered speech signal using sliding EVD-WVD technique, $L = 1199$ samples, number of components to extract $(r) = 6$, and $\delta = 100$ is considerd. The proposed technique gives better TFD as compared to SPWVD, spectrogram, CW distribution, and EMD-WVD which can be seen from Fig. 3.20. Here, spectrogram is considered to know about the true components of the real-world signal. For the spectrogram computation, a Hamming window of length 400 samples with 390 samples overlap is considered. The TFD obtained from proposed technique found to be cross-term free with good resolution as compared to baselines. Hence, we can say that the sliding EVD-WVD is suitable for the analysis of real-world signals.

Atlast, the computational time required by WVD, SPWVD, CWD, EMD-WVD, and sliding EVD-WVD techniques is shown in Table 3.2 for both synthetic ($y_1[n]$, $y_2[n]$, $y_3[n]$) and real-world speech signals. All simulations were performed with the help of MATLAB R2020B on a personal computer setup having Intel Core i7-4790 vPro CPU @ 3.60 GHz $\times$ 8, with 28 GB RAM, and Ubuntu 20.04.3 LTS operating system. From the table it can be observed that EMD-WVD and sliding EVD-WVD have much more computational time as compared to WVD, this is because these two methods first decompose the signal into its components and then WVD is applied on each of the decomposed components. While the computational time required for EMD-WVD is slightly less than sliding EVD-WVD for synthetic signal but due to better TFD of proposed technique over EMD-WVD, this small difference in computational time can be overlooked.

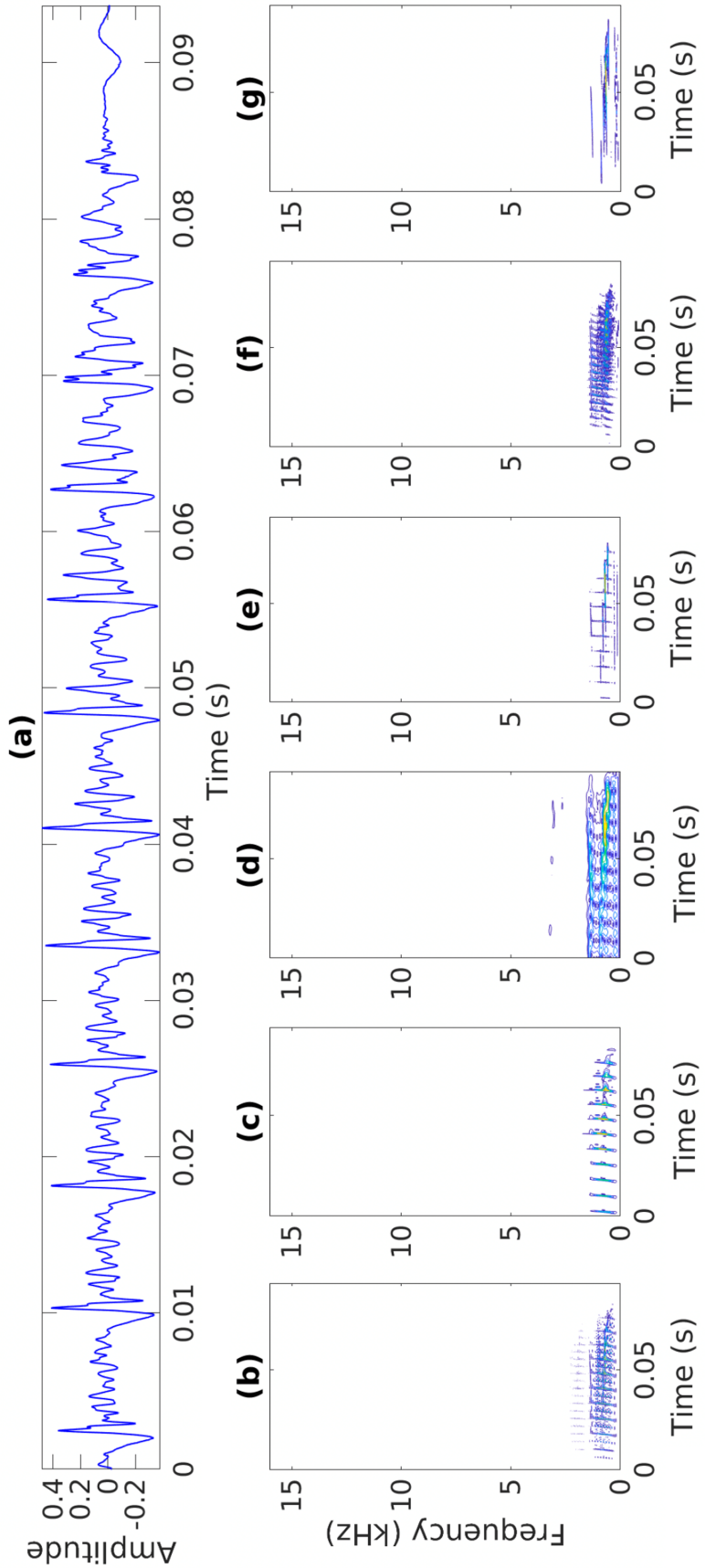

Figure 3.20: The time-domain representation of the voiced phoneme of speech signal is represented in (a). The TFDs of the aforementioned signal obtained from WVD, SPWVD, spectrogram, CW distribution, EMD-WVD, and proposed sliding EVD-WVD methods are shown in (b)–(g), respectively.

Table 3.2: The computational time required to get TFDs using the WVD, SPWVD, CWD, EMD-WVD, and sliding EVD-WVD techniques for cosidered synthetic and real-world signals are provided. The computational time mentioned in this table is in seconds.

Signal	WVD	SPWVD	CWD	EMD-WVD	Sliding EVD-WVD
$y_1[n]$	0.0977	0.0862	0.2646	0.6484	2.6391
$y_2[n]$	0.0965	0.0933	0.2589	0.9475	1.0308
$y_3[n]$	0.1022	0.0931	0.2644	0.7681	0.9750
Speech	1.1951	0.9833	3.2765	10.3203	8.2302

3.6 Summary

This chapter introduced a new signal decomposition method namely, sliding EVD to decompose the signal into its constituent components. The sliding EVD method is able to separate the components which have overlapped frequency spectrum. The ablation study for component tracking step in sliding EVD-HSA method is studied, to showcase its need in sliding EVD method. Additionally, sensitivity analysis of sliding EVD-HSA is studied for the parameters window length and step size. The change in the values of aforementioned parameters resulted into increase in QRF value initially and later decreased. Hence, selection of optimal values of window length and step size is crucial for getting better performance. The performance of the sliding EVD-HSA for an abruptly changing synthetic signal is studied. The sliding EVD-HSA provided high resolution TFD for the considered abruptly changing signal. The TFD of the signal obtained using sliding EVD-HSA is compared with TFDs obtained from improved EVDHM-HSA and HHT methods and found to be providing high resolution TFD. Furthermore, a new method, called sliding EVD–WVD, is proposed for obtaining the cross-term-free WVD of multicomponent signals. The proposed technique decomposes the multicomponent signal into its mono-component signals, and the WVDs are obtained from the signal components individually. Further, in order to get cross-term free TFD, WVDs of each component are added together. The proposed

technique has been verified on both synthetic and real-world signals. For synthetic signals, the method has been tested in various noisy conditions and found to be robust to AWGN. The Rényi entropy has been used as the performance measure. The proposed technique found to be giving cross-term-free TFD even in the noisy scenario. It has also been verified on a real-world speech signal and found to be providing cross-term-free TFD with good resolution.

The component tracking corresponding to consecutive frames in sliding EVD becomes difficult when a multicomponent signal has a large number of mono-components or components are very close to each other in time–frequency plane. So, this can be improved as part of the future work of this carried out research.

Chapter 4

EMD-like eigenvalue decomposition of Hankel matrix for signal analysis

4.1 Introduction

Generally, the signals acquired in real-life possess non-stationary characteristics. This is mainly due to the presence of time-localized events in the process, which change the frequency and amplitude of the modes present in the signal over time. Also, the short-duration signal acquisition can make the stationary signal, non-stationary [16]. A few examples of non-stationary signal we observe in nature are: (1) power-line fault signal [180]; (2) physiological signals like, EEG [181], ECG [182], EMG [183], etc.; (3) seismic signal [184]; (4) underwater acoustic signal [185]; etc. Time-frequency analysis methods are used for analysis of non-stationary signals in order to have complete and meaningful information, as they provide the time-varying frequency spectrum of the signal, known as TFD [30].

For obtaining the TFD of a non-stationary signal, there are several techniques presented in the literature with various preliminary assumptions about the signal. The STFT provides the TFD of a signal by window based Fourier analysis [36]. Preliminary assumption made while computing STFT is that signal should be stationary within the analysis window which

is not always the case with real-time signals. Also, choosing a proper window length for STFT based analysis is a challenging task. In adaptive STFT, the window length of the signal is computed adaptively from the signal using the cone length of optimal cone kernel distribution (CKD) [22]. The optimal CKD cone length is the duration over which the signal is either stationary or has slowly varying frequency structure [23].

To overcome the issue of fixed basis and constant window length of STFT, the wavelet transform was proposed. The wavelet transform offers flexibility on basis selection based on our suitability for analysis [13]. Also, the variable window length for analysis of different frequency components in the signal provides multi-resolution time-frequency analysis. The squared magnitude of CWT is known as scalogram [13]. However, the CWT contains some redundant information and to overcome this, DWT was presented [24].

The STFT and wavelet transforms are fixed basis techniques for signal analysis. There are several data-adaptive basis-based signal analysis techniques in literature like, EMD [16], SSA [49], iterative filtering [186, 187], EWT [46], FBSE-EWT [48], VMD [45], FDM [54], EFDM [55], improved EVDHM [53], etc. The EMD decomposes the multicomponent non-linear non-stationary signal into a set of IMFs by using the sifting process. Later, the obtained IMFs are processed through HSA, which provides the TFD of the signal [16]. The EMD suffers from the mode-mixing problem. Furthermore, the IMFs of noisy signals suffer from noise due to the completeness of the EMD technique. To overcome these problems of EMD, the EEMD was proposed in literature [44]. The steps involved in the EMD and EEMD process are intuitive and do not have a mathematical foundation.

The EWT was proposed in literature for decomposition of the signal in terms of empirical modes by adaptive segmentation of its Fourier spectrum using Littlewood-Paley and Meyer's wavelet [46]. This also provides a complete decomposition of the signal, which is not a good selection for signal analysis in noisy conditions, as noise is present in the decom-

posed components. The FBSE-EWT decomposes the multicomponent signal into sub-band signals by adaptive segmentation of the FBSE spectrum [48]. There is one more technique in the literature based on adaptive spectral segmentation of the signal, i.e., VMD. The VMD first computes the N local maxima and then optimizes the bandwidth around the obtained maxima [45]. In this way, it provides the signal modes.

The SSA and improved EVDHM are the data-adaptive signal decomposition techniques, which first compute the Hankel matrix corresponding to the input signal and then perform singular value decomposition and eigenvalue decomposition, respectively followed by diagonal averaging of the obtained symmetric matrices to get the elementary components [49, 52, 53, 75]. Consequently, the grouping of elementary components is performed in order to obtain the mono-component signals. There are two methods in literature to perform grouping, i.e., spectral overlap-based grouping [52, 53] and agglomerative hierarchical clustering [75, 175]. The HSA of the obtained mono-component signals provides the TFD of the signal. The improved EVDHM-based techniques fail to decompose the components that are overlapped in the frequency domain. To do so, the sliding eigenvalue decomposition technique is presented in the literature [175, 188]. The sliding EVD-based HSA provides high-resolution TFD compared to the improved EVDHM-based HSA [188].

In this chapter, a novel signal decomposition framework is proposed that is based on the EVDHM and the sifting approach. This method extracts the dominant component of the signal in each iteration and considers the residue as the signal for the next iteration until there is no dominant component to extract in residue. The dominant components are extracted from elementary components of each iteration using a grouping method. The component grouping methods studied in the literature are based on time- or frequency-domain parameters [52, 175] However, the time-frequency domain provides more insight into the signal compared to individual domains. Furthermore, frequency spread and IF-

based criterion is presented in literature to identify whether the sum of two mono-component signals is mono-component or multicomponent [145]. Hence, a new component grouping method using frequency spread and IF-based criterion is also proposed to extract the DMSs in each iteration. The main contributions of this work are listed below.

1. A novel iterative EVDHM-based framework is proposed for the extraction of DMSs.
2. The empirical parameter and minimum description length (MDL)-based two approaches are proposed for eigenvalue threshold computation.
3. The frequency spread and IF-based component grouping method is proposed to extract DMSs in each iteration.

The proposed signal decomposition framework is termed as EMD-like EVDHM. Further, HSA is applied to the DMSs to obtain TFD. The performance of the proposed framework is verified on various clean and noisy synthetic and real-time voiced speech signals. For the performance measure, the QRF [50] and average correlation [50] are used. The results obtained from the proposed methods are further compared with EMD [16], EEMD [44], VMD [45], iterative filtering [186], FDM [54], EFDM [55], EWT [46], FBSE-EWT [48], SSA [75], and improved EVDHM [53] for the aforementioned signal cases and found to provide better performance in terms of QRF and average correlation and the resulting high resolution TFD. Further, the analysis of synthetic signals is performed in noisy conditions.

4.2 Empirical mode decomposition-like eigenvalue decomposition of Hankel matrix method

In this section, a detailed description of the proposed EMD-like EVDHM method is provided to extract DMSs from a signal in an iterative way just as in the EMD method. In

each iteration, the proposed method decomposes the signal using EVDHM and performs the grouping of the components based on a new component grouping method to extract the MDMS of that iteration, while residue is considered as the signal for the next iteration. The steps involved to decompose the signal $x[n]$ for $n = 0, 1, \ldots, N-1$ using the proposed framework are explained below. To start the decomposition process, the iteration number (r) is set equal to 1.

Step 1: A Hankel matrix X is obtained from the signal $x[n]$ defined using Step 1 described in Section 2.1.

Step 2: The eigenvalue decomposition of matrix X is performed to obtain the set of eigenvalues $(\lambda_1, \lambda_2, \ldots, \lambda_K)$ and corresponding eigenvectors $(u_1, u_2, \ldots, u_K)$ using Step 2 described in Section 2.1.

Step 3: The eigenvalue threshold (λ_{th}) is computed in the first iteration ($r = 1$) for selection of significant eigenvalue pairs, as not all the eigenvalue pairs convey significant information. The following two approaches are proposed for threshold computation:

1. Empirical approach:

$$\lambda_{\text{th}} = 0.001 \times \rho(X) \times \left(1 + \frac{1000}{\text{SNR}}\right). \tag{4.1}$$

where $\rho(X)$ is the spectral radius of the matrix X, which represents the maximum value of the magnitude of eigenvalues of X and SNR represents the signal to noise ratio of a noisy signal. The value of $\frac{1}{\text{SNR}}$ is assigned 0 for analysis of clean signal. With an increase in the SNR of a noisy signal, the magnitude of the eigenvalues associated with the noise components also increases. Therefore, in order to effectively eliminate the influence of noise components from the analy-

sis, it becomes essential to design the threshold as a function of SNR to enhance the robustness of the method against noise.

2. MDL-based approach [189]:

$$\text{MDL}(p) = \frac{p \ln(N)}{2} + \sum_{n=0}^{N-1} \ln\left(\cosh\left((x[n] - \hat{x}_p[n])^2\right)\right) \tag{4.2}$$

where p is the number of significant eigenvalue considered for reconstruction, $\hat{x}_p[n]$ is the reconstructed signal using p eigenvalue pairs, $\cosh(\cdot)$ is the hyperbolic cosine function, and $\ln(\cdot)$ is the natural logarithm function. Here, the log-hyperbolic cosine loss function is considered in place of log-mean squared error loss function because it is robust to outliers [190]. The threshold is computed as $\lambda_{\text{th}} = \min(|\lambda_P|, |\lambda_{K-P+1}|) - \epsilon$ where $P = \text{argmin MDL}(p)$ and ϵ is the tolerance in threshold. The tolerance parameter ϵ is introduced because the magnitude of the eigenvalue corresponding to a given component vary slightly across different iterations. The same can be seen from decomposition of the signal $x[n] = \sin\left(320\pi\frac{n}{f_s}\right) + 0.8\cos\left(2\pi\left(100 + 5\frac{n}{f_s}\right)\frac{n}{f_s}\right)$, where f_s = 1000 Hz, and $n = 0, 1, 2, ..., 1000$. The decomposition provides the sets of eigenvalue pairs $\{(-250.5023, 250.4939), \quad (-126.1962, 126.2065), \quad (-120.4310, 120.2396), (-89.7321, 89.1136), \ldots\}$ and $\{(-126.1860, 126.1967), (-120.4137, 120.2218), (-89.7352, 89.1032), \ldots\}$ in iterations 1 and 2, respectively. Here, the magnitude of eigenvalues of remaining components slightly changes after first component is extracted, and it continues in subsequent iterations. In this study, $\epsilon = 0.5$ is considered.

Step 4: The set of significant eigenvalue pairs are computed using the significant eigenvalue

threshold λ_{th} as defined below,

$$I = \left\{ i \ : \ |\lambda_i| > \lambda_{\text{th}} \text{ or } |\lambda_{K-i+1}| > \lambda_{\text{th}} \ \forall \ i \in \left\{ 1, 2, \ldots, \left\lfloor \frac{K}{2} \right\rfloor \right\} \right\} \tag{4.3}$$

After this, we have a set of significant eigenvalue and eigenvector pairs (λ_i, λ_{K-i+1}) and (u_i, u_{K-i+1}) $\forall \ i \ \in \ I$, respectively. If $I = \emptyset$, the decomposition process is terminated. Else, i^{th} symmetric matrix X_i corresponding to i^{th} significant eigenvalue and eigenvector pairs is obtained as [52],

$$X_i = u_i \lambda_i (u_i)^T + u_{K-i+1} \lambda_{K-i+1} (u_{K-i+1})^T \ \forall \ i \in I \tag{4.4}$$

Step 5: The averaging of skew diagonal elements of X_i is performed, using Step 5 described in Section 2.1, in order to obtain i^{th} component ($x_i[n]$) of the signal $x[n]$. After this step, the signal $x[n]$ can be represented as,

$$x[n] \approx \sum_{i \in I} x_i[n] \tag{4.5}$$

Step 6: The MDMS is computed in each iteration using algorithm 4.1. The same has been discussed in detailed in section 4. The r^{th} DMS of the signal is the MDMS of the r^{th} iteration.

Step 7: The residue signal $x_{\text{res}}[n]$ is computed as $x_{\text{res}}[n] = x[n] - x_i^{\text{dec}}[n]$. The residue signal $x_{\text{res}}[n]$ is considered as input signal $x[n]$ for the next iteration, i.e., r will be replaced by $r + 1$ and the process is repeated from Step 1.

[1]The `length` function returns the length of the input vector.

[2]The function `extr` takes a vector input and returns number of extrema (e_{num}) and number of zero-crossing (z_{num}) as output.

Algorithm 4.1 Extraction of MDMS ($x_r^{\text{dec}}[n]$) for r^{th} iteration.

Require: $x_i[n]\ \forall\ i \in I$ for the r^{th} iteration, ind $= \emptyset$.

procedure
  ind $\leftarrow 1$
  for $i = 2 : I$ **do**
    for $a = 1 : \texttt{length}^1(\text{ind})$ **do**
      $k = \text{ind}[a]$
      $x_{i+k}[n] = x_i[n] + x_k[n]$
      $[e_{\text{num}}, z_{\text{num}}] = \texttt{extr}^2(x_{i+k}[n])$
      if $|e_{\text{num}} - z_{\text{num}}| < 2$ **then**
        $a_i[n] = |x_i[n] + j\mathcal{H}\{x_i[n]\}|$ and $a_k[n] = |x_k[n] + j\mathcal{H}\{x_k[n]\}|$
        $\phi_i[n] = \angle(x_i[n] + j\mathcal{H}\{x_i[n]\})$ and $\phi_k[n] = \angle(x_k[n] + j\mathcal{H}\{x_k[n]\})$
        $\omega_i[n] = \phi_i[n] - \phi_i[n-1]$ and $\omega_k[n] = \phi_k[n] - \phi_k[n-1]$
        $\text{th}_i = 0.1\max(a_i[n])$ and $\text{th}_k = 0.1\max(a_k[n])$
        $L = \{n : a_i[n] \geq \text{th}_i \text{ and } a_k[n] \geq \text{th}_k\}$
        if $0.5(\sigma_{\omega_i}[n] + \sigma_{\omega_k}[n]) < |\omega_i[n] - \omega_k[n]|\ \forall\ n \in L$ is not satisfied **then**
          ind $\leftarrow i$
          Exit from **for** of a
        end if
      end if
    end for
  end for
  $x_r^{\text{dec}}[n] = \sum_{i \in \text{ind}} x_i[n]$
end procedure

At the end of above iteration, the signal $x[n]$ can be represented as,

$$x[n] = \sum_{r=1}^{R} x_r^{\text{dec}}[n] + x_{\text{res}}[n] \tag{4.6}$$

where R is the number of obtained DMS and $x_{\text{res}}[n]$ is the noise or insignificant part of the signal $x[n]$. The block diagram of the decomposition process is shown in Fig. 4.1. The proposed method decomposes the signal based on the sifting approach, that is, extracts the dominant component in each iteration, and the residue is used as the signal for the next iteration, similar to the EMD method. Therefore, it is named the EMD-like EVDHM method.

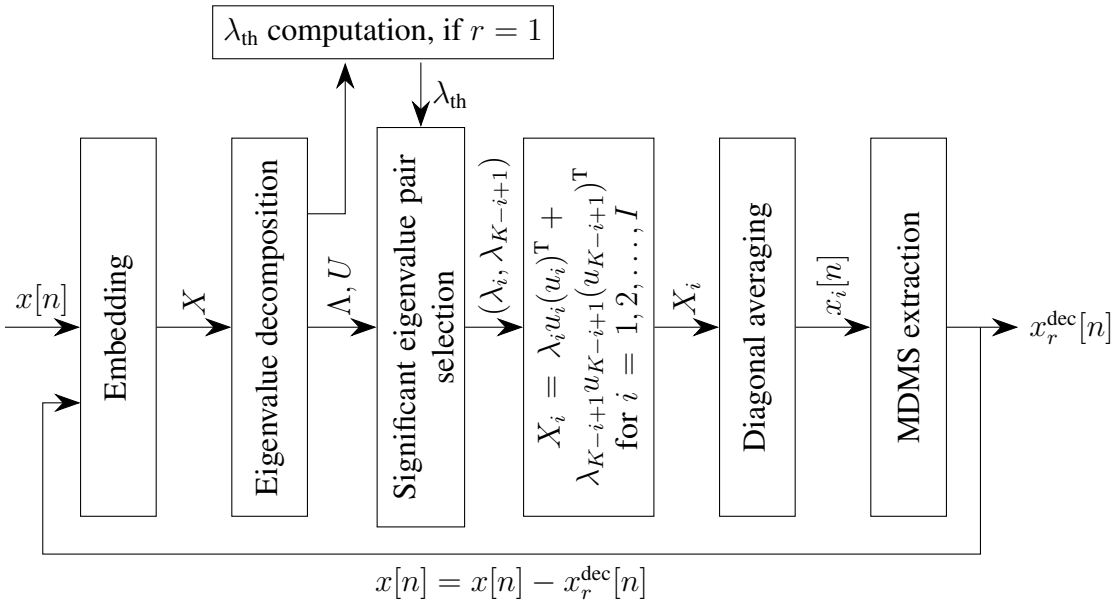

Figure 4.1: Block diagram representation of the proposed EMD-like EVDHM technique for signal decomposition.

4.3 Frequency spread and instantaneous frequency-based method for efficient grouping of components

In this section, a frequency spread and IF-based criterion is used to check whether the summation of two decomposed components is a mono-component or multicomponent signal. Consider a signal $x(t)$ represented as the sum of two signals, i.e.,

$$x(t) = x_1(t) + x_2(t) = a_1(t)e^{j\phi_1(t)} + a_2(t)e^{j\phi_2(t)} \tag{4.7}$$

The signal $x(t)$ will be a multicomponent signal if the following condition is satisfied [145]:

$$\frac{1}{2}\left(\left|\frac{a_1'(t)}{a_1(t)}\right| + \left|\frac{a_2'(t)}{a_2(t)}\right|\right) < |\omega_1(t) - \omega_2(t)| \tag{4.8}$$

where $a_1'(t) = \frac{da_1(t)}{dt}$, $a_2'(t) = \frac{da_2(t)}{dt}$, $\omega_1(t) = \frac{d\phi_1(t)}{dt}$, and $\omega_2(t) = \frac{d\phi_2(t)}{dt}$. Otherwise, the signal $x(t)$ will be a mono-component signal. Similarly, the aforementioned criterion for

the discrete-time signal $x[n] = x_1[n] + x_2[n] = a_1[n]e^{j\phi_1[n]} + a_2[n]e^{j\phi_2[n]}$ will be a multi-component signal, if,

$$\frac{1}{2}\left(\left|\frac{a_1[n] - a_1[n-1]}{a_1[n]}\right| + \left|\frac{a_2[n] - a_2[n-1]}{a_2[n]}\right|\right) < |\omega_1[n] - \omega_2[n]| \tag{4.9}$$

or

$$0.5\left(\sigma_{\omega_1}[n] + \sigma_{\omega_2}[n]\right) < |\omega_1[n] - \omega_2[n]| \tag{4.10}$$

In order to check whether the summation of two decomposed components $x_i[n]$ and $x_k[n]$ is a mono-component or multicomponent signal, the following steps are followed:

Step 1: The AEs ($a_i[n]$ and $a_k[n]$) and IFs ($\omega_i[n]$ and $\omega_k[n]$) are computed from signals $x_i[n]$ and $x_k[n]$.

Step 2: The thresholds are computed to identify the significant local energy of $x_i[n]$ and $x_k[n]$ as $a_{\text{th},i} = 0.1\max\{a_i[n]\}$ and $a_{\text{th},k} = 0.1\max\{a_k[n]\}$, respectively.

Step 3: A set of indices is computed where the two components have significant local energy as $L = \{n : a_i[n] \geq a_{\text{th},i}\ \&\ a_k[n] \geq a_{\text{th},k}\}$.

Step 4: The number of extrema (N_e) and the number of zero crossings (N_z) are calculated for $x_i[n] + x_k[n]$.

Step 5: The summation $x_i[n]+x_k[n]$ is a mono-component signal if $0.5\left(\sigma_{\omega_i}[n] + \sigma_{\omega_k}[n]\right) < |\omega_i[n] - \omega_k[n]|\ \forall\ n \in L$ is not satisfied and $|N_e - N_z| < 2$, otherwise it is a multi-component signal.

In the last step, condition $|N_e - N_z| < 2$ ensures that the sum of the components provides an oscillatory signal [16]. The components ($x_i[n]$) of the signal $x[n] = \sin\left(320\pi\frac{n}{f_s}\right) + 0.8\cos\left(2\pi\left(100 + 5\frac{n}{f_s}\right)\frac{n}{f_s}\right)$ for $n = 0, 1, 2, \ldots, 1000$ with $f_s = 1000$ are obtained at the

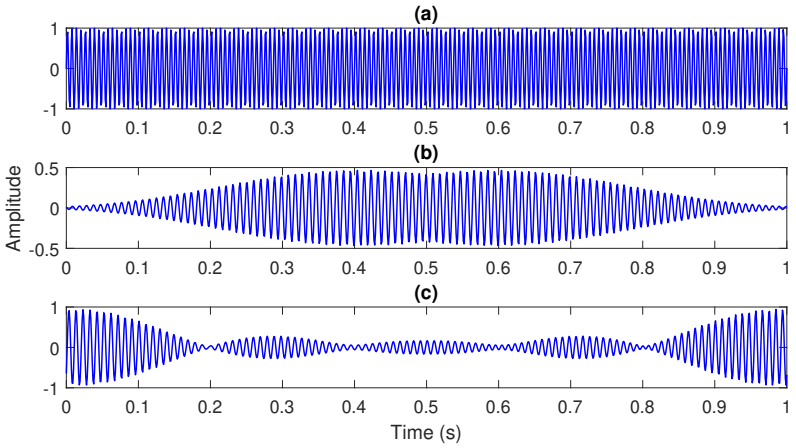

Figure 4.2: The time-domain representation of first, second, and fourth components ($x_1[n]$, $x_2[n]$ and $x_4[n]$) of the clean signal $x[n]$, obtained at the end of Step 5 of iteration 1 of empirical threshold-based EMD-like EVDHM, are shown in (a), (b), and (c), respectively.

end of Step 5 of first iteration of empirical approach-based EMD-like EVDHM method. Thereafter, first, second, and fourth components are considered for analysis in this subsection and their time-domain representations are shown in Fig. 4.2. In the aforementioned figure, the decomposed components in Figs. 4.2 (b) and (c) are parts of a mono-component signal, while the decomposed component in Fig. 4.2 (a) is of different frequency than these two. To verify the effectiveness of the equation (4.10) in identifying whether the sum of two signals will be multicomponent or not, the following two cases are studied:

1. Two decomposed components are considered of different frequencies, i.e., $x_1[n]$ and $x_2[n]$. The parameters $0.5\left(\sigma_{\omega_1}[n] + \sigma_{\omega_2}[n]\right)$ and $|\omega_1[n] - \omega_2[n]|$ are shown in Fig. 4.3(a). From this figure, it can be seen that $0.5(\sigma_{\omega_1}[n] + \sigma_{\omega_2}[n])$ is greater than $|\omega_1[n] - \omega_2[n]|$ for the time instances when both components have significant local energy. Following equation (4.10), it implies that $x_1[n] + x_2[n]$ is a multicomponent signal.

2. Two decomposed components of same frequencies, i.e., $x_2[n]$ and $x_4[n]$, are considered. The plots of $0.5(\sigma_{\omega_2}[n] + \sigma_{\omega_4}[n])$ and $|\omega_2[n] - \omega_4[n]|$ are shown in Fig. 4.3(b).

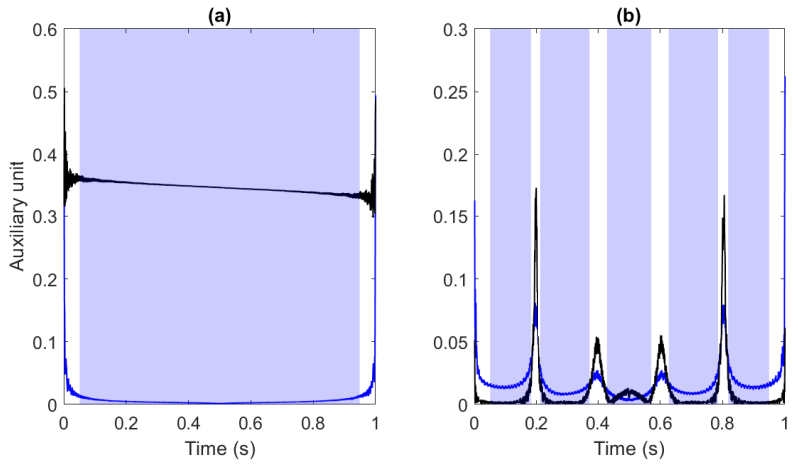

Figure 4.3: The plots of $0.5\left(\sigma_{\omega_1}[n]+\sigma_{\omega_2}[n]\right)$ and $0.5\left(\sigma_{\omega_2}[n]+\sigma_{\omega_4}[n]\right)$ are sketched with blue solid line in (a) and (b), respectively. The plots of $|\omega_1[n]-\omega_2[n]|$ and $|\omega_2[n]-\omega_4[n]|$ are represented with black solid lines in (a) and (b), respectively. The blue rectangular boxes in (a) represent the time instances where $x_1[n]$ and $x_2[n]$ have significant local energy. Similarly, the rectangular boxes in (b) represent the time instances where $x_2[n]$ and $x_4[n]$ have significant local energy.

From the aforementioned figure, it can be observed that $0.5(\sigma_{\omega_2}[n]+\sigma_{\omega_4}[n])$ is not greater than $|\omega_2[n]-\omega_4[n]|$ for the time instances when both components have significant local energy, which implies that $x_2[n]+x_4[n]$ is a mono-component signal.

Hence, it can be concluded that the above-discussed method is effective in identifying whether the summation of two components is a mono-component signal or not. The aforementioned grouping method has been utilized to compute the MDMS from the decomposed components of each iteration in the proposed EMD-like EVDHM technique.

4.4 Hilbert spectrum analysis for time-frequency distribution

In order to obtain the TFD, the idea is to compute the instantaneous energy and IF of the DMSs and represent them in time-frequency plane [16]. The AE and IF of the DMSs are computed using HSA-based method as discussed in section 1.2.4 [35]. Further, the

instantaneous energy is computed as the square of AE. Consider the AE and IF of the r^{th} DMS $x_r^{\text{dec}}[n]$ are $a_r[n]$ and $f_r[n]$, respectively. The instantaneous energy is represented as $e_r[n] = (a_r[n])^2$. Next, the instantaneous energy ($e_r[n]$) and IF ($f_r[n]$) parameters of the DMSs ($x_r^{\text{dec}}[n]$ for $r = 1, 2, \ldots, R$) are represented in time-frequency plane. The same is mathematically represented using the following expression [191]:

$$X[n, f] = \sum_{r=1}^{R} X_r[n, f] \tag{4.11}$$

and

$$X_r[n, f] = e_r[n]\delta\left[f - f_r[n]\right] \tag{4.12}$$

where $\delta[.]$ is the Kronecker delta function. After obtaining the $X[n, f]$ matrix, the TFD is obtained using image representation of it. The process of obtaining $X[n, f]$ is known as HSA and matrix $X[n, f]$ is known as Hilbert spectrum.

4.5 Results and discussion

The effectiveness of the proposed method for signal decomposition is assessed through four cases, namely, the separation of two sinusoidal signals, the separation of a sinusoidal signal and a chirp signal, the separation of two chirp signals, and decomposition of a real-time voiced speech signal. All the synthetic signal models are designed by considering the sampling rate $f_s = 1000$ Hz. The real-life voiced speech signal is taken from CMU ARCTIC speech database, having sampling rate $f_s^{\text{speech}} = 32000$ Hz [1]. The proposed methods with empirical and MDL-based eigenvalue threshold computations are termed as EMD-like EVDHM1 and EMD-like EVDHM2, respectively. For noisy condition analysis, AWGN corresponding to 5, 10, 15, and 20 dB SNRs are added to the signal. Further, the comparative analysis of the proposed methods is performed with a total of ten baseline methods

using clean and noisy synthetic signals. The baseline methods considered for study are, EMD [16], EEMD [44], FDM [54], EFDM [55], EWT [46], iterative filtering [186], FBSE-EWT [48], VMD [45], SSA [75], and improved EVDHM [53]. To analyze the decomposition quality of the proposed technique and its comparative analysis with baselines, the QRF [50] and average correlation [50] are used as objective measures. For the simulation using SSA, the ASTRES toolbox [192] has been used, and the number of components to be extracted for the synthetic signal is set to the number of constituent mono-components in the signal. For VMD, the model parameters are considered as the default values set in MATLAB 2023a. In EWT and FBSE-EWT methods, the boundary detection is performed using the scalespace method [48]. The QRF for r^{th} decomposed component ($x_r^{\text{dec}}[n]$) with i^{th} actual signal component ($x_r^{\text{true[n]}}$) is computed using equation (3.9). The average correlation measure of signal $x[n]$ (avgcorr$_x$) is expressed by equation (4.13).

$$\text{avgcorr}_x = \frac{1}{R}\sum_{r=1}^{R}\left(\frac{|\langle x_r^{\text{true}}[n], x_r^{\text{dec}}[n]\rangle|}{||x_r^{\text{true}}[n]||_2\,||x_r^{\text{dec}}[n]||_2}\right) \tag{4.13}$$

The best results in the tables provided in this section are highlighted with bold font. The detailed analysis of all the signal models are presented in the following subsection:

4.5.1 Separation of two sinusoidal signals

For this analysis, we have considered the signal model $x[n]$ for $n = 0, 1, \ldots, N-1$ with $N = 1001$ as expressed by equation (4.14). The signal is the sum of two sinusoidal modes, $x_1^{\text{true}}[n]$ and $x_2^{\text{true}}[n]$.

$$x[n] = \underbrace{\sin\left(2\pi f_0 \frac{n}{f_s} + \phi\right)}_{x_1^{\text{true}}[n]} + \underbrace{A\sin\left(2\pi f_1 \frac{n}{f_s} + \phi\right)}_{x_2^{\text{true}}[n]} \tag{4.14}$$

where $A = 0.85$, $f_0 = 150$ Hz, $\phi = \frac{\pi}{2}$ radians, and f_1 is varied from 100 Hz to 200 Hz with a step size of 0.5 Hz, in order to analyze the frequency separability limit of the proposed decomposition method. The decomposition quality is measured using average correlation between the signal components ($x_1^{\text{true}}[n]$, $x_2^{\text{true}}[n]$) and the DMSs ($x_1^{\text{dec}}[n]$, $x_2^{\text{dec}}[n]$), which is computed using the equation (4.13) and shown in Fig. 4.4 (a). In the aforementioned study, if $f_1 = 150$ Hz, then there is only one component in the signal, and the average correlation equal to 1 is achieved. Whereas, for f_1 very close to 150 Hz, the average correlation below 0.9 is achieved. This indicates that the proposed method is not able to separate very close frequencies, i.e., f_1 in the range 148 to 152 Hz, excluding 150 Hz.

Additionally, an amplitude separability study is performed using the signal $x[n]$ defined in equation (4.14) with the parameters $f_0 = 150$ Hz, $f_1 = 140$ Hz, $\phi = \frac{\pi}{2}$ radians, and A is varied from 0.5 to 1.5 with a step size of 0.01. The average correlation of the DMSs with constituent components for different values of A is shown in Fig. 4.4 (b). The average correlation value of more than 0.9 is achieved for all values of A, indicating that amplitude does not significantly affect the sinusoid separation using the proposed framework.

Furthermore, the effect of a change in signal length on sinusoidal separation is studied. Here, the signal $x[n]$ for $n = 0, 1, \ldots, N-1$ defined by equation (4.14) is considered with parameters $f_0 = 150$ Hz, $\phi = \frac{\pi}{2}$, $A = 0.8$, and $f_1 = 140$ HZ. The value of N, ranging from 495 to 1005 with a step size of 10, is considered. The average correlation for the decomposition of clean signal ($x[n]$) and noisy signal (AWGN noise added to $x[n]$) for different values of N is always greater than 0.975 as shown in Fig. 4.4 (c). It shows that a change in the length of the signal does not have a significant impact on sinusoidal separation, especially in presence of noise. The computation time required to decompose the signal $x[n]$ using the proposed method with empirical threshold computation for different values of N is shown in Fig. 4.4 (d). It shows that the computation time increases with an increase in

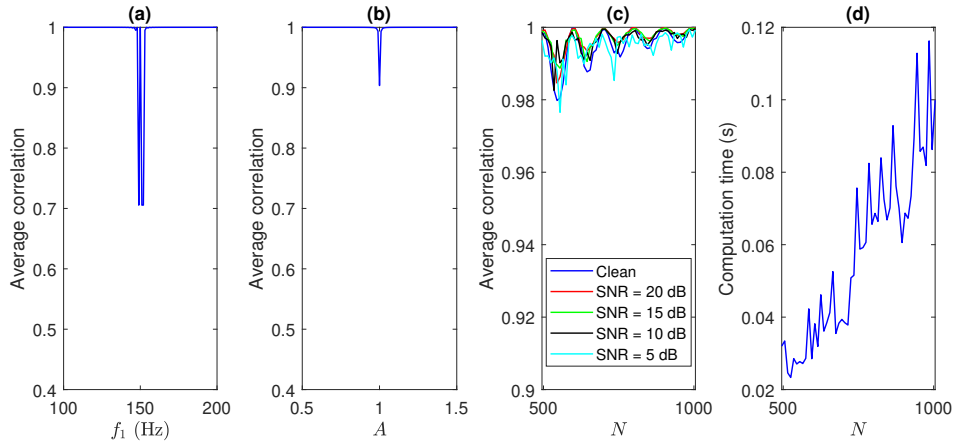

Figure 4.4: The plots in (a) and (b) represent the average correlation for the frequency and amplitude separability analysis, respectively, for the signal $x[n]$. The plots in (c) and (d) represent the average correlation and computation time, respectively, for the sinusoidal separation task at different signal lengths.

signal length.

The aforementioned simulation results show the following key points when we are separating the two sinusoidal signals using the EMD-like EVDHM method:

(a) The values of the amplitude of sinusoids do not have as much effect on separability as the values of their frequencies.

(b) When the frequencies are too close ($f_0 \approx f_1$), then the sinusoids are not separable; otherwise, they are separable.

(c) The change in signal length does not have a significant impact on sinusoidal separation.

In order to compare the proposed technique with the baselines , the signal $x[n]$ is considered as expressed in equation (4.14) with the parameters, $f_0 = 100$ Hz, $\phi = \frac{\pi}{2}$ radians/sec, $A = 0.8$, and $f_1 = 80$ Hz. The time-domain representation of signal $x[n]$ is shown in Fig. 4.5(a). The decomposition of the signal $x[n]$ is performed using two proposed methods and other baseline methods in clean and noisy (AWGN added to the signal with SNRs

Table 4.1: The obtained QRF performance measure for the decomposed components of the synthetic signals $x[n]$, $y[n]$, and $z[n]$ obtained using EMD, EEMD, EWT, iterative filtering, FBSE-EWT, VMD, SSA, FDM, EFDM, improved EVDHM, EMD-like EVDHM1, and EMD-like EVDHM2 methods.

Signal	SNR	Signal component	QRF (dB)											
			EMD	EEMD	VMD	Iterative filtering	FDM	EFDM	EWT	FBSE-EWT	SSA	Improved EVDHM	EMD-like EVDHM1	EMD-like EVDHM2
$x[n]$	Clean signal	$x_1^{\text{true}}[n]$	2.02	3.77	27.03	1.96	1.94	28.52	10.26	10.16	53.49	**47.03**	**47.03**	**47.03**
		$x_2^{\text{true}}[n]$	0.07	1.23	26.63	0.02	0	26.58	8.32	8.23	51.56	45.09	**58.68**	**58.68**
	20	$x_1^{\text{true}}[n]$	1.07	3.57	24.81	1.85	1.83	18.07	1.92	1.92	31.76	**37.50**	**37.50**	**37.50**
		$x_2^{\text{true}}[n]$	0	0.92	25.31	0.01	0	21.81	-0.02	-0.01	21.01	38.69	**40.26**	**40.26**
	15	$x_1^{\text{true}}[n]$	1.82	2.80	22.49	1.87	1.65	19.22	1.80	1.78	28.10	31.99	**36.04**	**36.04**
		$x_2^{\text{true}}[n]$	0	0.30	22.52	0.02	0	17.05	-0.13	-0.12	10.06	35.23	**36.06**	**36.06**
	10	$x_1^{\text{true}}[n]$	1.35	2.31	17.52	1.63	1.68	11.04	1.57	1.53	7.11	**32.59**	**32.59**	**32.59**
		$x_2^{\text{true}}[n]$	0	0.38	15.75	0.01	0	13.59	-0.29	-0.09	21.87	26.17	**33.65**	**33.65**
	5	$x_1^{\text{true}}[n]$	0.41	2.43	13.15	1.08	7.69	5.87	0.65	0.65	1.72	**22.95**	**22.95**	**22.95**
		$x_2^{\text{true}}[n]$	0	0.53	13.51	-0.01	5.69	10.16	-0.89	-0.89	-2.13	24.44	**28.34**	**28.34**
$y[n]$	Clean signal	$y_1^{\text{true}}[n]$	2.26	3.68	23.54	2.50	6.73	26.19	8.15	18.74	20.05	**43.37**	21.67	**43.38**
		$y_2^{\text{true}}[n]$	0	2.05	2.35	0.04	4.23	23.79	5.67	11.64	17.38	19.09	**19.18**	19.05
	20	$y_1^{\text{true}}[n]$	1.85	3.21	20.27	2.39	6.64	22.53	2.44	2.44	20.04	**37.35**	**37.35**	**37.35**
		$y_2^{\text{true}}[n]$	0	1.20	3.60	0.01	4.16	16.35	-0.07	-0.02	15.85	3.56	**18.39**	**18.39**
	15	$y_1^{\text{true}}[n]$	2.29	3.04	19.38	2.57	5.54	18.43	2.37	2.37	19.44	**34.97**	**34.97**	**34.97**
		$y_2^{\text{true}}[n]$	0	0.87	3.58	0	3.01	11.81	-0.08	-0.03	8.71	1.70	**17.72**	**17.72**
	10	$y_1^{\text{true}}[n]$	1.64	2.45	16.54	2.55	6.21	14.87	1.94	2.06	19.03	**34.99**	**34.99**	**34.99**
		$y_2^{\text{true}}[n]$	-0.02	-0.12	3.74	0	3.74	9.60	-0.17	-0.11	4.78	2.18	**16.97**	**16.97**
	5	$y_1^{\text{true}}[n]$	0.48	1.37	12.57	1.52	4.42	16.25	0.42	-0.44	15.79	**31.19**	**31.19**	**31.19**
		$y_2^{\text{true}}[n]$	-0.02	-0.93	4.62	0	3.32	0.95	-0.96	-0.42	-0.13	6.42	10.64	**12.13**
$z[n]$	Clean signal	$z_1^{\text{true}}[n]$	19.43	16.98	25.19	2.47	15.97	6.07	**31.01**	26.01	2.49	18.22	21.21	19.07
		$z_2^{\text{true}}[n]$	16.72	17.56	1.81	0	13.47	3.53	6.99	13.94	0	14.92	**18.97**	10.41
	20	$z_1^{\text{true}}[n]$	15.29	16.24	3.83	2.38	14.79	6.02	20.85	20.74	2.47	5.44	**21.63**	19.06
		$z_2^{\text{true}}[n]$	10.76	13.12	2.47	0	11.84	3.43	17.89	18.26	-0.04	1.38	21.36	**21.59**
	15	$z_1^{\text{true}}[n]$	14.60	13.48	3.78	2.11	13.11	5.93	16.61	16.56	2.16	12.78	**20.03**	17.59
		$z_2^{\text{true}}[n]$	8.75	9.82	2.50	0	9.80	2.95	13.05	14.62	-0.05	4.90	18.55	**19.73**
	10	$z_1^{\text{true}}[n]$	8.06	9.03	4.04	1.26	9.57	1.09	10.89	10.82	1.13	-2.46	14.67	**17.49**
		$z_2^{\text{true}}[n]$	2.95	4.59	3.65	0	5.94	-1.63	9.68	9.48	-0.04	2.96	13.68	**14.37**
	5	$z_1^{\text{true}}[n]$	5.19	5.36	5.10	7.38	5.33	5.28	6.28	6.06	1.56	2.56	**13.24**	**13.24**
		$z_2^{\text{true}}[n]$	-0.03	0.06	3.47	1.06	4.95	0.92	6.29	6.05	-2.78	1.44	11.59	**11.87**

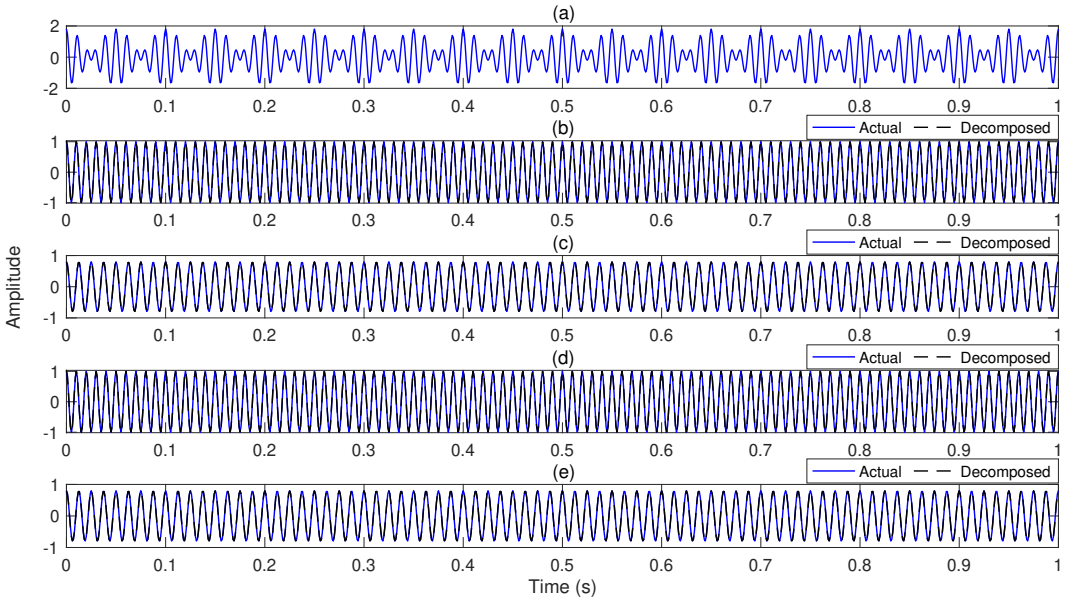

Figure 4.5: The time-domain representation of the signal $x[n]$ in (a). The first two EMD-like EVDHM1-based decomposed components of $x[n]$ overlapped to their respective actual components are shown in (b) and (c). The first two EMD-like EVDHM2-based decomposed components of $x[n]$ overlapped to their respective actual components are shown in (d) and (e).

of 5, 10, 15, and 20 dB) cases. The decomposed components of $x[n]$ obtained from proposed method and their respective true components are shown in Fig. 4.5. The true and decomposed components in the two end regions are very similar, indicating that there is no significant end effect. The values of QRF and average correlation obtained from decomposition of $x[n]$ using proposed and baseline methods are presented in Table 4.1 and Fig. 4.6, respectively. The results presented in Table 4.1 indicate that the proposed technique provides highest QRF than the baselines for both clean and noisy signals. The TFDs of the clean signal $x[n]$ obtained using the proposed and baseline methods are shown in Fig. 4.7. From the aforementioned figure, it can be said that the VMD, EFDM, EWT, FBSE-EWT, SSA, improved EVDHM, EMD-like EVDHM1, and EMD-like EVDHM2 methods are able to separate the two components of the multicomponent signal $x[n]$. However, the resolution of TFDs of VMD, EFDM, SSA, improved EVDHM, EMD-like EVDHM1, and EMD-like

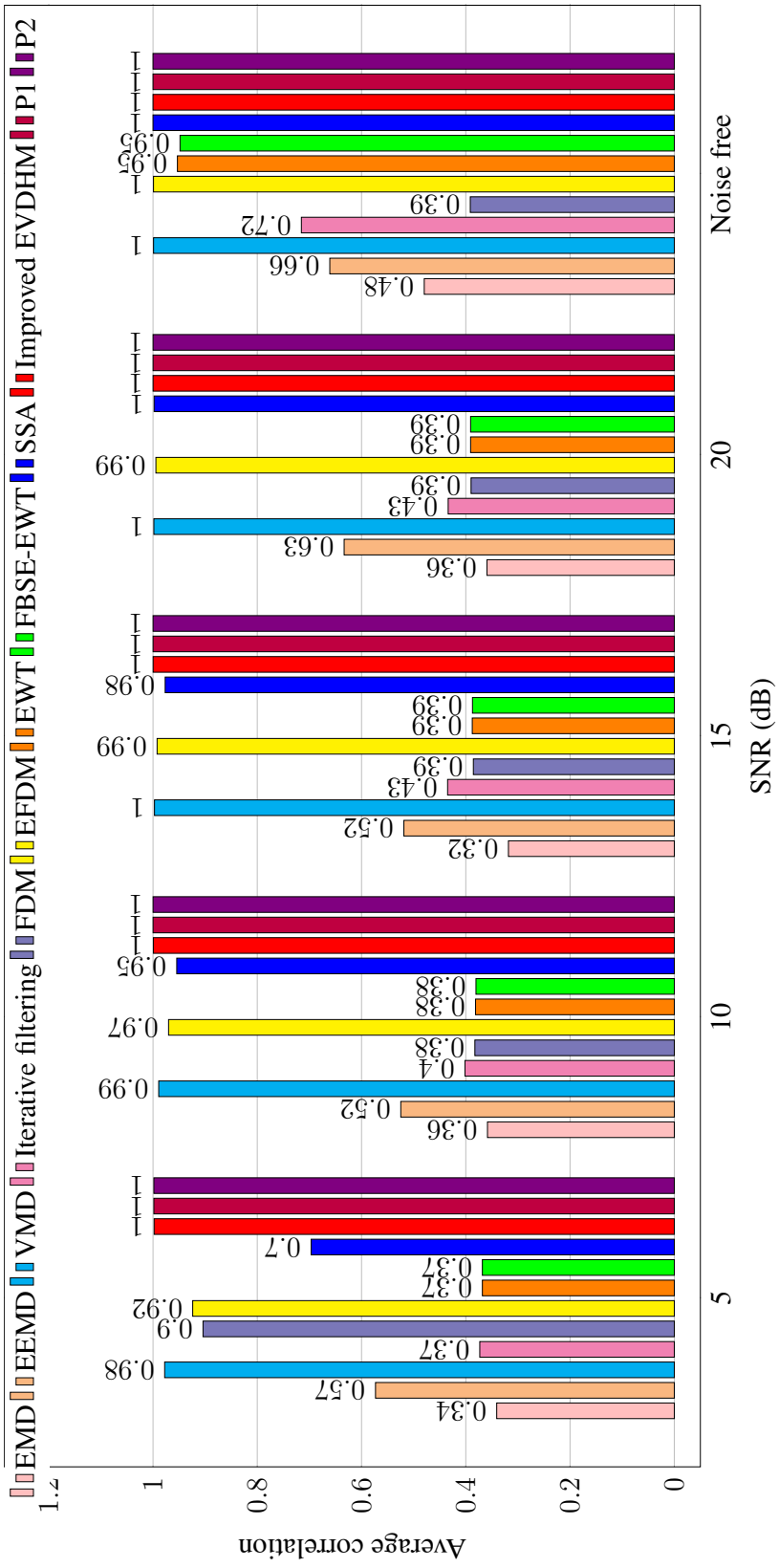

Figure 4.6: Bar plot representing average correlation values obtained after decomposition of signal $x[n]$ with different SNR values using the proposed and baseline methods. Here, P1 and P2 are EMD-like EVDHM1 and EMD-like EVDHM2 methods, respectively.

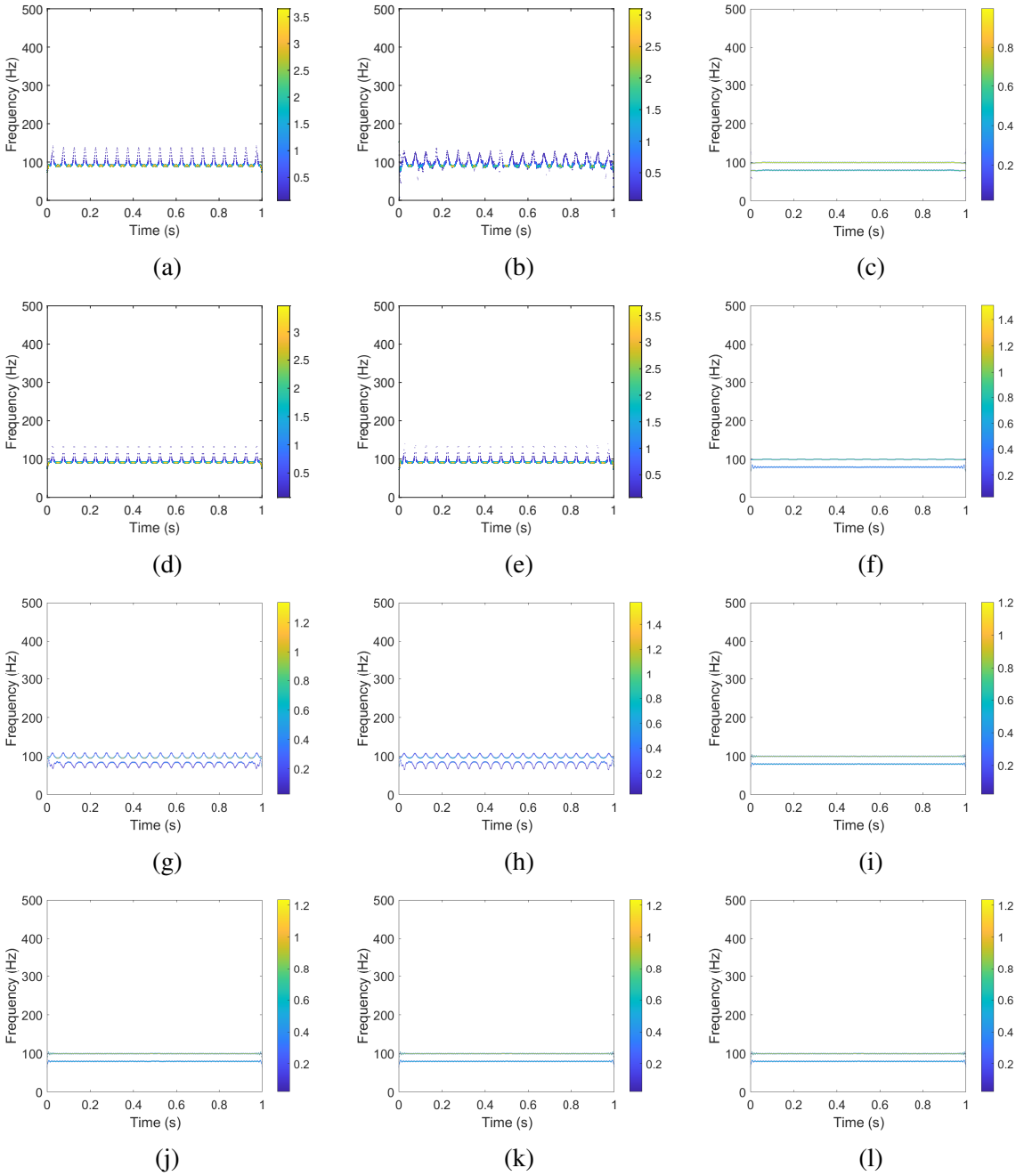

Figure 4.7: The HSA-based TFD of the signal $x[n]$ obtained using (a) EMD, (b) EEMD, (c) VMD, (d) iterative filtering, (e) FDM, (f) EFDM, (g) EWT, (h) FBSE-EWT, (i) SSA, (j) improved EVDHM, (k) EMD-like EVDHM1, and (l) EMD-like EVDHM2 methods.

EVDHM2 methods are of high resolution compared to the resolution of TFDs of EWT and FBSE-EWT methods. This can also be evidenced from very high average correlation and QRF values corresponding to these methods as shown in Fig. 4.6 and Table 4.1, respectively.

Table 4.2: The computation time required by proposed and baseline methods to decompose $x[n]$, $y[n]$, and $z[n]$ signals.

Methods	Computation time (s)		
	$x[n]$	$y[n]$	$z[n]$
EMD	0.02	0.03	0.01
EEMD	0.23	0.37	0.60
VMD	0.09	0.19	0.33
Iterative filtering	0.02	0.03	0.03
FDM	0.11	0.19	0.19
EFDM	**0.001**	**0.01**	**0.001**
EWT	0.01	0.02	0.02
FBSE-EWT	0.01	0.03	0.03
SSA	0.02	0.05	0.07
Improved EVDHM	0.03	0.16	0.25
EMD-like EVDHM1	0.09	0.20	0.37
EMD-like EVDHM2	0.78	0.84	0.91

Additionally, the improved EVDHM, EMD-like EVDHM1, and EMD-like EVDHM2 methods provided average correlation values of 1 for all the studied SNR values of noisy signals. This shows their robustness to noise for sinusoidal signal separation. The computation time required to decompose the signal $x[n]$ is provided in Table 4.2. The EMD-like EVDHM2 has the highest computation time, even compared to EMD-like EVDHM1. It is because of the MDL-based threshold computation step, where all the elementary components need to be computed in iteration 1 of the decomposition before threshold computation.

4.5.2 Separation of a sinusoidal and a chirp signals

The signal $y[n]$ for $n = 0, 1, \ldots, N-1$ with $N = 1001$ is considered for separation analysis of combination of a sinusoidal signal and a chirp signal. The mathematical expression for the same is defined as,

$$y[n] = \underbrace{\cos\left(2\pi f_1 \frac{n}{f_s}\right)}_{y_1^{\text{true}}[n]} + \underbrace{A\cos\left(2\pi\left(f_2 + \beta\frac{n}{f_s}\right)\frac{n}{f_s} + \phi\right)}_{y_2^{\text{true}}[n]} \tag{4.15}$$

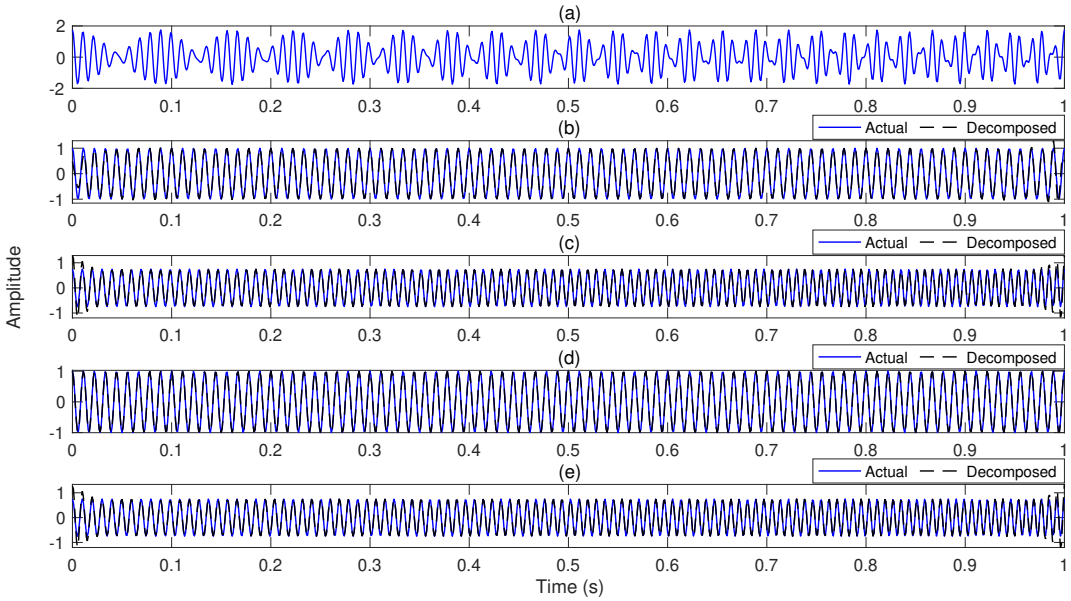

Figure 4.8: Signal $y[n]$ is shown in (a). The EMD-like EVDHM1-based decomposed components of $y[n]$ overlapped with their respective true components are shown in (b) and (c). The EMD-like EVDHM2-based decomposed components of $y[n]$ overlapped with their respective true components are shown in (d) and (e).

where $f_1 = 90$ Hz, $A = 0.75$, $f_2 = 100$ Hz, $\beta = 15$, and $\phi = 0$ radians. The time-domain representation of the signal $y[n]$ is shown in Fig. 4.8(a). The signal $y[n]$ is decomposed into basic components using the proposed and baseline methods. The true signal components overlapped with decomposed components obtained from proposed methods are shown in Figs. 4.8(b)–(e). Minor distortions are observed in the end regions of the decomposed components obtained from both proposed methods. The QRF and average correlation values obtained from the decomposed components of the clean and noisy signals are provided in Table 4.1 and depicted in Fig. 4.9, respectively. The EMD-like EVDHM1, and EMD-like EVDHM2 methods have achieved average correlation ≥ 0.98 for noisy signal with all noise level studied. Additionally, these methods achieved QRF values more than 10 which indicate the robustness of these methods to noise for separation of sinusoidal and linear chirp components. Further, the HSA is used to obtain the TFD from the decomposed

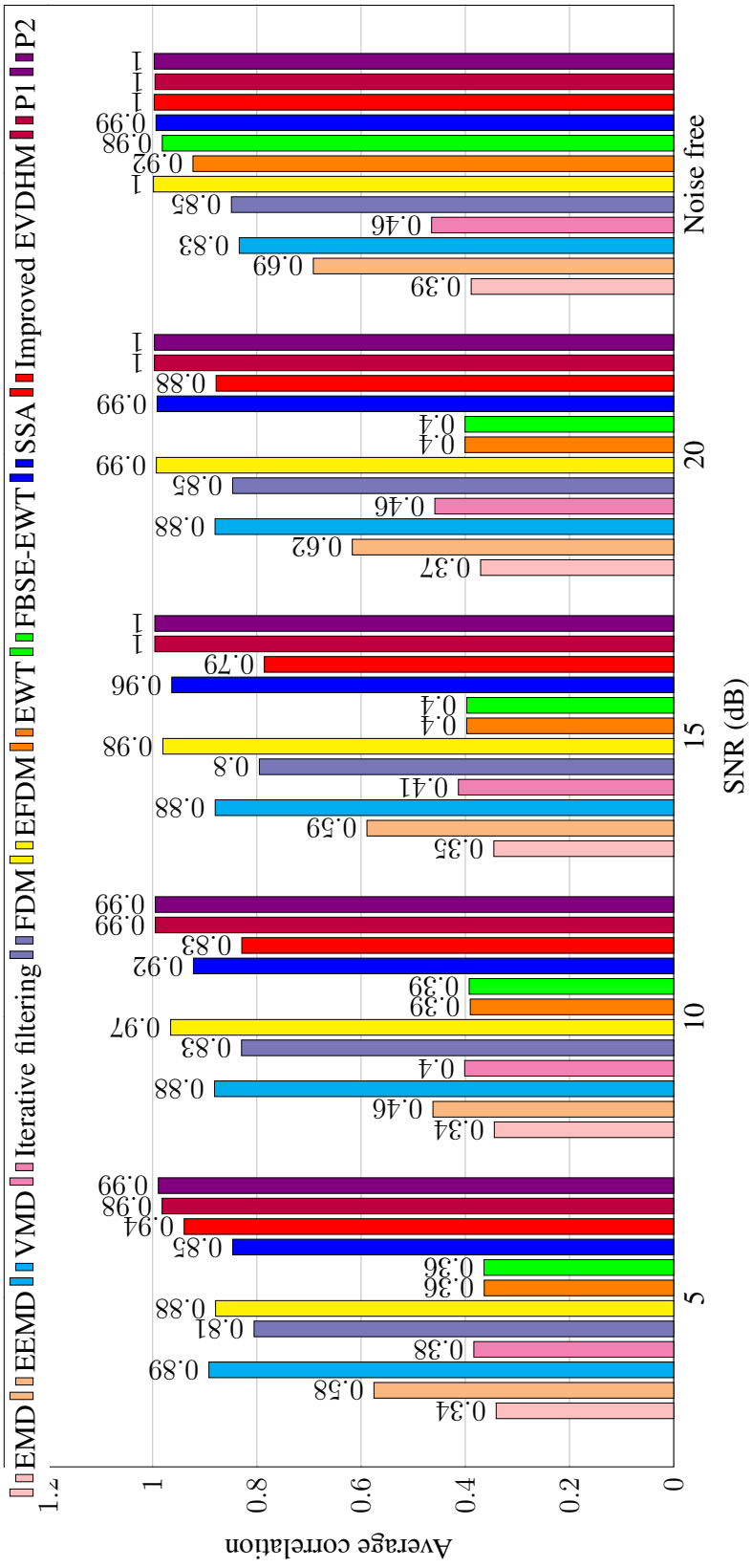

Figure 4.9: The average correlation values obtained for the signal $y[n]$ in clean and noisy conditions. Here, P1 and P2 are EMD-like EVDHM1 and EMD-like EVDHM2 methods, respectively.

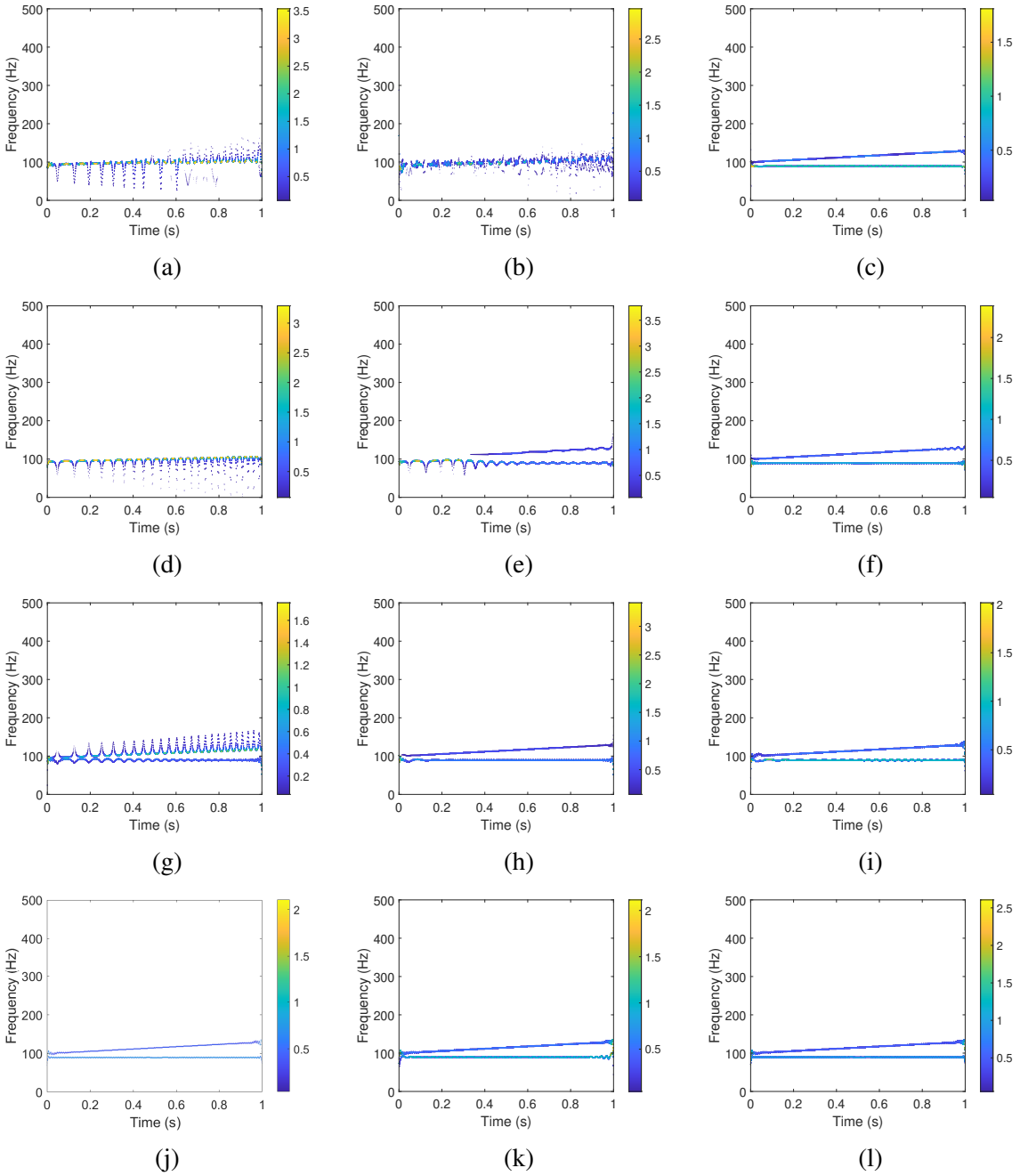

Figure 4.10: The HSA-based TFD of the signal $y[n]$ obtained using the following methods: (a) EMD, (b) EEMD, (c) VMD, (d) iterative filtering, (e) FDM, (f) EFDM, (g) EWT, (h) FBSE-EWT, (i) SSA, (j) improved EVDHM, (k) EMD-like EVDHM1, and (l) EMD-like EVDHM2.

components of signal $y[n]$ obtained using the baseline and proposed methods, and these are shown in Fig. 4.10. The TFDs obtained using VMD, EFDM, FBSE-EWT, SSA, improved

EVDHM, EMD-like EVDHM1, and EMD-like EVDHM2 are able to clearly represent the components of $y[n]$ in time-frequency plane. Hence, it can be said that proposed method is more suitable for separation of sinusoidal and linear chirp signals (in clean and noisy cases) as compared to other compared methods from literature. The computation time required to decompose the signal $y[n]$ using proposed and basline methods is provided in Table 4.2. The EMD-like EVDHM2 requires the highest computation time, whereas EMD-like EVDHM1 is faster than EEMD method.

4.5.3 Separation of two chirp signals

For the separation analysis of two chirp signals, the signal $z[n]$ for $n = 0, 1, \ldots, 1000$ is considered which is mathematically defined as,

$$z[n] = \underbrace{\cos\left(2\pi\left(f_1 + \beta_1\frac{n}{f_s}\right)\frac{n}{f_s}\right)}_{z_1^{\text{true}}[n]} + \underbrace{A\cos\left(2\pi\left(f_2 + \beta_2\frac{n}{f_s}\right)\frac{n}{f_s}\right)}_{z_2^{\text{true}}[n]} \tag{4.16}$$

where f_1 = 100 Hz, β_1 = 15, A = 0.75, f_2 = 200 Hz, and β_2 = 20. The baseline and proposed methods are studied for decomposition of the signal into simple components. The time-domain representation of the multicomponent signal $z[n]$ is provided in Fig. 4.11(a). The true components overlapped with respective decomposed components of $z[n]$ obtained from EMD-like EVDHM1 are shown in Figs. 4.11(b) and (c). Similarly, Figs. 4.11(d) and (e) represent the first two decomposed components of $z[n]$ obtained from EMD-like EVDHM2 overlapped with their respective true components. Figure 4.11 indicates the presence of end effect in decomposed components with minor distortion. The HSA is applied to the decomposed components to obtain the TFD. The resultant TFD is depicted in Fig. 4.12. All the studied methods except iterative filtering, EFDM, and SSA are able to separately represent the components of the signal $z[n]$ in the time-frequency plane. The VMD, EWT,

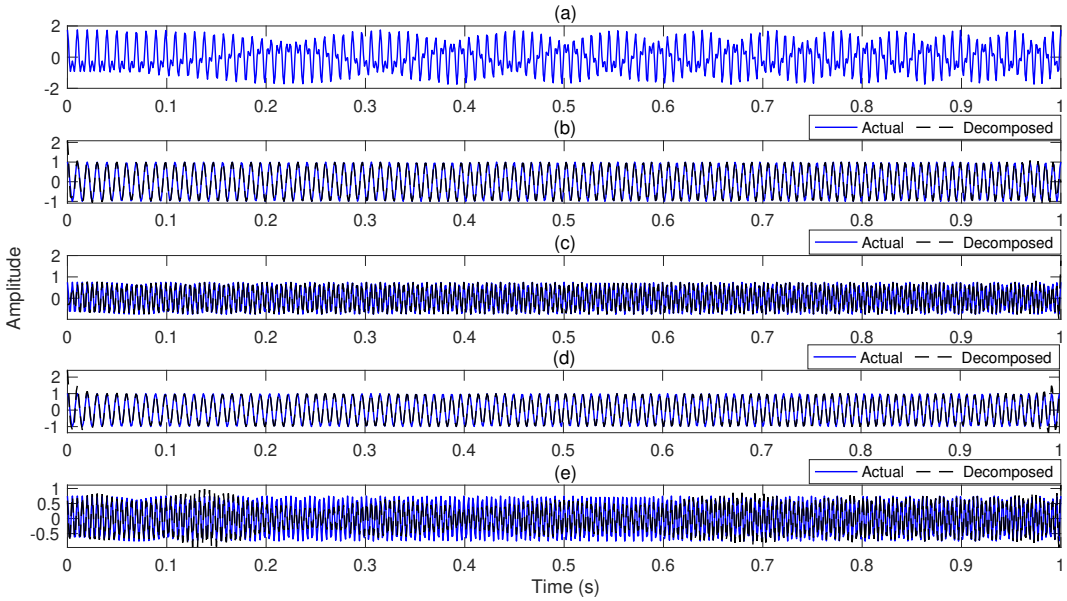

Figure 4.11: The time-domain representation of the signal $z[n]$ in (a). The first two EMD-like EVDHM1-based decomposed components of $z[n]$ overlapped to their respective actual components are shown in (b) and (c). The first two EMD-like EVDHM2-based decomposed components of $z[n]$ overlapped to their respective actual components are shown in (d) and (e).

FBSE-EWT, improved EVDHM, EMD-like EVDHM1, and EMD-like EVDHM2 methods provide high resolution TFD of $z[n]$. Furthermore, the average correlation value for the proposed methods is only greater than 0.95. Additionally, QRF values of proposed methods for the signal $z[n]$ are more than 10 as presented in Table 4.1, indicating its robustness to noise for the separation of two chirp signals among the studied methods. The computation time required by the proposed and baseline methods to decompose the signal $z[n]$ is provided in Table 4.2. The EMD-like EVDHM2 requires the highest amount of time to decompose $z[n]$ as compared to all the compared methods.

From the results shown in Table 4.1, Figs. 4.6 , 4.9, and 4.13, the EMD-like EVDHM2 method is found to provide the highest QRF and highest average correlation values among all the studied methods for all the studied clean synthetic signals and noisy synthetic signals (with the SNR value 5 dB or higher), except for a few cases of signal $z[n]$ where EMD-

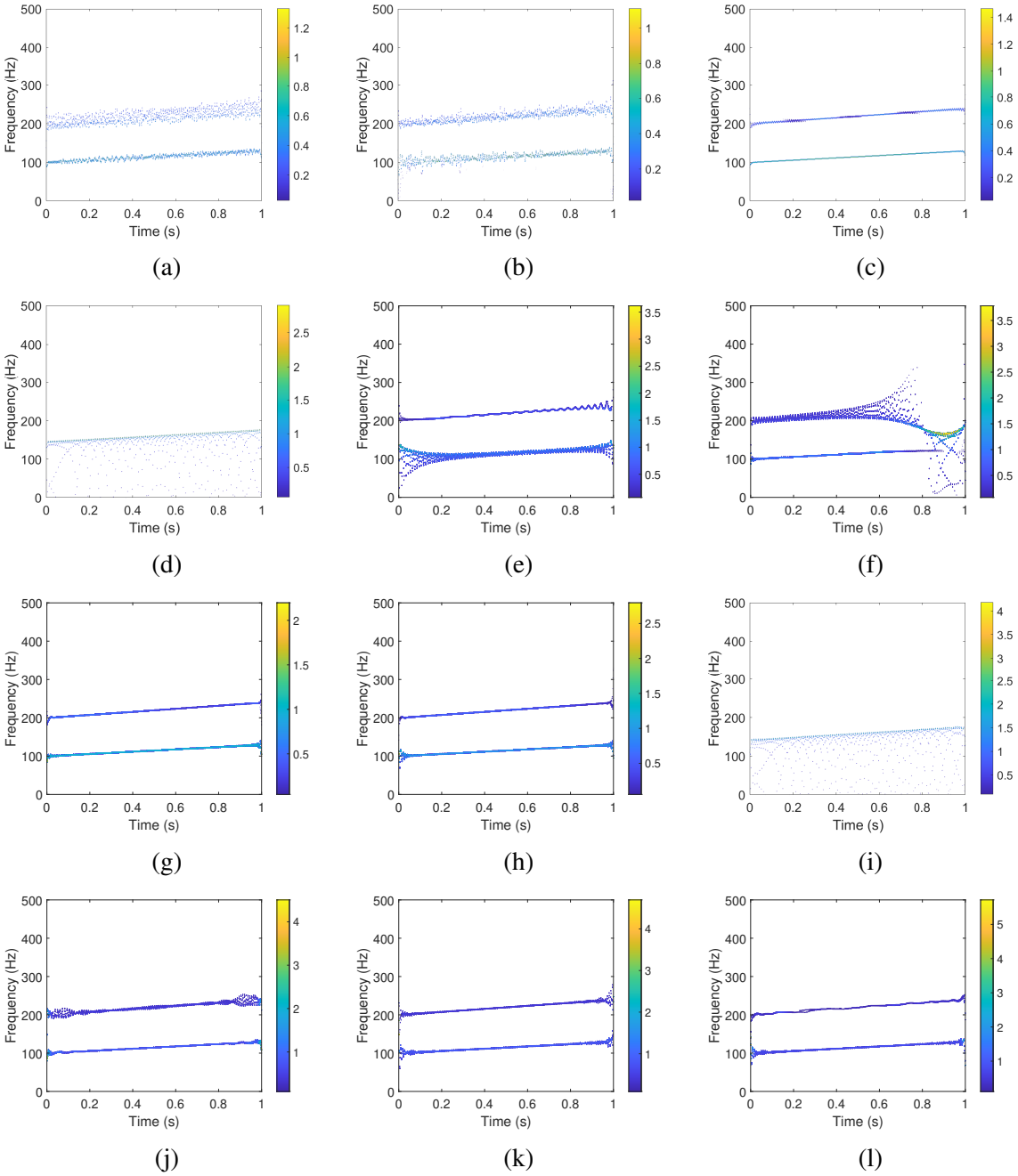

Figure 4.12: The HSA-based TFD of the signal $z[n]$ obtained using EMD, EEMD, VMD, iterative filtering, FDM, EFDM, EWT, FBSE-EWT, SSA, improved EVDHM, EMD-like EVDHM1, and EMD-like EVDHM2 methods in (a)–(l), respectively.

like EVDHM1 surpasses it. However, the eigenvalue threshold computation in EMD-like EVDHM1 requires SNR value as input, which is not possible for real-life signals; whereas, the MDL-based eigenvalue threshold computation in EMD-like EVDHM is adaptive in na-

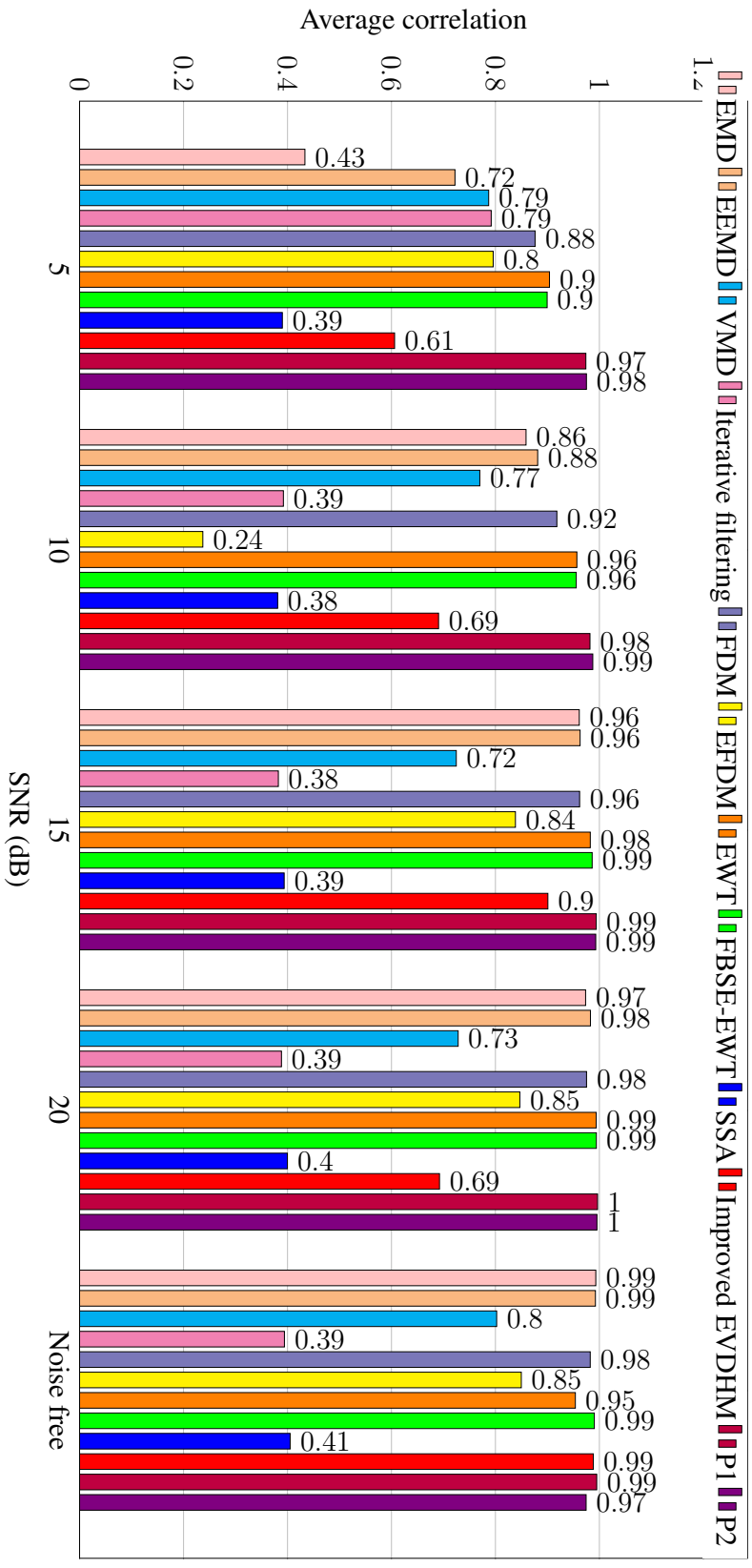

Figure 4.13: Bar plot representation of the average correlation values obtained after decomposition of noise free and noisy signal $z[n]$ using the proposed method and baselines. Here, P1 and P2 are EMD-like EVDHM1 and EMD-like EVDHM2 methods, respectively.

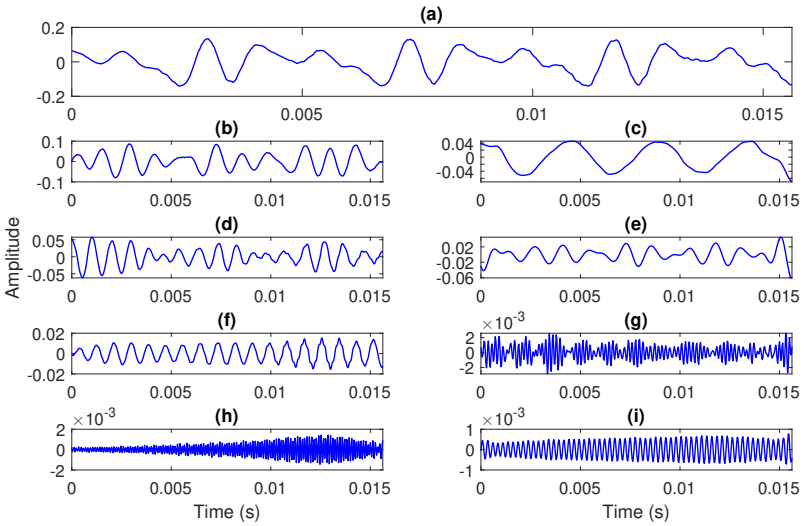

Figure 4.14: Time domain representation of (a) voiced speech frame and (b)–(i) the DMSs obtained from the EMD-like EVDHM with MDL-based threshold method.

ture. These two measures indicate the superior decomposition performance of the EMD-like EVDHM2. Hence, EMD-like EVDHM2 has been considered for further study in the next section.

4.5.4 Analysis of speech signal

A clean speech signal from the CMU ARCTIC speech database is considered to evaluate the performance of the proposed method on real-life signals [1]. A 15.6 ms duration voiced speech segment is used for analysis. The time-domain representation of the considered speech signal and its DMSs obtained from the EMD-like EVDHM2 are shown in Fig. 4.14. The spectrogram of the speech signal obtained using 230 samples length Hamming window with an overlap of 229 samples is shown in Fig. 4.15(a). The scalogram of the speech signal obtained using analytic Morlet wavelet is shown in Fig. 4.15(b). The TFD of the speech signal obtained from EMD, EEMD, VMD, iterative filtering, FDM, EFDM, EWT, FBSE-EWT, SSA, improved EVDHM, EMD-like EVDHM1, and EMD-like EVDHM2 is depicted in Fig. 4.15(c)–(n). The TFD of the speech signal is plotted for the frequency range 0 to

4000 Hz. The comparison of spectrogram and scalogram show that there are three components in the signal and energy of two components with frequencies close to 1000 Hz is much lower at time $t = 0.005$ and 0.01 s. From Fig. 4.15, it can be seen that TFDs obtained from EMD, VMD, FDM, EMD-like EVDHM1, and EMD-like EVDHM2 methods are able to represent the signal component in the time-frequency plane. The VMD-based TFD, shown in Fig. 17(e), has high frequency resolution. However, it is not able to accurately represent the energy of the components throughout time, as observed by comparing it with spectrogram and scalogram (in Figs. 17(a) and (b)). The comparison of Figs. 17(a), (b) and (l) shows that the improved EVDHM method also provided high resolution TFD, but it is not able to represent the component near to 1000 Hz in time-frequency plane. The TFDs obtained from proposed methods are capable of representing all significant components of the signal in time-frequency plane. Additionally, they have better energy representation of component throughout time in time-frequency plane as compared to VMD, as illustrated in Figs. 17(m) and (n). However, the components obtained from proposed methods exhibit wider bandwidth. There are 28, 85, and 43 significant eigenvalue pairs or respective components obtained for grouping in the improved EVDHM, EMD-like EVDHM1, and EMD-like EVDHM2 methods, respectively, for the considered speech signal. In the proposed methods, the extracted components, obtained after grouping in each iteration, are verified to satisfy the mono-component criteria defined in Section 4.2. However, the actual component of the signal might have been split as the mono-component criterion is not checked for the decomposed components in the improved EVDHM method.

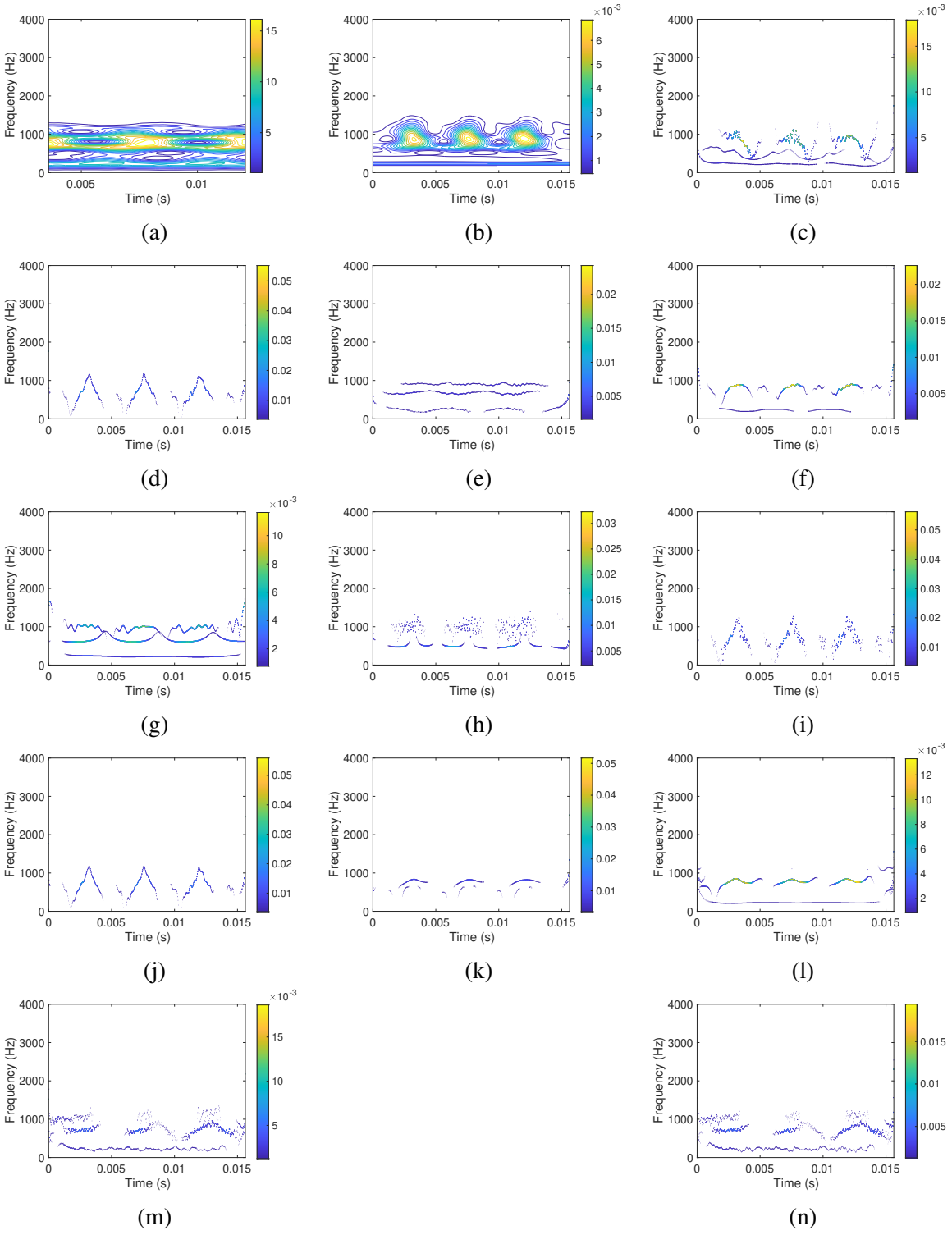

Figure 4.15: The spectrogram and scalogram of speech signal are shown in (a) and (b), respectively. The HSA-based TFD of a 15.6 ms duration voiced speech signal obtained using the following methods: EMD, EEMD, VMD, iterative filtering, FDM, EFDM, EWT, FBSE-EWT, SSA, improved EVDHM, EMD-like EVDHM1, and EMD-like EVDHM2 are shown in (c)–(n), respectively.

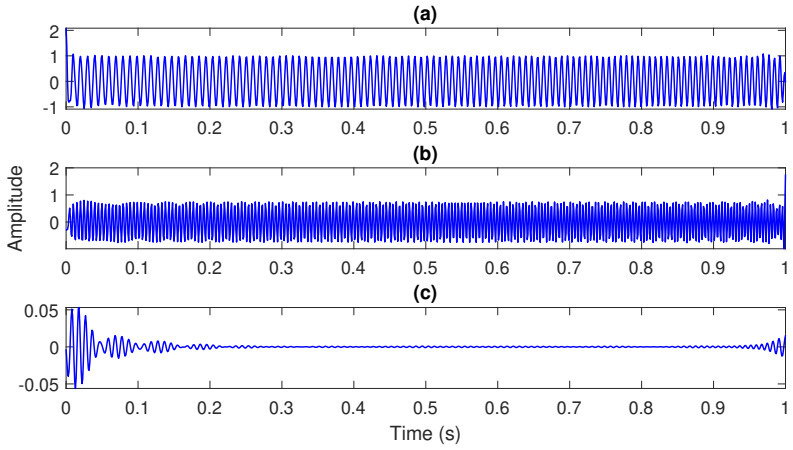

Figure 4.16: The DMSs of $z[n]$ obtained using EMD-like EVDHM with empirical threshold computation are shown in (a)–(c).

4.5.5 Error propagation study for change in eigenvalue threshold

A change in the eigenvalue threshold may lead to inaccurate extraction of the first few components. Hence, it becomes of interest to study the possibility of error propagation in the subsequent DMSs. The signal $z[n]$, defined by equation (4.16), is considered for this analysis. The EMD-like EVDHM method is considered for the decomposition of $z[n]$ using both empirical and MDL-based eigenvalue threshold computation approaches. The computed eigenvalue thresholds are 0.0913 and 91.2871 for the empirical and MDL-based approaches, respectively. The DMSs obtained using the proposed method for both thresholds are provided in Figs. 4.16 and 4.17. In Fig. 4.16, the first signal component is partially decomposed but does not affect the extraction of the second signal component. Additionally, the remaining part of the first signal component is extracted as the third DMS. Similarly, in Fig. 4.17, the proposed method with MDL-based threshold computation extracts the first signal component. However, the second signal component is extracted as two DMSs. This concludes that the change in the eigenvalue threshold may lead to over-decomposition of a signal component, but it does not have an effect on the extraction of other signal components.

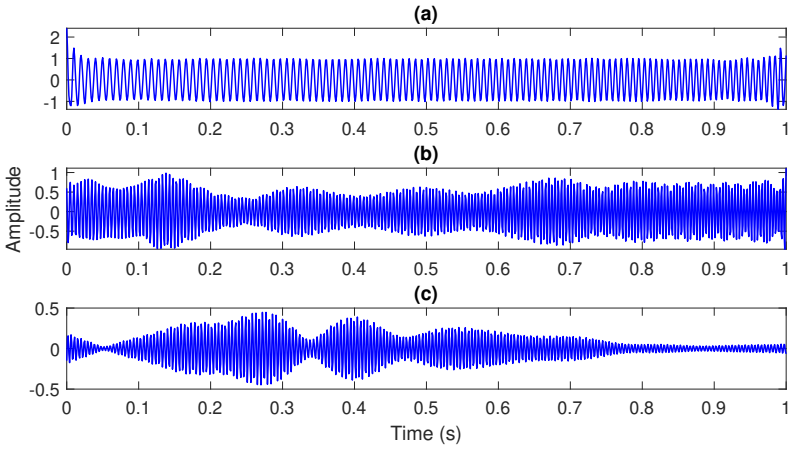

Figure 4.17: The plots in (a)–(c) are the DMSs of $z[n]$ obtained using EMD-like EVDHM with MDL-based threshold computation.

4.6 Trend line and weak component extraction using proposed method

In this section, the proposed method is evaluated for the tasks of obtaining the trend line of a signal and extracting the weak component of a PQD signal. The EMD-like EVDHM method with MDL-based threshold computation is studied, as it demonstrated better performance than EMD-like EVDHM with empirical threshold computation for synthetic signals.

4.6.1 Trend line extraction

We have considered a signal $p[n]$ for $n = 0, 1, \ldots, N-1$ defined by equation (4.17) for the trend extraction analysis [193].

$$p[n] = 10^{-11}\left(\frac{n}{f_s} - 10\right)\left(\frac{n}{f_s} - 70\right)\left(\frac{n}{f_s} - 160\right)^2\left(\frac{n}{f_s} - 290\right)^2 + e^{0.01\frac{n}{f_s}}\sin\left(\frac{2\pi n}{12 f_s}\right) + \varepsilon_n \tag{4.17}$$

where $\varepsilon_n = \mathcal{N}(0, 4)$, $\mathcal{N}(0, 4)$ is the Gaussian distribution with mean 0 and variance 4, $f_s = 5500$ Hz, and $N = 299$. To extract the trend line of the signal $p[n]$, it is decomposed using the EMD-like EVDHM method into a set of DMS $p_i^{\text{dec}}[n]$. Additionally, the mean

frequency (MNF_i) of the DMS ($p_i^{\text{dec}}[n]$) is computed using [78],

$$\text{MNF}_i = \frac{\sum_{k=0}^{\frac{N+1}{2}} f_k |P[k]|^2}{\sum_{k=0}^{\frac{N+1}{2}} |P[k]|^2} \tag{4.18}$$

where $P[k]$ is discrete Fourier transform of $p[n]$ and $f_k = \frac{k}{N} f_s$. DMS with a mean angular frequency less than or equal to $\frac{\pi}{10}$ are added together to obtain the trend line of the signal. The signal and the extracted trend using the proposed method are shown in Fig. 4.18(a) and (b), respectively. Furthermore, Fig. 4.18(c) shows the true and extracted trends plotted together for visual comparison, indicating that the extracted trend closely follows the true trend. This analysis shows the ability of the proposed method in extracting the trend line of a signal.

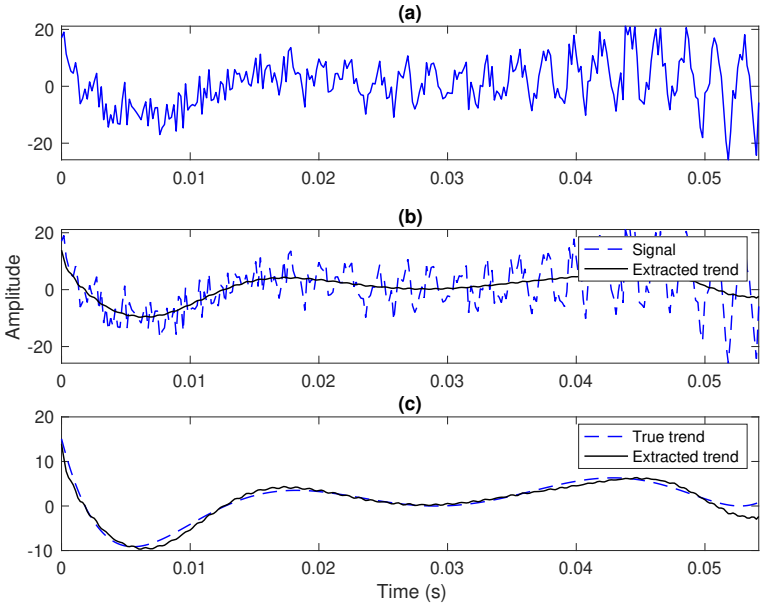

Figure 4.18: The time-domain representation of the signal $p[n]$ is shown in (a). The extracted trend line overlapped on the signal $p[n]$ and true trend is depicted in (b) and (c), respectively.

4.6.2 Weak component extraction in power quality disturbance signal

A power quality disturbance (PQD) signal is considered to study the extraction of weak components from the signal. For the study, a PQD signal consisting of sag with harmonic disturbances is considered, which is mathematically represented by [194],

$$s(t) = A\left(1 - \alpha\left(u(t-t_1) - u(t-t_2)\right)\right)\sin(\omega_0 t) + \sum_{i=\{3,5,7\}} k_i \sin(i\omega_0 t) \tag{4.19}$$

where $A = 1$, $\alpha = 0.75$, $t_1 = 0.11$, $t_2 = 0.15$, $u(t)$ is an unit step function, $\omega_0 = 100\pi$, $k_1 = 0.25$, $k_2 = 0.22$, and $k_3 = 0.21$. An AWGN of 10 dB SNR is added to the signal. In this study, the sampled version of $s(t)$ ($s[n]$) sampled at 3200 Hz is considered for simulation purposes [195]. The sampled PQD signal $s[n]$ is depicted in Fig. 4.19 (a), where the blue rectangular box indicates the location of the sag distortion. The signal $s[n]$ is decomposed using the EMD-like EVDHM2 method and the DMSs obtained are shown in Fig. 4.19 (b)–(e). The first DMS belongs to the power line signal affected by sag distortion, as evidenced by the decrease in its AE (plotted using the solid black line in Fig. 4.19 (b)) from 0.11 to 0.15 s. Furthermore, the second and subsequent DMSs are the harmonics of the power line, which are the weak components of the PQD signal. This study shows the effectiveness of the proposed method in extracting weak signal components.

4.7 Summary

The EMD-like EVDHM has been proposed for the decomposition of non-stationary multicomponent signals in terms of DMSs. The proposed method is a sifting-based framework, and it decomposes the signal based on EVDHM. There are two approaches, namely, empirical and MDL-based approaches, proposed for eigenvalue threshold computation. Furthermore, a frequency spread and IF-based component grouping method is proposed to ob-

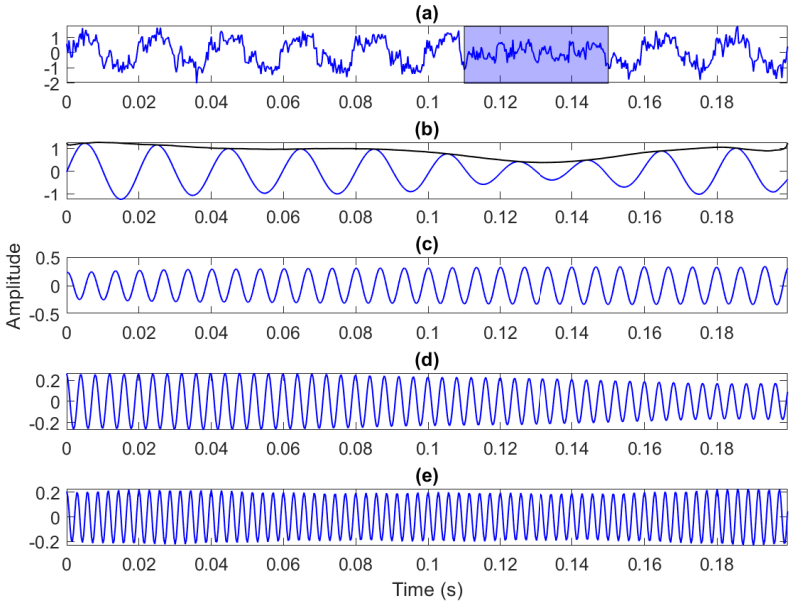

Figure 4.19: The PQD signal ($s[n]$) is shown in (a), while the DMSs obtained using the EMD-like EVDHM2 method are presented in (b)–(e). The duration of the sag in the PQD is indicated in (a) using blue rectangular box. The AE of first DMS is shown in (b) with a solid blue line.

tain the mono-component signal from elementary components. Later, HSA is applied to the decomposed components to obtain the TFD of the signal. The results obtained from the proposed method are compared with EMD, EEMD, VMD, iterative filtering, FDM, EFDM, EWT, FBSE-EWT, SSA, and improved EVDHM methods. The QRF and average correlation measures are considered for performance comparison of the proposed method with baselines. Firstly, the amplitude and frequency separability of the proposed method is studied using a multicomponent signal consisting of two sinusoidal mono-component signals. The change in amplitude or signal length has a minimal effect on sinusoid separation using the proposed method. Whereas, the sinusoidal components are not well separated using the proposed method when their frequencies are very close to each other. Later, the performance of the proposed method is compared with baselines for the separation of two sinusoids, a sinusoid and a chirp, and two chirps in clean and noisy cases. The proposed method

with MDL-based threshold computation surpassed the compared methods in terms of average correlation and QRF, while providing better TFD. Additionally, the TFDs of a speech signal obtained using the proposed method and baselines are compared; and the proposed method, along with EMD, VMD, and FDM methods, are able to represent the components of the speech signal in the time-frequency plane. After that, the effect of error propagation in the proposed method is studied by changing the eigenvalue threshold. The proposed method shows no error propagation. Lastly, the proposed method with MDL-based threshold computation extracted the trend line and extracted the weak component from the PQD signal. The computation time required by the proposed method is high compared to baseline methods due to its iterative nature. However, it has superior performance compared to them. The proposed method consists of a time-frequency parameter-based component grouping method. Additionally, the MDL-based eigenvalue threshold computation method is data-adaptive is nature, whereas other eigenvalue threshold computation methods in the literature are empirically defined.

Chapter 5

Multichannel extension of eigenvalue decomposition of Hankel matrix with application to eye movement and Alzheimer's disease detection

Due to recent sensor technologies, multichannel signals are generated in daily life applications. To process these signals while preserving mutual information between the components, the multivariate signal decomposition methods are proposed in literature [80]. There are several multichannel signal decomposition methods in the literature, namely multivariate EMD [83], multivariate EWT [85], multivariate VMD [88], multivariate IF [78], multivariate swarm sparse decomposition method [139], etc. These methods are briefly discussed in section 1.3.2. However, the extension of the EVDHM method is not developed in the literature. In this chapter, the two different multichannel extensions of the EVDHM method are developed to decompose the multichannel signals into their constituent components. The first developed method is named multichannel EVDHM or MCh-EVDHM. Further, an iterative decomposition framework based on MCh-EVDHM is proposed, termed im-

proved MCh-EVDHM. Later these methods have been applied to eye movement detection and Alzheimer's disease (AD) detection.

The eye tracking technology is useful in various applications like human-computer interface, augmented reality, diagnosis of pathologies of the human oculomotor system etc. [196–199]. The electrooculogram (EOG) signals capture the change in electric potential of the eye muscles as the electric dipole rotates during the eye movement, and this is assumed to be the most stable physiological signals [200, 201]. There are majorly four broad classes of eye movement, among several others exhibited by the human oculomotor system, and those are fixations, saccades, convergence, and blinking [200].

In [202], the two-channel EOG signal is filtered and amplitude scaled then the left, center, and right movements from horizontal preprocessed EOG and up, center, and down movements from vertical preprocessed EOG are identified using an ensemble of machine learning methods. In [201], the EOG signal is filtered then the saccade regions are extracted. Further, eight different saccades are identified by applying appropriate thresholding on the peaks of both channels of the EOG signal. In [200, 203], a two-channel EMG of extraocular muscles, i.e., EOG dataset for six eye movements (four saccades, eye blink, and no movement), is created. Further, a machine learning-based framework is presented for the eye movement detection task. In [204], the same dataset is studied to classify six eye movements using the FBSE-EWT method.

Comparison of [200] and [204] indicates that features extracted from the data-adaptive decomposition of EOG signals are more effective than statistical features extracted from EOG signals. The MCh-EVDHM method developed in this chapter preserves mutual information among the channels. Motivated by this, we propose an MCh-EVDHM-based framework for eye movement detection from a two-channel EOG signal. Further, we obtained an optimal framework with a trade-off between performance and model size so that

it can be deployed in a resource-constrained environment.

The AD is the most common cause of dementia, with 60-70% of total cases [205]. It generally affects people with the age above 65 years. Dementia is a state of the brain with symptoms like impaired logical thinking, decision making, emotional regulation, and memory [206]. The AD is an incurable disease, and an early diagnosis of it can help in slowing down its progression by timely medication or treatment [207].

The EEG is the recording of electrical brain activity by placing electrodes or sensors. The processing of EEG signals using suitable signal processing techniques results in the extraction of neurophysiological AD biomarkers [208]. Several automated AD diagnosis systems using EEG signals have been presented in the literature. In [209], a dual branch fusion network is developed to detect AD from EEG signals. It is a hybrid network developed by merging the strengths of convolutional neural networks and visual transformers. In [210], deep ensemble learning and 2-dimensional convolutional neural networks are used to classify the EEG signals corresponding to AD and healthy subjects. In [211], the 19 EEG channels are selected using the entropy-based method. The temporal and regional features are extracted from these EEG signals using bidirectional long short-term memory and convolutional neural networks, respectively. The artificial neural network is used to classify extracted features into AD and normal classes.

In [212], EEG rhythms are separated using the Daubechies 5 wavelet, and statistical and power features extracted from these rhythms are employed for AD detection using a long short-term memory (LSTM) network. Similarly, in [213], the rhythms are separated using the Daubechies 4 wavelet, followed by feature extraction and classification for AD detection. These AD detection frameworks use fixed-basis function-based signal analysis techniques for rhythm separation. This motivated us to develop a new data-adaptive rhythm separation algorithm based on the improved MCh-EVDHM method, which is then

employed for AD detection from EEG signals.

5.1 Multichannel eigenvalue decomposition of Hankel matrix for multichannel signal decomposition

In this section, the proposed MCh-EVDHM method for decomposition of multichannel signal is explained, which is later used to analyze the EOG signals. Consider an L-channel signal $x_{\text{MC}}[n] = [x^1[n];\ x^2[n];\ \ldots;\ x^L[n]] \in \mathbb{R}^{L\times N}$, where $x^i[n] \in \mathbb{R}^{1\times N}$ is the i^{th} channel signal. The steps involved in the decomposition of the multichannel signal using MCh-EVDHM are defined using the following steps,

Step 1: The Hankel matrix X^i of i^{th} channel signal $x^i[n]$ for $n = 0, 1, \ldots, N-1$ is obtained using Step 1 described in Section 2.1. In a similar manner, the Hankel matrices of all channels are computed. Then the sum of Hankel matrices (X^i) of all channels are obtained, which represents the Hankel matrix corresponding to the signal $x[n] = \sum_{i=1}^{L} x^i[n]$ as, $X = \sum_{i=1}^{L} X^i$.

Step 2: The EVD of the Hankel matrix X is performed to obtain the set of eigenvalues $(\lambda_1, \lambda_2, \ldots, \lambda_K)$ and corresponding eigenvectors $(u_1, u_2, \ldots, u_K)$ using Step 2 described in Section 2.1 [52].

Step 3: The number of eigenvalues (J) of the Hankel matrix X for a signal comprising of M sinusoidal signals is equal to $2M$. In the previous study, the significant eigenvalue pairs are those pairs which have magnitude of one of its eigenvalues greater than or equal to 10% of the maximum eigenvalue of X [52]. In order to apply our proposed MCh-EVDHM method for EOG signal analysis, the number of significant eigenvalue pairs is selected based on experimental performance. The significant eigenvectors

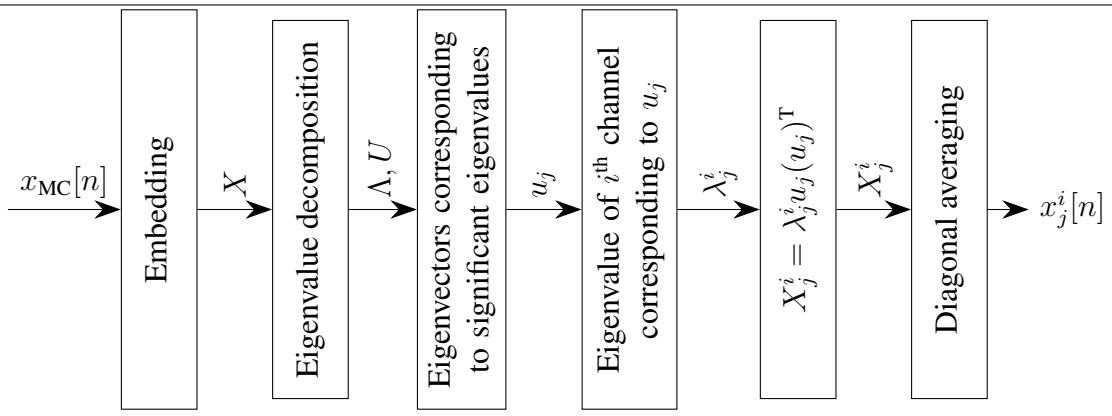

Figure 5.1: Block diagram representation of MCh-EVDHM technique to decompose the multichannel signal $x_{\text{MC}}[n] = \left[x^1[n]; x^2[n]; \ldots; x^C[n]\right]$ is shown.

are selected as the eigenvectors corresponding to the obtained significant eigenvalue pairs.

Step 4: The eigenvalue corresponding to eigenvector u_j for the i^{th} channel-signal is computed as, $\lambda_j^i = u_j^{\text{T}} X^i u_j$. Then, the rank one orthogonal elementary matrix corresponding to eigenvector u_j and eigenvalue λ_j^i is obtained as, $X_j^i = u_j \lambda_j^i u_j^{\text{T}}$.

Step 5: The significant elementary component ($x_j^i[n]$) of X_j^i is obtained by performing averaging of skew-diagonal elements of it using Step 5 described in Section 2.1. Hence, the signal $x^i[n]$ is represented into a set of significant elementary components as,

$$\left\{x_1^i[n], x_2^i[n], \ldots, x_R^i[n]\right\}, \text{ for } i = 1, 2, \ldots, L. \tag{5.1}$$

In case of synthetic signals, the significant elementary components obtained from an eigenvalue pair correspond to the same signal component, hence, they can be added together. Block diagram representation of the MCh-EVDHM-based signal decomposition is presented in the Fig. 5.1.

For analysis of synthetic signal using the MCh-EVDHM method, we have considered a three-channel synthetic signal having 5 different sinusoidal components defined

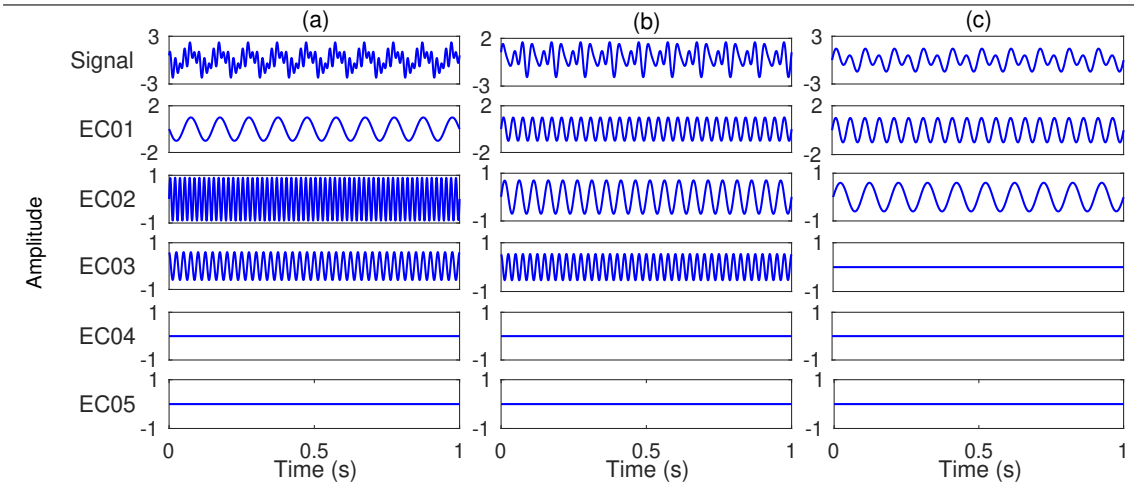

Figure 5.2: The three-channel synthetic signal and decomposed components corresponding to each channel signals obtained using EVDHM method are shown in (a), (b), and (c), respectively.

by, $x^i[n] = \sum_{j=1}^{5} A^i[j] \sin\left(2\pi f^i[j] \frac{n}{f_s}\right)$, for $i = 1, 2, 3$, where $A^1 = [-1\ 0\ 0\ 0.6\ 0.9]$, $A^2 = [0\ 0.7\ 1\ 0.54\ 0]$, $A^3 = [0.6\ 1\ 0\ 0\ 0]$, $f^1 = f^2 = f^3 = [10\ 20\ 30\ 40\ 60]$ Hz, $A^i[j]$ and $f^i[j]$ are the j^{th} elements of A^i and f^i, respectively, $f_s = 1000$ Hz and $n = 0, 1, 2, \ldots, 1000$. Firstly, the multichannel signal $x[n] = [x^1[n];\ x^2[n];\ x^3[n]]$ is decomposed using the EVDHM method, considering 5 eigenvalue pairs as significant, in which each channel is separately decomposed. The multichannel signal $x[n]$ and its decomposed elementary components obtained using EVDHM method are shown in Fig. 5.2. Then, the multichannel signal is decomposed using MCh-EVDHM considering $J = 10$. The multichannel signal $x[n]$ and and its decomposed elementary components obtained from MCh-EVDHM are shown in Fig. 5.3. Comparison of Figs. 5.2 and 5.3 show that the MCh-EVDHM method preserves mode alignment among the decomposed elementary components, while EVDHM does not preserve mode alignment.

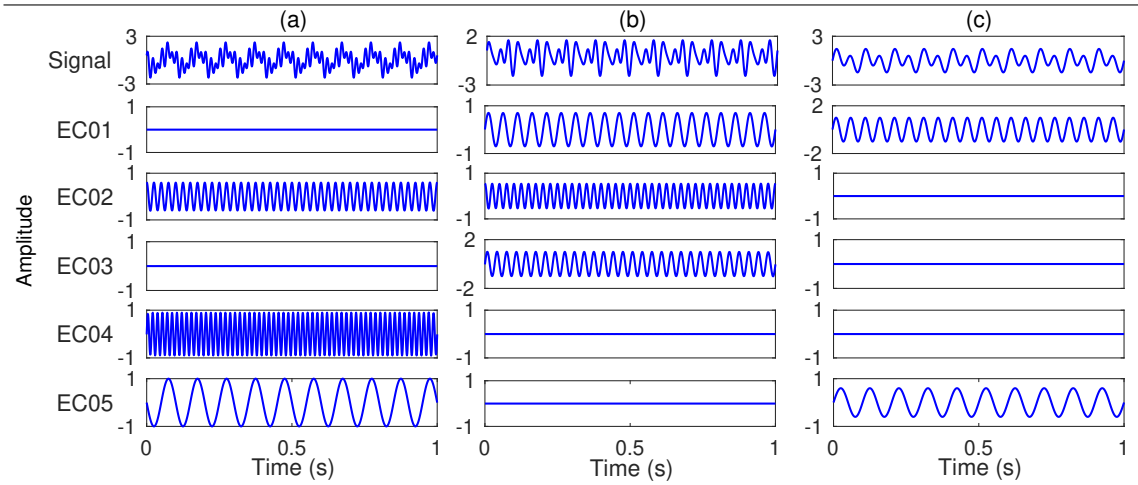

Figure 5.3: Time-domain representation of the signals in channel 1, 2, and 3 along with their decomposed components (EC01, EC02, . . . , EC05) obtained using MCh-EVDHM are shown in (a), (b), and (c), respectively.

5.2 Improved multichannel eigenvalue decomposition of Hankel matrix for signal decomposition

The improved MCh-EVDHM is motivated by the improved EVDHM method [53] to iteratively decompose a multichannel signal into a set of elementary components that satisfy the mono-component criteria. A multichannel signal $x_{\text{MC}}[n] = \left[x^1[n]; x^2[n]; \ldots; x^C[n]\right]$ for $n = 0, 1, \ldots, N-1$, where C is the number of channels, is considered. The elementary components of the signal $x_{\text{MC}}[n]$ are obtained using the improved MCh-EVDHM following Steps 1 to 5 in different iterations:

Step 1: The sum of Hankel matrix X of a multichannel $x_{\text{MC}}[n]$ is computed using Step 1 described in Section 5.1.

Step 2: The EVD is performed on the matrix X, to obtain the set of orthogonal eigenvectors $(u_1, u_2, \ldots, u_K)$ and the corresponding set of eigenvalues $(\lambda_1, \lambda_2, \ldots, \lambda_K)$ using Step 2 described in Section 2.1.

Step 3: The set of significant eigenvalue pairs $(\lambda_j, \lambda_{K-j+1})$ are selected based on STP [52]

and corresponding eigenvectors (u_j, u_{K-j+1}) for $j = 1, 2, \ldots, J$ are obtained. In this study, the value of STP equal to 5% of the maximum eigenvalue of X obtained in iteration 1 is considered.

Step 4: The set of elementary components for each channel is computed by performing the averaging of skew-diagonal elements of the matrix $X_j^i = u_j \lambda_j^i u_j^{\mathrm{T}} + u_{K-j+1} \lambda_{K-j+1}^i u_{K-j+1}^{\mathrm{T}}$ where $\lambda_j^i = u_j^{\mathrm{T}} X^i u_j$ using Step 5 described in Section 2.1.

Step 5: It is verified whether the elementary components of channel 1 satisfy the MMSC or not [53]. The MMSC criteria is defined as follows:

- The difference between the number of zero crossings and extrema is equal to either zero or one.
- The mean value of the upper and lower envelopes is zero.

Thereafter, we categorize the elementary components as a set that satisfies the MMSC and as a set that does not satisfy the MMSC. The elementary components that do not satisfy the MMSC, corresponding components of all the channels are required to follow steps from S1 in the next iteration. The process terminates at the end of the third iteration. After that, the components that do not satisfy the MMSC and have a frequency deviation less than $0.2 \times F_s$ are also considered in the analysis, where F_s is the sampling rate of the signal [53].

At the end of decomposition, the multichannel signal can be represented as a set of components $\{x_1^i[n], x_2^i[n], \ldots, x_R^i[n]\}$ for $i = 1, 2, \ldots, C$ where R is the total number of components.

5.3 Eye movement detection based on multichannel eigenvalue decomposition of Hankel matrix

In this section, we present a brief introduction to the dataset. Then, we present an MCh-EVDHM-based framework for eye movement detection from the two-channel EOG signals. In this framework, the EOG signal is decomposed into a set of elementary components from which the features are extracted, followed by machine learning-based classification into different eye movement classes.

5.3.1 Dataset

For the analysis, the EMG of extraocular muscles dataset is used which is publicly available on IEEE dataport [203]. This dataset was developed using two vertical, two horizontal, and one reference sensor. The recorded bioelectric signals have been amplified using an AD620 instrumentation amplifier. The signals are sampled at a sampling rate equal to 120 Hz. The dataset contains 2.083 s duration two-channel EOG signals of 10 pseudo-random repetitions of six different eye movements, namely, up, down, right, left, blink, and no movement by 10 subjects. Further, the signals have been filtered in the frequency range from 0.2 Hz to 40 Hz as it reflects the range of frequencies of the ocular muscle movements. The signals corresponding to each of the six different eye movement classes are provided in Fig. 5.4. The aforementioned two-channel EOG signals are used to train and test the developed classification framework.

5.3.2 Feature extraction

For feature extraction, the two-channel EOG signal $[x^1[n]; x^2[n]]$ is decomposed into a set of significant elementary components $x_r^i[n],\ i = 1, 2$ and $r = 1, 2, \ldots, R$. The mean of

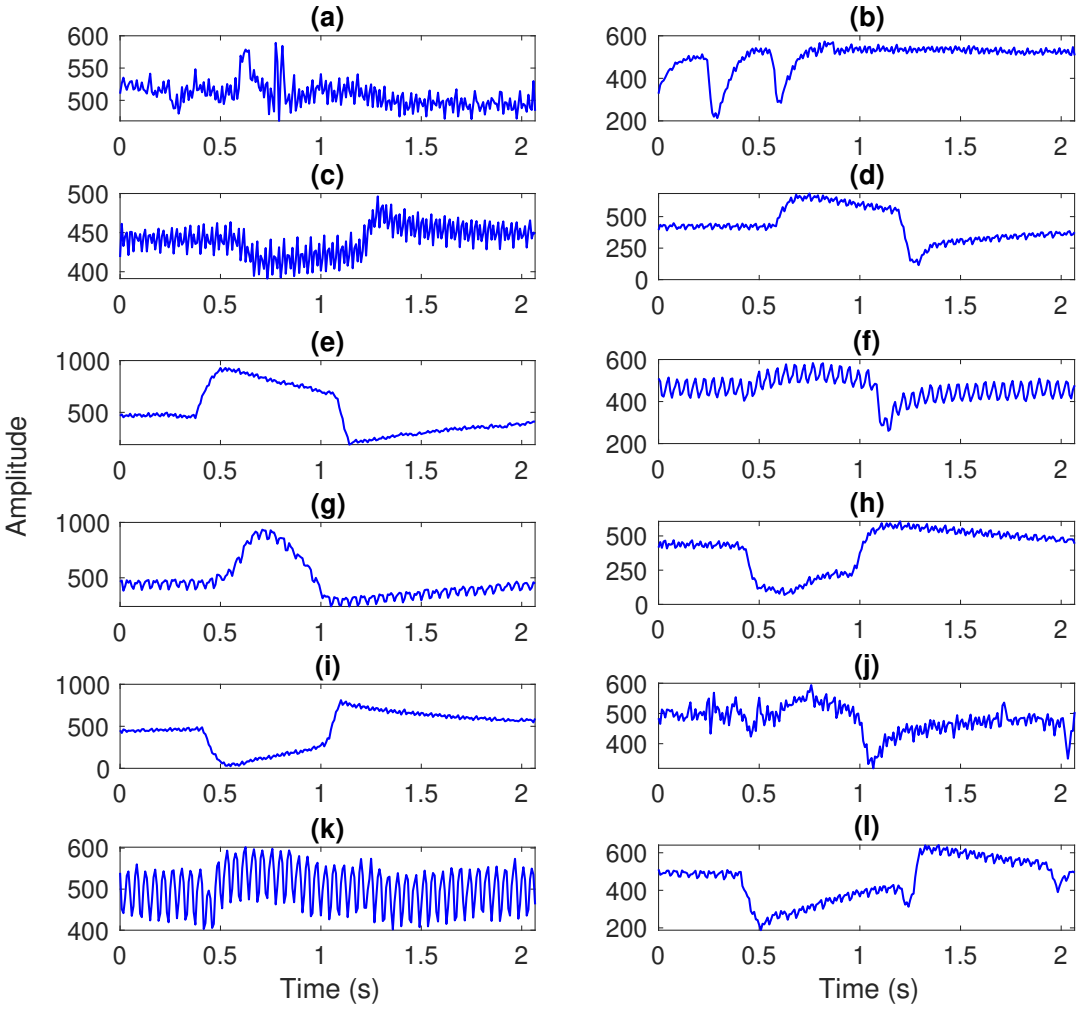

Figure 5.4: Time-domain representation of the two-channels of the EOG signals corresponding to no eye movement are shown in (a) and (b); downward eye movement are shown in (c) and (d); leftward eye movement are shown in (e) and (f); eye blink are shown in (g) and (h); rightward eye movement are shown in (i) and (j); and upward eye movement are shown in (k) and (l).

the IF and total energy of each significant elementary component are computed as features. For the computation of the aforementioned features, IF ($f_r^i[n]$) and instantaneous energy ($e_r^i[n]$) of $x_r^i[n]$ are required and they are computed as [2],

$$f_r^i[n] = \phi_r^i[n+1] - \phi_r^i[n]; \quad e_r^i[n] = \left(a_r^i[n]\right)^2 \tag{5.2}$$

where $\phi_r^i[n]$ and $a_r^i[n]$ are the instantaneous phase and AE of the analytic signal representation of $x_r^i[n]$ which is represented as,

$$z_r^i[n] = x_r^i[n] + j\mathcal{H}\{x_r^i[n]\} = a_r^i[n]e^{j\phi_r^i[n]}, \tag{5.3}$$

As the r^{th} significant elementary component of all the channels are extracted from a common eigenvector as defined in Section 5.1, the mean frequency (F_j) feature is extracted only for the $x_r^1[n]$ which is mathematically expressed as [2],

$$F_r = \frac{\sum_{n=0}^{N-1} f_r^1[n]e_r^1[n]}{\sum_{n=0}^{N-1} e_r^1[n]},\ j = 1, 2, \ldots, R \tag{5.4}$$

The total energy of the r^{th} significant elementary components of the i^{th} channel is computed as [2],

$$E_r^i = \sum_{n=0}^{N-1} e_r^i[n],\ i = 1, 2 \text{ and } r = 1, 2, \ldots, R \tag{5.5}$$

The value of R is set to 12 for the decomposition of EOG signals in the proposed framework. Hence, we have a total of 36 features for each EOG segment.

5.3.3 Classifiers

For the classification of the extracted features into different eye movement classes, four classifiers have been trained and tested which are ensemble bagged tree, linear SVM, quadratic SVM, and cubic SVM [214, 215]. These aforementioned classifiers are described below.

5.3.3.1 Ensemble bagged tree

It is an improved tree-based classifier in which the training set is first divided into K subsets or bags based on bootstrap resampling. Each of these subsets is used to train K

different trees. The output of the ensemble bagged tree is the majority of the output of the aforementioned K decision trees [214]. The majority voting system ensures the improvement of the overall classification of the tree-based classifier model. We have considered $K = 30$ in the presented study.

5.3.3.2 Support vector machine

The SVM classifier finds a hyperplane that separates the different classes with the largest margin possible between the classes. It uses kernels to transform the feature vectors into higher dimensional space such that the classes are easily separable [215]. In this study, linear, quadratic, and cubic kernels are utilized.

5.3.4 Classification framework and simulation setup

To classify six different eye movements, i.e., upward, downward, right, left, blink, and no movement, the two-channel EOG signals are first decomposed into a set of 12 significant elementary components for each channel using the MCh-EVDHM technique. Then, the mean frequency and total energy features of the significant elementary components are computed. The computed features are used to train and validate the classifier model. Then, a set of untrained features is used to test the validated classifier model. The proposed framework with linear SVM classifier is depicted in Fig. 5.5.

5.4 Alzheimer's disease detection using improved multichannel eigenvalue decomposition of Hankel matrix

This section provides the database description and proposed framework for AD detection from EEG signals. The improved MCh-EVDHM, an improved version of MCh-EVDHM, is presented in section 5.2 to decompose the multichannel EEG signals. Further,

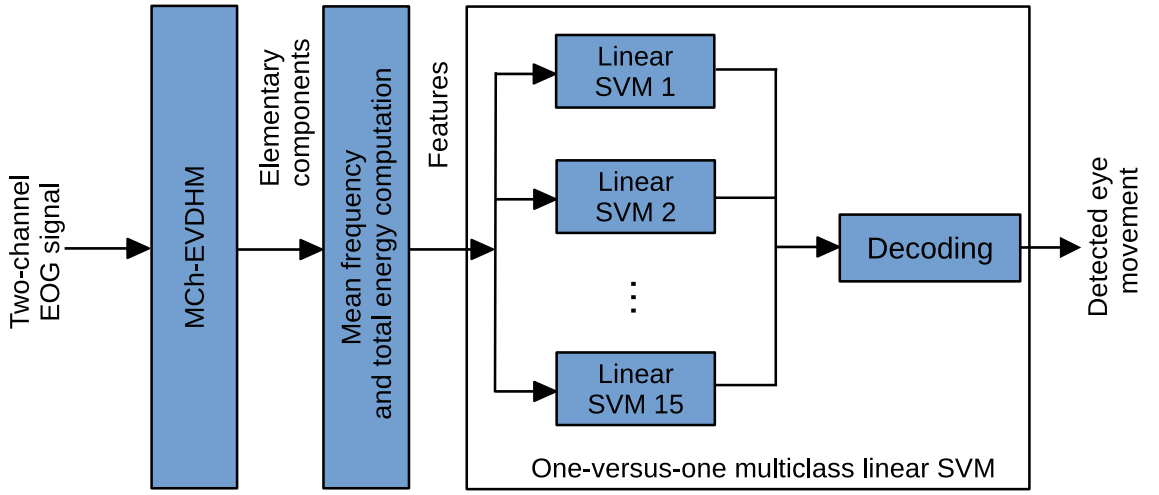

Figure 5.5: Block diagram representation of the proposed framework using linear SVM classifier is shown.

a rhythms separation method is presented from the decomposed components of EEG signals. Then, feature extraction from EEG rhythms and the classification process is presented.

5.4.1 Database

The EEG database used in this study is made available by researchers at Florida State University. It contains four different groups of EEG signals: Group 1: 12 healthy subjects with eyes closed during the recording of data; Group 2: 80 AD patients who kept their eyes closed during the recording of data; Group 3: 12 healthy subjects who kept their eyes open during the recording of data; and Group 4: 80 AD patients who kept their eyes open during the recording of data [213, 216]. The age of the healthy subjects ranges from 61 to 83 years [208, 213]. The EEG recordings are performed using a 19-channel scalp electrode positioned according to the international 10-20 technique at a sampling rate of 128 Hz. Each EEG segment is of 8 s duration. The signals are band-limited to the range of 0.5-30 Hz and movement artifacts are removed by an EEG technician.

5.4.2 Rhythm separation based on improved multichannel eigenvalue decomposition of Hankel matrix

The EEG rhythms are separated using components obtained from the decomposition of EEG signals using improved MCh-EVDHM. We calculate the mean frequency of the extracted components and compare them with the boundary frequencies of the different rhythms, i.e., delta rhythms from 0.5 to 4 Hz, theta rhythm from 4 to 8 Hz, alpha rhythm from 8 to 13 Hz, and beta rhythm from 13 to 30 Hz [213]. Since the EEG signals considered in this work are band-limited in the range of 0.5-30 Hz, the gamma rhythm is not separated. The gamma rhythms can be separated using the proposed approach. The components of a particular frequency region or rhythm are added together to obtain their respective rhythms [217]. The mean frequency of a component $x_r^i[n]$ is calculated as [2],

$$\langle f_r^i \rangle = \frac{\sum_{n=0}^{N-1} f_r^i[n] e_r^i[n]}{\sum_{n=0}^{N-1} e_r^i[n]} \tag{5.6}$$

where $f_r^i[n]$ and $e_r^i[n]$ are the IF and instantaneous energy of $x_j^i[n]$. The IF $f_r^i[n] = \frac{f_s}{2\pi}\left(\phi_r^i[n+1] - \phi_r^i[n]\right)$ and instantaneous energy $e_r^i[n] = \left(a_r^i[n]\right)^2$ where $x_r^i[n] + j\mathcal{H}\{x_r^i[n]\} = a_r^i[n]e^{j\phi_r^i[n]}$ [2]. Figures 5.6 and 5.7 show the extracted rhythms from the T3, T4, T5, and T6 channel EEG signals corresponding to healthy and AD subjects, respectively.

5.4.3 Feature extraction

Three features are extracted from each separated EEG rhythm: total energy, standard deviation, and skewness [2, 218]. The mathematical expression for computation of total

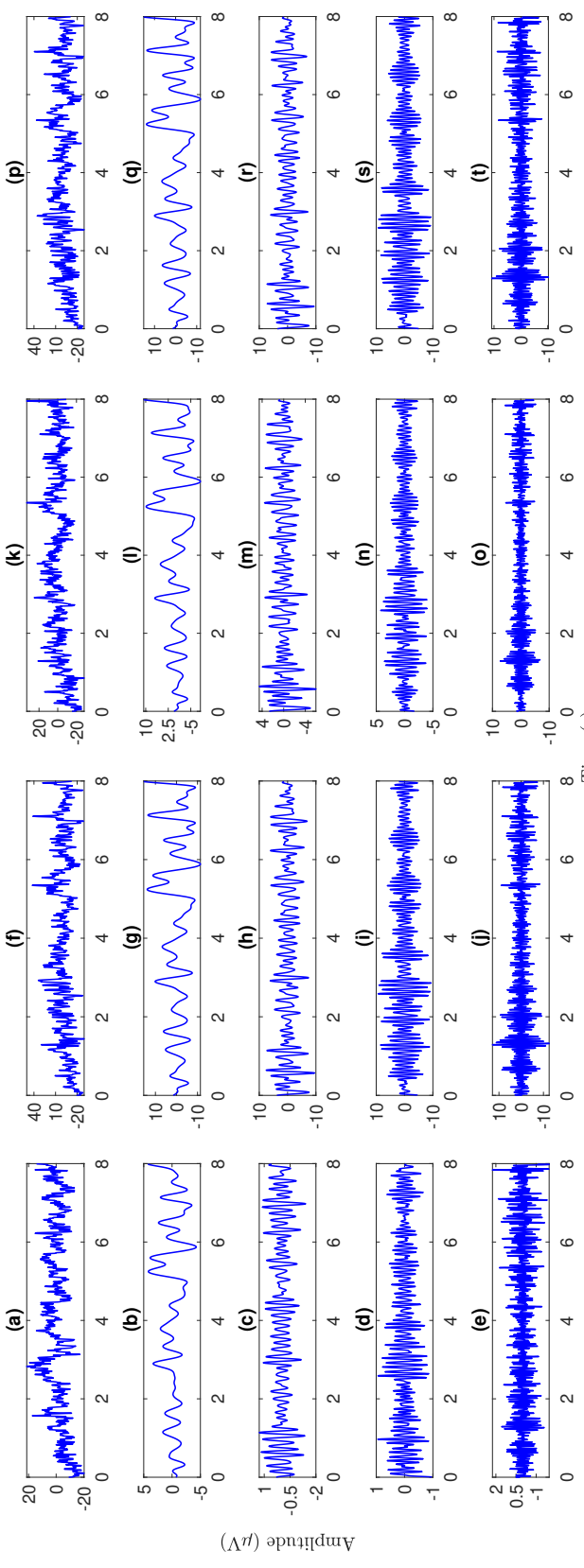

Figure 5.6: The plots of EEG signals of a healthy subject corresponding to the channels T3 in (a), T4 in (f), T5 in (k), and T6 in (p) are shown along with their rhythms in (b)–(e), (g)–(j), (l)–(o), and (q)–(t), respectively.

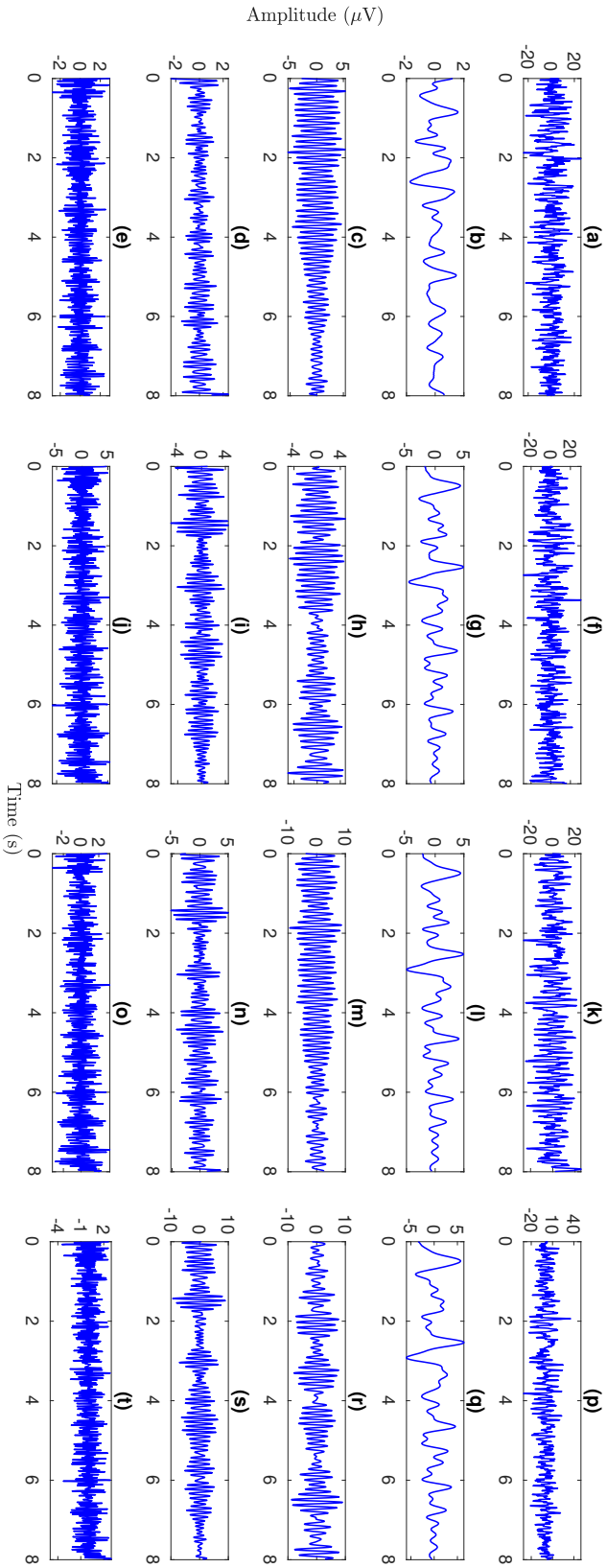

Figure 5.7: The plots of EEG signals corresponding to channels T3, T4, T5, and T6 of an AD patient are shown in (a), (f), (k), and (p), respectively, along with their rhythms in (b)–(e), (g)–(j), (l)–(o), and (q)–(t), respectively.

energy feature from a signal $y[n]$ for $n = 1, 2, \ldots, N$ is given by [2],

$$E = \sum_{n=1}^{N} (y[n])^2 \tag{5.7}$$

The computation of the standard deviation (σ) and skewness (S) from the signal $y[n]$ is performed using the following expressions:

$$\sigma = \sqrt{\frac{1}{N} \sum_{n=1}^{N} (y[n] - \mu)^2} \tag{5.8}$$

and

$$S = \frac{1}{N\sigma^3} \sum_{n=1}^{N} (y[n] - \mu)^3 \tag{5.9}$$

where $\mu = \frac{1}{N} \sum_{n=1}^{N} y[n]$ [218].

5.4.4 Classification

The classification of the computed features is performed using a suitable classifier. The linear discriminant analysis, ensemble subspace discriminant, and quadratic SVM classifiers are considered for the classification of features extracted from EEG signals in this study based on a thorough literature review [219, 220]. The linear discriminant analysis projects the features into low dimensional space while maximizing the separation between two classes and then performing linear classification [220]. The ensemble subspace discriminant uses the random subspace ensembles to improve the accuracy of the discriminant analysis [219, 221]. The SVM classifier transforms the feature vectors into higher dimensional space using kernel functions such that the classes are easily separable [219, 220]. In our study, we have considered the quadratic kernel.

The block diagram representation of the proposed AD detection framework based on

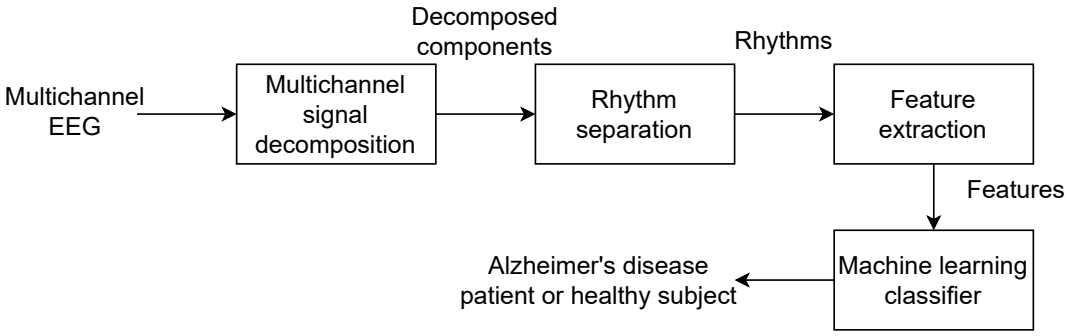

Figure 5.8: Block diagram representation of the proposed AD detection framework using imrpoved MCh-EVDHM method is shown.

improved MCh-EVDHM and machine learning from EEG signals is shown in Fig. 5.8.

5.5 Results and discussion

In this section, we present the simulation results of two classification frameworks based on MCh-EVDHM and improved MCh-EVDHM methods as described in sections 5.3 and 5.4.

5.5.1 Application to eye movement detection from EOG signals

In this subsection, we present and discuss the analysis of synthetic multichannel signal using MCh-EVDHM and identification of different eye movements from the EOG using MCh-EVDHM based framework. The proposed method for EOG classification has been compared with other existing methods in the literature. The compared methods have been studied on the same dataset. Our study considers the following two cases: In case 1, the whole dataset has been considered for training and validation purposes in 5-fold cross-validation, and in case 2, the 10% of the dataset is considered as untrained test set and performed training and validation in a 5-fold cross-validation on the remaining 90% of the dataset. The decomposition results of downward eye movement EOG signal using MCh-

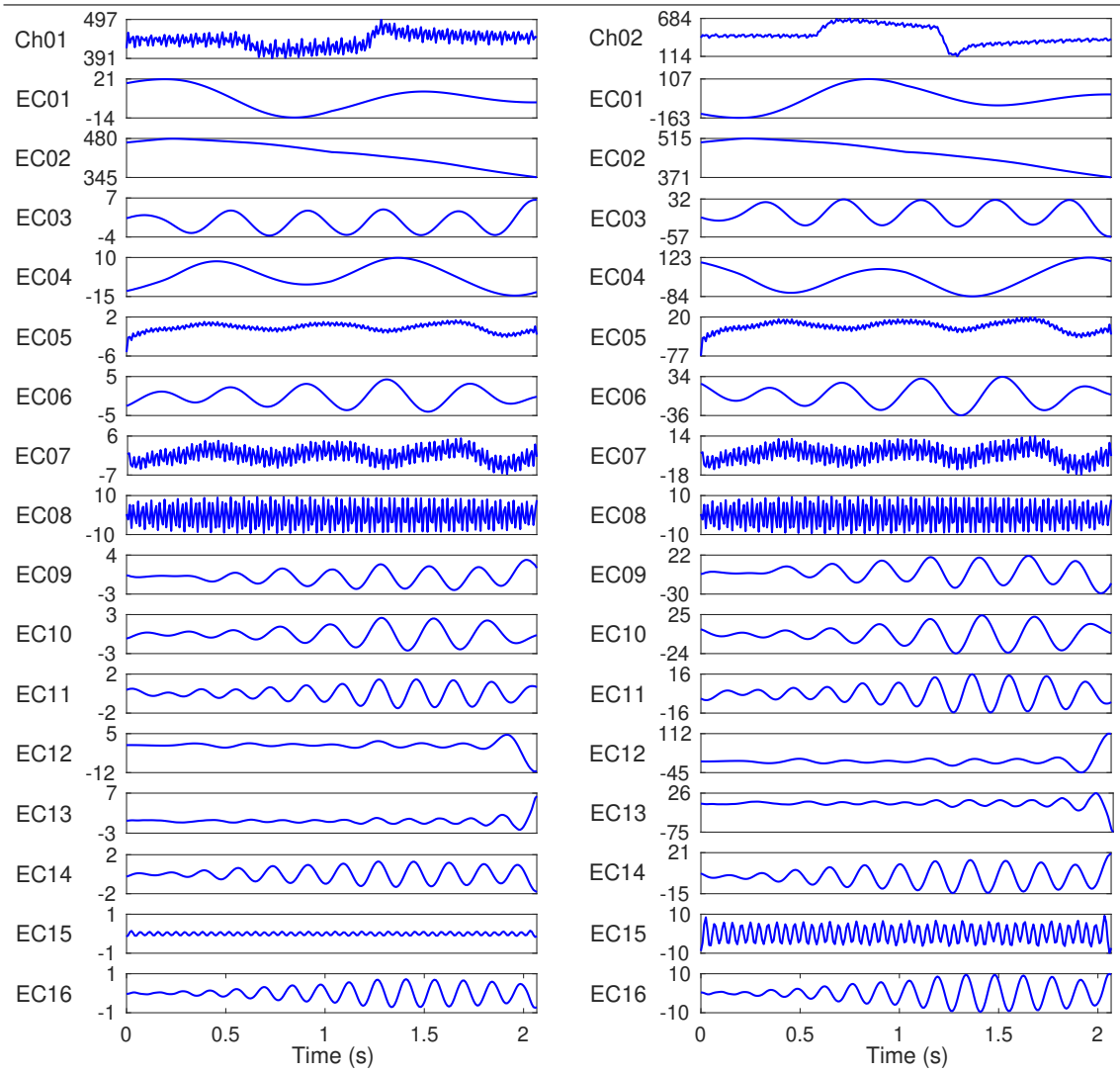

Figure 5.9: Time-domain representation of the channel 1 (Ch01) and channel 2 (Ch02) of EOG signal are shown on top of the figure along with their corresponding significant decomposed components (EC01, EC02, . . . , EC12) obtained using MCh-EVDHM method are shown below to them.

EVDHM are shown in Fig. 5.9.

For case 1 of study, we train and validate the proposed framework using 2.083 s duration two-channel EOG. The comparison of proposed and compared methods is presented in Table 5.1. The proposed framework with ensemble bagged tree has achieved highest specificity of 99.27% among all. It has only 1.87% and 1.90% relative reduction in sensitivity and specificity, respectively compared to model with statistical & time and frequency do-

Table 5.1: The validation performance metrics of the proposed and existing methods for eye movement classification.

Method	Feature type (number of features)	Classifier	Performance metrics (in %)					Model size (in kB)
			VACC	VSEN	VSPE	VPRE	VF1-score	
Asanza et. al. [200]	Statistical (12)	Cubic SVM	93.50	NR	NR	NR	NR	NR
Khan et.al. [204]	TAFD (56)	Multiclass SVM	97.12	95.33	97.90	95.35	NR	NR
	Statistical & TAFD (72)	Multiclass SVM	98.91	98.17	99.11	98.20	NR	NR
Proposed method	Mean frequency and total energy (36)	Linear SVM	94.83	94.83	98.97	94.87	94.81	147
		Quadratic SVM	95.33	95.33	99.07	95.34	95.32	287
		Cubic SVM	94.83	94.83	98.97	94.81	94.81	313
		Ensemble bagged tree	96.33	96.33	99.27	96.33	96.33	524

Note: NR: not reported, VACC: validation accuracy, VSEN: validation sensitivity, VSPE: validation specificity, VPRE: validation precision, VF1-score: validation F1-score.

Table 5.2: The validation accuracy and testing performance metrics of the proposed framework for case 2 analysis.

Method	Feature type (number of features)	Classifier	Performance metrics (in %)						Model size (in kB)
			VACC	ACC	SEN	SPE	PRE	F1-score	
Proposed method	Mean frequency and total energy (36)	Cubic SVM	94.07	96.67	96.67	99.33	97.22	96.63	313
		Quadratic SVM	93.89	96.67	96.67	99.33	97.22	96.63	281
		Linear SVM	94.44	98.33	98.33	99.67	98.48	98.33	147
		Ensemble bagged tree	94.81	100	100	100	100	100	503

Note: VACC: validation accuracy, ACC: accuracy, SEN: sensitivity, SPE: specificity, PRE: precision.

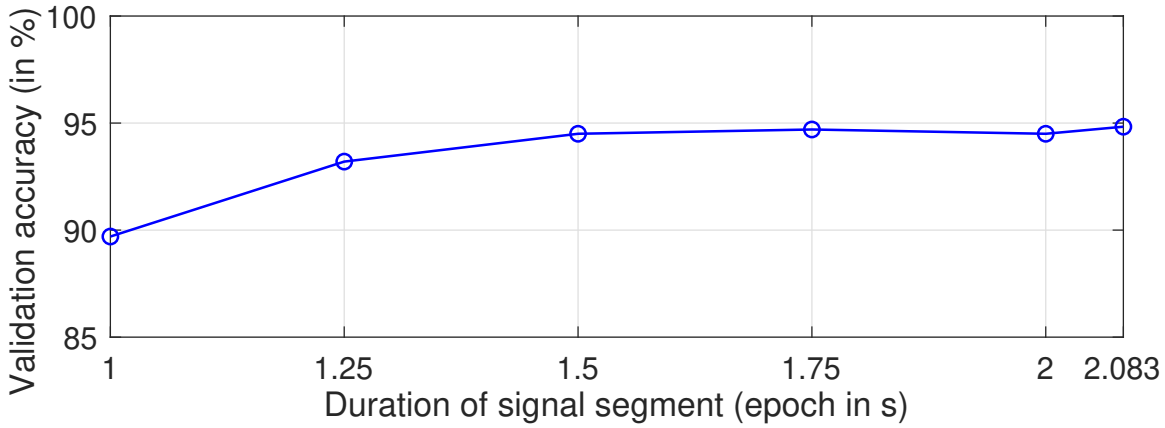

Figure 5.10: Plot of signal segment (epoch) duration versus validation accuracy is shown.

main (TAFD) features with half of the feature size [204]. It has 0.81% and 2.61% relative reduction in accuracy when compared to models with TAFD features and statistical & TAFD features, respectively [204]. The proposed framework achieves good performance with very few number of features as compared to models with TAFD features and statistical & TAFD features [204]. Whereas, in the method presented in [200], 12 features are extracted which is less than the number of features in the proposed framework, but the relative accuracy reduction in their method is approximately 3% as compared to proposed framework. Furthermore, we have performed performance analysis of linear SVM-based framework (as it gives comparable performance with very small model size) by varying the duration of the signal segment. The duration of signal segment versus the validation accuracy plot for linear SVM is shown in Fig. 5.10. Further, it can be observed that, the validation accuracy is smallest and highest for epoch size 1 s and 2.083 s, respectively among the considered segment (epoch) sizes.

In case 2 of the analysis, we perform training, validation, and testing of the proposed framework using 2.083 s duration two-channel EOG signals. The results for this case are presented in Table 5.2. The ensemble bagged tree-based framework has achieved the highest testing performance metrics of 100% among all four compared models. However, the

linear SVM classifier is the smallest model in terms of model size (147 kB), which is approximately 70.77% smaller than that of the ensemble bagged tree classifier in the proposed framework. Whereas the decision-bagged tree-based framework has relatively 1.67%, 1.67%, 0.33%, 1.52%, and 1.67% higher testing accuracy, sensitivity, specificity, and precision, respectively, than that of linear SVM-based framework. While considering both performance as well as model size, the linear SVM-based framework is the best framework among all the considered frameworks as it gives relatively good performance with a very small model size.

5.5.2 Alzheimer's disease detection from EEG signals

This subsection presents and discusses the results obtained from the proposed framework. We present three different analysis cases to validate the proposed framework for AD detection from EEG signals. In the first case, the EEG signals for the eyes open case are considered for classification. The EEG signals corresponding to the eyes closed case are considered in the second case. The third case considers the EEG signals corresponding to both eyes open and eyes closed.

In the eyes-closed case, we trained and validated the proposed framework using EEG signals corresponding to different brain regions, and the results are presented in Table 5.3. The performance of the developed framework consisting of a quadratic SVM classifier using T3, T4, T5, and T6 channels of EEG signals has achieved the highest accuracy of 98.9%, which is better than the performance obtained from the EEG signals corresponding to other regions of the brain. Hence, the T3, T4, T5, and T6 channel EEG signals are considered for further analysis. In the eyes-open case, the performance of the developed framework is computed from the T3, T4, T5, and T6 channels of EEG signals, and the results are presented in Table 5.4. The system with the quadratic SVM classifier has achieved an

Table 5.3: Performance of the proposed framework for AD detection using EEG signals corresponding to different regions of the brain.

Channels selected	Classifier	Performance metrics (in %)				
		ACC	SEN	SPE	PRE	F1-score
T3, T4, T5, and T6	QSVM	98.9	98.76	100	100	0.9938
P3, P4, and Pz	ESD	96.7	96.36	100	100	0.9816
C3, C4, and Cz	ESD	92.4	92.94	85.71	98.75	0.9576
O1 and O2	ESD	93.5	95.72	80	97.5	0.9660
Fp1 and Fp2	ESD	93.5	94.04	87.5	98.75	0.9634
F3, F4, F7, F8, and Fz	ESD	91.3	93.9	70	96.25	0.9506

Note: ACC: accuracy, SEN: sensitivity, SPE: specificity, PRE: precision, QSVM: quadratic SVM, ESD: ensemble subspace discriminant.

accuracy of 95.6%, and the model size of the classifier is 23 kB.

The performance of the proposed framework is also compared with the performance of earlier published methods from the literature, presented in Table 5.4. The method in [213] uses different channels for different eye states. The method in literature has achieved the highest accuracy of 100% and 98.9% in the eyes closed and eyes open states, respectively. Whereas the proposed framework using T3, T4, T5, and T6 channel EEG signals has achieved the accuracy of 98.9% and 95.6% in eyes closed and eyes open states, respectively, comparable to the method available in the literature. It should be noted that the method in literature used different channels for different eye states, whereas the proposed method uses T3, T4, T5, and T6 channel EEG signals.

There is no analysis yet presented in the literature for eyes state independent case on the considered dataset as per our best knowledge. In the third case, we have combined the EEG signals corresponding to the eyes open and eyes closed states to develop a eyes state independent framework for AD detection. The proposed framework from the combined

Table 5.4: Performance comparison of the proposed framework with existing state-of-the-art for AD detection from EEG signals recorded during various states of the eyes.

Method	Features	EEG segment length in number of samples	Electrodes	Eyes state	Classifier	Performance metrics (in %)					Model size (in kB)
						ACC	SEN	SPE	PRE	F1-score	
Vicchietti et al. [213]	Wavelet coherence	500	T3-O2	Open	SVM	97.8	98.7	91.7	NA	NA	NA
			T3-C4	Closed	SVM	97.8	98.7	91.7	NA	NA	NA
	Fractal dimensions	600	F1	Open	SVM	95.6	98.7	75	NA	NA	NA
			T6	Closed	SMV	94.6	100	58.3	NA	NA	NA
	Quadratic entropy	700	T6	Open	SVM	97.8	100	83.3	NA	NA	NA
			F7	Closed	SVM	94.6	98.7	66.7	NA	NA	NA
	Wavelet energy	800	T6	Open	SVM	88	100	83	NA	NA	NA
			F7	Closed	SVM	91.3	98.7	41.7	NA	NA	NA
	Quantiles graphs	900	O2	Open	SVM	98.9	100	91.7	NA	NA	NA
			F3	Closed	SVM	100	100	100	NA	NA	NA
	Visibility graphs	1000	T6	Open	SMV	90.2	97.5	41.7	NA	NA	NA
			F3	Closed	SMV	90.2	96.2	50	NA	NA	NA
Proposed method	Total energy, STD, skewness	1023	T3, T4, T5, T6	Open	QSVM	95.6	97.50	81.81	97.50	0.9750	23
				Closed	QSVM	98.9	98.76	100	100	0.9938	17
				Closed or open	LDA	97.3	98.14	90.48	98.75	0.9844	49

Note: ACC: accuracy, SEN: sensitivity, SPE: specificity, PRE: precision, NA: not available, STD: standard deviation, QSVM: quadratic SVM, LDA: linear discriminant analysis.

EEG signals using an ensemble subspace discriminant classifier has achieved an accuracy of 97.3%. The model size of the trained classifier is obtained to be 49 kB.

From the above discussion, it can be observed that the proposed framework using the EEG signals corresponding to T3, T4, T5, and T6 channels has achieved good performance for the eyes open and eyes closed states whereas the methods from the literature considered different channels for different eyes states. Additionally, the performance of the proposed framework for AD detection from eyes states independent EEG signals has achieved good performance. This comparison proves the robustness of the developed framework compared to the existing method.

5.6 Summary

The MCh-EVDHM is proposed to decompose multichannel multicomponent signals into a set of mode-aligned elementary components. Further, an extension of it, i.e., improved MCh-EVDHM, is proposed to decompose the multichannel signal in an iterative manner. Then, a framework for the classification of six eye movements is proposed using the MCh-EVDHM. The ensemble bagged tree classifier-based classification framework achieved the highest validation specificity of 99.27% and relatively comparable accuracy, sensitivity, and precision when compared with the best-performing baseline, that too by using half the number of features. The proposed framework with an ensemble bagged tree classifier has achieved the highest testing performance metrics of 100%. The proposed MCh-EVDHM technique can be explored to analyze various real-time multichannel signals like electroencephalograms.

The AD is a progressive dementia, a timely diagnosis of which can help in slowing down its progression with proper medication. A new EEG rhythm separation method is presented using the improved MCh-EVDHM technique. A robust AD detection framework is devel-

oped using the separated rhythms from EEG signals. The proposed framework achieved 98.9%, 95.6%, and 97.3% accuracy for eyes closed, eyes open, and eyes open or closed states, respectively. The performance of the proposed framework is found to be more robust as compared to the methods from the literature with comparable performance measures in the eyes open and eyes closed states. The proposed framework is suitable for deployment in resource constrained environment because of the small model size of the classifier. The proposed rhythm separation method can be used for the analysis of EEG signals in various applications.

The proposed methods MCh-EVDHM and improved MCh-EVDHM are found to be performing well for real-life signals in the respective studies. However, improved MCh-EVDHM method is suggested to choose in the studies involving computation of TFD of a multichannel signal, as the decomposed components obtained from improved MCh-EVDHM is checked to satisfy mono-component criteria.

Chapter 6

Time-varying eigenvalues-based time-frequency distribution for signal analysis

6.1 Introduction

Non-stationary signals are observed in various domains, like biomedical engineering [53], mechanical engineering, communication systems, power systems [222], etc. Analysis of such signals using the Fourier transform provides either time-domain or frequency-domain information. However, these signals are characterized by a time-varying spectral content which is known as TFD. There are various signal analysis techniques in literature to obtain TFD of a signal namely, STFT [2], STFT-based synchrosqueezing transform (FSST) [223, 224], wavelet transform [2, 13], WVD [14], etc.

The square of the magnitude of STFT is the spectrogram of a signal. The resolution of the spectrogram depends on the width and type of the window considered for the analysis of the signal. For longer-duration windows, the time resolution is poor, the frequency resolution is good, and vice-versa [2]. The scalogram is the representation of wavelet transform

coefficients in a time-scale plane. The low-frequency regions have poor time resolution and good frequency resolution, whereas the high-frequency regions have good time resolution and poor frequency resolution [13]. The WVD provides a very high-resolution TFD. However, there are cross-term present in the TFD of a multicomponent signal obtained using the WVD technique, which causes ambiguity in the analysis [31].

The decomposition technique and Hilbert transform-based approaches have been proposed in the literature to obtain the TFD of a signal [16]. In these approaches, the decomposition techniques decompose the signal into a set of signal components. The HSA is applied to these components to obtain the TFD of the signal. There are various methods in the literature, like HHT [16], improved EVDHM and Hilbert transform [53], FDM-based HSA [54], VMD-based HSA [45] etc.

The EVDHM technique decomposes the signal into a set of signal components [74]. The concept of iterative EVDHM technique is presented to improve the frequency localization of the components [52]. Furthermore, a grouping technique based on spectral overlapping of the components is presented to obtain more meaningful components. The improved EVDHM technique is presented to obtain better signal components [53]. The Hilbert transform-based TFD of the signal is obtained using the improved EVDHM technique [53]. The sliding EVD technique is presented to decompose the signals into a set of components, and the TFD of the signal is obtained by applying HSA on these components [188].

In this work, the relationship between the signal amplitude and the significant eigenvalue pair of a sinusoidal signal is derived. The relationship between the phase shift of sinusoidal signal and the phase shift of the eigenvector corresponding to the significant eigenvalue pair for a sinusoidal signal is also derived. Furthermore, a new technique to obtain the TFD of the signal is proposed by representing the mean of magnitude of significant eigenvalue pairs (MMSEP), obtained from short-duration EVDHM, in time-frequency plane. The effect of

change in the window length on the resolution of the obtained TFD is studied. Later, the TFD obtained using the proposed method is compared with the spectrogram, scalogram, FSST, and VMD-based HSA. The proposed framework is the first of its kind for the analysis of signals by representing eigenvalue-based parameter in a time-frequency plane.

The organization of this chapter is as follows. Section 6.2 presents the derivation of the relationship between the amplitude of a sinusoidal signal and significant eigenvalue pairs obtained by applying EVDHM to the signal. Additionally, it presents the relation between the phase shift of the sinusoidal signal and the phase shift of the eigenvectors corresponding to the eigenvalue pair obtained using EVDHM. Section 6.3 presents the proposed method for obtaining the TFD using time-varying eigenvalues. Section 6.4 presents the comparison of the TFDs obtained from the proposed method and other baseline methods. Section 6.5 presents the summary of the presented work in this chapter.

6.2 Relation between eigenvalues and amplitude of sinusoidal signals

In this section, a derivation of the relationship between the eigenvalues of a sinusoidal signal obtained from EVDHM and the amplitude of corresponding sinusoidal signal is presented. A signal $x[n]$ for $n = 0, 1, \ldots, N-1$ is considered, and its corresponding Hankel matrix X is obtained using Step 1 described in Section 2.1. The matrix X has an eigenvector $v[n]$ and corresponding eigenvalue λ, if [225]

$$\begin{bmatrix} x[0] & x[1] & \ldots & x[K-1] \\ x[1] & x[2] & \ldots & x[K] \\ \vdots & \vdots & \ddots & \vdots \\ x[K-1] & x[K] & \ldots & x[N-1] \end{bmatrix} \begin{bmatrix} v[0] \\ v[1] \\ \vdots \\ v[K-1] \end{bmatrix} = \lambda \begin{bmatrix} v[0] \\ v[1] \\ \vdots \\ v[K-1] \end{bmatrix} \tag{6.1}$$

Equation (6.1) can be expanded as follows:

$$\lambda v[0] = \sum_{n=0}^{K-1} x[n]v[n] \tag{6.2}$$

$$\lambda v[1] = \sum_{n=0}^{K-1} x[n+1]v[n] \tag{6.3}$$

Similarly,

$$\lambda v[k] = \sum_{n=0}^{K-1} x[n+k]v[n] \tag{6.4}$$

Now, consider the signal $x[n] = A\sin\left(2\pi f\frac{n}{f_s} + \phi\right)$ for $n = 0, 1, \ldots, N-1$ and corresponding eigenvector as $v[n] = B\sin\left(2\pi f\frac{n}{f_s} + \theta\right)$ for $n = 0, 1, \ldots, K-1$, such that $||v[n]||_2 = 1$, has the same frequency and different amplitude and phase shift. By putting the values of $x[n]$ and $v[n]$ in equation (6.4), the following equation is obtained:

$$\lambda B\sin\left(2\pi f\frac{k}{f_s} + \theta\right) = \sum_{n=0}^{K-1} A\sin\left(2\pi f\frac{n+k}{f_s} + \phi\right) B\sin\left(2\pi f\frac{n}{f_s} + \theta\right) \tag{6.5}$$

$$\lambda B\sin\left(2\pi f\frac{k}{f_s} + \theta\right) = \frac{AB}{2}\sum_{n=0}^{K-1}\left\{\cos\left(2\pi f\frac{k}{f_s} + \phi - \theta\right) - \cos\left(2\pi f\frac{2n+k}{f_s} + \phi + \theta\right)\right\} \tag{6.6}$$

$$\lambda B\sin\left(2\pi f\frac{k}{f_s} + \theta\right) = \frac{ABK}{2}\cos\left(2\pi f\frac{k}{f_s} + \phi - \theta\right) - \frac{AB}{2}\sum_{n=0}^{K-1}\cos\left(2\pi f\frac{2n}{f_s} + \phi + 2\pi f\frac{k}{f_s} + \theta\right) \tag{6.7}$$

$$\lambda B\sin\left(2\pi f\frac{k}{f_s} + \theta\right) = \frac{ABK}{2}\cos\left(2\pi f\frac{k}{f_s} + \phi - \theta\right) - \frac{AB}{2}\sum_{n=0}^{K-1}\left\{\cos\left(2\pi f\frac{2n}{f_s} + \phi\right)\cos\left(2\pi f\frac{k}{f_s} + \theta\right) - \sin\left(2\pi f\frac{2n}{f_s} + \phi\right)\sin\left(2\pi f\frac{k}{f_s} + \theta\right)\right\} \tag{6.8}$$

$$\lambda B \sin\left(2\pi f \frac{k}{f_s} + \theta\right) = \frac{ABK}{2} \cos\left(2\pi f \frac{k}{f_s} + \phi - \theta\right) + \frac{AB}{2} \sin\left(2\pi f \frac{k}{f_s} + \theta\right) \sum_{n=0}^{K-1} \sin\left(2\pi f \frac{2n}{f_s} + \phi\right) - \frac{AB}{2} \cos\left(2\pi f \frac{k}{f_s} + \theta\right) \sum_{n=0}^{K-1} \cos\left(2\pi f \frac{2n}{f_s} + \phi\right) \quad (6.9)$$

$$\lambda B \sin\left(2\pi f \frac{k}{f_s} + \theta\right) = \frac{ABK}{2} \cos\left(2\pi f \frac{k}{f_s} + \phi - \theta\right) + \frac{AB}{2} \frac{\sin\left(2\pi f \frac{K}{f_s}\right)}{\sin\left(2\pi f \frac{1}{f_s}\right)} \sin\left(2\pi f \frac{K-1}{f_s} + \phi\right) \sin\left(2\pi f \frac{k}{f_s} + \theta\right) - \frac{AB}{2} \frac{\sin\left(2\pi f \frac{K}{f_s}\right)}{\sin\left(2\pi f \frac{1}{f_s}\right)} \cos\left(2\pi f \frac{K-1}{f_s} + \phi\right) \cos\left(2\pi f \frac{k}{f_s} + \theta\right) \quad (6.10)$$

Additionally, trace of the Hankel matrix X as [52],

$$\text{Tr}(X) = \sum_{n=0}^{K-1} x[2n] = \sum_{n=0}^{K-1} A \sin\left(2\pi f \frac{2n}{f_s} + \phi\right) \quad (6.11)$$

$$\text{Tr}(X) = A \frac{\sin\left(2\pi f \frac{K}{f_s}\right)}{\sin\left(2\pi f \frac{1}{f_s}\right)} \sin\left(2\pi f \frac{K-1}{f_s} + \phi\right) \quad (6.12)$$

Now, the relationship between the amplitude and phase shift of a sinusoidal signal $x[n] = A \sin\left(2\pi f \frac{n}{f_s} + \phi\right)$ and the eigenvalues and phase shift of eigenvectors of significant eigenvalue pair in EVDHM method, respectively, is derived with the help of following two theorems:

Theorem 6.2.1. *The eigenvalue pair and corresponding eigenvectors of the Hankel matrix X of a sinusoidal signal $x[n] = A \sin\left(2\pi f \frac{n}{f_s} + \phi\right)$ for $n = 0, 1, \ldots, N-1$ are $\left\{\frac{AK}{2}, -\frac{AK}{2}\right\}$ and $\left\{B \sin\left(2\pi f \frac{n}{f_s} + \frac{\phi}{2} + (4p+1)\frac{\pi}{4}\right), B \sin\left(2\pi f \frac{n}{f_s} + \frac{\phi}{2} + (4p+3)\frac{3\pi}{4}\right)\right\}$, respectively provided $K = \frac{\sigma N_0}{2}$, where $K = \frac{N+1}{2}$, p is an integer, σ is a positive integer, and $N_0 = \frac{f_s}{f}$ is the fundamental period of $x[n]$.*

Proof: For the case $K = \frac{\sigma N_0}{2}$, the value of $\sin\left(2\pi f \frac{K}{f_s}\right)$ in equation (6.10) becomes zero. Hence, equation (6.10) can be simplified as,

$$\lambda B \sin\left(2\pi f \frac{k}{f_s} + \theta\right) = \frac{ABK}{2} \cos\left(2\pi f \frac{k}{f_s} + \phi - \theta\right) \tag{6.13}$$

$$\lambda B \sin\left(2\pi f \frac{k}{f_s} + \theta\right) = (-1)^b \frac{ABK}{2} \sin\left(2\pi f \frac{k}{f_s} + \phi - \theta + (2b+1)\frac{\pi}{2}\right) \tag{6.14}$$

where b is an integer. For the equality to hold, $\lambda = (-1)^b \frac{AK}{2}$ and $\theta = \frac{\phi}{2} + (2b+1)\frac{\pi}{4}$ is necessary. The trace of a Hankel matrix obtained from a sinusoidal signal is equal to sum of its non-zero eigenvalues [52, 147]. Additionally, the number of non-zero eigenvalues is equal to two for a Hankel matrix of a sinusoidal signal, irrespective of the value of K [52, 226, 227], which implies to

$$\text{Tr}(X) = \lambda_1 + \lambda_2 \tag{6.15}$$

By putting $K = \frac{\sigma N_0}{2}$ in equation (6.12), $\text{Tr}(X) = 0 \implies \lambda_1 = -\lambda_2$. The only possible eigenvalues of X with the constraint $K = \frac{\sigma N_0}{2}$ becomes $-\frac{AK}{2}$ and $\frac{AK}{2}$ which is obtained by keeping b as odd value ($b = 2p$) and even value ($b = 2p+1$), respectively, where p is an integer. Hence, eigenvalue decomposition of a Hankel matrix X obtained from a sinusoidal signal $x[n]$ have a significant eigenvalue pair $\left\{\frac{AK}{2}, -\frac{AK}{2}\right\}$ and corresponding eigenvectors $\left\{B \sin\left(2\pi f \frac{n}{f_s} + \frac{\phi}{2} + (4p+1)\frac{\pi}{4}\right), B \sin\left(2\pi f \frac{n}{f_s} + \frac{\phi}{2} + (4p+3)\frac{\pi}{4}\right)\right\}$, respectively.

The eigenvalue pair of the Hankel matrix X_1 of a sinusoidal signal $x_1[n]$ for $n = 0, 1, \ldots, N-1$ defined by equation (6.16) is theoretically computed.

$$x_1[n] = A_1 \cos\left(2\pi f_1 \frac{n}{f_s} + \phi_1\right) \tag{6.16}$$

where $f_s = 100$ Hz. Additionally, the significant eigenvalue pair of $x_1[n]$ is obtained from EVDHM-based simulation. The theoretical and simulation results for different values of

Table 6.1: The significant eigenvalue pair for the sinusoidal signal $x_1[n]$ obtained using theoretical formula provided in Theorem 6.2.1 and using EVDHM-based simulation, with constraint $K = \frac{\sigma N_0}{2}$.

Parameters		Eigenvalue pair	
		Theoretical	Simulation
$A_1 = 0.94$, $f_1 = 20$ Hz, and $N = 99$	$\phi_1 = 0$	$\{-23.75, 23.75\}$	$\{-23.75, 23.75\}$
	$\phi_1 = \pi/7$	$\{-23.75, 23.75\}$	$\{-23.75, 23.75\}$
	$\phi_1 = \pi/4$	$\{-23.75, 23.75\}$	$\{-23.75, 23.75\}$
$A = 0.94$, $\phi = \pi/7$, and $N = 99$	$f = 25$ Hz	$\{-23.75, 23.75\}$	$\{-23.75, 23.75\}$
	$f = 30$ Hz	$\{-23.75, 23.75\}$	$\{-23.75, 23.75\}$
	$f = 35$ Hz	$\{-23.75, 23.75\}$	$\{-23.75, 23.75\}$
$f = 20$ Hz, $\phi = \pi/7$, and $N = 99$	$A = 0.5$	$\{-12.50, 12.50\}$	$\{-12.50, 12.50\}$
	$A = 0.75$	$\{-18.75, 18.75\}$	$\{-18.75, 18.75\}$
	$A = 1$	$\{-25.00, 25.00\}$	$\{-25.00, 25.00\}$
$A = 0.94$, $f = 20$ Hz, and $\phi = \pi/7$	$N = 39$	$\{-9.40, 9.40\}$	$\{-9.40, 9.40\}$
	$N = 49$	$\{-11.75, 11.75\}$	$\{-11.75, 11.75\}$
	$N = 59$	$\{-14.10, 14.10\}$	$\{-14.10, 14.10\}$

A_1, f_1, ϕ_1, and N considering $K = \frac{\sigma N_0}{2}$, that is, $N = \sigma N_0 + 1$, are provided in Table 6.1 for comparison. The comparison indicates that the magnitude of significant eigenvalues of a sinusoidal signal $x_1[n]$ does not change by varying frequency f_1 and phase shift ϕ_1. However, the magnitude of significant eigenvalues of the signal $x_1[n]$ is linearly dependent on its amplitude A_1 and the number of samples N, which is also confirmed by Theorem 6.2.1.

Theorem 6.2.2. *The significant eigenvalue pair and corresponding eigenvectors of the Hankel matrix X of a sinusoidal signal $x[n] = A\sin\left(2\pi f\frac{n}{f_s} + \phi\right)$ for $n = 0, 1, \ldots, N-1$ are $\left\{-\frac{A}{2}\left(K - \frac{\sin\left(2\pi f\frac{K}{f_s}\right)}{\sin\left(2\pi f\frac{1}{f_s}\right)}\right), \frac{A}{2}\left(K + \frac{\sin\left(2\pi f\frac{K}{f_s}\right)}{\sin\left(2\pi f\frac{1}{f_s}\right)}\right)\right\}$ and $\left\{B\sin\left(2\pi f\frac{n}{f_s} + \frac{\phi}{2} + (4p+1)\frac{\pi}{4}\right), B\sin\left(2\pi f\frac{n}{f_s} + \frac{\phi}{2} + (4p+3)\frac{\pi}{4}\right)\right\}$, respectively, provided $K = \frac{\sigma N_0}{4} + 1$ and $\phi = (2q+1)(\sigma+1)\frac{\pi}{2}$, where $K = \frac{N-1}{2}$; p, σ, and q are integers; and N_0 is the fundamental period of $x[n]$.*

Proof: For the case when $K = \frac{\sigma N_0}{4} + 1$ and $\phi = (2q+1)(\sigma+1)\frac{\pi}{2}$, the value of

$\cos\left(2\pi f\frac{K-1}{f_s}+\phi\right)$ becomes zero. Hence, equation (6.10) can be simplified as,

$$\lambda B\sin\left(2\pi f\frac{k}{f_s}+\theta\right)=\frac{ABK}{2}\cos\left(2\pi f\frac{k}{f_s}+\phi-\theta\right)+\frac{AB}{2}\frac{\sin\left(2\pi f\frac{K}{f_s}\right)}{\sin\left(2\pi f\frac{1}{f_s}\right)}\sin\left(2\pi f\frac{k}{f_s}+\theta\right) \quad (6.17)$$

$$\lambda B\sin\left(2\pi f\frac{k}{f_s}+\theta\right)=(-1)^b\frac{ABK}{2}\sin\left(2\pi f\frac{k}{f_s}+\phi-\theta+(2b+1)\frac{\pi}{2}\right)+\frac{AB}{2}\frac{\sin\left(2\pi f\frac{K}{f_s}\right)}{\sin\left(2\pi f\frac{1}{f_s}\right)}\sin\left(2\pi f\frac{k}{f_s}+\theta\right) \quad (6.18)$$

The equality holds if,

$$\lambda=\frac{A}{2}\left((-1)^bK+\frac{\sin\left(2\pi f\frac{K}{f_s}\right)}{\sin\left(2\pi f\frac{1}{f_s}\right)}\right)\text{ and }\theta=\frac{\phi}{2}+(2b+1)\frac{\pi}{4} \quad (6.19)$$

A Hankel matrix X obtained from the sinusoidal signal $x[n]$ has two non-zero eigenvalues [51]. Hence, $\text{Tr}(X)=\lambda_1+\lambda_2$. By putting constraints $K=\frac{\sigma N_0}{4}+1$ and $\phi=(2q+1)(\sigma+1)\frac{\pi}{2}$ in equation (6.12) and comparing with $\text{Tr}(X)=\lambda_1+\lambda_2$, the sum of two non-zero eigenvalues of X is,

$$\lambda_1+\lambda_2=A\frac{\sin\left(2\pi f\frac{K}{f_s}\right)}{\sin\left(2\pi f\frac{1}{f_s}\right)} \quad (6.20)$$

The aforementioned equality holds if one of the eigenvalues obtained considering even values of b and other one considering odd value of b in equation (6.19), i.e., $\lambda_1=\frac{A}{2}\left(K+\frac{\sin\left(2\pi f\frac{K}{f_s}\right)}{\sin\left(2\pi f\frac{1}{f_s}\right)}\right)$ and $\lambda_2=\frac{A}{2}\left(-K+\frac{\sin\left(2\pi f\frac{K}{f_s}\right)}{\sin\left(2\pi f\frac{1}{f_s}\right)}\right)$ and their respective eigenvectors are $B\sin\left(2\pi f\frac{n}{f_s}+\frac{\phi}{2}+(4p+1)\frac{\pi}{4}\right), B\sin\left(2\pi f\frac{n}{f_s}+\frac{\phi}{2}+(4p+3)\frac{\pi}{4}\right)$.

The significant eigenvalue pair of the Hankel matrix X_1 of signal $x_1[n]$ for $n=$

Table 6.2: The significant eigenvalue pair of the sinusoidal signal $x_1[n]$ obtained using theoretical formula provided in Theorem 6.2.2 and using simulation based on EVDHM, with constraints $K = \frac{\sigma N_0}{4} + 1$ and $\phi = (2q+1)(\sigma+1)\frac{\pi}{2}$.

Parameters		Eigenvalue pair	
		Theoretical	Simulation
$A_1 = 0.9$, $N = 41$, and $f_1 = 2.5$ Hz	$\phi_1 = \pi/2$	$\{-9.00, 9.90\}$	$\{-9.00, 9.90\}$
	$\phi_1 = 3\pi/2$	$\{-9.90, 9.00\}$	$\{-9.90, 9.00\}$
$A = 0.9$, $\phi = \pi$, and $N = 61$	$f = 2.5$ Hz	$\{-16.7912, 11.1088\}$	$\{-16.7912, 11.1088\}$
	$f = 7.5$ Hz	$\{-14.8332, 13.0668\}$	$\{-14.8332, 13.0668\}$
$\phi = \pi$, $N = 61$, and $f = 7.5$ Hz	$A = 0.4$	$\{-6.5925, 5.8075\}$	$\{-6.5925, 5.8075\}$
	$A = 0.7$	$\{-11.5369, 10.1631\}$	$\{-11.5369, 10.1631\}$
$A = 0.9$, $f = 2.5$ Hz, and $\phi = \pi/2$	$N = 81$	$\{-18.00, 18.90\}$	$\{-18.00, 18.90\}$
	$N = 121$	$\{-27.00, 27.90\}$	$\{-27.00, 27.90\}$

$0, 1, \ldots, N-1$ defined by equation (6.16) is theoretically calculated. Additionally, the significant eigenvalue pair of $x_1[n]$ is obtained using EVDHM-based simulation. The eigenvalues of $x_1[n]$, with constraints $K = \frac{\sigma N_0}{4} + 1$ and $\phi = (2q+1)(\sigma+1)\frac{\pi}{2}$, obtained using theoretical calculation and EVDHM-based simulation are provided in Table 6.2 for comparison. The comparison in Table 6.2 indicates that magnitude of the significant eigenvalue pair of a sinusoidal signal changes with the change in its amplitude A_1, signal length N, and frequency f_1. This satisfies the relationship between eigenvalues of a sinusoidal with its parameters provided in Theorem 6.2.

However, the MMSEP ($\frac{1}{2}(|\lambda_1| + |\lambda_2|)$) of the Hankel matrix X of a sinusoidal signal $x[n]$ is equal to $\frac{AK}{2}$ for either $K = \frac{\sigma N_0}{2}$ or $K = \frac{\sigma N_0}{4} + 1$ and $\phi = (2q+1)(\sigma+1)\frac{\pi}{2}$. Furthermore, the relationship between MMSEP computed from EVDHM-based simulation and parameter $\frac{A_1 K}{2}$ for a sinusoidal signal $x_1[n]$, without imposing any constraint on K, is studied by varying the signal parameters A_1, f_1, and N. The results are shown in Fig. 6.1. Figures 6.1(a) and (b) show that the MMSEP of $x_1[n]$ obtained from simulation closely follows the $\frac{A_1 K}{2}$, when varying A_1 and N, respectively. However, Fig. 6.1(c) shows that the MMSEP of $x_1[n]$ obtained from the simulation closely follows the $\frac{A_1 K}{2}$ curve as f_1 varies,

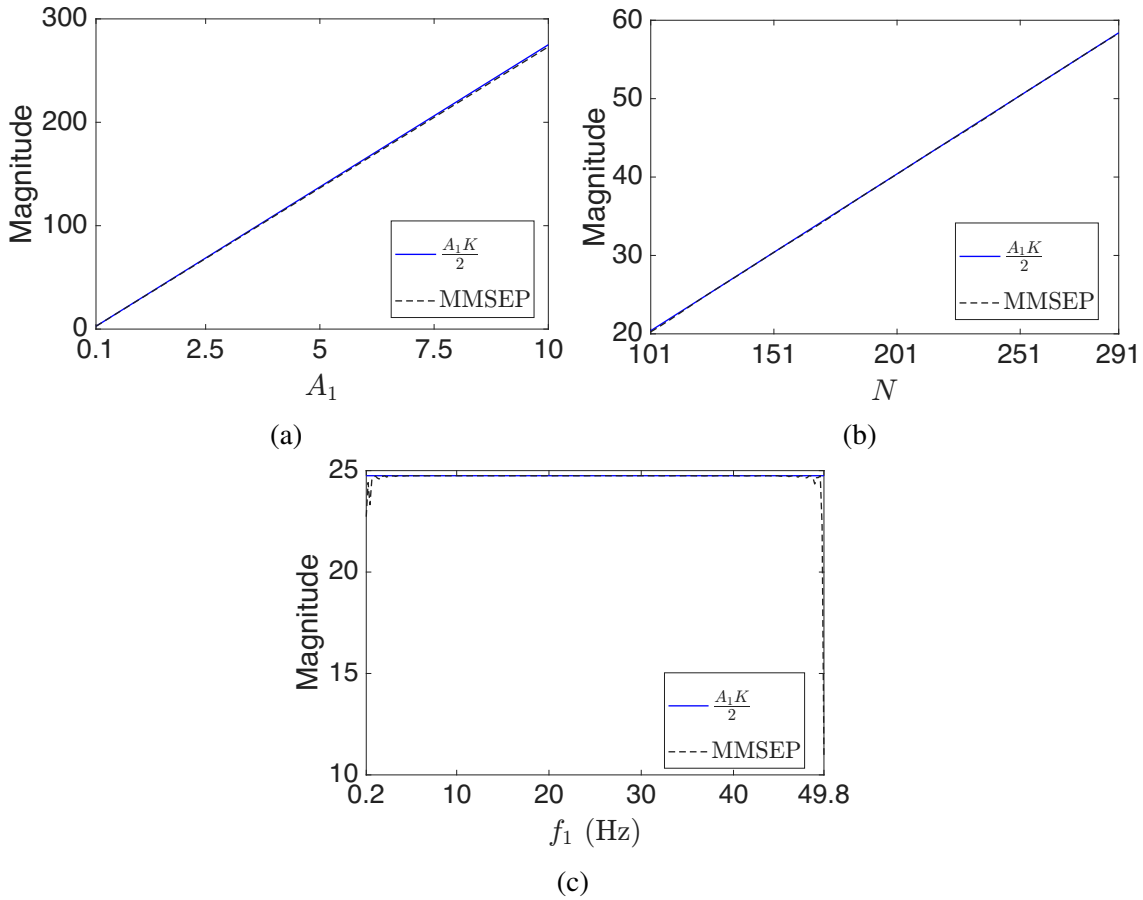

Figure 6.1: Comparison of MMSEP of signal $x_1[n]$ obtained from simulation and $\frac{A_1K}{2}$ by varying signal parameters A_1, N, and f_1 are shown in (a), (b), and (c), respectively.

except at very low and very high frequencies. Hence, it can be concluded that MMSEP of a sinusoidal signal $x[n]$ closely approximates the parameter $\frac{AK}{2}$.

6.3 Time-varying eigenvalues-based time-frequency distribution

This section presents a new technique to obtain TFD of a signal using short-duration EVDHM. The signal is segmented into small duration signal frames using a rectangular window, considering signal is stationary within the window duration. Each frame is decomposed using EVDHM-based method, and MMSEPs are computed. The MMSEPs are

then represented in the time-frequency plane based on the mean frequency and bandwidth of their respective signal components. The detailed method to obtain the TFD of a signal $x[n]$ for $n = 0, 1, \ldots, N-1$ is presented with the help of the following steps:

Step 1: The i^{th} frame of the signal $x[n]$ is computed as $x^{(i)}[n] = x[(i-1)N_s + n]$ for $n = 1, 2, \ldots, N_w - 1$ where $N_s = N_w - N_o$, N_w is the length of the window, and N_o is the overlap length.

Step 2: The Hankel matrix $X^{(i)}$ is computed from $x^{(i)}[n]$ using Step 1 described in Section 2.1 [51].

Step 3: The EVD of the matrix $X^{(i)}$ is computed to obtain the set of eigenvectors ($u_1^{(i)}$, $u_2^{(i)}$, $\ldots$, $u_K^{(i)}$) and the corresponding eigenvalues ($\lambda_1^{(i)}$, $\lambda_2^{(i)}$, $\ldots$, $\lambda_K^{(i)}$) with the help of Step 2 described in Section 2.1 [51].

Step 4: The set of significant eigenvalue pairs is obtained using Step 3 described in Section 2.2 [52]. In this study, the value of STP is considered as 10%. Furthermore, the symmetric matrix ($X_l^{(i)}$) corresponding to l^{th} eigenvalue pair $\{\lambda_l^{(i)}, \lambda_{K-l+1}^{(i)}\}$ is computed using Step 4 described in Section 2.1.

Step 5: The signal component corresponding to the l^{th} eigenvalue pair is obtained by averaging the skew diagonal elements of $X_l^{(i)}$ using Step 5 described in Section 2.1 [51].

Step 6: The mean frequency and 3 dB bandwidth of the signal components obtained from significant eigenvalue pairs, which represent its characteristics in the frequency domain. The mean frequency of the signal components is computed using the following

mathematical expressions [78]:

$$\text{MNF}_l^{(i)} = \frac{\sum_{k=0}^{k_1} f_k |X_l^{(i)}[k]|^2}{\sum_{k=0}^{k_1} |X_l^{(i)}[k]|^2} \tag{6.21}$$

where $k_1 = \frac{N_w+1}{2}$, $f_k =$, and $X_l^{(i)}[k]$ is the discrete Fourier transform of the signal $x_l^{(i)}[n]$. Furthermore, the 3 dB bandwidth ($\text{BW}_l^{(i)}$) of the decomposed component ($x_l^{(i)}[n]$) is computed.

Step 7: The MMSEP is directly associated with the amplitude of a sinusoidal signal as discussed in Section 6.2. Hence, the MMSEP is used for the time-frequency representation. Additionally, the mean frequency and the 3 dB bandwidth of signal component corresponding to significant eigenvalue pair are used to accurately localize the respective MMSEP in the frequency domain. The TFD is computed as follows:

$$X[i,\zeta] = \sum_{l=1}^{L} \frac{\left|\lambda_l^{(i)}\right| + \left|\lambda_{K-l+1}^{(i)}\right|}{2} \delta[\zeta - \zeta_l], \text{ for } \text{MNF}_l^{(i)} - \frac{\text{BW}_l^{(i)}}{2} \leq \zeta_l \leq \text{MNF}_l^{(i)} + \frac{\text{BW}_l^{(i)}}{2} \tag{6.22}$$

where $|\cdot|$ provides the absolute value and $\delta[\cdot]$ is the Kronecker delta function.

The process from Step 1 to Step 7 is repeated for all the frames in order to obtain the complete TFD of the signal $x[n]$.

6.4 Results and discussion

In the proposed technique, the selection of window size controls the TFD resolution. For the same, an analysis of TFD obtained from the proposed technique is performed by varying the window size. Furthermore, the TFDs of a synthetic and a real-life signal obtained using the proposed technique are presented and compared with the methods from the literature.

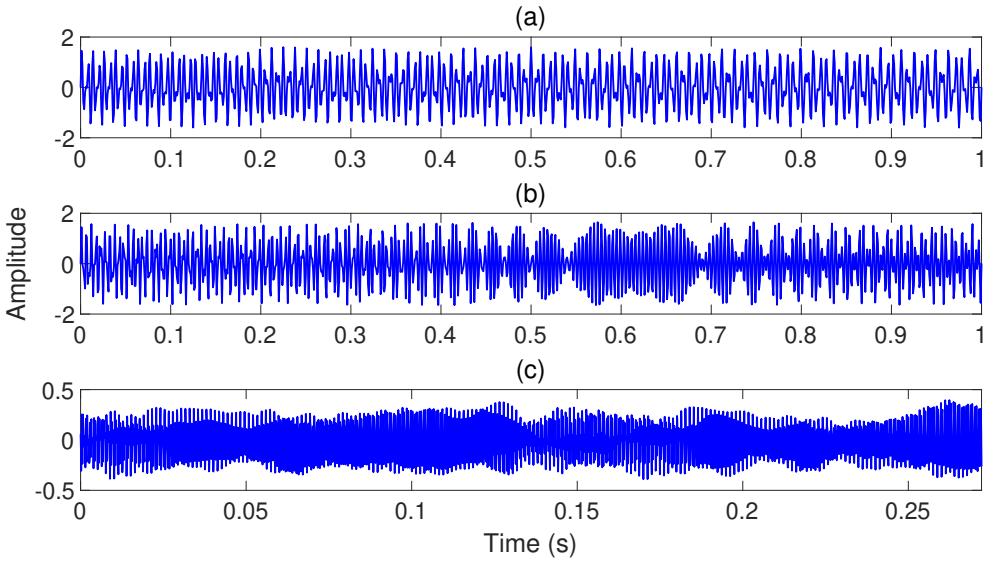

Figure 6.2: Time-domain representation of the $x_2[n]$, $x_3[n]$, and real-life cello note signal are shown in (a), (b), and (c), respectively.

6.4.1 Study on effect of window size on time-frequency distribution

In this study, a synthetic multicomponent signal $x_1[n]$ consisting of two linearly FM mono-component signals is considered for analysis which is represented as follows:

$$x_1[n] = 0.9\sin\left(2\pi\left(160 - 15\frac{n}{f_s}\right)\frac{n}{f_s}\right) + 0.7\sin\left(2\pi\left(240 - 15\frac{n}{f_s}\right)\frac{n}{f_s}\right) \tag{6.23}$$

where $n = 0, 1, 2, \ldots, 1000$ and $f_s = 1000$ Hz. The time-domain representation and the reference TFD of the signal $x_1[n]$ are shown in Fig. 6.2(a) and 6.3(a), respectively. The TFDs of the signal obtained using the proposed technique with window sizes 71, 91, 111, 131, and 151 samples are shown in Figs. 6.3(b)–(f), respectively. From the aforementioned figures, it can be observed that the resolution of the TFD obtained using the proposed technique is poor for small-duration windows and high for large-duration windows. Furthermore, it can be observed that an increase in the window size leads to an increase in the magnitude of the respective eigenvalue of a particular component. This may happen because of the linear proportionality of the eigenvalue of a sinusoidal with the window size.

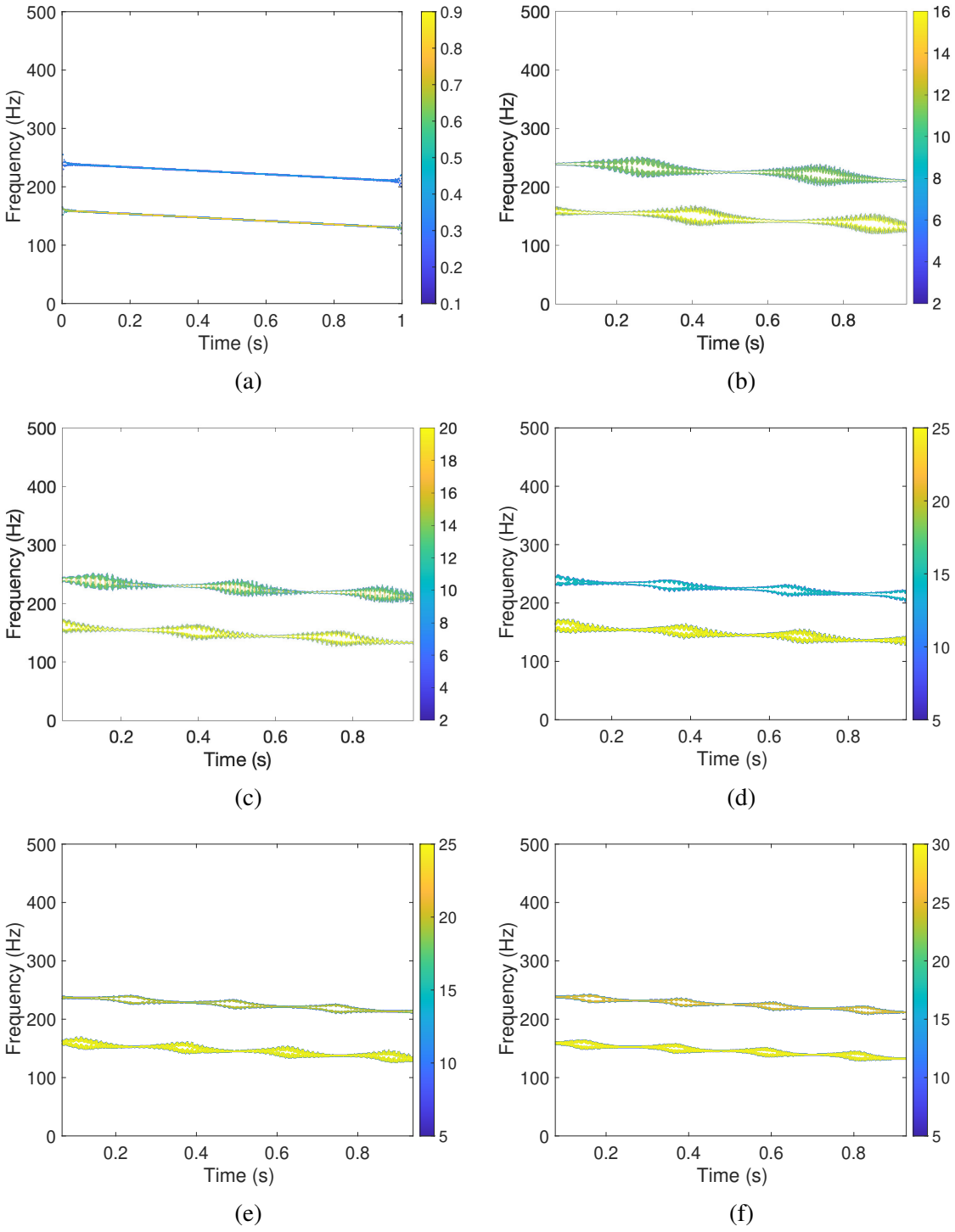

Figure 6.3: The reference TFD of the signal $x_2[n]$ is shown in (a). The TFDs of $x_1[n]$ obtained using the proposed technique with window lengths $W = 71, 91, 111, 131$, and 151 samples are shown in (b)–(f), respectively.

6.4.2 Comparison with methods from literature

In this subsection, the TFDs of synthetic and real-life signals obtained using proposed technique are compared with TFDs provided by spectrogram, scalogram, FSST, and VMD-based HSA. For the computation of the scalogram, the Morse wavelet with symmetry parameter $\gamma = 3$ is considered. The VMD parameters used for analysis are absolute tolerance $= 5 \times 10^{-6}$, penalty factor = 1000, and Lagrange multiplier update rate $= 0.01$. The FSST is computed using the MATLAB code provided at `https://github.com/phamduonghung/FSSTn` [224]. For this study, a synthetic signal consisting of two linear chirp signals is considered and an audio signal is considered. The detailed analysis is presented in the following subsubsections:

6.4.2.1 Synthetic signal

A synthetic signal $x_2[n]$ for $n = 0, 1, 2, \ldots, N$ is considered for analysis is defined as,

$$x_2[n] = 0.95 \sin\left(2\pi\left(190 + 40\frac{n}{f_s}\right)\frac{n}{f_s}\right) + 0.7 \sin\left(2\pi\left(350 - 90\frac{n}{f_s}\right)\frac{n}{f_s}\right) \tag{6.24}$$

where $N = 1000$ and $f_s = 1000$ Hz. The time-domain representation of the signal $x_2[n]$ is shown in Fig. 6.2(b). The TFD of the signal obtained using the proposed technique, spectrogram, scalogram, FSST, and VMD-based HSA techniques are shown in Fig. 6.4. For spectrogram computation, the Hamming window of length 125 samples with an overlap of 124 samples is considered. In Fig. 6.4, the resolution of the scalogram is the poorest among the compared techniques. The VMD-HSA-based TFD is not consistent, i.e., some of the information is not preserved in the TFD. The spectrogram, FSST, and proposed technique are able to obtain proper TFD of the signals among these; the resolution of TFD obtained using the proposed technique is highest.

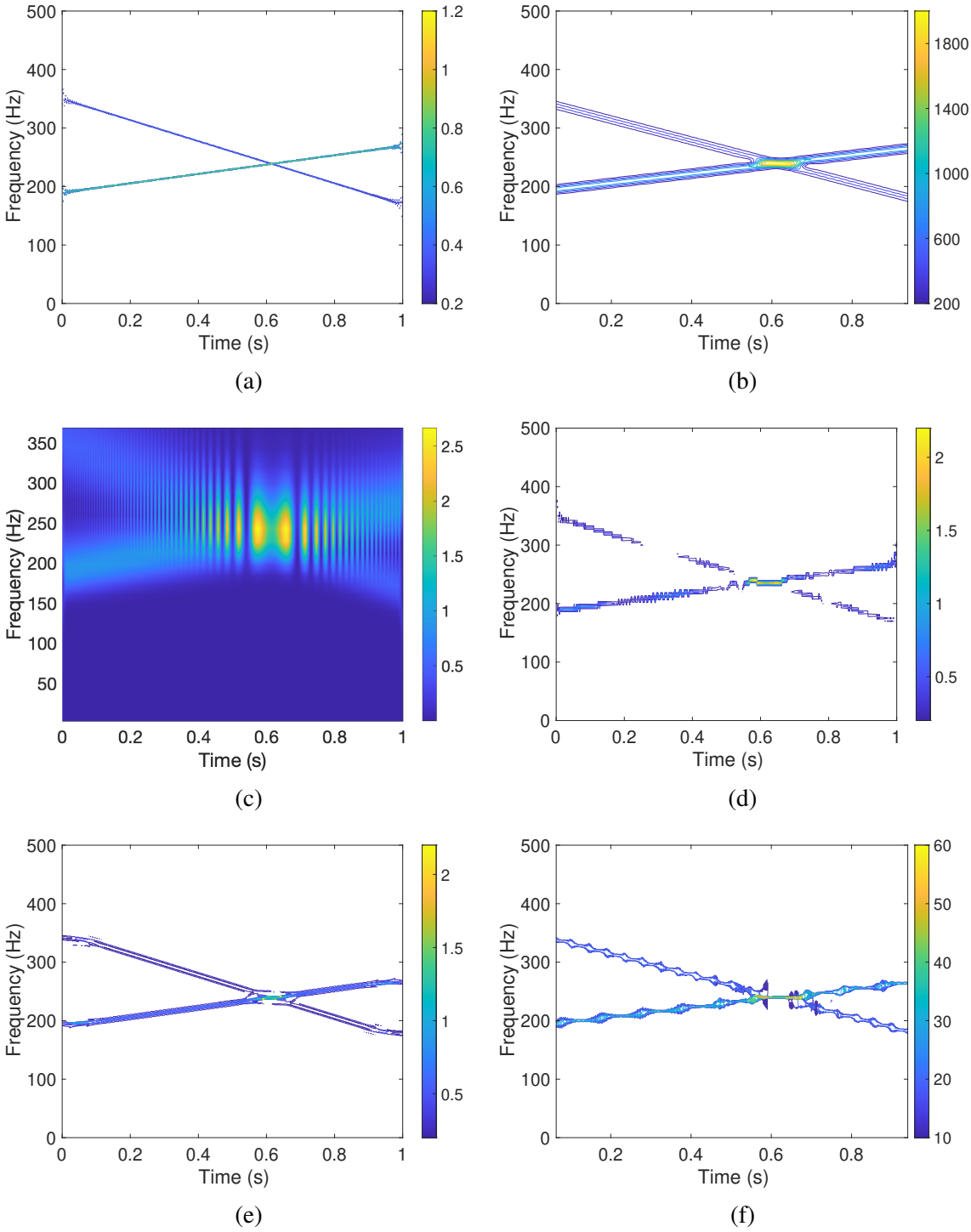

Figure 6.4: Reference TFD of the signal $x_3[n]$ is shown in (a) and its corresponding TFDs obtained using STFT, CWT, VMD and HSA, FSST-based techniques, and proposed technique are shown in (b), (c), (d), (e), and (f), respectively.

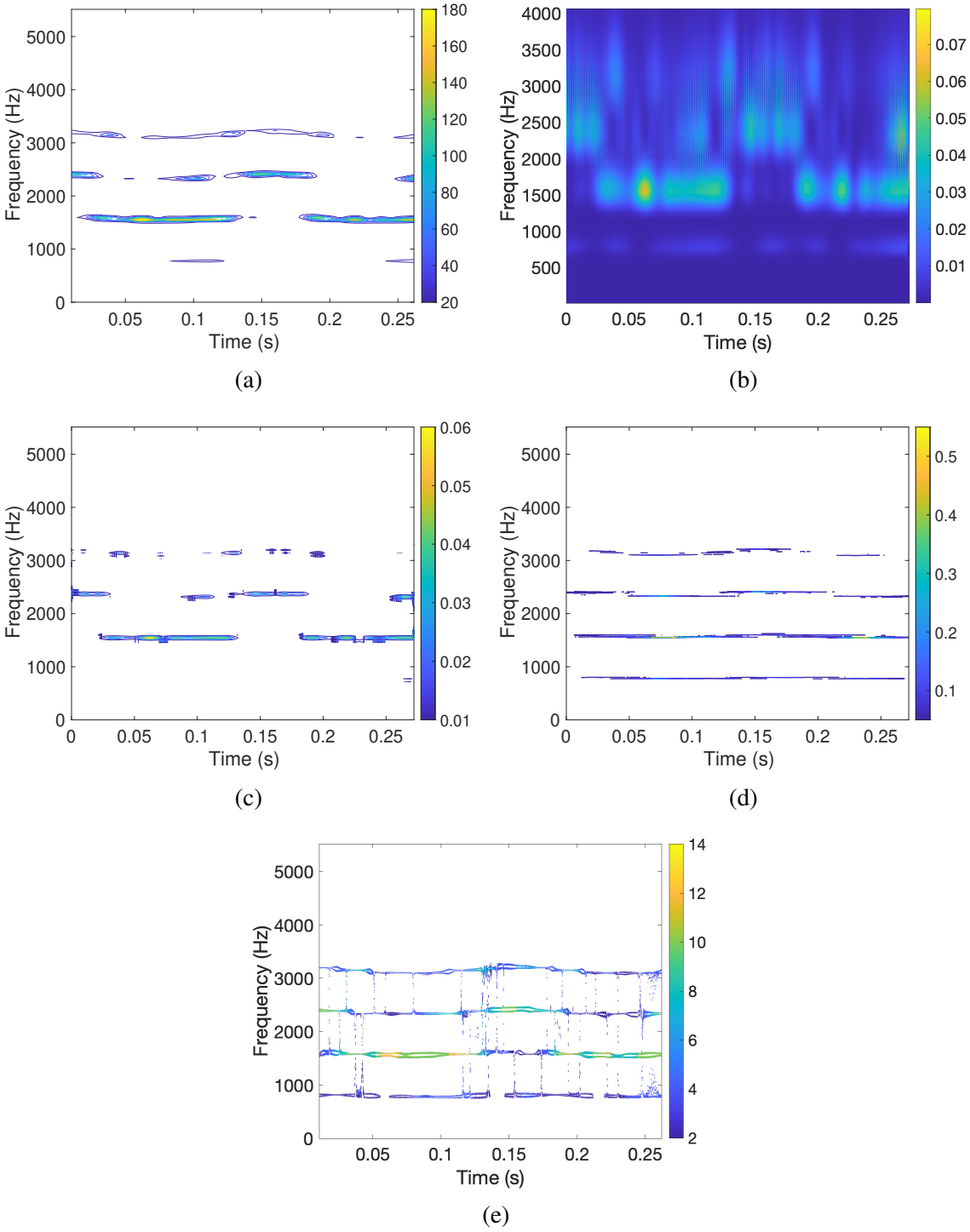

Figure 6.5: The TFD of a real-life cello G5 note signal obtained using (a) spectrogram, (b) scalogram, (c) VMD-based HSA technique, (d) FSST, and (e) proposed EVDHM-based technique.

6.4.2.2 Real-life signal

For validation of the proposed technique on real-life signals, an audio signal corresponding to cello G5 note [50] is considered which is shown in Fig. 6.2(c). The sampling rate of the considered signal is 11025 Hz and has 3001 samples. The signal is provided along with the ASTRES toolbox which can be downloaded from `https://github.com/dfourer/ASTREStoolbox` [192]. The spectrogram, scalogram, TFD-based on VMD and HSA-technique, FSST, and TFD-based on the proposed technique are presented in Fig. 6.5. A Hamming window of size 231 samples and an overlap length of 230 samples is considered for the computation of the spectrogram of the signal. In the spectrogram and TFD based on the VMD and HSA of the signal, the lowest frequency component is not correctly represented as in the remaining TFDs. Furthermore, the scalogram, FSST, and TFD obtained using the proposed technique are able to represent all the components of the signal in the TFD. Still, the resolution of the scalogram is poor among the studied methods. Also, the FSST is not able to reflect the energy changes over time of the components whereas the proposed TFD is able to do so. Hence, the proposed technique shows better resolution of the components of the signal in time-frequency plane among the compared methods.

6.5 Summary

In this chapter, the expression of the significant eigenvalues of the Hankel matrix of a sinusoidal signal are derived. The obtained eigenvalues and corresponding eigenvectors are found to be dependent on the parameters of the sinusoidal signal. Furthermore, the MMSEP of the Hankel matrix of the sinusoidal signal is observed to be proportional to amplitude and length of the sinusoidal signal, i.e., MMSEP can be used to represent the strength of a sinusoidal signal. Motivated from this, the short-duration EVDHM-based new method to

obtain the TFD of a signal is proposed in which the MMSEPs of the windowed signal are represented in the time-frequency plane. Furthermore, the effect of the length of the analysis window on the obtained TFD is analyzed using a synthetic signal. Also, the TFD obtained from the proposed technique is compared with the spectrogram, scalogram, FSST, and TFR obtained from VMD and HSA-based techniques for a synthetic and real-life signal. The proposed technique provided better component representation in the time-frequency domain as compared to the compared methods.

Chapter 7

Computationally efficient eigenvalue decomposition of Hankel matrix for signal decomposition

7.1 Introduction

Several applications of biomedical signal processing like atrial fibrillation detection from ECG signals [228, 229], seizure detection from EEG signals [230–232], etc. require the processing of the physiological signals in real-time with low computational complexity. Also, there has been a demand for biomedical signal processing systems on wearable devices [229]. However, these devices have limited computational resources. To fulfill these requirements, there have been several efforts in literature to develop computationally efficient signal processing methods.

In [8], a faster method is provided to compute the DFT coefficients of a signal. The traditional N-point DFT method requires N^2 number of operations where the method proposed in [8] requires number of operations proportional to $N \log N$ by factoring the DFT matrix of size $N \times N$ into m sparse matrices, where value of m is proportional to $\log N$.

In [233], the serial EMD method is proposed to decompose the multichannel signals requiring less computation time as compared to multivariate EMD. In serial EMD, the multichannel signal is concatenated which is decomposed using EMD. The decomposed IMFs are then reshaped to obtain the multivariate IMFs. In [93], the multivariate fast iterative filtering is proposed to decompose the multichannel signals into mode-aligned modes. The aforementioned method was found to be very computationally efficient when compared with multivariate EMD and multivariate VMD. The grasp motor imagery identification task has been successfully performed by using multivariate fast iterative filtering method from EEG signals [234]. Furthermore, the multivariate iterative filtering is proposed which is based on obtaining common filter length for all the channels of the multichannel signal and found to be more computationally efficient than multivariate fast iterative filtering [78]. Later, it has been applied to schizophrenia detection from EEG signals.

The EVDHM-based method has shown its suitability in various biomedical tasks like seizure detection from EEG signals [53], amyotrophic lateral sclerosis and myopathy classification based on EMG signals [156], etc. In this work, a faster alternative of EVDHM, termed as CEEVDHM, is proposed to decompose the signal into components using the concepts of EVD and convolution. In this chapter, two approaches for CEEVDHM are proposed one based on time-domain convolution and the other based on frequency-domain multiplication. The computation time required to decompose synthetic and real-valued signals using CEEVDHM is studied and compared with computation time required by EVDHM method for various signal lengths. Furthermore, decomposed components obtained from CEEVDHM-based signal decomposition are compared with EVDHM-based components.

7.2 Computationally efficient eigenvalue decomposition of Hankel matrix

In this section, the proposed fast alternative of EVDHM, i.e., the CEEVDHM method, is discussed. To improve the computational complexity of the EVDHM method, the symmetric matrix computation and averaging of skew diagonal element steps are proposed to replace with a convolution-based approach, which is motivated from study in [146]. The derivation for the same is provided in this section. Consider a signal $x[n]$ for $n = 0, 1, 2, \ldots, N-1$, the decomposition of the signal $x[n]$ using the proposed approach is mentioned as follows:

The Hankel matrix X of the signal $x[n]$ for $n = 0, 1, \ldots, N-1$ is obtained using Step 1 mentioned in Section 2.1. The eigenvalues $(\lambda_1, \lambda_2, \ldots, \lambda_K)$ and corresponding eigenvectors $(u_1, u_2, \ldots, u_K)$ of the matrix X are obtained using EVD with the help of Step 2 defined in Section 2.1 [51]. Thereafter, all the eigenvalue pairs are considered significant eigenvalue pairs in this study, i.e., $(\lambda_i, \lambda_{K-i+1})$ for $i = 1, 2, \ldots, \lfloor \frac{K}{2} \rfloor$. The next two steps to obtain i^{th} signal component $x_i[n]$ corresponding to i^{th} eigenvalue pair $(\lambda_i, \lambda_{K-i+1})$ is symmetric matrix computation followed by averaging of skew diagonal elements (as described in steps Step 4 and Step 5 of section 2.1). However, motivated from study in [146], a faster alternative of component extraction from eigenvalue pairs is derived based on convolution of eigenvectors. The same is discussed below in detail. The symmetric corresponding to the i^{th} eigenvalue (λ_i) is computed as, $\tilde{X}_i = \lambda_i u_i \left(u_i\right)^T$ is represented using equation (7.1).

$$\tilde{X}_i = \lambda_i \begin{bmatrix} u_i[0]u_i[0] & u_i[0]u_i[1] & \ldots & u_i[0]u_i[K-1] \\ u_i[1]u_i[0] & u_i[1]u_i[1] & \ldots & u_i[1]u_i[K-1] \\ \vdots & \vdots & \ddots & \vdots \\ u_i[K-1]u_i[0] & u_i[K-1]u_i[1] & \ldots & u_i[K-1]u_i[K-1] \end{bmatrix} \tag{7.1}$$

Here, the eigenvector u_i, a sequence of length K, is denoted as $u_i[n]$ for $n = 0, 1, \ldots, K-1$. The component $\tilde{x}_i[n]$ corresponding to eigenvalue λ_i is obtained by performing averaging of skew-diagonal elements of $\tilde{X}_i$. The same is represented using equation (7.2).

$$\tilde{x}_i[n] = \lambda_i \begin{bmatrix} u_i[0]u_i[0] & \frac{1}{2}u_i[0]u_i[1] & \frac{1}{3}u_i[0]u_i[2] & \ldots & \\ & + & + & & \\ & \frac{1}{2}u_i[1]u_i[0] & \frac{1}{3}u_i[1]u_i[1] & \ldots & \\ & & + & & \\ & & \frac{1}{3}u_i[2]u_i[0] & \ldots & \\ & & & \ddots & \\ & & & \ldots & u_i[K-1]u_i[K-1] \end{bmatrix} \tag{7.2}$$

where $\tilde{x}_i[n]$ is λ_i times n^{th} indexed element of row matrix on right hand side. The averaging factor for each value of n is taken outside the matrix which is defined by $w[n]$ as,

$$w[n] = \begin{cases} \frac{1}{n+1}, & \text{if } 0 \leq n \leq K-1 \\ \frac{1}{N-n}, & \text{if } K \leq n \leq N-1 \end{cases} \tag{7.3}$$

Now, the component $\tilde{x}_i[n]$ is represented as,

$$\tilde{x}_i[n] = \lambda_i w[n] \begin{bmatrix} u_i[0]u_i[0] & u_i[0]u_i[1] & u_i[0]u_i[2] & \ldots & \\ & + & + & & \\ & u_i[1]u_i[0] & u_i[1]u_i[1] & \ldots & \\ & & + & & \\ & & u_i[2]u_i[0] & \ldots & \\ & & & \ddots & \\ & & & \ldots & u_i[K-1]u_i[K-1] \end{bmatrix} \tag{7.4}$$

In the aforementioned equation, the term inside the matrix is linear convolution $u_i[n]$ with

itself which is described by equation (7.5).

$$\tilde{x}_i[n] = \lambda_i w[n] \left(u_i[n] * u_i[n]\right) \tag{7.5}$$

Similarly, the i^{th} signal component corresponding to i^{th} eigenvalue pair $(\lambda_i, \lambda_{K-i+1})$ is obtained as,

$$x_i[n] = w[n]((\lambda_i \left(u_i[n] * u_i[n]\right) + \lambda_{K-i+1} \left(u_{K-i+1}[n] * u_{K-i+1}[n]\right)) \tag{7.6}$$

The computation of $x_i[n]$ using equation (7.6) can be performed using two approaches, i.e., time-domain or frequency-domain, depending on whether convolution is performed in time-domain or frequency-domain, respectively.

Time-domain-based approach: The i^{th} signal component corresponding to the eigenvalue pair $(\lambda_i, \lambda_{K-i+1})$ can be obtained by performing the convolution operation of equation (7.6) in time-domain as [235, 236],

$$x_i[n] = w[n] \left(\lambda_i \sum_{m=0}^{N-1} u_i[m] u_i[(n-m)_N] + \lambda_{K-i+1} \sum_{m=0}^{N-1} u_{K-i+1}[m] u_{K-i+1}[(n-m)_N] \right) \tag{7.7}$$

where $N = 2K - 1$.

Frequency-domain-based approach: The linear convolution of two sequences of length K samples can be performed in the frequency-domain by multiplying N-point DFT coefficients followed by inverse DFT [237]. Hence, the extraction of the signal component corresponding to the eigenvalue pair $(\lambda_i, \lambda_{K-i+1})$ can be obtained as,

$$x_i[n] = w[n] \left(\lambda_i \sum_{k=0}^{N-1} U_i[k] U_i[k] e^{j2\pi \frac{nk}{N}} + \lambda_{K-i+1} \sum_{k=0}^{N-1} U_{K-i+1}[k] U_{K-i+1}[k] e^{j2\pi \frac{nk}{N}} \right) \tag{7.8}$$

where $U_i[k] = \sum_{n=0}^{N-1} u_i[n] e^{-j2\pi \frac{nk}{N}}$ is N-point DFT of $u_i[n]$.

The signal $x[n]$ can be represented as sum of decomposed components $x_i[n]$ as,

$$x[n] = \sum_{i=1}^{\lfloor \frac{K}{2} \rfloor} x_i[n] \tag{7.9}$$

The proposed method with time-domain-based approach is named as TDA-CEEVDHM, and with frequency-domain-based approach is named as FDA-CEEVDHM.

7.3 Results and discussion

The computation time obtained from the proposed method is compared with the EVDHM method (as described in section 2.1). Additionally, the average of the total squared error of the decomposed components obtained from CEEVDHM and EVDHM is computed for the studied signals to evaluate the similarity between the extracted components using both methods. For the simulation study, two synthetic signals (with sampling frequency $f_s = 1000$ Hz) and a real-life speech signal (with sampling frequency $f_s = 32000$ Hz) are considered.

7.3.1 Comparison of asymptotic complexity

In this subsection, the asymptotic computational complexity of the proposed methods (TDA- and FDA-CEEVDHM) and EVDHM method is provided in Table 7.1 for comparison. All three compared methods have two common steps, i.e., embedding and EVD. The embedding and EVD steps have complexity of $\mathcal{O}(K^2)$ [146] and $\mathcal{O}(K^3)$ [238], respectively. Then, the EVDHM method requires two more steps to obtain the decomposed components, i.e., symmetric matrix generation and diagonal averaging with each having computational complexities $\mathcal{O}(K^3)$ [146]. However, these two steps are replaced with time-domain convolution having complexity of $\mathcal{O}(K^3)$ in TDA-CEEVDHM and frequency-

Table 7.1: Asymptotic computational complexity of the EVDHM and proposed CEEVDHM methods.

Method	Embedding	EVD	Symmetric matrix generation	Diagonal averaging
EVDHM	$\mathcal{O}\left(K^2\right)$	$\mathcal{O}\left(K^3\right)$	$\mathcal{O}\left(K^3\right)$	$\mathcal{O}\left(K^3\right)$
TDA-CEEVDHM			$\mathcal{O}\left(K^3\right)$	
FDA-CEEVDHM			$\mathcal{O}\left(K^3\right)$	

domain multiplication having complexity of $\mathcal{O}\left(K^3\right)$ in FDA-CEEVDHM. The proposed method reduces computational complexity by replacing two steps of complexity $\mathcal{O}\left(K^3\right)$ with a single step of complexity $\mathcal{O}\left(K^3\right)$. Furthermore, the computational complexity of the proposed method in term of run time is studied in next Section 7.3.2.

7.3.2 Comparison of computational time

Synthetic multicomponent signals $x[n]$ and $y[n]$ for $n = 0, 1, \ldots, N-1$ are considered for this analysis. The signal $x[n]$ is mathematically described by,

$$x[n] = \sin\left(40\pi\frac{n}{f_s}\right) + 0.8\sin\left(100\pi\frac{n}{f_s}\right) + 0.78\sin\left(160\pi\frac{n}{f_s}\right) + 0.65\sin\left(170\pi\frac{n}{f_s}\right) + 0.59\sin\left(220\pi\frac{n}{f_s}\right) + 0.5\sin\left(300\pi\frac{n}{f_s}\right) \quad (7.10)$$

Whereas, the signal $y[n]$ is mathematically defined as,

$$y[n] = 0.9\sin\left(20\pi\frac{n}{f_s}\right) + 0.6\sin\left(2\pi\left(40 + 16\frac{n}{f_s}\right)\frac{n}{f_s}\right) \quad (7.11)$$

Furthermore, a speech signal taken from CMU ARCTIC speech database [1] is also considered for this study. These signals are decomposed using EVDHM, TDA-CEEVDHM, and FDA-CEEVDHM methods considering all the eigenvalue pairs as significant, for various signal lengths, i.e., $N = 1001, 2001, 3001, 4001$, and 5001. The time-domain representations of the considered signals with $N = 5001$ samples are shown in Fig. 7.1.

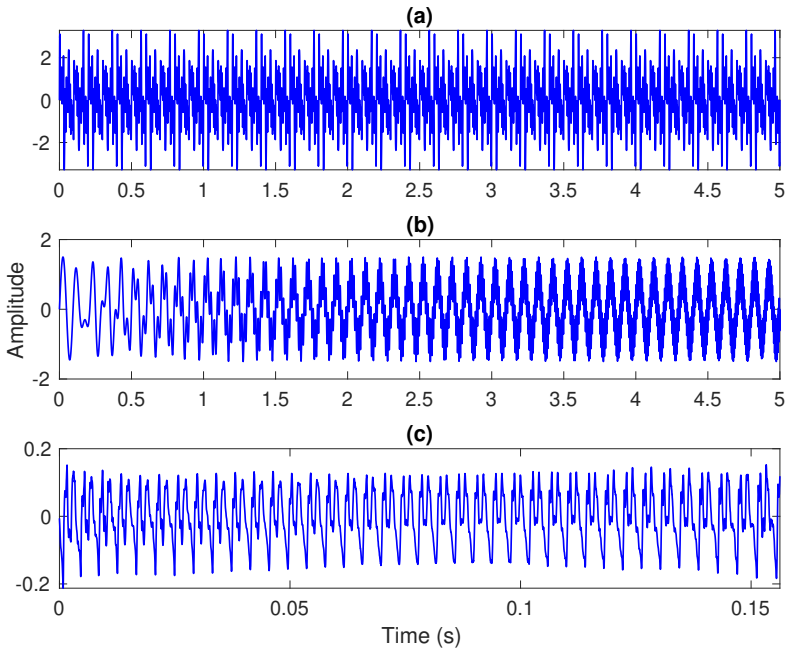

Figure 7.1: The synthetic signals $x[n]$ and $y[n]$ are plotted in (a) and (b), respectively. The speech signal is shown in (c).

The computation time required to decompose the signal is provided in Table 7.2. The simulations are performed on a Dell Optiplex 9020 system with 28 GB RAM. The mean and standard deviation of the computation times for the three studied signals at a given signal length are calculated. The plot illustrating computation time with respect to signal length is shown in Fig. 7.2. In this figure, the plots represent the mean computation time versus signal length, while the error bars indicate the corresponding standard deviation. The results provided in Fig. 7.2 and Table 7.2 indicate that the computation time required to obtain the decomposed components from the signal increases in a non-linear manner as the length of the signal increases. However, the time required by TDA-CEEVDHM and FDA-CEEVDHM methods is much less than that of the EVDHM method, indicating the computational efficiency of the developed method compared to the EVDHM method. The TDA-CEEVDHM method has provided faster computation compared to the FDA-CEEVDHM method.

Table 7.2: Computation time required by CEEVDHM and EVDHM methods for synthetic and real-time signals of different lengths.

Signal	Number of samples	Computation time (s)		
		EVDHM	CEEVDHM	
			TDA	FDA
$x[n]$	1001	1.1454	0.0376	0.0421
	2001	10.5747	0.1539	0.2071
	3001	41.7487	0.4807	0.7783
	4001	100.3418	1.1407	1.6608
	5001	206.7609	2.2838	3.3840
$y[n]$	1001	1.3442	0.0254	0.0399
	2001	11.1088	0.1592	0.2225
	3001	42.4705	0.4887	0.7823
	4001	101.1991	1.1181	1.6798
	5001	206.6292	2.3194	3.3966
Speech signal	1001	1.1638	0.0355	0.0475
	2001	10.6475	0.1607	0.2316
	3001	41.7925	0.5294	0.8207
	4001	101.0479	1.2140	1.7076
	5001	206.9538	2.3994	3.6552

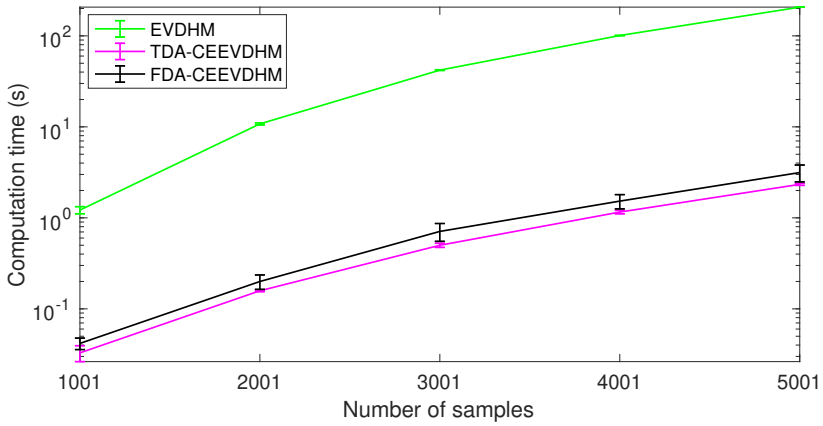

Figure 7.2: Mean computation time required to decompose three studied signal versus signal length is shown with standard deviations represented by errorbars.

7.3.3 Comparative study of decomposed components

In this study, the decomposed components of the signal obtained using EVDHM and CEEVDHM methods are compared. Firstly, the i^{th} error signal $e_i[n]$ is computed using $\hat{x}_i[n]$ and $x_i[n]$ as,

$$e_i[n] = \hat{x}_i[n] - x_i[n] \tag{7.12}$$

where $\hat{x}_i[n]$ and $x_i[n]$ are the i^{th} decomposed components of $x[n]$ using CEEVDHM and EVDHM methods, respectively. Then, the total squared error E_i is computed from i^{th} error signal using the following expression:

$$E_i = \sum_{n=0}^{N-1} \left(e_i[n]\right)^2 \tag{7.13}$$

Finally, the mean of total squared error of all the decomposed components is computed as,

$$E_{\text{mean}} = \frac{1}{\lfloor \frac{K}{2} \rfloor} \sum_{i=1}^{\lfloor \frac{K}{2} \rfloor} E_i \tag{7.14}$$

This measure represents the average energy of the error signal in the decomposition. The values of E_{mean} for all three studied signals are computed and provided in Table 7.3. In this study, it is observed that the average energy of the error is very negligible. However, TDA-CEEVDHM has provided comparatively less error as compared to the FDA-based approach. The time-domain representation of the first six decomposed components of the signals $x[n]$, $y[n]$, and speech signal with $N = 1001$ samples obtained using EVDHM and TDA-CEEVDHM are shown in Figs. 7.3, 7.4, 7.5, respectively. The aforementioned figures show that EVDHM and TDA-CEEVDHM provided the similar component for the studied signals. The same has been observed from the mean squared error as mentioned in Table 7.3.

Furthermore, the comparison of first six decomposed components obtained from

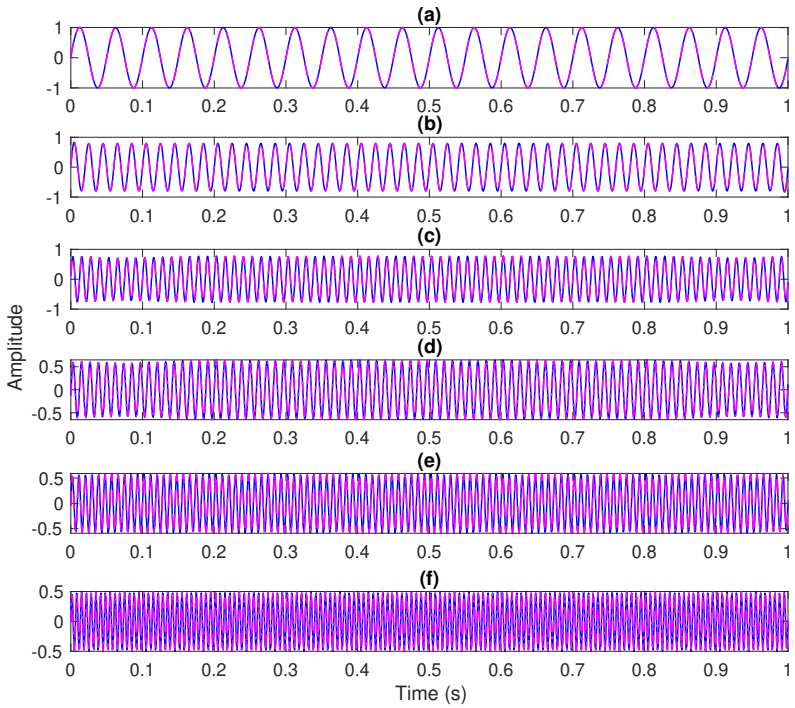

Figure 7.3: The decomposed components of $x[n]$ from (a) to (f) in solid blue line using EVDHM method and dashed pink lines using TDA-CEEVDHM method.

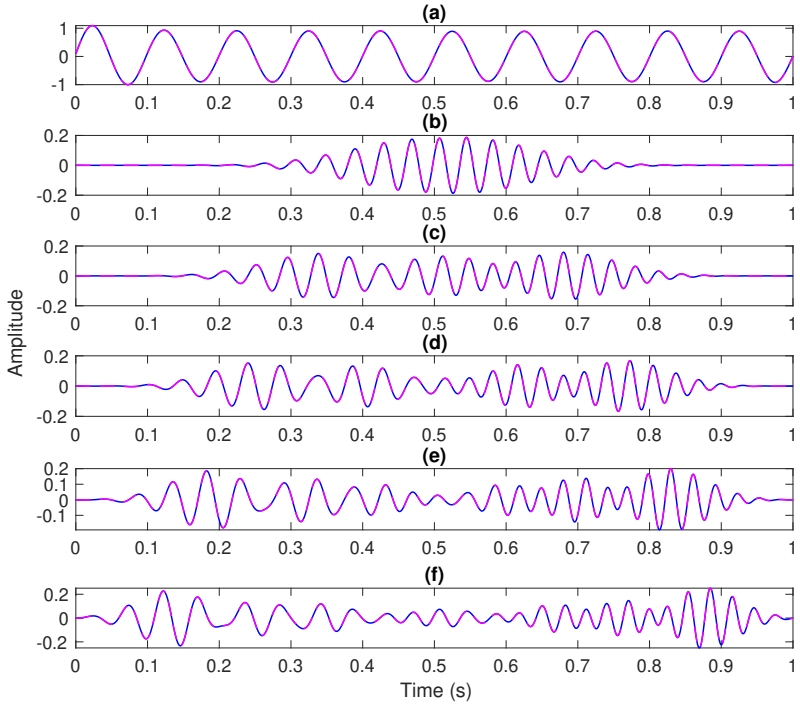

Figure 7.4: The plots (a)–(f) in solid blue line represent decomposed components of the signal $y[n]$ obtained using EVDHM method and dashed pink lines using TDA-CEEVDHM method.

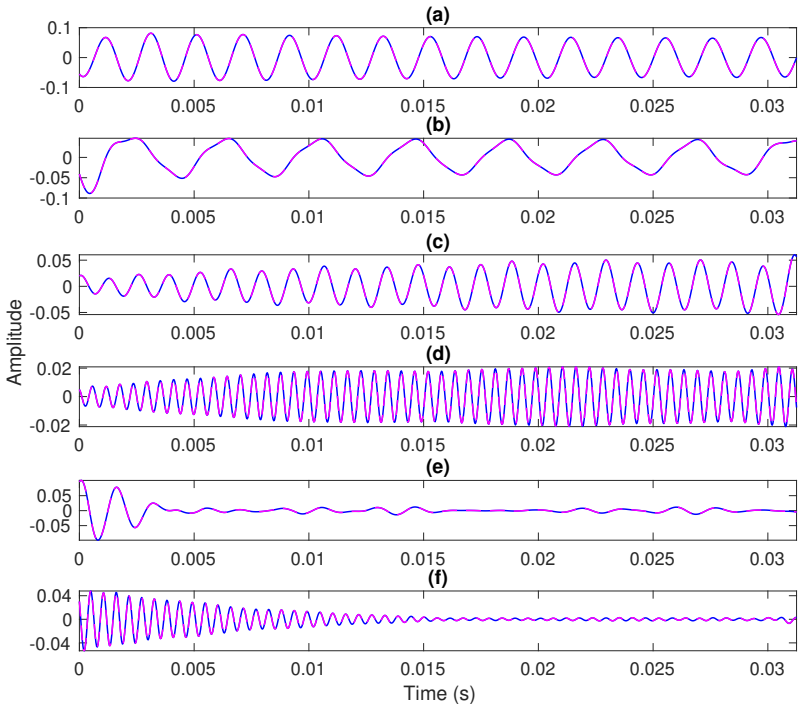

Figure 7.5: The decomposed components of 1001 sample segment of considered voiced speech signals in (a)–(f) using EVDHM and TDA-CEEVDHM methods in solid blue and dashed pink lines, respectively.

EVDHM and FDA-CEEVDHM method-based decomposition of studied signals are shown in Figs. 7.6, 7.7, and 7.8. The decomposed components obtained from both the compared methods are same and the same can be observed from result provided in Table 7.3.

It can be concluded that both TDA and FDA-based CEEVDHM requires relatively less computation time as compared to EVDHM method providing similar decomposed components as provided by EVDHM. Hence, these approaches can be considered as a faster alternative of EVDHM method.

7.4 Summary

A fast alternative to the EVDHM method is proposed named CEEVDHM. There are two approaches presented in this chapter for CEEVDHM. The proposed method requires comparatively less computation time to decompose the signal than EVDHM method. Further-

Table 7.3: The mean of total squared error computed for CEEVDHM method for the studied signal with various signal lengths.

Signal	Number of samples	E_{mean}	
		CEEVDHM	
		TDA	FDA
$x[n]$	1001	2.3707×10^{-30}	5.0706×10^{-29}
	2001	6.4338×10^{-30}	1.6980×10^{-28}
	3001	1.1749×10^{-29}	1.0372×10^{-27}
	4001	2.3904×10^{-29}	6.7178×10^{-28}
	5001	3.7716×10^{-29}	7.8170×10^{-28}
$y[n]$	1001	5.5228×10^{-31}	2.4195×10^{-29}
	2001	1.0655×10^{-30}	2.7145×10^{-29}
	3001	1.5502×10^{-30}	2.3452×10^{-28}
	4001	1.966×10^{-30}	1.3086×10^{-28}
	5001	2.4351×10^{-30}	5.1565×10^{-28}
Speech signal	1001	5.3438×10^{-33}	9.6922×10^{-32}
	2001	1.2646×10^{-32}	2.9095×10^{-31}
	3001	1.8209×10^{-32}	4.7222×10^{-30}
	4001	2.4567×10^{-32}	4.3416×10^{-30}
	5001	3.0469×10^{-32}	3.6858×10^{-30}

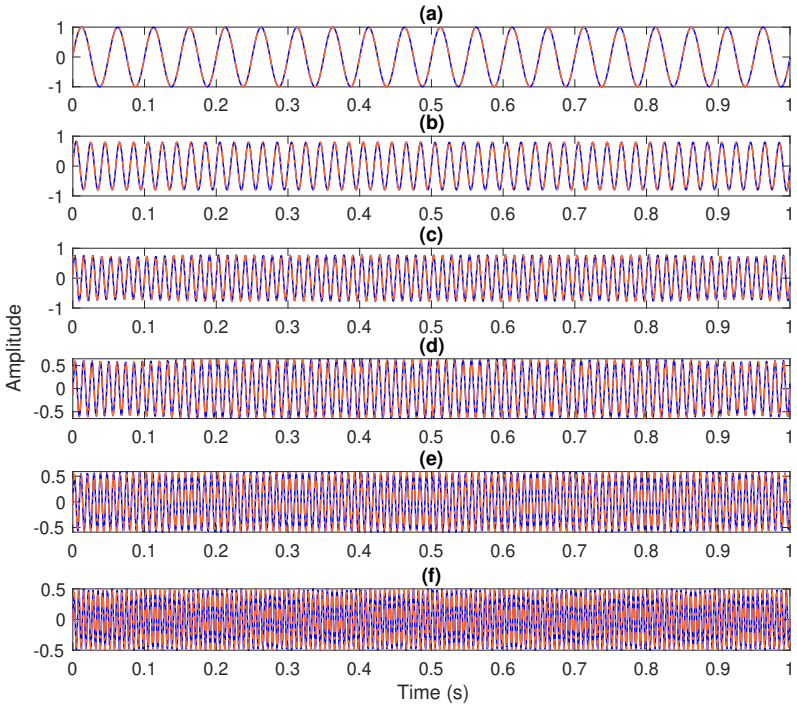

Figure 7.6: The decomposed components of $x[n]$ from (a) to (f) in solid blue line using EVDHM method and dash-dot orange lines using FDA-CEEVDHM method.

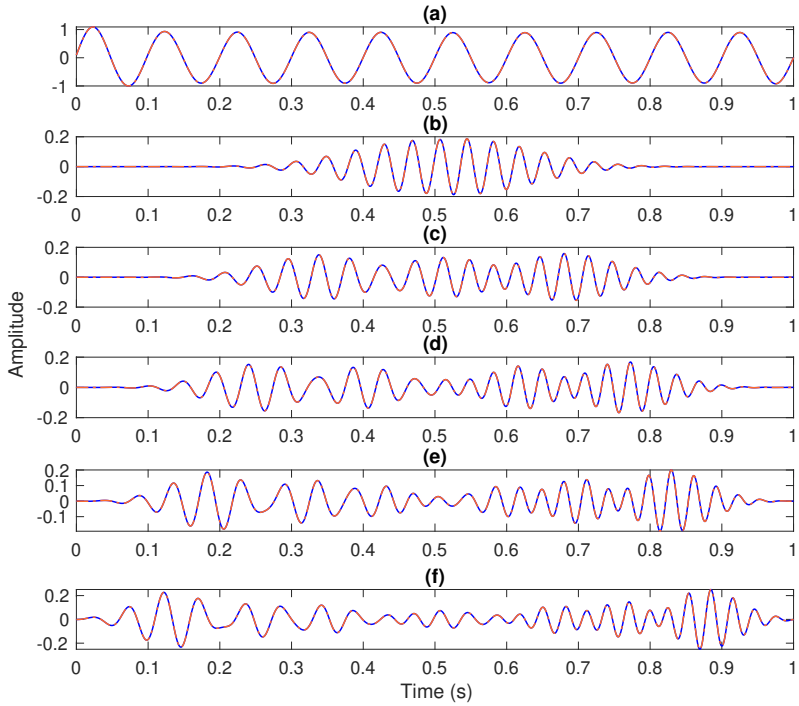

Figure 7.7: The plots (a)–(f) in solid blue line represent decomposed components of $y[n]$ obtained using EVDHM method and dash-dot orange lines using FDA-CEEVDHM method.

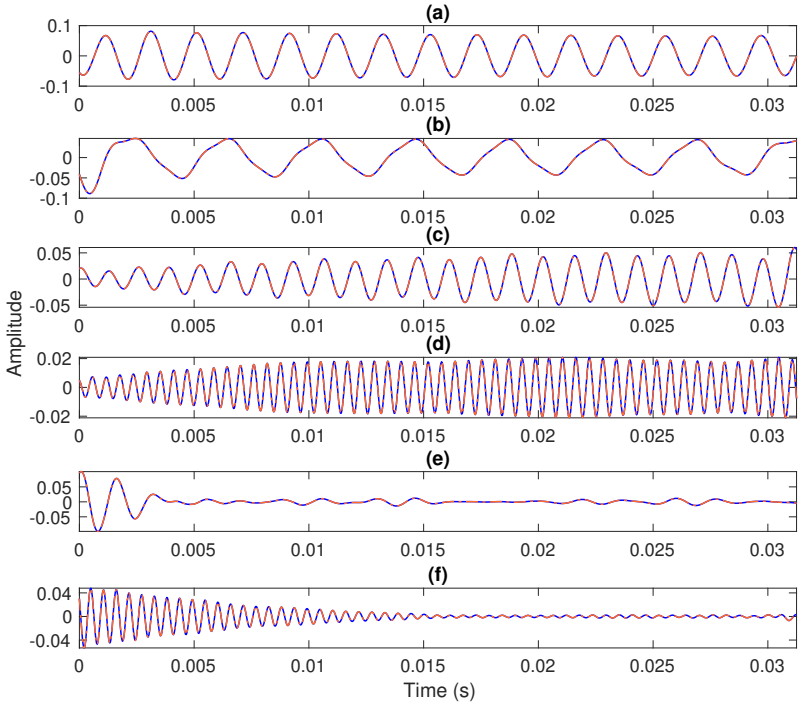

Figure 7.8: The decomposed components of 1001 samples segment of considered speech signals in (a)–(f) using EVDHM and FDA-CEEVDHM methods in solid blue and dash-dot orange lines, respectively.

more, the average of total squared error between the decomposed components of EVDHM and CEEVDHM methods is found to be of negligible. The decomposed components of the studied synthetic and speech signal obtained from EVDHM method are compared with components obtained from TDA and FDA-based CEEVDHM method. This signifies the CEEVDHM method provides same decomposed components as EVDHM but with reduced computation time. The developed method can be utilized to enhance the computational efficiency of other EVDHM-based methods which can be further utilized in developing real-time or near real-time systems.

Chapter 8

Conclusion and future works

8.1 Conclusion

We have proposed the sliding EVD method for decomposition of signal. The sliding EVD method separates the signal components based on short-duration automated EVD method. It successfully separates the signal components with overlapping frequency spectra. Further, TFD of the signal is obtained by applying the HSA method to the decomposed components. The sliding EVD-HSA provided a relatively high-resolution TFD compared to the improved EVDHM-HSA and HHT. Furthermore, we developed the sliding EVD-WVD technique to obtain cross-term-free WVDs of multicomponent signals. It demonstrated the resilience to noise using Rényi entropy as a performance measure.

We have developed an EMD-like EVDHM method to iteratively decompose non-stationary multicomponent signals into DMS using the frequency spread and IF parameters-based component grouping approach. In the proposed framework, two different eigenvalue threshold computation methods are studied. The first threshold computation requires SNR value for noisy signal. However, the second method, which is MDL-based method, is data-adaptive and have shown robustness against noise. The performance of EMD-like EVDHM method has been validated against various baseline techniques, achieving superior decom-

position performance and higher resolution of obtained TFD for synthetic and speech signals, even under noisy conditions. Then, the MDL-based EMD-like EVDHM is studied for trend line extraction and weak component extraction and is found to be effective.

The MCh-EVDHM and its iterative extension (improved MCh-EVDHM) are introduced, enabling mode-aligned decomposition of multichannel multicomponent signals. The MCh-EVDHM is further utilized to develop a classification framework for six eye movements. It achieved exceptional specificity and accuracy with reduced number of features when compared with frameworks from the literature, thus proving its efficacy for real-time multichannel signal analysis and classification. An AD detection framework is developed utilizing rhythm separation from EEG signals via the improved MCh-EVDHM method. This framework achieved remarkable accuracy across various states (eyes closed, eyes open, and eyes open and closed) and demonstrated robust performance with a lightweight classifier, indicating its suitability in resource-constrained environments.

The relation between eigenvalue of a Hankel matrix of the sinusoidal signal and amplitude of the sinusoidal signal is derived, and found to be linearly related to each other. Thereafter, a novel concept for representing time-varying eigenvalues of signals in the time-frequency plane using short-duration EVDHM is presented. The obtained TFD follows the uncertainty principle by achieving higher time resolution and poor frequency resolution for small duration segments considered for analysis and vice-versa. This approach provided superior TFDs compared to spectrograms, scalograms, FSST, and VMD-based methods.

A new method named CEEVDHM is developed to improve the computational efficiency of EVDHM method. The developed method replaces the symmetric matrix computation and skew diagonal averaging with a convolution-based method. This modification improved the computation complexity of EVDHM method significantly. In CEEVDHM, two approaches are proposed for convolution, one based on time-domain and other based on frequency-

domain. However, the time-domain-based CEEVDHM found to be relatively faster than the frequency-domain-based method.

In short, the thesis developed a short-duration EVDHM-based method to separate components overlapped in frequency-domain. Further, an iterative signal decomposition method is proposed to decompose signals based on sifting process. Additionally, multichannel extensions of EVDHM are proposed based on which classification frameworks are developed. Then, a novel TFD is proposed based on short-duration EVDHM to represent the time-varying eigenvalues of the signal in time-frequency plane. Lastly, a faster version of EVDHM is proposed to improve its computational efficiency.

8.2 Future works

Apart from the work carried out in the thesis, the EVDHM-based methods can be explored further. In the thesis, EVDHM-based methods together with HSA have been studied to obtain the TFD of the signal. However, it can be studied to obtain the TFD by applying methods, like discrete energy separation algorithm, spectrogram, scalogram, superlet transform, synchrosqueezing transform, etc., to the decomposed components obtained from the EVDHM-based signal decomposition.

There are two classification frameworks studied in this thesis. Other feature extraction and classification methods for the studied classification problem can be explored and compared with the presented work. The developed framework in this thesis can be studied for analysis and classification of other biomedical signals like magnetoencephalogram, photoplethysmogram, phonocardiogram, galvanic skin response, respiratory signals, etc. The TFD of the signals, obtained from EVDHM-based methods, can be provided as input to deep learning networks like 2-dimensional convolutional neural networks and 2-dimensional long-short-term memory networks for the classification tasks. The EVDHM-

based methods can be explored for the analysis and classification of non-stationary signals encountered in various fields like mechanical engineering, earthquake engineering, etc.

The proposed eigenvalues-based methods can be studied for signal denoising, signal compression, signal characterization, and system characterization. The utility of the developed frameworks can be explored for various technologies like brain-computer interface, smart health monitoring, telemedicine, speech recognition systems, speech synthesizers, computer-aided medical diagnosis systems, etc.

There have been recent advancements toward real-time analysis and classification of signals based on wearable devices and stand-alone hardware. The developed classification and analysis framework can be studied to deploy it on resource-constrained computing platforms including edge devices and internet-of-things-enabled hardware.

The EVDHM-based signal analysis methods have not been studied for image analysis. The same can be explored in future research work. The matrix-based methods can also be taken as a part of future work to improve the computational efficiency.

References

[1] J. Kominek and A. W. Black, "The CMU arctic speech databases," in *Fifth ISCA workshop on Speech Synthesis*, 2004.

[2] R. B. Pachori, *Time-frequency analysis techniques and their applications*. CRC Press, 2023.

[3] T. F. Quatieri, *Discrete-time speech signal processing: Principles and practice*. Pearson Education India, 2002.

[4] L. R. Rabiner, *Digital processing of speech signals*. Pearson Education India, 1978.

[5] R. C. Gonzalez, *Digital image processing*. Pearson Education India, 2009.

[6] L. Cohen, *Time-frequency analysis*. Prentice Hall PTR New Jersey, 1995, vol. 778.

[7] R. M. Gray and J. W. Goodman, *Fourier transforms: An introduction for engineers*. Springer Science & Business Media, 2012, vol. 322.

[8] J. W. Cooley and J. W. Tukey, "An algorithm for the machine calculation of complex Fourier series," *Mathematics of Computation*, vol. 19, no. 90, pp. 297–301, 1965.

[9] W. T. Cochran, J. W. Cooley, D. L. Favin, H. D. Helms, R. A. Kaenel, W. W. Lang, G. C. Maling, D. E. Nelson, C. M. Rader, and P. D. Welch, "What is the fast Fourier transform?" *Proceedings of the IEEE*, vol. 55, no. 10, pp. 1664–1674, 1967.

[10] G. D. Bergland, "A guided tour of the fast Fourier transform," *IEEE Spectrum*, vol. 6, no. 7, pp. 41–52, 1969.

[11] F. Owens and M. Murphy, "A short-time Fourier transform," *Signal Processing*, vol. 14, no. 1, pp. 3–10, 1988.

[12] M. Portnoff, "Time-frequency representation of digital signals and systems based on short-time Fourier analysis," *IEEE Transactions on Acoustics, Speech, and Signal Processing*, vol. 28, no. 1, pp. 55–69, 1980.

[13] S. Mallat, *A wavelet tour of signal processing*. Academic Press, 1999.

[14] T. A. C. M. Claasen and W. F. G. Mecklenbräuker, "The Wigner distribution — A tool for time-frequency signal analysis, Part I: Continuous-time signals," *Philips Journal of Research*, vol. 35, pp. 217–250, 1980.

[15] T. A. C. M. Claasen and W. F. G. Mecklenbräuker, "The Wigner distribution — A tool for time-frequency signal analysis, Part II: Discrete-time signals," *Philips Journal of Research*, vol. 35, pp. 276–300, 1980.

[16] N. E. Huang, Z. Shen, S. R. Long, M. C. Wu, H. H. Shih, Q. Zheng, N.-C. Yen, C. C. Tung, and H. H. Liu, "The empirical mode decomposition and the Hilbert spectrum for nonlinear and non-stationary time series analysis," *Proceedings of the Royal Society of London. Series A: Mathematical, Physical and Engineering Sciences*, vol. 454, no. 1971, pp. 903–995, 1998.

[17] A. V. Oppenheim, "Speech spectrograms using the fast Fourier transform," *IEEE Spectrum*, vol. 7, no. 8, pp. 57–62, 1970.

[18] J. L. Flanagan, *Speech analysis synthesis and perception*. Springer Berlin, Heidelberg, 1972, vol. 2.

[19] W.-k. Lu and Q. Zhang, "Deconvolutive short-time Fourier transform spectrogram," *IEEE Signal Processing Letters*, vol. 16, no. 7, pp. 576–579, 2009.

[20] S. H. Nawab and T. F. Quatieri, "Short-time Fourier transform," in *Advanced Topics in Signal Processing*. Prentice-Hall, 1988, pp. 289–337.

[21] S. Cheung and J. Lim, "Combined multi-resolution (wideband/narrowband) spectrogram," in *International Conference on Acoustics, Speech, and Signal Processing*. IEEE, 1991, pp. 457–460.

[22] R. N. Czerwinski and D. L. Jones, "Adaptive short-time Fourier analysis," *IEEE Signal Processing Letters*, vol. 4, no. 2, pp. 42–45, 1997.

[23] R. N. Czerwinski and D. L. Jones, "Adaptive cone-kernel time-frequency analysis," *IEEE Transactions on Signal Processing*, vol. 43, no. 7, pp. 1715–1719, 1995.

[24] I. Daubechies, *Ten lectures on wavelets*. SIAM, 1992.

[25] I. Daubechies, "The wavelet transform, time-frequency localization and signal analysis," *IEEE Transactions on Information Theory*, vol. 36, no. 5, pp. 961–1005, 2002.

[26] O. Rioul and M. Vetterli, "Wavelets and signal processing," *IEEE Signal Processing Magazine*, vol. 8, no. 4, pp. 14–38, 1991.

[27] K. Schneider and M. Farge, "Wavelets: Mathematical theory," in *Encyclopedia of Mathematical Physics*. Academic Press, 2006, pp. 426–438.

[28] S. Mallat and W. L. Hwang, "Singularity detection and processing with wavelets," *IEEE Transactions on Information Theory*, vol. 38, no. 2, pp. 617–643, 1992.

[29] J. Ville, "Theorie et application dela notion de signal analysis," *Câbles et transmissions*, vol. 2, no. 1, pp. 61–74, 1948.

[30] B. Boashash, *Time-frequency signal analysis and processing: A comprehensive reference*. Academic Press, 2015.

[31] S. Kadambe and G. F. Boudreaux-Bartels, "A comparison of the existence of 'cross terms' in the Wigner distribution and the squared magnitude of the wavelet transform and the short-time Fourier transform," *IEEE Transactions on Signal Processing*, vol. 40, no. 10, pp. 2498–2517, 1992.

[32] R. B. Pachori and P. Sircar, "A new technique to reduce cross terms in the Wigner distribution," *Digital Signal Processing*, vol. 17, no. 2, pp. 466–474, 2007.

[33] B. Boashash, "Note on the use of the Wigner distribution for time-frequency signal analysis," *IEEE Transactions on Acoustics, Speech, and Signal Processing*, vol. 36, no. 9, pp. 1518–1521, 1988.

[34] B. Bouachache and P. Flandrin, "Wigner-Ville analysis of time-varying signals," in *ICASSP'82. IEEE International Conference on Acoustics, Speech, and Signal Processing*, vol. 7. IEEE, 1982, pp. 1329–1332.

[35] A. Potamianos and P. Maragos, "A comparison of the energy operator and the Hilbert transform approach to signal and speech demodulation," *Signal Processing*, vol. 37, no. 1, pp. 95–120, 1994.

[36] D. Gabor, "Theory of communication. part 1: The analysis of information," *Journal of the Institution of Electrical Engineers-Part III: Radio and Communication Engineering*, vol. 93, no. 26, pp. 429–441, 1946.

[37] B. Boashash, "Estimating and interpreting the instantaneous frequency of a signal. I. Fundamentals," *Proceedings of the IEEE*, vol. 80, no. 4, pp. 520–538, 1992.

[38] P. J. Loughlin and B. Tacer, "Comments on the interpretation of instantaneous frequency," *IEEE Signal Processing Letters*, vol. 4, no. 5, pp. 123–125, 1997.

[39] L. Marple, "Computing the discrete-time "analytic" signal via FFT," *IEEE Transactions on Signal Processing*, vol. 47, no. 9, pp. 2600–2603, 1999.

[40] A. Reilly, G. Frazer, and B. Boashash, "Analytic signal generation-tips and traps," *IEEE Transactions on Signal Processing*, vol. 42, no. 11, pp. 3241–3245, 1994.

[41] B. Boashash and A. Reilly, "Algorithms for time-frequency signal analysis," in *Methods and Applications of Time-Frequency Signal Analysis*. Longman Cheshire, 1992.

[42] D. Childers, R. Varga, and N. Perry, "Composite signal decomposition," *IEEE Transactions on Audio and Electroacoustics*, vol. 18, no. 4, pp. 471–477, 1970.

[43] T. Eriksen and N. u. Rehman, "Data-driven nonstationary signal decomposition approaches: A comparative analysis," *Scientific Reports*, vol. 13, no. 1, p. 1798, 2023.

[44] Z. Wu and N. E. Huang, "Ensemble empirical mode decomposition: A noise-assisted data analysis method," *Advances in Adaptive Data Analysis*, vol. 1, no. 01, pp. 1–41, 2009.

[45] K. Dragomiretskiy and D. Zosso, "Variational mode decomposition," *IEEE Transactions on Signal Processing*, vol. 62, no. 3, pp. 531–544, 2013.

[46] J. Gilles, "Empirical wavelet transform," *IEEE Transactions on Signal Processing*, vol. 61, no. 16, pp. 3999–4010, 2013.

[47] K. Zhang, L. Shi, Y. Hu, P. Chen, and Y. Xu, "Variable spectral segmentation empirical wavelet transform for noisy signal processing," *Digital Signal Processing*, vol. 117, p. 103151, 2021.

[48] A. Bhattacharyya, L. Singh, and R. B. Pachori, "Fourier–Bessel series expansion based empirical wavelet transform for analysis of non-stationary signals," *Digital Signal Processing*, vol. 78, pp. 185–196, 2018.

[49] H. Hassani, "Singular spectrum analysis: Methodology and comparison," *Journal of Data Science*, vol. 5, pp. 239–257, 2007.

[50] J. Harmouche, D. Fourer, F. Auger, P. Borgnat, and P. Flandrin, "The sliding singular spectrum analysis: A data-driven nonstationary signal decomposition tool," *IEEE Transactions on Signal Processing*, vol. 66, no. 1, pp. 251–263, 2017.

[51] P. Jain and R. B. Pachori, "GCI identification from voiced speech using the eigen value decomposition of Hankel matrix," in *2013 8th International Symposium on Image and Signal Processing and Analysis (ISPA)*. IEEE, 2013, pp. 371–376.

[52] P. Jain and R. B. Pachori, "An iterative approach for decomposition of multi-component non-stationary signals based on eigenvalue decomposition of the Hankel matrix," *Journal of the Franklin Institute*, vol. 352, no. 10, pp. 4017–4044, 2015.

[53] R. R. Sharma and R. B. Pachori, "Time–frequency representation using IEVDHM–HT with application to classification of epileptic EEG signals," *IET Science, Measurement & Technology*, vol. 12, no. 1, pp. 72–82, 2018.

[54] P. Singh, S. D. Joshi, R. K. Patney, and K. Saha, "The Fourier decomposition method for nonlinear and non-stationary time series analysis," *Proceedings of the Royal Society A: Mathematical, Physical and Engineering Sciences*, vol. 473, no. 2199, p. 20160871, 2017.

[55] W. Zhou, Z. Feng, Y. Xu, X. Wang, and H. Lv, "Empirical Fourier decomposition: An

accurate signal decomposition method for nonlinear and non-stationary time series analysis," *Mechanical Systems and Signal Processing*, vol. 163, p. 108155, 2022.

[56] J.-R. Yeh, J.-S. Shieh, and N. E. Huang, "Complementary ensemble empirical mode decomposition: A novel noise enhanced data analysis method," *Advances in Adaptive Data Analysis*, vol. 2, no. 02, pp. 135–156, 2010.

[57] M. E. Torres, M. A. Colominas, G. Schlotthauer, and P. Flandrin, "A complete ensemble empirical mode decomposition with adaptive noise," in *2011 IEEE International Conference on Acoustics, Speech and Signal Processing (ICASSP)*. IEEE, 2011, pp. 4144–4147.

[58] M. A. Colominas, G. Schlotthauer, and M. E. Torres, "Improved complete ensemble EMD: A suitable tool for biomedical signal processing," *Biomedical Signal Processing and Control*, vol. 14, pp. 19–29, 2014.

[59] Y. Hu, F. Li, H. Li, and C. Liu, "An enhanced empirical wavelet transform for noisy and non-stationary signal processing," *Digital Signal Processing*, vol. 60, pp. 220–229, 2017.

[60] S. M. Bhuiyan, R. R. Adhami, and J. F. Khan, "Fast and adaptive bidimensional empirical mode decomposition using order-statistics filter based envelope estimation," *EURASIP Journal on Advances in Signal Processing*, vol. 2008, pp. 1–18, 2008.

[61] J. Schroeder, "Signal processing via Fourier-Bessel series expansion," *Digital Signal Processing*, vol. 3, no. 2, pp. 112–124, 1993.

[62] R. B. Pachori and P. Sircar, "Analysis of multi-component non-stationary signals using Fourier-Bessel transform and Wigner distribution," in *2006 14th European Signal Processing Conference*. IEEE, 2006, pp. 1–5.

[63] R. B. Pachori and A. Nishad, "Cross-terms reduction in the Wigner–Ville distribution using tunable-Q wavelet transform," *Signal Processing*, vol. 120, pp. 288–304, 2016.

[64] P. K. Chaudhary, V. Gupta, and R. B. Pachori, "Fourier-Bessel representation for signal processing: A review," *Digital Signal Processing*, vol. 135, p. 103938, 2023.

[65] J. Gilles and K. Heal, "A parameterless scale-space approach to find meaningful modes in histograms—Application to image and spectrum segmentation," *International Journal of Wavelets, Multiresolution and Information Processing*, vol. 12, no. 06, p. 1450044, 2014.

[66] N. Otsu *et al.*, "A threshold selection method from gray-level histograms," *Automatica*, vol. 11, no. 285-296, pp. 23–27, 1975.

[67] D. P. Bertsekas, "Multiplier methods: A survey," *Automatica*, vol. 12, no. 2, pp. 133–145, 1976.

[68] J. Nocedal and S. J. Wright, *Numerical optimization*. Springer, 1999.

[69] M. R. Hestenes, "Multiplier and gradient methods," *Journal of Optimization Theory and Applications*, vol. 4, no. 5, pp. 303–320, 1969.

[70] R. T. Rockafellar, "A dual approach to solving nonlinear programming problems by unconstrained optimization," *Mathematical programming*, vol. 5, no. 1, pp. 354–373, 1973.

[71] J. Lian, Z. Liu, H. Wang, and X. Dong, "Adaptive variational mode decomposition method for signal processing based on mode characteristic," *Mechanical Systems and Signal Processing*, vol. 107, pp. 53–77, 2018.

[72] M. Nazari and S. M. Sakhaei, "Successive variational mode decomposition," *Signal Processing*, vol. 174, p. 107610, 2020.

[73] J. Gilles, G. Tran, and S. Osher, "2D empirical transforms. wavelets, ridgelets, and curvelets revisited," *SIAM Journal on Imaging Sciences*, vol. 7, no. 1, pp. 157–186, 2014.

[74] P. Jain and R. B. Pachori, "Event-based method for instantaneous fundamental frequency estimation from voiced speech based on eigenvalue decomposition of the Hankel matrix," *IEEE/ACM Transactions on Audio, Speech, and Language Processing*, vol. 22, no. 10, pp. 1467–1482, 2014.

[75] J. Harmouche, D. Fourer, P. Flandrin, F. Auger, and P. Borgnat, "One or two components? The singular spectrum analysis answers," *Reconstruction*, vol. 1, p. 1, 2015.

[76] L. Stanković, M. Brajović, M. Daković, and D. Mandić, "Two-component bivariate signal decomposition based on time-frequency analysis," in *2017 22nd International Conference on Digital Signal Processing (DSP)*. IEEE, 2017, pp. 1–5.

[77] A. Ahrabian, D. Looney, L. Stanković, and D. P. Mandic, "Synchrosqueezing-based time-frequency analysis of multivariate data," *Signal Processing*, vol. 106, pp. 331–341, 2015.

[78] K. Das and R. B. Pachori, "Schizophrenia detection technique using multivariate iterative filtering and multichannel EEG signals," *Biomedical Signal Processing and Control*, vol. 67, p. 102525, 2021.

[79] J. M. Lilly and S. C. Olhede, "Bivariate instantaneous frequency and bandwidth," *IEEE Transactions on Signal Processing*, vol. 58, no. 2, pp. 591–603, 2009.

[80] J. M. Lilly and S. C. Olhede, "Analysis of modulated multivariate oscillations," *IEEE Transactions on Signal Processing*, vol. 60, no. 2, pp. 600–612, 2011.

[81] H. Niederreiter, *Random number generation and quasi-Monte Carlo methods*. Society for Industrial and Applied Mathematics, 1992.

[82] J. Cui and W. Freeden, "Equidistribution on the sphere," *SIAM Journal on Scientific Computing*, vol. 18, no. 2, pp. 595–609, 1997.

[83] N. Rehman and D. P. Mandic, "Multivariate empirical mode decomposition," *Proceedings of the Royal Society A: Mathematical, Physical and Engineering Sciences*, vol. 466, no. 2117, pp. 1291–1302, 2010.

[84] X. Lang, Q. Zheng, Z. Zhang, S. Lu, L. Xie, A. Horch, and H. Su, "Fast multivariate empirical mode decomposition," *IEEE Access*, vol. 6, pp. 65 521–65 538, 2018.

[85] A. Bhattacharyya and R. B. Pachori, "A multivariate approach for patient-specific EEG seizure detection using empirical wavelet transform," *IEEE Transactions on Biomedical Engineering*, vol. 64, no. 9, pp. 2003–2015, 2017.

[86] A. Bhattacharyya, R. K. Tripathy, L. Garg, and R. B. Pachori, "A novel multivariate-multiscale approach for computing EEG spectral and temporal complexity for human emotion recognition," *IEEE Sensors Journal*, vol. 21, no. 3, pp. 3579–3591, 2020.

[87] W. Huang, J. Zeng, Z. Wang, and J. Liang, "Partial noise assisted multivariate EMD: An improved noise assisted method for multivariate signals decomposition," *Biomedical Signal Processing and Control*, vol. 36, pp. 205–220, 2017.

[88] N. ur Rehman and H. Aftab, "Multivariate variational mode decomposition," *IEEE Transactions on Signal Processing*, vol. 67, no. 23, pp. 6039–6052, 2019.

[89] Q. Chen, L. Xie, and H. Su, "Multivariate nonlinear chirp mode decomposition," *Signal Processing*, vol. 176, p. 107667, 2020.

[90] Q. Chen, X. Lang, L. Xie, and H. Su, "Multivariate intrinsic chirp mode decomposition," *Signal Processing*, vol. 183, p. 108009, 2021.

[91] J. Huang, C. Li, X. Xiao, T. Yu, X. Yuan, and Y. Zhang, "Adaptive multivariate chirp mode decomposition," *Mechanical Systems and Signal Processing*, vol. 186, p. 109897, 2023.

[92] P. C. Rodrigues and R. Mahmoudvand, "The benefits of multivariate singular spectrum analysis over the univariate version," *Journal of the Franklin Institute*, vol. 355, no. 1, pp. 544–564, 2018.

[93] A. Cicone and E. Pellegrino, "Multivariate fast iterative filtering for the decomposition of nonstationary signals," *IEEE Transactions on Signal Processing*, vol. 70, pp. 1521–1531, 2022.

[94] Q. Zhang, R. Yuan, Y. Lv, Z. Li, and H. Wu, "Multivariate dynamic mode decomposition and its application to bearing fault diagnosis," *IEEE Sensors Journal*, vol. 23, no. 7, pp. 7514–7524, 2023.

[95] A. S. S. Reddy and R. B. Pachori, "Multivariate dynamic mode decomposition for automatic imagined speech recognition using multichannel EEG signals," *IEEE Sensors Letters*, vol. 8, no. 2, p. 6001604, 2024.

[96] H. Amoud, H. Snoussi, D. Hewson, and J. Duchêne, "Univariate and bivariate empirical mode decomposition for postural stability analysis," *EURASIP Journal on Advances in Signal Processing*, vol. 2008, pp. 1–11, 2008.

[97] S. L. Goh, D. Popovic, and D. Mandic, "Complex-valued estimation of wind profile and wind power," in *Proceedings of the 12th IEEE Mediterranean Electrotechnical Conference (IEEE Cat. No. 04CH37521)*, vol. 3. IEEE, 2004, pp. 1037–1040.

[98] S. L. Goh, M. Chen, D. Popović, K. Aihara, D. Obradovic, and D. Mandic, "Complex-valued forecasting of wind profile," *Renewable Energy*, vol. 31, no. 11, pp. 1733–1750, 2006.

[99] D. Mandic, S. Javidi, S. Goh, A. Kuh, and K. Aihara, "Complex-valued prediction of wind profile using augmented complex statistics," *Renewable Energy*, vol. 34, no. 1, pp. 196–201, 2009.

[100] T. Tanaka and D. P. Mandic, "Complex empirical mode decomposition," *IEEE Signal Processing Letters*, vol. 14, no. 2, pp. 101–104, 2007.

[101] Y. Wang, F. Liu, Z. Jiang, S. He, and Q. Mo, "Complex variational mode decomposition for signal processing applications," *Mechanical Systems and Signal Processing*, vol. 86, pp. 75–85, 2017.

[102] V. K. Kashyap, R. R. Sharma, and R. B. Pachori, "Complex flexible analytic wavelet transform for UAV state identification using RF signal," *IEEE Transactions on Aerospace and Electronic Systems*, vol. 60, no. 2, pp. 1471–1481, 2023.

[103] J. Gilles, "Continuous empirical wavelets systems," *Advances in Data Science and Adaptive Analysis*, vol. 12, no. 03n04, p. 2050006, 2020.

[104] R. R. Sharma and R. B. Pachori, "Eigenvalue decomposition of Hankel matrix-based time-frequency representation for complex signals," *Circuits, Systems, and Signal Processing*, vol. 37, pp. 3313–3329, 2018.

[105] A. Tyagi, V. K. Singh, and R. B. Pachori, "FBSE-EWT technique-based complex-valued signal analysis," *Circuits, Systems, and Signal Processing*, pp. 1–22, 2024.

[106] Z.-T. Liu, Q. Xie, M. Wu, W.-H. Cao, D.-Y. Li, and S.-H. Li, "Electroencephalogram emotion recognition based on empirical mode decomposition and optimal feature selection," *IEEE Transactions on Cognitive and Developmental Systems*, vol. 11, no. 4, pp. 517–526, 2018.

[107] S. K. Khare and V. Bajaj, "An evolutionary optimized variational mode decomposition for emotion recognition," *IEEE Sensors Journal*, vol. 21, no. 2, pp. 2035–2042, 2020.

[108] N. Salankar, P. Mishra, and L. Garg, "Emotion recognition from EEG signals using empirical mode decomposition and second-order difference plot," *Biomedical Signal Processing and Control*, vol. 65, p. 102389, 2021.

[109] P. T. Krishnan, A. N. Joseph Raj, and V. Rajangam, "Emotion classification from speech signal based on empirical mode decomposition and non-linear features: Speech emotion recognition," *Complex & Intelligent Systems*, vol. 7, pp. 1919–1934, 2021.

[110] Z.-T. Liu, S.-J. Hu, J. She, Z. Yang, and X. Xu, "Electroencephalogram emotion recognition using combined features in variational mode decomposition domain," *IEEE Transactions on Cognitive and Developmental Systems*, vol. 15, no. 3, pp. 1595–1604, 2023.

[111] S.-T. Pan and X.-Y. Li, "An FPGA-based embedded robust speech recognition system designed by combining empirical mode decomposition and a genetic algorithm,"

IEEE Transactions on Instrumentation and measurement, vol. 61, no. 9, pp. 2560–2572, 2012.

[112] I. C. Yadav, S. Shahnawazuddin, and G. Pradhan, "Addressing noise and pitch sensitivity of speech recognition system through variational mode decomposition based spectral smoothing," *Digital Signal Processing*, vol. 86, pp. 55–64, 2019.

[113] M. Sidi Yakoub, S.-a. Selouani, B.-F. Zaidi, and A. Bouchair, "Improving dysarthric speech recognition using empirical mode decomposition and convolutional neural network," *EURASIP Journal on Audio, Speech, and Music Processing*, vol. 2020, pp. 1–7, 2020.

[114] C. Tantibundhit, J. R. Boston, C.-C. Li, J. D. Durrant, S. Shaiman, K. Kovacyk, and A. El-Jaroudi, "New signal decomposition method based speech enhancement," *Signal Processing*, vol. 87, no. 11, pp. 2607–2628, 2007.

[115] L. Zão, R. Coelho, and P. Flandrin, "Speech enhancement with EMD and Hurst-based mode selection," *IEEE/ACM Transactions on Audio, Speech, and Language Processing*, vol. 22, no. 5, pp. 899–911, 2014.

[116] A. Upadhyay and R. B. Pachori, "Speech enhancement based on mEMD-VMD method," *Electronics Letters*, vol. 53, no. 7, pp. 502–504, 2017.

[117] H. Liang, Q.-H. Lin, and J. D. Z. Chen, "Application of the empirical mode decomposition to the analysis of esophageal manometric data in gastroesophageal reflux disease," *IEEE Transactions on Biomedical Engineering*, vol. 52, no. 10, pp. 1692–1701, 2005.

[118] V. Bajaj and R. B. Pachori, "Classification of seizure and nonseizure EEG signals us-

ing empirical mode decomposition," *IEEE Transactions on Information Technology in Biomedicine*, vol. 16, no. 6, pp. 1135–1142, 2011.

[119] G. R. Naik, S. E. Selvan, and H. T. Nguyen, "Single-channel EMG classification with ensemble-empirical-mode-decomposition-based ICA for diagnosing neuromuscular disorders," *IEEE Transactions on Neural Systems and Rehabilitation Engineering*, vol. 24, no. 7, pp. 734–743, 2015.

[120] P. Ren, S. Tang, F. Fang, L. Luo, L. Xu, M. L. Bringas-Vega, D. Yao, K. M. Kendrick, and P. A. Valdes-Sosa, "Gait rhythm fluctuation analysis for neurodegenerative diseases by empirical mode decomposition," *IEEE Transactions on Biomedical Engineering*, vol. 64, no. 1, pp. 52–60, 2016.

[121] A. Smruthy and M. Suchetha, "Real-time classification of healthy and apnea subjects using ECG signals with variational mode decomposition," *IEEE Sensors Journal*, vol. 17, no. 10, pp. 3092–3099, 2017.

[122] S. I. Khan and R. B. Pachori, "Automated classification of lung sound signals based on empirical mode decomposition," *Expert Systems with Applications*, vol. 184, p. 115456, 2021.

[123] L. Cohen and C. Lee, "Instantaneous bandwidth for signals and spectrogram," in *International Conference on Acoustics, Speech, and Signal Processing*. IEEE, 1990, pp. 2451–2454.

[124] J. A. Suykens and J. Vandewalle, "Least squares support vector machine classifiers," *Neural Processing Letters*, vol. 9, pp. 293–300, 1999.

[125] S. Pal and M. Mitra, "Empirical mode decomposition based ECG enhancement and QRS detection," *Computers in Biology and Medicine*, vol. 42, no. 1, pp. 83–92, 2012.

[126] C. Park, D. Looney, N. ur Rehman, A. Ahrabian, and D. P. Mandic, "Classification of motor imagery BCI using multivariate empirical mode decomposition," *IEEE Transactions on Neural Systems and Rehabilitation Engineering*, vol. 21, no. 1, pp. 10–22, 2012.

[127] H. Ramoser, J. Muller-Gerking, and G. Pfurtscheller, "Optimal spatial filtering of single trial EEG during imagined hand movement," *IEEE Transactions on Rehabilitation Engineering*, vol. 8, no. 4, pp. 441–446, 2000.

[128] R.-N. Duan, J.-Y. Zhu, and B.-L. Lu, "Differential entropy feature for EEG-based emotion classification," in *2013 6th International IEEE/EMBS Conference on Neural Engineering (NER)*. IEEE, 2013, pp. 81–84.

[129] M. Wu, T. Wan, X. Wan, Y. Du, and J. She, "Fast, accurate localization of epileptic seizure onset zones based on detection of high-frequency oscillations using improved wavelet transform and matching pursuit methods," *Neural Computation*, vol. 29, no. 1, pp. 194–219, 2017.

[130] M. K. Arjmandi and M. Pooyan, "An optimum algorithm in pathological voice quality assessment using wavelet-packet-based features, linear discriminant analysis and support vector machine," *Biomedical Signal Processing and Control*, vol. 7, no. 1, pp. 3–19, 2012.

[131] T. Chen and C. Guestrin, "XGBoost: A scalable tree boosting system," in *Proceedings of the 22nd ACM SIGKDD International Conference on Knowledge Discovery and Data Mining*, 2016, pp. 785–794.

[132] J. Snoek, H. Larochelle, and R. P. Adams, "Practical Bayesian optimization of ma-

chine learning algorithms," *Advances in Neural Information Processing Systems*, vol. 25, 2012.

[133] H. Cao, L. Peyrodie *et al.*, "Variational mode decomposition-based simultaneous R peak detection and noise suppression for automatic ECG analysis," *IEEE Sensors Journal*, vol. 23, no. 8, pp. 8703–8713, 2023.

[134] Z. Wang, L. Chen, H. Chen, and N. ur Rehman, "Monthly ship price forecasting based on multivariate variational mode decomposition," *Engineering Applications of Artificial Intelligence*, vol. 125, p. 106698, 2023.

[135] W. Liu, S. Cao, and Y. Chen, "Seismic time–frequency analysis via empirical wavelet transform," *IEEE Geoscience and Remote Sensing Letters*, vol. 13, no. 1, pp. 28–32, 2015.

[136] A. Anuragi and D. S. Sisodia, "Empirical wavelet transform based automated alcoholism detecting using EEG signal features," *Biomedical Signal Processing and Control*, vol. 57, p. 101777, 2020.

[137] B. Fatimah, P. Singh, A. Singhal, and R. B. Pachori, "Hand movement recognition from sEMG signals using Fourier decomposition method," *Biocybernetics and Biomedical Engineering*, vol. 41, no. 2, pp. 690–703, 2021.

[138] V. K. Mehla, A. Singhal, and P. Singh, "A novel approach for automated alcoholism detection using Fourier decomposition method," *Journal of Neuroscience Methods*, vol. 346, p. 108945, 2020.

[139] S. V. Bhalerao and R. B. Pachori, "Automated classification of cognitive visual objects using multivariate swarm sparse decomposition from multichannel EEG-MEG signals," *IEEE Transactions on Human-Machine Systems*, 2024.

[140] B. Boashash, G. Azemi, and J. M. O'Toole, "Time-frequency processing of nonstationary signals: Advanced TFD design to aid diagnosis with highlights from medical applications," *IEEE Signal Processing Magazine*, vol. 30, no. 6, pp. 108–119, 2013.

[141] L. Stanković, "A measure of some time–frequency distributions concentration," *Signal Processing*, vol. 81, no. 3, pp. 621–631, 2001.

[142] B. B. Chaudhuri and N. Sarkar, "Texture segmentation using fractal dimension," *IEEE Transactions on Pattern Analysis and Machine Intelligence*, vol. 17, no. 1, pp. 72–77, 1995.

[143] S. Pertuz, D. Puig, and M. A. Garcia, "Analysis of focus measure operators for shape-from-focus," *Pattern Recognition*, vol. 46, no. 5, pp. 1415–1432, 2013.

[144] R. R. Sharma, A. Kumar, R. B. Pachori, and U. R. Acharya, "Accurate automated detection of congestive heart failure using eigenvalue decomposition based features extracted from HRV signals," *Biocybernetics and Biomedical Engineering*, vol. 39, no. 2, pp. 312–327, 2019.

[145] L. Cohen, "What is a multicomponent signal?" in *[Proceedings] ICASSP-92: 1992 IEEE International Conference on Acoustics, Speech, and Signal Processing*, vol. 5. IEEE, 1992, pp. 113–116.

[146] H. Zhang, W. Lu, J. Wei, X. Huang, X. Yang, and X. Lu, "Efficient singular spectrum mode ensemble for extracting wide-band components in overlapping spectral environments," *IEEE Transactions on Signal Processing*, 2024.

[147] J. Gilbert and L. Gilbert, *Linear algebra and matrix theory*. Elsevier, 2014.

[148] R. R. Sharma and R. B. Pachori, "A new method for non-stationary signal analysis using eigenvalue decomposition of the Hankel matrix and Hilbert transform," in *2017*

4th International Conference on Signal Processing and Integrated Networks (SPIN). IEEE, 2017, pp. 484–488.

[149] R. R. Sharma and R. B. Pachori, "Baseline wander and power line interference removal from ECG signals using eigenvalue decomposition," *Biomedical Signal Processing and Control*, vol. 45, pp. 33–49, 2018.

[150] R. R. Sharma, M. Kumar, and R. B. Pachori, "Automated CAD identification system using time–frequency representation based on eigenvalue decomposition of ECG signals," in *Machine Intelligence and Signal Analysis*. Springer, 2019, pp. 597–608.

[151] R. J. Martis, U. R. Acharya, and L. C. Min, "ECG beat classification using PCA, LDA, ICA and discrete wavelet transform," *Biomedical Signal Processing and Control*, vol. 8, no. 5, pp. 437–448, 2013.

[152] B. Boashash, N. A. Khan, and T. Ben-Jabeur, "Time–frequency features for pattern recognition using high-resolution TFDs: A tutorial review," *Digital Signal Processing*, vol. 40, pp. 1–30, 2015.

[153] R. R. Sharma, M. Kumar, S. Maheshwari, and K. P. Ray, "EVDHM-ARIMA-based time series forecasting model and its application for COVID-19 cases," *IEEE Transactions on Instrumentation and Measurement*, vol. 70, pp. 1–10, 2020.

[154] R. R. Sharma and R. B. Pachori, "Improved eigenvalue decomposition-based approach for reducing cross-terms in Wigner–Ville distribution," *Circuits, Systems, and Signal Processing*, vol. 37, pp. 3330–3350, 2018.

[155] R. R. Sharma, P. Chandra, and R. B. Pachori, "Electromyogram signal analysis using eigenvalue decomposition of the Hankel matrix," in *Machine Intelligence and Signal Analysis*. Springer, 2019, pp. 671–682.

[156] R. R. Sharma, M. Kumar, and R. B. Pachori, "Classification of EMG signals using eigenvalue decomposition-based time-frequency representation," in *Biomedical and Clinical Engineering for Healthcare Advancement*. IGI Global, 2020, pp. 96–118.

[157] K. Nithya, S. Sharma, and R. R. Sharma, "Eigenvalues of Hankel matrix based epilepsy detection using EEG signals," in *2023 2nd International Conference on Paradigm Shifts in Communications Embedded Systems, Machine Learning and Signal Processing (PCEMS)*. IEEE, 2023, pp. 1–6.

[158] M. G. Amin, "Interference mitigation in spread spectrum communication systems using time-frequency distributions," *IEEE Transactions on Signal Processing*, vol. 45, no. 1, pp. 90–101, 1997.

[159] Y. Wang, H. Ling, and V. C. Chen, "ISAR motion compensation via adaptive joint time-frequency technique," *IEEE Transactions on Aerospace and Electronic Systems*, vol. 34, no. 2, pp. 670–677, 1998.

[160] S. Madhavan, R. K. Tripathy, and R. B. Pachori, "Time-frequency domain deep convolutional neural network for the classification of focal and non-focal EEG signals," *IEEE Sensors Journal*, vol. 20, no. 6, pp. 3078–3086, 2019.

[161] R. B. Pachori and P. Sircar, "Analysis of multicomponent AM-FM signals using FB-DESA method," *Digital Signal Processing*, vol. 20, no. 1, pp. 42–62, 2010.

[162] J. C. O'Neill, P. Flandrin, and W. J. Williams, "On the existence of discrete Wigner distributions," *IEEE Signal Processing Letters*, vol. 6, no. 12, pp. 304–306, 1999.

[163] H.-I. Choi and W. J. Williams, "Improved time-frequency representation of multicomponent signals using exponential kernels," *IEEE Transactions on Acoustics, Speech, and Signal Processing*, vol. 37, no. 6, pp. 862–871, 1989.

[164] P. Gonçalves and R. G. Baraniuk, "Pseudo affine Wigner distributions: Definition and kernel formulation," *IEEE Transactions on Signal Processing*, vol. 46, no. 6, pp. 1505–1516, 1998.

[165] P. Flandrin and O. Rioul, "Affine smoothing of the Wigner-Ville distribution," in *International Conference on Acoustics, Speech, and Signal Processing*. IEEE, 1990, pp. 2455–2458.

[166] G. Andria and M. Savino, "Interpolated smoothed pseudo Wigner-Ville distribution for accurate spectrum analysis," *IEEE Transactions on Instrumentation and Measurement*, vol. 45, no. 4, pp. 818–823, 1996.

[167] R. R. Sharma, A. Kalyani, and R. B. Pachori, "An empirical wavelet transform-based approach for cross-terms-free Wigner–Ville distribution," *Signal, Image and Video Processing*, vol. 14, pp. 249–256, 2020.

[168] Y. Chai and X. Zhang, "EMD-WVD time-frequency distribution for analysis of multi-component signals," in *Fourth International Conference on Wireless and Optical Communications*, vol. 9902. SPIE, 2016, pp. 190–196.

[169] X. Liu, Y. Jia, Z. He, and J. Zhou, "Application of EMD-WVD and particle filter for gearbox fault feature extraction and remaining useful life prediction," *Journal of Vibroengineering*, vol. 19, no. 3, pp. 1793–1808, 2017.

[170] L. Jiangting, Z. Kaifeng, and H. Yue, "EMD-WVD method based high-frequency current analysis of low voltage arc," in *2018 Condition Monitoring and Diagnosis (CMD)*. IEEE, 2018, pp. 1–5.

[171] R. Panda, S. Jain, R. Tripathy, R. R. Sharma, and R. B. Pachori, "Sliding mode singu-

lar spectrum analysis for the elimination of cross-terms in Wigner–Ville distribution," *Circuits, Systems, and Signal Processing*, vol. 40, no. 3, pp. 1207–1232, 2021.

[172] D. Ping, P. Zhao, and B. Deng, "Cross-terms suppression in Wigner-Ville distribution based on image processing," in *The 2010 IEEE International Conference on Information and Automation*. IEEE, 2010, pp. 2168–2171.

[173] N. A. Khan, I. A. Taj, M. N. Jaffri, and S. Ijaz, "Cross-term elimination in Wigner distribution based on 2D signal processing techniques," *Signal Processing*, vol. 91, no. 3, pp. 590–599, 2011.

[174] L. L. McQuitty, "Hierarchical linkage analysis for the isolation of types," *Educational and Psychological Measurement*, vol. 20, no. 1, pp. 55–67, 1960.

[175] V. K. Singh and R. B. Pachori, "Sliding eigenvalue decomposition for non-stationary signal analysis," in *2020 International Conference on Signal Processing and Communications (SPCOM)*. IEEE, 2020, pp. 1–5.

[176] G. Rilling, P. Flandrin, P. Goncalves *et al.*, "On empirical mode decomposition and its algorithms," in *IEEE-EURASIP Workshop on Nonlinear Signal and Image Processing*, vol. 3, no. 3. Grado: IEEE, 2003, pp. 8–11.

[177] P. Flandrin, R. G. Baraniuk, and O. Michel, "Time-frequency complexity and information," in *Proceedings of ICASSP'94. IEEE International Conference on Acoustics, Speech and Signal Processing*, vol. 3. IEEE, 1994, pp. III–329.

[178] J. M. O'Toole, "Choi-Williams distribution code," http://otoolej.github.io/code/fast-tfds/, 2010, Accessed: 26 May, 2021.

[179] P. Flandrin, "EMD method code," http://perso.ens-lyon.fr/patrick.flandrin/emd.html, 2007, Accessed: 20 August, 2021.

[180] O. P. Mahela, B. Khan, H. H. Alhelou, and P. Siano, "Power quality assessment and event detection in distribution network with wind energy penetration using Stockwell transform and fuzzy clustering," *IEEE Transactions on Industrial Informatics*, vol. 16, no. 11, pp. 6922–6932, 2020.

[181] V. Padhmashree and A. Bhattacharyya, "Human emotion recognition based on time–frequency analysis of multivariate EEG signal," *Knowledge-Based Systems*, vol. 238, p. 107867, 2022.

[182] A. J. D. Krupa, S. Dhanalakshmi, and R. Kumar, "Joint time-frequency analysis and non-linear estimation for fetal ECG extraction," *Biomedical Signal Processing and Control*, vol. 75, p. 103569, 2022.

[183] J. R. Torres-Castillo, C. O. López-López, and M. A. Padilla-Castañeda, "Neuromuscular disorders detection through time-frequency analysis and classification of multimuscular EMG signals using Hilbert-Huang transform," *Biomedical Signal Processing and Control*, vol. 71, p. 103037, 2022.

[184] Y. Wang, "Time–frequency domain local spectral analysis of seismic signals with multiple windows," *Proceedings of the Royal Society A*, vol. 478, no. 2265, p. 20220251, 2022.

[185] C.-M. Tsai, C.-S. Wang, Y.-J. Chung, Y.-D. Sun, and J.-W. Perng, "Multisensor fusion time–frequency analysis of thruster blade fault diagnosis based on deep learning," *IEEE Sensors Journal*, vol. 22, no. 20, pp. 19 761–19 771, 2022.

[186] A. Cicone, J. Liu, and H. Zhou, "Adaptive local iterative filtering for signal decomposition and instantaneous frequency analysis," *Applied and Computational Harmonic Analysis*, vol. 41, no. 2, pp. 384–411, 2016.

[187] L. Lin, Y. Wang, and H. Zhou, "Iterative filtering as an alternative algorithm for empirical mode decomposition," *Advances in Adaptive Data Analysis*, vol. 1, no. 04, pp. 543–560, 2009.

[188] V. K. Singh and R. B. Pachori, "Sliding eigenvalue decomposition-based cross-term suppression in Wigner–Ville distribution," *Journal of Computational Electronics*, vol. 20, pp. 2245–2254, 2021.

[189] M. H. Hansen and B. Yu, "Model selection and the principle of minimum description length," *Journal of the American Statistical Association*, vol. 96, no. 454, pp. 746–774, 2001.

[190] J. Terven, D.-M. Cordova-Esparza, J.-A. Romero-González, A. Ramírez-Pedraza, and E. Chávez-Urbiola, "A comprehensive survey of loss functions and metrics in deep learning," *Artificial Intelligence Review*, vol. 58, no. 7, p. 195, 2025.

[191] L. Stankovic, M. Daković, and T. Thayaparan, *Time-frequency signal analysis with applications*. Artech House, 2014.

[192] D. Fourer, J. Harmouche, J. Schmitt, T. Oberlin, S. Meignen, F. Auger, and P. Flandrin, "The ASTRES toolbox for mode extraction of non-stationary multicomponent signals," in *2017 25th European Signal Processing Conference (EUSIPCO)*. IEEE, 2017, pp. 1130–1134.

[193] T. Alexandrov, "A method of trend extraction using singular spectrum analysis," *Statistical Journal*, vol. 7, no. 1, pp. 1–22, 2009.

[194] J. Li, Z. Teng, Q. Tang, and J. Song, "Detection and classification of power quality disturbances using double resolution S-transform and DAG-SVMs," *IEEE Transactions on Instrumentation and Measurement*, vol. 65, no. 10, pp. 2302–2312, 2016.

[195] V. Mishra, V. K. Singh, and R. B. Pachori, "Automated power quality assessment using IEVDHM technique," in *2025 10th International Conference on Signal Processing and Communication (ICSC)*. IEEE, 2025, pp. 642–647.

[196] J. Heo, H. Yoon, and K. S. Park, "A novel wearable forehead EOG measurement system for human computer interfaces," *Sensors*, vol. 17, no. 7, p. 1485, 2017.

[197] Q. Huang, S. He, Q. Wang, Z. Gu, N. Peng, K. Li, Y. Zhang, M. Shao, and Y. Li, "An EOG-based human–machine interface for wheelchair control," *IEEE Transactions on Biomedical Engineering*, vol. 65, no. 9, pp. 2023–2032, 2017.

[198] M.-C. Chen, J.-X. Chen, R.-G. Hsu, J.-P. Su, W.-J. Chang, and Y.-K. Ou, "A gesture control system based on augmented reality and eye tracking technologies for a 3D-printed prosthetic arm," in *2024 IEEE International Conference on Consumer Electronics (ICCE)*. IEEE, 2024, pp. 1–3.

[199] R. S. Hessels and I. T. Hooge, "Eye tracking in developmental cognitive neuroscience–The good, the bad and the ugly," *Developmental Cognitive Neuroscience*, vol. 40, p. 100710, 2019.

[200] V. Asanza, J. Miranda, J. Miranda, L. Rivas, D. H. Peluffo-Ordóñez, E. Pelaez, F. Loayza, and O. Alejandro, "Electrooculography signals classification for FPGA-based human-computer interaction," in *2022 IEEE ANDESCON*. IEEE, 2022, pp. 1–7.

[201] C.-T. Lin, J.-T. King, P. Bharadwaj, C.-H. Chen, A. Gupta, W. Ding, and M. Prasad, "EOG-based eye movement classification and application on HCI baseball game," *IEEE Access*, vol. 7, pp. 96 166–96 176, 2019.

[202] A. López, J. R. Villar, M. Fernández, and F. J. Ferrero, "Comparison of classification techniques for the control of EOG-based HCIs," *Biomedical Signal Processing and Control*, vol. 80, p. 104263, 2023.

[203] V. Asanza, J. Miranda, N. Sánchez, E. Peláez, F. Loayza, and D. H. Peluffo-Ordóñez, "Electromyography (EMG) of the extraocular muscles (EOM)," 2021. [Online]. Available: https://dx.doi.org/10.21227/bhpj-mz94

[204] S. I. Khan and R. B. Pachori, "Automated eye movement classification based on EMG of EOM signals using FBSE-EWT technique," *IEEE Transactions on Human-Machine Systems*, vol. 53, no. 2, pp. 346–356, 2023.

[205] World Health Organization, "Dementia," 2023. [Online]. Available: https://www.who.int/news-room/fact-sheets/detail/dementia

[206] A. E. Budson and P. R. Solomon, *Memory Loss, Alzheimer's Disease, and Dementia*. Elsevier, 2015.

[207] Mayo Clinic, "Alzheimer's disease," 2024. [Online]. Available: https://www.mayoclinic.org/diseases-conditions/alzheimers-disease/diagnosis-treatment/drc-20350453

[208] A. M. Pineda, F. M. Ramos, L. E. Betting, and A. S. Campanharo, "Quantile graphs for EEG-based diagnosis of Alzheimer's disease," *Plos One*, vol. 15, no. 6, p. e0231169, 2020.

[209] Y. Chen, H. Wang, D. Zhang, L. Zhang, and L. Tao, "Multi-feature fusion learning for Alzheimer's disease prediction using EEG signals in resting state," *Frontiers in Neuroscience*, vol. 17, p. 1272834, 2023.

[210] M. Nour, U. Senturk, and K. Polat, "A novel hybrid model in the diagnosis and classification of Alzheimer's disease using EEG signals: Deep ensemble learning (DEL) approach," *Biomedical Signal Processing and Control*, vol. 89, p. 105751, 2024.

[211] M. Imani, "Alzheimer's diseases diagnosis using fusion of high informative BiLSTM and CNN features of EEG signal," *Biomedical Signal Processing and Control*, vol. 86, p. 105298, 2023.

[212] S. Siuly, Ö. F. Alçin, H. Wang, Y. Li, and P. Wen, "Exploring rhythms and channels-based EEG biomarkers for early detection of Alzheimer's disease," *IEEE Transactions on Emerging Topics in Computational Intelligence*, 2024.

[213] M. L. Vicchietti, F. M. Ramos, L. E. Betting, and A. S. Campanharo, "Computational methods of EEG signals analysis for Alzheimer's disease classification," *Scientific Reports*, vol. 13, no. 1, p. 8184, 2023.

[214] R. E. Banfield, L. O. Hall, K. W. Bowyer, and W. P. Kegelmeyer, "A comparison of decision tree ensemble creation techniques," *IEEE Transactions on Pattern Analysis and Machine Intelligence*, vol. 29, no. 1, pp. 173–180, 2006.

[215] M. A. Hearst, S. T. Dumais, E. Osuna, J. Platt, and B. Scholkopf, "Support vector machines," *IEEE Intelligent Systems and Their Applications*, vol. 13, no. 4, pp. 18–28, 1998.

[216] M. L. Vicchietti, F. M. Ramos, L. E. Betting, and A. S. Campanharo, "Data from: Computational methods of EEG signals analysis for Alzheimer's disease classification," Feb 2023. [Online]. Available: osf.io/2v5md

[217] A. Nalwaya, V. K. Singh, and R. B. Pachori, "Emotion identification based on EEG rhythms separated using improved eigenvalue decomposition of Hankel matrix," in *2023 9th International Conference on Signal Processing and Communication (ICSC)*. IEEE, 2023, pp. 562–567.

[218] D. P. Doane and L. E. Seward, "Measuring skewness: A forgotten statistic?" *Journal of Statistics Education*, vol. 19, no. 2, 2011.

[219] T. Van Huynh *et al.*, "Classification I-EEG signals using ensemble algorithms," in *2022 9th NAFOSTED Conference on Information and Computer Science (NICS)*. IEEE, 2022, pp. 235–240.

[220] K. Das and R. B. Pachori, "Multivariate iterative filtering-based SSVEP detection in mobile environment for brain–computer interface application," *IEEE Sensors Letters*, vol. 8, no. 4, p. 6003604, 2024.

[221] A. S. Ashour, Y. Guo, A. R. Hawas, and G. Xu, "Ensemble of subspace discriminant classifiers for schistosomal liver fibrosis staging in mice microscopic images," *Health Information Science and Systems*, vol. 6, pp. 1–10, 2018.

[222] A. Zamora-Mendez, R. D. R. de Luna, J. A. de la O Serna, J. H. Chow, and M. R. A. Paternina, "Electromechanical modes identification based on an iterative eigenvalue decomposition of the Hankel matrix," *IEEE Transactions on Power Systems*, vol. 38, no. 1, pp. 155–167, 2022.

[223] T. Oberlin, S. Meignen, and V. Perrier, "The Fourier-based synchrosqueezing transform," in *2014 IEEE international conference on acoustics, speech and signal processing (ICASSP)*. IEEE, 2014, pp. 315–319.

[224] D.-H. Pham and S. Meignen, "High-order synchrosqueezing transform for multicomponent signals analysis—With an application to gravitational-wave signal," *IEEE Transactions on Signal Processing*, vol. 65, no. 12, pp. 3168–3178, 2017.

[225] G. Strang, *Introduction to linear algebra*. SIAM, 2022.

[226] C. L. DiMonte and K. Arun, "Tracking the frequencies of superimposed time-varying harmonics," in *International Conference on Acoustics, Speech, and Signal Processing*. IEEE, 1990, pp. 2539–2542.

[227] M. W. Poon, R. H. Khan, and S. Le-Ngoc, "A singular value decomposition (SVD) based method for suppressing ocean clutter in high frequency radar," *IEEE Transactions on Signal Processing*, vol. 41, no. 3, pp. 1421–1425, 1993.

[228] N. Phukan, M. S. Manikandan, and R. B. Pachori, "Fast straightforward RR interval extraction based atrial fibrillation detection using Shannon entropy and machine learning classifiers for wearables," in *2023 IEEE 9th International Conference on Smart Instrumentation, Measurement and Applications (ICSIMA)*. IEEE, 2023, pp. 24–29.

[229] N. Phukan, M. S. Manikandan, and R. B. Pachori, "Fast and resource efficient atrial fibrillation detection framework for long term health monitoring devices," *IEEE Sensors Letters*, vol. 8, no. 4, pp. 1–4, 2024.

[230] L. S. Vidyaratne and K. M. Iftekharuddin, "Real-time epileptic seizure detection using EEG," *IEEE Transactions on Neural Systems and Rehabilitation Engineering*, vol. 25, no. 11, pp. 2146–2156, 2017.

[231] D. Sopic, A. Aminifar, and D. Atienza, "e-Glass: A wearable system for real-time

detection of epileptic seizures," in *2018 IEEE International Symposium on Circuits and Systems (ISCAS)*. IEEE, 2018, pp. 1–5.

[232] A. S. Zandi, M. Javidan, G. A. Dumont, and R. Tafreshi, "Automated real-time epileptic seizure detection in scalp EEG recordings using an algorithm based on wavelet packet transform," *IEEE Transactions on Biomedical Engineering*, vol. 57, no. 7, pp. 1639–1651, 2010.

[233] J. Zhang, F. Feng, P. Marti-Puig, C. F. Caiafa, Z. Sun, F. Duan, and J. Solé-Casals, "Serial-EMD: Fast empirical mode decomposition method for multi-dimensional signals based on serialization," *Information Sciences*, vol. 581, pp. 215–232, 2021.

[234] S. Sharma, A. Shedsale, and R. R. Sharma, "Multivariate fast iterative filtering based automated system for grasp motor imagery identification using EEG signals," *International Journal of Human–Computer Interaction*, vol. 40, no. 23, pp. 7915–7923, 2024.

[235] G. E. Carlson, *Signal and linear system analysis*. John Wiley Hoboken, NJ, 1998.

[236] M. Mandal and A. Asif, *Continuous and discrete time signals and systems*. Cambridge University Press, 2007.

[237] W. K. Chen, *The electrical engineering handbook*. Academic Press, 2005.

[238] M. Tammen, I. Kodrasi, and S. Doclo, "Complexity reduction of eigenvalue decomposition-based diffuse power spectral density estimators using the power method," in *2018 IEEE International Conference on Acoustics, Speech and Signal Processing (ICASSP)*. IEEE, 2018, pp. 451–455.

List of Publications

Outcomes from Ph.D. thesis work

In Refereed Journals

1. **V. K. Singh** and R. B. Pachori, "Iterative eigenvalue decomposition of Hankel matrix: An EMD like tool," *Journal of the Franklin Institute*, vol. 362, no. 17, p. 108104, 2025.

2. **V. K. Singh** and R. B. Pachori, "Detection of Alzheimer's disease from EEG signals using improved MCh-EVDHM-based rhythm separation," *IEEE Sensors Letters*, vol. 8, no. 10, p. 6013104, 2024.

3. **V. K. Singh** and R. B. Pachori, "Multichannel eigenvalue decomposition of Hankel matrix based classification of eye movements from electrooculogram," *IEEE Sensors Letters*, vol. 8, no. 7, p. 6008204, 2024.

4. **V. K. Singh** and R. B. Pachori, "Sliding eigenvalue decomposition-based cross-term suppression in Wigner–Ville distribution," *Journal of Computation Electronics*, vol. 20, pp. 2245–2254, 2021.

5. **V. K. Singh** and R. B. Pachori, "Eigenvalues-based time-frequency analysis," *Journal of the Franklin Institute*, Under review.

6. **V. K. Singh** and R. B. Pachori, "Computationally efficient eigenvalue decomposition of Hankel matrix, " *Signal Processing*, Under review.

In Refereed Conferences

1. **V. K. Singh** and R. B. Pachori, "Sliding eigenvalue decomposition for non-stationary signal analysis,"in 2020 *International Conference on Signal Processing and Communication (SPCOM)*, pp. 1-5, 2020.

Outcomes from other than Ph.D. thesis work

In Refereed Journals

1. K. K. Makam, **V. K. Singh**, and R. B. Pachori, "Eye movement detection based on SM-SSA and quantum CNN from EMG of EOM signals," *IEEE Sensors Letters*, vol. 9, no. 5, p. 6004504, 2025.

2. A. Tyagi, **V. K. Singh**, and R. B. Pachori, "FBSE-EWT technique-based complex-valued signal analysis," *Circuits, Systems, and Signal Processing*, vol. 44, pp. 1349–1370, 2025.

3. K. K. Makam, **V. K. Singh**, and R. B. Pachori, "ALS detection framework based on automatic singular spectrum analysis and quantum convolutional neural network from EMG signals," *IEEE Sensors Letters*, vol. 8, no. 9, p. 6012004, 2024.

4. A. Nalwaya, **V. K. Singh**, and R. B. Pachori, "Emotion identification from physiological signals using iterative filtering-based empirical wavelet transform," *IEEE Sensors Journal*, Under review.

5. A. Nalwaya, **V. K. Singh**, and R. B. Pachori, "Signal processing and machine learning techniques for human emotion identification using EEG, ECG, and PCG: A review, To be submitted.

In Refereed Conferences

1. A. Nalwaya, **V. K. Singh**, and R. B. Pachori, "Emotion identification based on EEG rhythms separated using improved eigenvalue decomposition of Hankel matrix," 2023 9th *International Conference on Signal Processing and Communication (ICSC)*, pp. 562-567, 2023.

2. V. Mishra, **V. K. Singh**, and R.B. Pachori, "Power quality assessment using IEVDHM technique," 2025 10th *International Conference on Signal Processing and Communication (ICSC)*, pp. 642-647, 2025.

In Book chapters

1. K. Das, **V. K. Singh**, and R. B. Pachori, "Introduction to EEG signal recording and processing,"*Artificial Intelligence Enabled Signal Processing based Models for Neural Information Processing*, CRC Press, pp. 1-19, 2024.

About the Author

Vivek Kumar Singh was born in Deoria, Uttar Pradesh, India, in February 1997. He received a Bachelor of Technology degree in Electronics and Communication Engineering from the Ambedkar Institute of Advanced Communication Technologies and Research, New Delhi, India, in 2017 and Master of Technology degree in Communication Systems from the National Institute of Technology Patna, Patna, India, in 2019. He joined the Ph.D. program in the Department of Electrical Engineering at the Indian Institute of Technology Indore, India in June 2019. His research interests include time-frequency analysis, non-stationary signal processing, and physiological signal processing.